

The Synthesis and Autoxidation of Polyisobutenyl Succinimide Dispersants for Engine Oil Lubricants

Jonathan Edward Ruffell

Doctor of Philosophy

University of York

Chemistry

September 2020

In memory of Crispin Rope

Abstract

Background: Polyisobutenyl succinimide (PIBSI) dispersants are amphiphiles used in engine oil lubricants to disperse insoluble autoxidation products. By maintaining lubricant viscosity and flow they increase lubricant and engine lifetime; however the effect of PIBSIs on lubricant autoxidation, and autoxidation on PIBSIs themselves, was previously unstudied.

Aim: Determine PIBSI synthesis and autoxidation mechanisms.

Methods: Radical reactions in polyisobutenyl succinic anhydride (PIBSA) synthesis—a key synthetic intermediate—were investigated using NMR spectroscopy. Alkenyl succinimides (ASIs)—high-purity chemical mimics for PIBSI dispersants—were synthesised and oxidised in bulk and when dissolved in a model oil (squalane). Product studies using GC-EI-MS and GC-FID identified and quantified oxidation products to determine ASI autoxidation mechanisms.

Results: A previously unknown and highly selective radical mechanism for PIBSA formation was elucidated. A carbon-centred radical forms by site-selective hydrogen abstraction from α -polyisobutene (α -PIB) which then adds to maleic anhydride. The resultant adduct abstracts a hydrogen atom from a second α -PIB equivalent forming PIBSA and generating another α -PIB radical, propagating the chain reaction.

When an n-alkyl chain was attached to the ASI nitrogen its high autoxidation rate was due to allylic hydrogen abstraction. The major degradation route of the resultant carbon-centred radical was recombination where larger molecules contributed to a 300-fold shear-dependent viscosity increase. 17% of reacted ASI underwent C–C bond cleavage, breaking the amphiphile and deactivating the dispersant.

ASIs containing linear-aminic hydrophiles were oxidised in a model lubricant. They acted as antioxidants. Tertiary amines were the most effective antioxidants and the alkene had minimal impact. Cope elimination products suggested nitrogen oxidation. It is proposed nitroxyl radicals are formed which destroy peroxides through the Denisov cycle. In industrial tests, diethylamino ASI showed improved oxidation performance over an antioxidant-free formulation and deposit formation equalled a commercial antioxidant.

Conclusions: Radicals are important in the synthesis of PIBSI dispersants and should be minimised to improve dispersant production. ASI models showed dispersant autoxidation could limit performance but the development of dual antioxidant-dispersant additives could improve lubricant performance.

Contents

Abstract	v
List of figures	xii
List of tables	xxii
Acknowledgements	xxvii
Declaration	xxix
1 General Introduction	1
1.1 General Background	2
1.2 Engine oil lubricants	3
1.2.1 Base oil	4
1.2.2 Lubrication and Newtonian viscosity	5
1.2.2.1 Viscosity index improvers	8
1.2.3 Non-Newtonian lubricant viscosity	8
1.3 Dispersants	10
1.3.1 PIBSI synthesis	12
1.3.1.1 PIB and PIBSA synthesis	13
1.3.1.2 Amines	15
1.3.2 Impact of dispersant structure	15
1.3.3 Dispersant interactions	16
1.3.3.1 Dispersants with zinc dialkyldithiophosphate (ZDDP) antiwear agents	17
1.3.3.2 Dispersants with molybdenum dithiocarbamate (MoDTC) friction modifiers	18
1.3.3.3 Dispersants with detergents	20
1.4 Autoxidation	21
1.4.1 Antioxidants	24
1.5 Dispersants and autoxidation	25
1.6 Project aims	26

2	Experimental	29
2.1	Experimental procedures supporting Chapter 3	30
2.1.1	PIBSA synthesis A	31
2.1.2	PIBSA synthesis B	31
2.1.3	PIBSA synthesis C	32
2.1.4	Bis-PIBSA formation under radical conditions	33
2.1.5	Bis-PIBSA formation under Alder ene conditions	33
2.1.6	Itaconic anhydride addition to PIB	33
2.1.7	Styrene-assisted MAH addition to PIB	34
2.1.8	PIBSA analysis	34
2.2	Experimental procedures supporting Chapter 4	35
2.2.1	General <i>N</i> -alkyl alkenyl succinimide (ASI) synthesis procedure	35
2.2.2	<i>N</i> -butyl ASI hydrogenation	35
2.2.3	Neat <i>N</i> -alkyl ASI autoxidation	36
2.2.4	<i>N</i> -alkyl ASI autoxidation in squalane	37
2.3	Experimental procedures supporting Chapter 5	38
2.3.1	Diethylamino alkenyl succinimide (DEA-ASI) synthesis	38
2.3.2	Dimethylamino alkenyl succinimide (DMA-ASI) synthesis	38
2.3.3	Monomethylamino alkenyl succinimide (MMA-ASI) synthesis	39
2.3.4	Dimethylamino alkenyl succinimide (DMA-ASI) hydrogenation	40
2.3.5	Amino ASI autoxidation in squalane	40
2.3.6	Performance testing of diethylamino ASI using industry-standard tests	41
2.3.6.1	Large scale diethylamino ASI (DEA-ASI) synthesis	41
2.4	Analysis	42
2.4.1	Gas chromatography with flame ionisation detection (GC-FID)	42
2.4.1.1	Shimadzu GC-17a gas chromatograph	42
2.4.1.2	Agilent 6890 gas chromatograph	43
2.4.1.3	Agilent 7890 gas chromatograph	43
2.4.1.4	GC-FID Calibration	44
2.4.2	Gas chromatography electron ionisation mass spectrometry (GC-EI-MS)	46
2.4.2.1	Unit mass GC-EI-MS	46
2.4.2.2	Accurate mass GC-EI-MS	47
2.4.2.3	GC-MS sample derivatisation	47

2.4.3	Electrospray ionisation mass spectrometry	48
2.4.4	Attenuated total reflectance Fourier transform infrared spectroscopy	48
2.4.5	Nuclear magnetic resonance spectroscopy	48
2.4.6	Rheometry	49
2.4.7	Oxygen consumption estimation	49
2.5	Materials	51
3	The role of radicals in the synthesis of polyisobutenyl succinic anhydrides	53
3.1	Introduction	54
3.2	Results	55
3.2.1	Conventional PIBSA synthesis	55
3.2.2	PIBSA 3 synthesis via radical addition	58
3.2.3	Radical initiator source	61
3.2.4	Competing PIB loss mechanisms	64
3.2.4.1	PIB loss through evaporation	64
3.2.4.2	PIB conversion through autoxidation	67
3.2.5	Further PIBSA synthesis results	69
3.2.5.1	Itaconic anhydride as an alternative to maleic anhydride	69
3.2.5.2	Styrene assisted MAH addition	70
3.2.5.3	The formation of bis-PIBSAs	70
3.3	Discussion	72
3.3.1	Initiation	74
3.3.2	MAH addition	76
3.3.3	Hydrogen transfer	79
3.3.4	Competing reactions during PIBSA synthesis	80
3.3.5	Comparison with industrial PIBSA	81
3.3.6	Implications for industry	83
3.4	Conclusion	84
4	The autoxidation of alkenyl succinimides—mimics for PIBSI dispersants	87
4.1	Introduction	88
4.2	Results	90
4.2.1	ASI autoxidation products	90
4.2.2	Characterisation of novel compounds from <i>N</i> -butyl ASI autoxidation	97

4.2.2.1	Product 5 - 3-Methyl, <i>N</i> -butyl ASI	97
4.2.2.2	Product 8 - succinimide aldehyde	98
4.2.2.3	Product 9 - α, β -unsaturated succinimide aldehyde	100
4.2.2.4	Product 10 - <i>N</i> -butyl ASI alcohol	103
4.2.2.5	Product 11 - <i>N</i> -butyl ASI ketone	105
4.2.2.6	Product 12 - <i>N</i> -butyl ASI dehydrodimer	108
4.2.2.7	Product 14 - succinimide acid	110
4.2.2.8	Product 15 - C ₂ ,C ₃ <i>N</i> -butyl ASI diol	112
4.2.3	Product distribution	116
4.2.4	Viscosity increase on autoxidation	119
4.2.5	ASI autoxidation in a model base oil	119
4.3	Discussion	121
4.3.1	ASI autoxidation mechanisms	121
4.3.1.1	Products from alkoxy radical formation	122
4.3.1.2	Hydroxyl radical addition to the alkene	124
4.3.1.3	Recombination	126
4.3.1.4	Mechanism overview	126
4.3.1.5	Relative reactivities	128
4.3.1.6	Viscosity increase	128
4.3.1.7	Implications for PIBSI dispersant degradation during use in engine lubricants	129
4.4	Conclusion	130
5	Amine-containing alkenyl succinimide dispersant mimics	131
5.1	Introduction	132
5.2	Results	133
5.2.1	Amino ASI autoxidation in a model lubricant	133
5.2.1.1	Oxygen consumption	134
5.2.1.2	GC-FID	137
5.2.1.3	Amino ASI autoxidation products	143
5.2.2	Oxidation in a real lubricant	148
5.3	Discussion	153
5.3.1	Formation of products 1 and 4	154
5.3.2	Formation of products 2 and 3	156

5.3.3	Antioxidant mechanisms of amino ASIs	157
5.3.4	ASI autoxidation in fully formulated lubricants	159
5.3.4.1	Implications for commercial dispersant behaviour	161
5.3.4.2	Implications for commercial dispersant development	163
5.4	Conclusion	163
6	Conclusions and future work	165
6.1	Radicals in polyisobutenyl succinic anhydride (PIBSA) synthesis	166
6.2	The autoxidation of <i>N</i> -alkyl alkenyl succinimides (ASIs)	167
6.3	The autoxidation of amine-containing alkenyl succinimides (ASIs)	168
6.4	Key learnings	168
6.5	Future work	169
6.6	The future of engine oil lubricants	170
7	Appendix	173
7.1	Supplementary information for Chapter 3	174
7.1.1	Structural assignment of PIBSA 3	174
7.1.2	The effect of MAH purity on PIBSA synthesis	176
7.1.3	Characterisation of low molecular weight polyisobutenes	177
7.2	Supplementary information for Chapter 4	179
7.2.1	Alkyl ASI characterisation	179
7.2.1.1	<i>N</i> -propyl ASI	179
7.2.1.2	<i>N</i> -butyl ASI	180
7.2.1.3	<i>N</i> -pentyl ASI	180
7.2.1.4	<i>N</i> -hexyl ASI	181
7.2.1.5	<i>N</i> -heptyl ASI	182
7.2.1.6	H ₂ - <i>N</i> -butyl ASI	183
7.2.2	Autoxidation product identification	184
7.2.3	Analysis of condensed-volatiles from the autoxidation of model lubricants with and without <i>N</i> -butyl ASI	187
7.3	Supplementary information for Chapter 5	190
7.3.1	Amino ASI characterisation	190
7.3.1.1	Diethylamino ASI	190
7.3.1.2	Dimethylamino ASI	190

Contents

7.3.1.3	Monomethylamino ASI	191
7.3.1.4	H ₂ -Dimethylamino ASI	192
	Abbreviations	195
	Bibliography	197

List of Figures

1.1	A reproduction of a wall painting found in the tomb of Djehutihotep c. 1880 BCE. Reproduced from Fall <i>et al.</i> 2014. ¹	2
1.2	Examples of possible hydrocarbon structures found in refined mineral oils.	4
1.3	Asperity contact between two metal surfaces (left) and the prevention of asperity contact by a lubricant film (right, yellow = lubricant film).	5
1.4	Absolute viscosity, reproduced from Prince. ⁷	6
1.5	Two common viscosity index improvers.	8
1.6	The structure of soot agglomerates reproduced from Growney <i>et al.</i> ¹⁷	9
1.7	A representation of dispersants breaking up polar agglomerates in a lubricant oil.	10
1.8	The effect of dispersant concentration on soot dispersion after a 288 hour sequence VE engine test. Reproduced from Seddon <i>et al.</i> ²²	11
1.9	The four main types of dispersant. R = alkyl chain, typically PIB. R ₁ is a poly alcohol.	11
1.10	The idealised structure of a polyisobutenyl succinimide dispersant where n is typically 16-60, m is typically 3 and R = NH ₂ or PIBSI. ³²	12
1.11	The general procedure for the synthesis of PIBSI dispersants where R is usually a polyamine.	12
1.12	Polyisobutenyl succinic anhydride (PIBSA).	13
1.13	Formation of PIBSAs by PIB chlorination and subsequent Diels-Alder maleic anhydride (MAH) addition.	13
1.14	The two major alkene isomers of commercial polyisobutene produced by BF ₃ catalysed polymerisation of isobutene. ⁴⁷	14
1.15	PIBSA formation by the Alder-ene addition of maleic anhydride (MAH) to vinylidene terminated PIB.	14
1.16	The formation of a bis-PIBSA by addition of MAH to PIBSA.	15
1.17	Tetraethylenepentamine.	15
1.18	The general structure of zinc dialkyldithiophosphate (ZDDP) where R is an alkyl chain. ⁷³	17
1.19	The dispersant/ZDDP complex proposed by Harrison <i>et al.</i> ⁷⁶	18

1.20	Two of the most common friction modifiers—oleamide and glycerol monooleate—and a representation of how they would arrange on a metal surface to prevent contact and reduce friction.	19
1.21	The general structure of molybdenum dithiocarbamate (MoDTC) where R is an alkyl chain. ⁸⁵	19
1.22	The four main detergent anions used in engine oil lubricants. R is an alkyl chain. For sulfonates, R = 15–30 carbon atoms. For phenates, R = 5–30 carbon atoms. For salicylates and carboxylates, R = 12–30 carbon atoms.	20
1.23	A representation of an over-based detergent colloid, where calcium carbonate is suspended in a detergent inverse micelle.	20
1.24	A simplified reaction mechanism for the autoxidation of alkanes to yield various oxygen containing products.	22
1.25	Squalane (2,6,10,15,19,23-hexamethyltetracosane) and pristane (2,6,10,14-tetramethylpentadecane).	23
1.26	The general structures of phenolic and aminic antioxidants where R is an alkyl chain.	24
1.27	Quenching of an alkyl radical by the antioxidant butylated hydroxytoluene (BHT).	24
1.28	Resonance stabilisation of the BHT radical.	25
1.29	The three ¹⁴ C labelled PIBSIs studied by Erdman. ¹¹³ * denotes the labelling sites.	26
2.1	A schematic of the experimental set up used for neat ASI autoxidation.	36
2.2	2,6,10,15,19,23-hexamethyltetracosane (C ₃₀ H ₆₂) commonly known as squalane.	37
2.3	The experimental set up used for ASI autoxidation in squalane.	37
2.4	An example of the calibration curves produced in this work along with the graph of response factor against effective carbon number (bottom right). Gradients and intercepts are shown with standard error. All intercept values are within two standard errors. The ECN calibration standard error is ±1.5%.	46
2.5	An example of the oxygen concentration and consumption during the oxidation of a model lubricant.	50
3.1	PIBSA formation by the Alder-ene addition of maleic anhydride (MAH) to vinylidene terminated PIB.	54

3.2	The three major PIBSA isomers characterised by Balzano <i>et al.</i> ³²	54
3.3	Formation mechanism of PIBSA 3 proposed by Balzano <i>et al.</i> ³²	54
3.4	The concentration of PIB and its conversion during the reaction of PIB and MAH on a 20 g scale at 200 °C with a 1:1 MAH:PIB ratio.	56
3.5	The PIBSA yield and PIBSA selectivity during the reaction of PIB and MAH on a 20 g scale at 200 °C with a 1:1 MAH:PIB ratio.	56
3.6	A comparison of the alkene region (4.5–5.5 ppm) of the ¹ H-NMR spectra of polyisobutene (bottom), PIBSA synthesised on a 20 g scale (middle) and PIBSA synthesised on a 100 g scale (top).	57
3.7	2,4,6-tri- <i>tert</i> -butylphenol, a radical scavenging antioxidant (AO).	60
3.8	NMR spectra in the alkene region (4.5–5.5 ppm) of PIBSA synthesised on a 500 mg scale under argon for five hours, either with (top) or without (bottom) a radical scavenging antioxidant (2,4,6-tri- <i>tert</i> -butylphenol).	61
3.9	The crude ¹ H-NMR spectra from five different 500 mg scale PIBSA synthesis reactions using a 1:1 PIB:MAH ratio. Corresponding procedures and PIBSA 3 yields are reported in Table 3.3.	63
3.10	A GC-FID chromatogram of Mn = 950 g mol ⁻¹ PIB with peaks labelled according to the number of isobutene units in the oligomer. Inset; an expansion of the chromatogram between 30 and 50 minutes denoting the number of isobutene units and the alkene isomer (α or β).	65
3.11	The concentrations of α and β PIB oligomers after heating of a 500 mg sample at 200 °C for 5 hours with an antioxidant present. Concentrations were determined by GC-FID and are reported relative to their concentration in PIB before heating.	67
3.12	1° and 2° PIB alcohols observed by ¹ H-NMR spectroscopy with resonances at 3.18 (H') and 3.75 (H'') ppm respectively. ¹³⁶	68
3.13	The concentrations of α and β PIB oligomers after heating to 200 °C for 5 hours under argon without AO. Concentrations were determined by GC-FID and are reported relative to their concentration prior to heating.	68
3.14	The possible reaction of MAH with PIBSA 3 by the Alder-ene and radical addition pathways.	71
3.15	The three main PIBSA isomers characterised by Balzano <i>et al.</i> ³²	72

3.16	PIBSA 1 formation by the Alder-ene addition of maleic anhydride (MAH) to vinylidene terminated PIB.	72
3.17	The formation of PIBSA 3 by Alder-ene addition of MAH to β PIB proposed by Balzano <i>et al.</i> ³²	72
3.18	The proposed radical chain mechanism for PIBSA 3 formation from α PIB initiated by O ₂ or radical products of thermal peroxide homolysis.	74
3.19	A comparison of the ¹ H-NMR spectra of lab synthesized PIBSA (top) with a commercial sample of comparable molecular weight (bottom) in the region showing alkene protons (4.5–5.5 ppm). PIBSA 1 (H ⁴) and PIBSA 3 (H ⁵ and H ⁶) are shown, along with known proton signals from PIBSA 2 (2), α PIB (A and A') and β PIB (B).	82
3.20	A comparison of the ¹ H-NMR spectra of lab synthesized PIBSA (top) with a commercial sample of comparable molecular weight (bottom) in the region showing succinic anhydride protons (1.5–3.5 ppm).	83
4.1	The idealised structure of a polyisobutenyl succinimide dispersant where n is typically 16-60, m is typically 3 and R = NH ₂ or alkenyl succinimide. ³²	88
4.2	<i>N</i> -butyl ASI, the main alkenyl succinimide studied in this chapter.	88
4.3	A comparison between the structures of PIBSI dispersants and ASI model dispersants.	89
4.4	The labelling system for ASIs, R = <i>n</i> -propyl to <i>n</i> -heptyl.	90
4.5	2,6,10,15,19,23-Hexamethyltetracosane (C ₃₀ H ₆₂) commonly known as squalane.	90
4.6	A GC-FID chromatogram of oxidised <i>N</i> -butyl ASI (autoxidation at 170 °C for 30 minutes) showing degradation products (1-9), unreacted <i>N</i> -butyl ASI, oxygenated ASI products 10 and 11 , and the <i>N</i> -butyl ASI dehydrodimer (12).	91
4.7	An expansion of the GC-FID chromatogram in Figure 4.6 showing unreacted <i>N</i> -butyl ASI and oxygenated ASI products 10 and 11 .	91
4.8	A GC-FID chromatogram of oxidised <i>N</i> -butyl ASI (autoxidation at 170 °C for 180 minutes) showing degradation products 13 and 14 , unreacted <i>N</i> -butyl ASI and oxygenated ASI product 15 .	92
4.9	An expansion of the GC-FID chromatogram in Figure 4.8 showing unreacted <i>N</i> -butyl ASI and oxygenated ASI products 10 , 11 and 15 .	93

4.10	GC-FID chromatograms of oxidised ASIs (<i>N</i> -propyl to <i>N</i> -heptyl, 170 °C, 30 minutes) between 0 and 35 minutes. Species with equivalent retention times (1 , 2 , 3 , 6 and 7) originate from the ASI “tail”. Species originating from the succinimide “head” group (4* , 5* , 8* and 9*) show increasing retention time with increasing <i>N</i> -alkyl chain lengths.	94
4.11	The structure of product 5 , 3-methyl, <i>N</i> -butyl succinimide.	97
4.12	The EI mass spectrum of product 5 , 3-methyl, <i>N</i> -butyl succinimide.	97
4.13	The structure of product 8 - succinimide aldehyde	98
4.14	An EI mass spectrum of the succinimide aldehyde, product 8 .	100
4.15	The structure of the α , β -unsaturated succinimide aldehyde, product 9 .	100
4.16	The EI mass spectrum of the α , β -unsaturated succinimide aldehyde, product 9 .	101
4.17	The four isomers of product 10 , <i>N</i> -butyl ASI alcohol, observed in this work.	103
4.18	An EI-MS spectrum of the four co-eluting silylated <i>N</i> -butyl ASI alcohols (green) overlaid with a spectrum from the <i>N</i> -butyl ASI alcohol (10 , red).	105
4.19	The structure of the C ₄ <i>N</i> -butyl ASI ketone, product 11 .	105
4.20	An EI mass spectrum of the C ₄ <i>N</i> -butyl ASI ketone (11).	107
4.21	The C ₄ -C ₄ <i>N</i> -butyl ASI dehydrodimer, an example structure for the one of the possible <i>N</i> -butyl ASI dehydrodimers.	108
4.22	An EI mass spectrum of the <i>N</i> -butyl ASI dehydrodimer with its molecular ion at <i>m/z</i> 640 and strong base peak at <i>m/z</i> 320.	109
4.23	The structure of the succinimide acid (14).	110
4.24	An expansion of the GC chromatogram showing the shark fin behaviour of peak 14 which is consistent with the elution of a highly polar species, such as a carboxylic acid, on a comparatively non-polar GC column.	110
4.25	The electron ionisation (EI) mass spectrum of the succinimide acid (14).	111
4.26	The EI mass spectrum of the silyl ester derivative of the succinimide acid (14).	111
4.27	C ₂ ,C ₃ <i>N</i> -butyl ASI diol (15).	112
4.28	The EI mass spectrum of the acetone derivative of the C ₂ ,C ₃ <i>N</i> -butyl ASI diol (15).	112
4.29	The EI mass spectrum of the bis-silylated C ₂ ,C ₃ <i>N</i> -butyl ASI diol (15).	114
4.30	The concentration <i>N</i> -butyl ASI alcohols, (10), <i>N</i> -butyl ASI ketone (11) and the C ₂ ,C ₃ <i>N</i> -butyl ASI diol (15) during the autoxidation. The concentration of <i>N</i> -butyl ASI is also shown.	116

- 4.31 The concentrations of the primary degradation products of *N*-butyl ASI and the *N*-butyl ASI dehydrodimer. Error bars of standard error are also shown. 117
- 4.32 The selectivity for all observed degradation products and all observed oxygenated ASI products. The concentration of *N*-butyl ASI is also shown. 118
- 4.33 The dynamic viscosity behaviour of *N*-butyl ASI after autoxidation at 170 °C for three hours. Three cycles are shown with shear rates between 50 s⁻¹ and 750 s⁻¹. 119
- 4.34 The natural logarithm of squalane, *N*-butyl ASI and H₂-*N*-butyl ASI concentrations during autoxidation at 170 °C. The data for squalane concentrations is from the autoxidation of squalane with no ASI present. Pseudo-first order rate constants were calculated from the linear fit after the 15-minute induction period. 120
- 4.35 The mechanism for ASI autoxidation showing the three major routes to the thirteen primary products identified of ASI autoxidation. 127
- 5.1 *N*-butyl ASI, the main dispersant mimic studied in Chapter 4. 132
- 5.2 The amine-containing ASIs studied in this chapter—diethylamino ASI (DEA-ASI), dimethylamino ASI (DMA-ASI), H₂-dimethylamino ASI (H₂-DMA-ASI) and monomethylamino ASI (MMA-ASI). 133
- 5.3 2,6,10,15,19,23-Hexamethyltetracosane (squalane, C₃₀H₆₂), the model base oil used in this study. 133
- 5.4 Oxygen consumption from the autoxidation of squalane and a 5% (w/w) solution of *N*-butyl ASI in squalane at 170 °C for 90 minutes. The data are an average of three experiments with error bars of one standard deviation. 135
- 5.5 Oxygen consumption from the autoxidation of squalane and 5% (w/w) solutions of three amino ASIs (MMA-ASI, DMA-ASI and DEA-ASI) in squalane oxidised at 170 °C for 90 minutes. The data shown are an average of three experiments with error bars of one standard deviation. 136
- 5.6 Oxygen consumption from the autoxidation of squalane and 5% (w/w) solutions of DMA-ASI and H₂-DMA-ASI in squalane oxidised at 170 °C for 90 minutes. The data shown are an average of three experiments with error bars of one standard deviation except for H₂-DMA-ASI which is from a single experiment. 137

-
- 5.7 GC-FID traces of model lubricants oxidised for 90 minutes at 170 °C. The figure shows the 90 minute traces for pure squalane (top), 5% (w/w) DEA-ASI in squalane (middle) and 5% (w/w) DMA-ASI in squalane (bottom). Samples were analysed at the same concentration and are presented at the same scale to allow visual, qualitative, comparison. 138
- 5.8 GC-FID traces of model lubricants oxidised for 90 minutes at 170 °C. The figure shows the 90 minute traces for pure squalane (top), 5% (w/w) MMA-ASI in squalane (middle) and 5% (w/w) H₂-DMA-ASI in squalane (bottom). Samples were analysed at the same concentration and are presented at the same scale to allow visual, qualitative, comparison. 139
- 5.9 The concentrations of DMA-ASI and DEA-ASI during the autoxidation of a 5% amino ASI solution in squalane at 170 °C for 90 minutes. The trend for *N*-butyl ASI (from Chapter 4) is shown for comparison. MMA-ASI could not be reliably quantified due to solubility issues. Experiments were conducted in triplicate from which averages and standard errors were calculated. 140
- 5.10 The concentration of squalane during the autoxidation of a 5% solution of amino ASI in squalane at 170 °C for 90 minutes. The trend for the autoxidation of pure squalane is also shown for comparison. Experiments were conducted in triplicate from which averages and standard errors were calculated. 141
- 5.11 The concentrations of DMA-ASI and H₂-DMA-ASI during the autoxidation of a 5% amino ASI solution in squalane at 170 °C for 90 minutes. The autoxidation of DMA-ASI was conducted in triplicate from which averages and standard errors were calculated. Data for H₂-DMA-ASI was collected from a single experiment. 142
- 5.12 The concentration of squalane during the autoxidation of a 5% amino ASI solution in squalane at 170 °C for 90 minutes. The autoxidation of DMA-ASI was conducted in triplicate from which averages and standard errors were calculated. Data for H₂-DMA-ASI was collected from a single experiment. 142
- 5.13 A zoomed view of the chromatograms in Figures 5.7 and 5.8 (pages 138 and 139) showing the four major amino ASI autoxidation products, **1/1'**, **2**, **3** and **4**. 143

- 5.14 The concentrations of products **1** and **4** during the autoxidation of alkyl ASIs (DMA-, DEA-, and H₂-DMA-ASI) as a 5% (w/w) solution in squalane. Values for DMA-ASI and DEA-ASI are averages of triplicate data with standard error bars shown. H₂-DMA-ASI data is from a single experiment. 146
- 5.15 The concentration of product **1'** during the autoxidation of DMA-ASI and DEA-ASI as 5% (w/w) solutions in squalane. Values are averages of triplicate data with standard error bars shown. Co-elution with an impurity from squalane resulted in a non-zero value at t = 0 minutes. 147
- 5.16 The concentrations of products **2** and **3** during the autoxidation of alkyl ASIs (DMA-, DEA-, and H₂-DMA-ASI) as a 5% (w/w) solution in squalane. Values for DMA-ASI and DEA-ASI are averages of triplicate data with standard error bars shown. H₂-DMA-ASI data is from a single experiment. 147
- 5.17 Diphenylamine (DPA). 148
- 5.18 The trend of kinematic viscosity at 100 °C (KV₁₀₀) over time for samples from the CEC L-109-14 oxidation test. The formulations tested were baseline, 1 and 2% DPA and 1 and 2% DEA-ASI. 150
- 5.19 The trend of oxidation by IR carbonyl area increase over time for samples from the CEC L-109-14 oxidation test. The formulations tested were baseline, 1 and 2% DPA and 1 and 2% DEA-ASI. 151
- 5.20 The mass of deposits formed during the TEOST test. Where possible, two runs were performed to indicate test repeatability. 152
- 5.21 The structure of a piperidine-based hindered amine light stabiliser (HALS) where X is typically a hydrogen or an alkyl chain. 153
- 5.22 A simplified mechanism of the Denisov cycle applied to HALS, reproduced from Hodgson *et al.*¹⁷³ X is typically a hydrogen or an alkyl chain. 154
- 5.23 The Cope elimination of an *N*-oxide to yield an alkene and a hydroxylamine. 154
- 5.24 *N*-oxide formation and Cope elimination applied to DMA- and DEA-ASI to form product **1**. 155
- 5.25 The proposed mechanism for the formation of products **2** and **3** starting from the nitroxyl radical resulting from amine oxidation. 157
- 5.26 The simplified Denisov cycle applied to amino ASIs where R is an alkyl tail, R₁ is H, methyl or ethyl, X is H, methyl or ethyl. R₂ and R₃ are lubricant-derived alkyl groups. 157

5.27	The activation of DMA-ASI using mechanisms proposed by Gryn'ova <i>et al.</i> for the activation of tertiary HALS. ¹⁷⁵	158
5.28	Tetraethylenepentamine (TEPA)	162
5.29	A selection of amines that could be found in commercial samples of TEPA, including two piperazines identified by Spell (bottom). ⁵¹	162
6.1	PIBSA 3.	166
6.2	<i>N</i> -butyl ASI.	167
6.3	Dimethylamino ASI (DEA-ASI).	168
6.4	PIBSI with a tri-isobutene tail.	169
7.1	Proton (left) and carbon (right) numbering for PIBSA 3.	174
7.2	¹ H-NMR spectrum of PIBSA 3.	175
7.3	The effect of MAH purification and maleic acid addition on the yield of PIBSA 3 in a 20 g scale reaction.	176
7.4	The EI mass spectra of the α isomer of tri-isobutene, characterised by cross reference to the NIST database.	177
7.5	The EI mass spectra of the β isomer of tri-isobutene, characterised by cross reference to the NIST database.	177
7.6	The EI mass spectra of the α isomer of tetra-isobutene, characterised by cross reference to the NIST database.	178
7.7	The EI mass spectra of the β isomer of tetra-isobutene, characterised by cross reference to the NIST database.	178
7.8	¹ H-NMR spectrum of <i>N</i> -propyl ASI.	179
7.9	¹ H-NMR spectrum of <i>N</i> -butyl ASI.	180
7.10	¹ H-NMR spectrum of <i>N</i> -pentyl ASI.	181
7.11	¹ H-NMR spectrum of <i>N</i> -hexyl ASI.	182
7.12	¹ H-NMR spectrum of <i>N</i> -heptyl ASI.	183
7.13	¹ H-NMR spectrum of H ₂ - <i>N</i> -butyl ASI.	184
7.14	The GC-MS TIC chromatogram from analysis of the aqueous phase of the volatiles condensed from exhaust gases during the autoxidation of squalane at 170 °C for 90 minutes. The products 4 and 5 cannot be observed.	188

- 7.15 The GC-MS TIC chromatogram from analysis of the aqueous phase of the volatiles condensed from exhaust gases during the autoxidation of a 5% (w/w) solution of *N*-butyl ASI in squalane at 170 °C for 90 minutes. The presence of products **4** and **5** were confirmed by their characteristic EI mass spectra. 188
- 7.16 The EI-MS spectrum of product **4** identified in the aqueous phase of the condensed exhaust gases from the autoxidation of a 5% (w/w) solution of *N*-butyl ASI in squalane at 170 °C for 90 minutes. Characterised by NIST database comparison. See Section 4.2.2.1 Page 97 and Section 7.2.2 Page 184 for further information. 189
- 7.17 The EI-MS spectrum of product **5** identified in the aqueous phase of the condensed exhaust gases from the autoxidation of a 5% (w/w) solution of *N*-butyl ASI in squalane at 170 °C for 90 minutes. See Section 4.2.2.1 Page 97 for further information. 189
- 7.18 ¹H-NMR spectrum of diethylamino alkenyl succinimide (DEA-ASI). 190
- 7.19 ¹H-NMR spectrum of dimethylamino alkenyl succinimide (DMA-ASI). 191
- 7.20 ¹H-NMR spectrum of monomethylamino alkenyl succinimide (MMA-ASI). 192
- 7.21 ¹H-NMR spectrum of H₂-DMA-ASI. 193

List of Tables

1.1	Specifications for the American Petroleum Institute (API) base oil groups I, II and III. ¹¹	5
2.1	Parameters used in PIBSA synthesis A. **purified by sublimation.	31
2.2	The parameters used for Shimadzu GC-17a GC-FID analysis.	42
2.3	The parameters used for Agilent 6890 gas chromatograph GC-FID analysis.	43
2.4	The parameters used for Agilent 7890 gas chromatograph GC-FID analysis.	44
2.5	Atomic contributions to effective carbon number. ¹²¹	45
2.6	The parameters used for gas chromatography - electron ionisation - mass spectrometry (GC-EI-MS) analysis.	47
2.7	Materials used in this project.	51
3.1	PIB conversion, PIBSA yields and PIBSA selectivities for the three PIBSA isomers from the 20 and 100 g PIBSA synthesis reactions.	57
3.2	PIBSA product distributions calculated from Balzano <i>et al.</i> and from this work.	58
3.3	The yield of PIBSA 3 under five different reaction conditions, calculated from the ¹ H-NMR spectra in Figure 3.9. The synthesis was conducted at 200 °C for 5 hours using a 1:1 PIB:MAH ratio. *Average value from four reactions with standard error, FPT = freeze pump thaw.	64
3.4	GC-FID retention times (R_t) the corresponding number of isobutene units and mass of the oligomer. Di-isobutene (2 isobutene units) was not observed.	66
3.5	A table of reaction conditions (MAH:PIB ratio and AO concentration) for the reaction of PIB and MAH on a 500 mg scale. PIB conversion and PIBSA selectivities are shown, and the optimum conditions for Alder-ene addition (rxn. 4) and radical addition (rxn. 7) are shown in bold.	71
3.6	Selected bond dissociation enthalpies (BDEs).	76
4.1	Identified products from the autoxidation of <i>N</i> -butyl ASI at 170 °C. ^a Identified by comparison to the NIST database. ^b EI-MS fragment assignments made and discussed later. ^c Silylated derivative observed. ^d Acetonide derivative observed.	95

4.1	Identified products from the autoxidation of <i>N</i> -butyl ASI at 170 °C. ^a Identified by comparison to the NIST database. ^b EI-MS fragment assignments made and discussed later. ^c Silylated derivative observed. ^d Acetonide derivative observed.	96
4.2	Fragment ion assignments for product 5 , 3-methyl <i>N</i> -butyl succinimide.	98
4.3	Fragment ion assignments for product 8 , succinimide aldehyde.	99
4.4	Fragment ion assignments for product 9 , α , β -unsaturated succinimide aldehyde.	102
4.5	EI-MS fragment ion assignments for silylated <i>N</i> -butyl ASI alcohols (10).	104
4.6	A summary of the fragment ions of the C ₄ <i>N</i> -propyl ASI ketone and the C ₄ <i>N</i> -butyl ASI ketone (11), their region of origin, and electronic character.	106
4.7	EI-MS fragment ion assignments for the C ₄ <i>N</i> -butyl ASI ketone (11).	107
4.8	EI-MS fragment ion assignments for the <i>N</i> -butyl ASI dehydrodimer.	109
4.9	EI-MS fragment ion assignments for the acetonide derivative of the C ₂ ,C ₃ <i>N</i> -butyl ASI diol (15).	113
4.10	EI-MS fragment ion assignments for the bis-silyl ether derivative of the C ₂ ,C ₃ <i>N</i> -butyl ASI diol (15).	115
4.11	The pseudo first order rate constant of squalane, <i>N</i> -butyl ASI and H ₂ - <i>N</i> -butyl ASI decay at 170 °C. Ageing experiments were conducted in triplicate from which the average and standard error was calculated.	121
5.1	Accurate mass data for amino ASI degradation products 1 , 1' , 2 , 3 and 4 .	145
5.2	The structures of compounds 1/1' , 2 , 3 and 4 .	145
5.3	The lubricants used for oxidation testing of DEA-ASI with an AO free baseline blend and diphenylamine (DPA) blends for comparison.	149
7.1	Olefinic, allylic, and succinic ¹ H-NMR shifts for PIBSA 3 .	174
7.2	Olefinic, allylic, and succinic ¹³ C-NMR shifts for PIBSA 3 .	174
7.3	Summary of EI fragmentation patterns obtained using accurate mass GC-EI-MS for compounds 1-4 , 6 , 7 and 13 . and their comparison to NIST library data.	184
7.3	Summary of EI fragmentation patterns obtained using accurate mass GC-EI-MS for compounds 1-4 , 6 , 7 and 13 . and their comparison to NIST library data.	185

- 7.3 Summary of EI fragmentation patterns obtained using accurate mass GC-EI-MS for compounds **1-4**, **6**, **7** and **13**. and their comparison to NIST library data. 186
- 7.4 Accurate mass data for compounds **1-4**, **6**, **7** and **13**. 187

Acknowledgements

I guess I should follow convention and thank my fantastic supervisors first. Dr Moray Stark, Dr Thomas Farmer and Dr Duncan Macquarrie. Moray, thank you for everything. Your kind and caring demeanour has been invaluable throughout this project. Enjoy Glasgow. Tom, thank you for your enthusiasm, encouragement and friendship. Duncan, thank you for all the insightful conversations and fantastic stories.

This thesis was not just a York effort and so thanks must be directed to Afton Chemical Ltd. for funding both me and my project, with special thanks to Dr Neil Harris and Dr Ali Brown. Neil, you are a good supervisor and a great friend, best of luck with your new career. Ali, since starting my Masters in 2015 you have always had my back and I hope to one day be as well respected as you are for your kindness and leadership. Thank you.

The last four years have been about far more than just Chemistry and the friendships I have made are some of the best I could ever have hoped for. To list everyone who has positively impacted my life over the last four years would take longer than writing this thesis, but I'll give it a go anyway. In no particular order, thank you Yann (Layla), the delightful Dina, various Jameses (especially desk-buddy Shannon), shower-buddy Dan, Los Tres Amigos Tom and Javier, Xiao, Katie, Joe, Joe's mum, Tabitha, Jenny, Becky and another James, Roxana, Ben, Rob, Fergal, Florent, my wonderful placement students Jess and Tom, Paul the cycling wizard, Hannah Briers and everyone else who keeps Green Chemistry going, my first chemistry friend Dr Jordan Herod, Mat with one t and Anya, brown chemistry Sophie, green chemistry Sophie and the rest of the pub gang, and the scores of wonderful Masters and Erasmus students who have been so much fun over the years.

This work represents just four years of my twenty-six year existence and so thanks are due to my wonderful family for getting me to the start line and supporting me throughout my work. I am very grateful to my GCSE Chemistry teacher Mr Shiplee who first sparked my interest in the topic and I am indebted to Crispin Rope for all of his support over the years. Thank you. And finally, thank you to Rowena for putting up with me writing a thesis in the midst of a global pandemic and making this last year an absolute joy.

Thank you, everyone. It has been a pleasure.

Declaration

The research described in this thesis is original work which I undertook at the University of York from September 2016 to September 2019. This work has not previously been presented for an award at this, or any other, University. All sources are acknowledged as References. Except where stated, all of the work contained within this thesis represents the original contribution of the author. Certain parts of the work described herein were undertaken by others, they are fully acknowledged below:

- Karl Heaton at University of York: High resolution GC-EI-MS and ESI-MS experimentation.
- Dr Neil Harris at Afton Chemical Ltd: Performance testing of diethylamino ASI including formulation, CEC L109-14 and ASTM D 7097 oxidation testing.

The work contained in Chapter 4 formed the following publication. The author of this thesis is responsible for the work within the publication.

Ruffell, J. E.; Farmer, T. J.; Macquarrie, D. J.; Stark, M. S. The Autoxidation of Alkenyl Succinimides—Mimics for Polyisobutenyl Succinimide Dispersants. *Ind. Eng. Chem. Res.* **2019**, 58 (42), 19649–19660, DOI: 10.1021/acs.iecr.9b02780

Chapter 1

General Introduction

1.1 General Background

Humans, as a species, like to move things. From Stonehenge to spaceships, humans have been moving things for millennia. But, something has been getting in our way.

Friction.

Friction increases both the force needed to move one surface over another and the wear suffered by those surfaces during movement. The earliest evidence of humans trying to reduce friction comes from Ancient Egypt, where a painting on the wall of a tomb dating back to 1880 BCE depicts people pouring a liquid (thought to be water) on the sand in front of a sledge to aid movement of a colossal monument (Figure 1.1). This simple act could have reduced friction by up to 40%.¹ Historically, friction has also been overcome on a smaller scale. From at least 1400 BCE, Egyptians were applying animal tallow to lubricate cart axles² to make pulling carts easier. Lubrication still keeps society moving smoothly to this day.

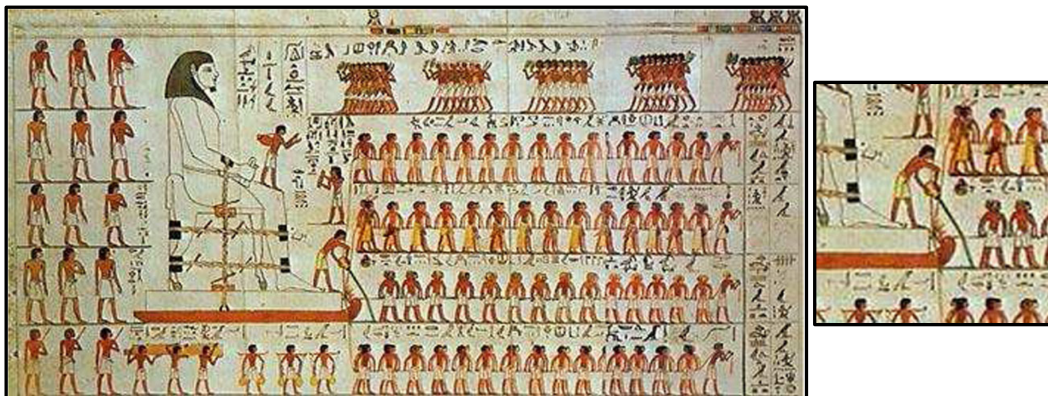


Figure 1.1 – A reproduction of a wall painting found in the tomb of Djehutihotep c. 1880 BCE. Reproduced from Fall *et al.* 2014.¹

While often misunderstood and taken for granted, the impacts of friction and the benefits of lubrication are enormous. In 1966, the Jost Report highlighted the cost of this misunderstanding.³ Jost calculated that overcoming friction, wear, corrosion, and mechanical failure cost the United Kingdom (UK) between 1.1–1.4% of Gross National Product.³ Jost also coined the term tribology: derived the Greek *tribos*, meaning “to rub”, tribology is the study of friction and lubrication.

A more recent tribology report, published in 2017 by Holmberg and Erdemir, supported the magnitude of Jost's findings on a global scale.⁴ The report stated that 23% of global energy consumption originates from surface contacts, 20% directly from overcoming friction and 3% from replacing worn parts.⁴ By using new surfaces, materials and lubricants, this energy demand could be reduced by 40% in just 15 years.⁴ This would save 1.4% of global Gross Domestic Product and reduce carbon emissions by 3,140 million tonnes CO₂, a significant gain in the fight against climate change.⁴

Holmberg and Erdemir identified transport as the area that could see the biggest efficiency gains. In just 15 years, transport could consume 55% less energy than it does today.⁴ Transport covers many areas, from shipping goods around the globe to a trip to the supermarket. Currently, going to buy a banana is generally accomplished by driving a car powered by an internal combustion engine. These engines are fundamentally crude in their nature. They convert the power generated by the combustion of a fuel and air mixture into rotational energy through a series of pistons and cranks, while wasting a lot of heat.

From a tribology perspective, these engines are highly complex as a multitude of components are moving against each other at different speeds, pressures and temperatures. Add to this the modern desire to have an engine oil lubricant that functions for up to twenty thousand miles before it need changing,⁵ and lubricating an internal combustion engine becomes quite challenging. Thankfully, lubricant chemists have many tools in their arsenal to achieve this.

1.2 Engine oil lubricants

A modern engine oil lubricant comprises an additive package, pour point depressant (PPD) and a viscosity index improver (VII) dissolved in a hydrocarbon base oil.⁶ When all the components are blended together you have a fully-formulated engine oil lubricant or finished fluid. The base oil provides the bulk of the lubrication by forming a thin film on engine surfaces. It also acts as an engine coolant. Hydrocarbon base oils are used due to their low volatility at engine temperatures and their low reactivity to the components of the engine.⁶ The VII and PPD are added to help the lubricant cope with extreme temperatures, and the components within the additive package increase the lifetime of both the lubricant and the engine. These components include dispersants, detergents, antiwear additives, antioxidants, and friction modifiers which are carefully blended together by specialist lubricant chemists known as formulators.⁶

1.2.1 Base oil

Most of the lubricant—usually between 78–85% in a modern lubricant—is a hydrocarbon base oil.⁶ Base oils are either refined crude oil (also known as mineral oil), a synthetically produced oil, or a mix of the two.⁶ There is a broad range of structures and compositions available in crude oil which vary based on the geographic source of the crude and its degree of refining. The structures include linear, branched and naphthene alkanes, alkenes, polyaromatics and mixed structures (Figure 1.2).⁷ This range of possibilities makes crude oil a very complex mixture. Additionally crude oil includes sulfur compounds. Derived from crude oil precursors,⁸ they further complicate the mixture.⁹

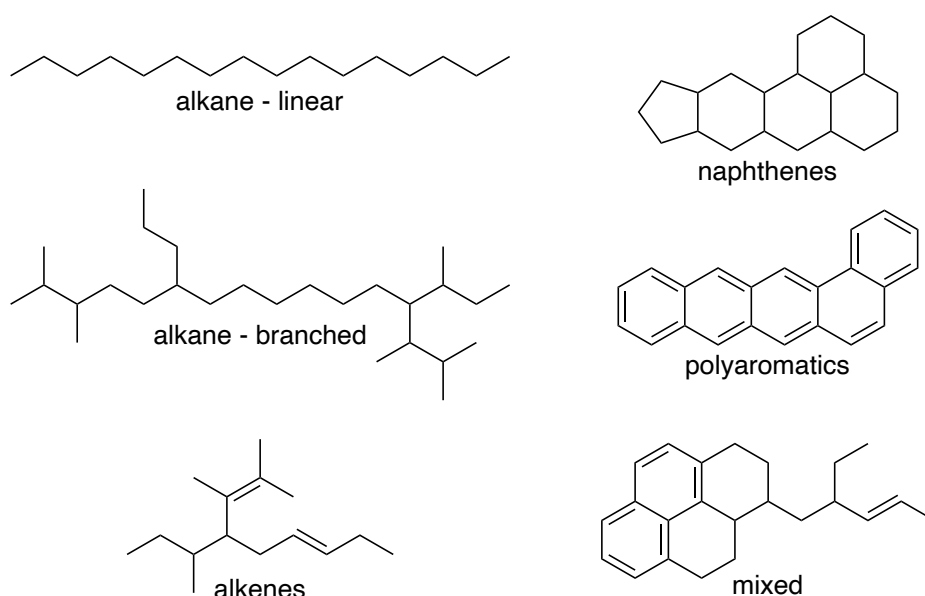


Figure 1.2 – Examples of possible hydrocarbon structures found in refined mineral oils.

Base oils are sorted into five groups by American Petroleum Institute (API) norms to distinguish their characteristics.¹⁰ Groups I–III are for base oils derived from crude oil. These are categorised based on the percentage of the compounds that are saturated alkanes, the sulfur content and the oil’s viscosity index (Table 1.1).¹¹ For an explanation of viscosity index, see Section 1.2.2.1.

Group IV is for synthetic polyalphaolefin (PAO) base oils that do not contain unsaturated hydrocarbons or sulfur compounds due to their manufacturing process.¹⁰ High purity alpha (α) olefins are polymerised to form higher molecular weight oligomers with base oil characteristics. Due to the high purity of the starting material, no sulfur is present and the

Table 1.1 – Specifications for the American Petroleum Institute (API) base oil groups I, II and III.¹¹

Group	Saturates (%)	Sulfur (%)	Viscosity index
I	<90	≥0.03	≥80, ≤120
II	≥90	≤0.03	≥80, ≤120
III	≥90	≤0.03	120

controlled process means no unsaturated hydrocarbons are formed. PAOs are the most commonly used synthetic base oil. Their branched structures give excellent lubricant flow at low temperatures. This is an important characteristic for lubricants used in cold climates which can otherwise precipitate wax and freeze, preventing flow and lubrication.¹⁰ Because of their high saturated hydrocarbon content, lubricants formulated with PAOs have excellent thermal and oxidative stability compared to lubricants formulated with mineral oil. Group V is for base oils that do not fit in the other categories such as polybutenes, synthetic esters and polyalkylene glycols.¹⁰

1.2.2 Lubrication and Newtonian viscosity

A lubricant base oil reduces friction by creating a thin film between two surfaces, separating them (Figure 1.3). This is necessary and beneficial because, no matter how well machined and smoothed, surfaces are covered in microscopic valleys and peaks (known as asperities). When two surfaces rub against each other without adequate lubrication, the asperities make contact which generates friction, heat and wear. Lubricants prevent this contact, reducing both friction and wear.

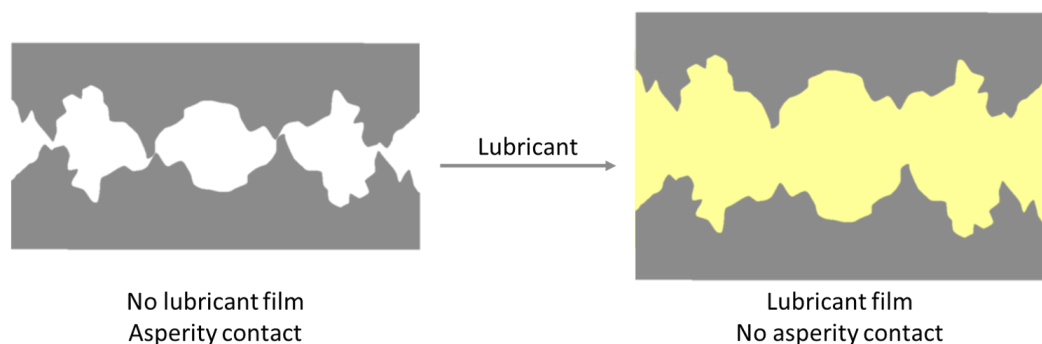


Figure 1.3 – Asperity contact between two metal surfaces (left) and the prevention of asperity contact by a lubricant film (right, yellow = lubricant film).

The key property enabling this is the viscosity of the lubricant. Liquids with a high viscosity are thicker than liquids with a low viscosity. When a liquid is viscous enough it can support the load from a surface pressing on it and keep the surfaces separated.

Viscosity results from the internal friction of a liquid.⁷ It is a force that will resist the motion of one object sliding over another when separated by a layer of liquid. Take for example the model system in Figure 1.4 where two plates of area A are separated by a distance, D . In this system, the top plate is supported by the liquid in the gap between the two plates. The bottom plate is held still and in order to move the top plate at a velocity, V , a force must be applied. This force is required to overcome the internal friction of the liquid, its viscosity.⁷

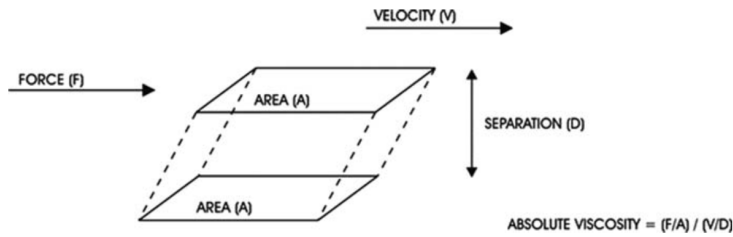


Figure 1.4 – Absolute viscosity, reproduced from Prince.⁷

The internal friction originates from the fact that the liquid closest to the top plate must move with the same velocity as the top plate, V .⁷ The liquid closest to the bottom plate must move at the same velocity as the static bottom plate where $V = 0$. Therefore, as you move up from the bottom plate to the top plate, the velocity of the liquid incrementally increases, effectively in layers. A given layer moves faster than the layer beneath it. Drag is generated by this relative movement and this is what constitutes the internal friction. From this system the equation for absolute viscosity, also known as dynamic viscosity, (η) is derived (Equation 1.1).⁷

$$\eta = (F/A)/(V/D) \tag{1.1}$$

The first term, F/A , is force divided by an area, i.e. pressure, the common unit being Pascals (Pa). The second term, V/D , is commonly known as the shear rate ($\dot{\gamma}$) and is given in units of reciprocal seconds (s^{-1}). Therefore, dynamic viscosity η has the units $Pa s$. However, the unit centipoise (cP) is more commonly used where $1 Pa s = 1000 cP$.⁷

The dynamic viscosity of a liquid can be measured using rotary viscometers, where a sample of liquid is placed between two plates. The top plate rotates at a given shear rate and the resistance to movement is measured from which dynamic viscosity is calculated. When the viscosity of the liquid does not change with shear rate, the liquid is said to show Newtonian viscosity.

Because its measurement is more simple, more commonly kinematic viscosity (KV) is used for lubricants. Kinematic viscosity is measured empirically by measuring the rate of flow of a lubricant through a tube or capillary. KV is related to the dynamic viscosity by Equation 1.2.⁷ This gives a value in units of $m^2 s^{-1}$ which is converted to centistokes (cSt) for convenience, where $1 \text{ cSt} = 10^{-6} m^2 s^{-1}$.

$$KV = \eta / \text{liquid density} \quad (1.2)$$

Kinematic viscosity is used to grade lubricants. More viscous lubricants impart greater wear protection through increased film thickness which prevents asperity contact (Figure 1.3). However, this comes at a cost of increased friction from the lubricant itself which reduces fuel economy. Therefore lubricating an engine for optimum performance is about balancing those two attributes.

The viscosity of a lubricant is advertised on the bottle by its viscosity grade. However, modern engine oil lubricants do not have just one viscosity grade, they have two. So-called “multi-grade” oils are designed to work all year round, through cold winters and into hot summers. They need to be specifically designed for this as the viscosity of a liquid changes with temperature. A liquid will have a higher viscosity when it is colder compared to when it is warmer.

But, not all oils respond to temperature equally. Some will have a larger change in viscosity over a given temperature range than others. This is measured by the viscosity index. The viscosity index is determined empirically by measuring the KV change between 40 and 100 °C.⁷ This viscosity change is compared to two historical reference oils, arbitrarily assigned viscosity index values of zero and 100. Oils with a higher viscosity index are desirable as they are better at maintaining their viscosity across a range of temperatures. If the viscosity gets too low, the fluid will not lubricate the system effectively. Conversely, if a lubricant gets too

viscous when it is cold, it will not flow properly when the engine is started in cold climates. This can mean that the engine is starved of lubricant, increasing wear.

1.2.2.1 Viscosity index improvers

Viscosity index improvers are used to increase the viscosity index of a lubricant oil. These are polymeric additives and the two most common structures are polymethacrylates and olefin copolymers (Figure 1.5).¹²

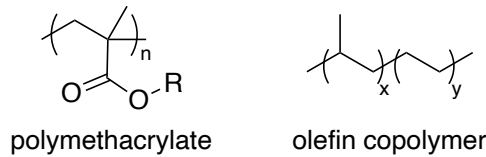


Figure 1.5 – Two common viscosity index improvers.

Viscosity index improvers are designed so that in low temperature conditions—like when the engine is first started on a cold day—the polymer folds up tightly, giving it a smaller effective size and reducing the viscosity of the liquid.¹² At higher temperatures—like when the engine is at operating temperature—the VII unfolds and interacts more with neighbouring molecules, increasing its effective size and increasing the viscosity of the liquid.¹² Therefore, VIIs can reduce the difference between a liquid’s viscosity across the range of engine operating temperatures, increasing its viscosity index and improving lubricant performance.

1.2.3 Non-Newtonian lubricant viscosity

The viscometric behaviour described so far has been Newtonian viscosity, where the viscosity of the fluid remains the same regardless of the shear rate ($\dot{\gamma}$) applied to it. Some liquids show non-Newtonian viscosity where their viscosity changes as a function of shear rate. Non-Newtonian behaviour can be observed in lubricants. During use, engine oil lubricants become contaminated with polar material.¹³ This is from two sources, soot from the incomplete combustion of fuel and so-called sludge from lubricant autoxidation.¹³ Soot enters the lubricant when blow-by gasses containing soot are forced past the engine pistons and into the sump where it mixes with oil.¹³ Soot is particularly prevalent in diesel engines. In an effort to reduce NOx emissions, exhaust gases are recirculated into the combustion

chamber to reduce the flame temperature.¹⁴ While this does reduce NO_x effectively, it also increases the amount of soot entering the lubricant in blow-by gasses.

The origins of sludge are less well understood and it has received far less attention in the literature. Insoluble polar molecules are formed through the autoxidation of the lubricant.¹³ These polar molecules mix with water in the sump to form a viscous gel that can block the flow of lubricant from the sump, starving the engine of lubrication.

In 1970 Forbes *et al.* isolated sludge from a used lubricant.¹⁵ After washing with apolar pentane, a fine black powder was afforded and through adsorption studies the sludge was shown to have a polar surface. The same is true for soot, where the surface of the soot particle can be oxidised¹⁶ to give a surface with high C–OH functionality.¹⁷ This oxygen-rich surface structure means both soot and sludge are relatively polar compared to the hydrocarbon base oil. Due to this polarity and hydrogen bonding ability, they aggregate and agglomerate in the oil, forming large intermolecularly bonded networks (Figure 1.6).¹⁷

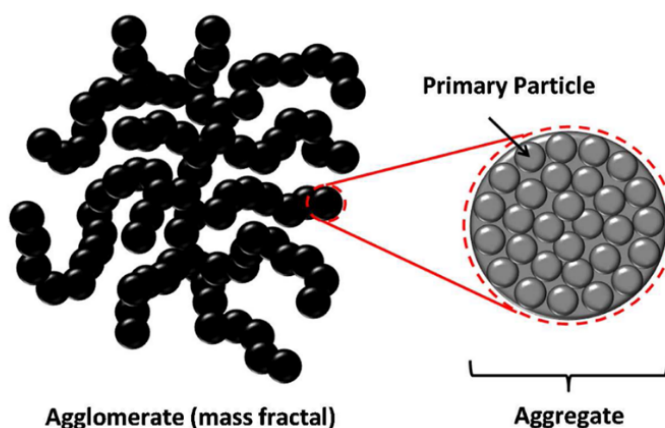


Figure 1.6 – The structure of soot agglomerates reproduced from Growney *et al.*¹⁷

In terms of viscosity, these large agglomerates behave like large molecules, resulting in a high liquid viscosity. However, as a shear rate is applied and increased, the relatively weak intermolecular bonds of the network break and the network disintegrates into smaller aggregates. These smaller aggregates give the liquid a lower viscosity. Hence, a highly-sooted lubricant, or one with a high sludge content, shows non-Newtonian behaviour.

In a mild case, the viscosity increase due to soot and sludge increases lubricant friction which decreases fuel economy.¹³ In an extreme case, the soot and sludge aggregates can completely gel the lubricant, stopping all lubricant flow. Without proper flow of the lubricant throughout

the engine, mechanical contacts quickly wear which causes catastrophic failure. Lubricant formulators can prevent gelling and maximise the lifetime of an initially optimally-viscous lubricant by minimising autoxidation—and hence sludge formation—through the use of more refined base oils and antioxidants. Autoxidation is discussed in greater detail in Section 1.4. Alternatively, components known as dispersants can be used to lessen the impact of sludge and soot on lubricant viscosity.

1.3 Dispersants

Dispersants are high molecular weight amphiphiles that solubilise sludge and soot, suspending it within the lubricant. This prevents agglomerate formation and the associated viscosity increase, and also means the polar material gets removed when the oil is changed. Effectively dispersing soot also helps to reduce component wear¹⁸⁻²⁰ which increases engine life.²¹ The dispersant’s polar head group binds to the polar particles forming inverse micelles where the hydrocarbon tail solubilises the particle in the hydrocarbon base oil (Figure 1.7).

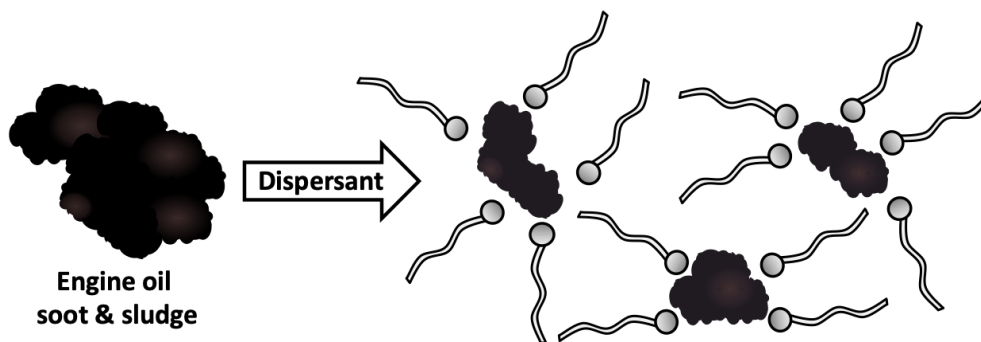


Figure 1.7 – A representation of dispersants breaking up polar agglomerates in a lubricant oil.

Figure 1.8 shows the results of three sludge-producing engine tests of lubricants with three different dispersant concentrations. Increasing the dispersant concentration significantly reduced the size of polar agglomerates found in the oil after the 288 hour test.

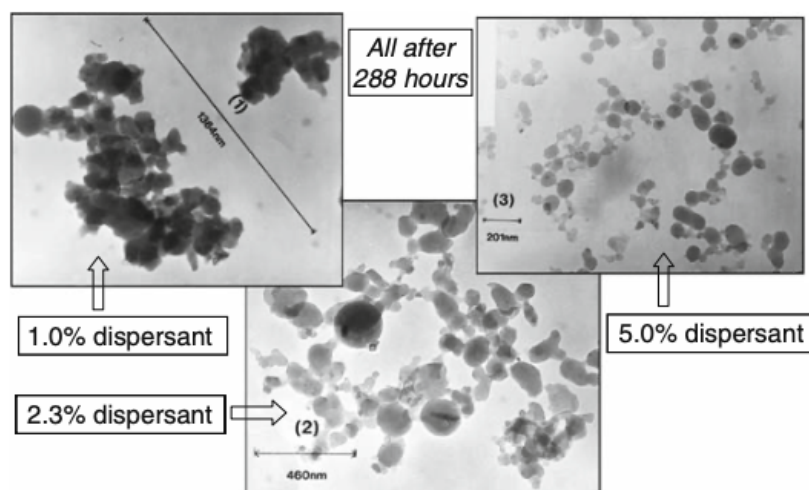


Figure 1.8 – The effect of dispersant concentration on soot dispersion after a 288 hour sequence VE engine test. Reproduced from Seddon *et al.*²²

There are four main types of dispersants: succinimide, succinate esters, Mannich, and phosphorous types²³ (Figure 1.9) and they typically make up 4–8% of the lubricant.²²

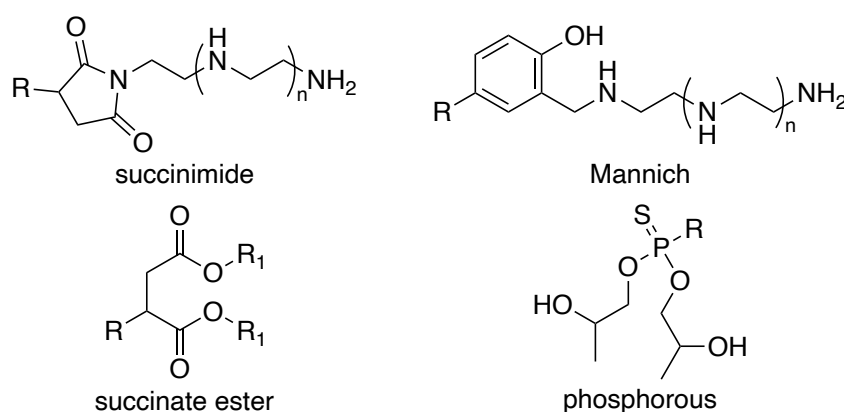


Figure 1.9 – The four main types of dispersant. R = alkyl chain, typically PIB. R₁ is a poly alcohol.

The most common dispersant type and the subject of this thesis—polyisobutenyl succinimides (PIBSIs) (Figure 1.10)—have been the most used dispersant since their development in the 1960s.²² PIBSIs constitute between 4 and 8% (w/w) of an engine oil lubricant but can also be used in fuels where they are known as detergents.²² At much lower treat rates (ppm levels) they increase engine cleanliness.^{24,25} They are also used further afield such as in ceramics dispersing slurries,^{26,27} in emulsion explosives,^{28,29} in cleaning waste water from flue gas desulfurisation,³⁰ and in hydrocracking asphaltenes.³¹

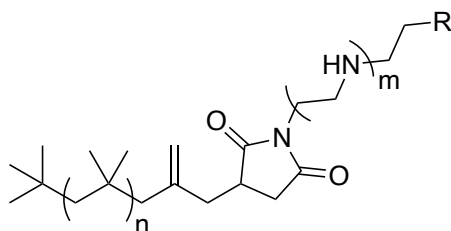


Figure 1.10 – The idealised structure of a polyisobutenyl succinimide dispersant where n is typically 16-60, m is typically 3 and $R = \text{NH}_2$ or PIBSI.³²

1.3.1 PIBSI synthesis

In PIBSIs the apolar tail is oligomeric polyisobutene (PIB), which typically has a molecular weight between 1000–2500 g mol⁻¹.²² Containing 70–180 carbons, this large tail is much bigger than conventional surfactants (detergents) and provides the stability to suspended particles in the lubricant. Unlike conventional detergents, the driving force for PIBSI dispersants stabilising particles is not micelle formation. When the dispersant is bonded to the sludge or soot surface, the sheer size of the PIB tail imparts “steric” stability that physically prevents two polar particles from interacting.^{15,33}

The PIB tail is joined to the polar head group via a succinimide linker which is formed using simple industrial methods. The synthesis is shown in Figure 1.11. First, PIB is reacted with maleic anhydride (MAH) to form polyisobutenyl succinic anhydride (PIBSA).²² The resultant anhydride can be readily reacted with a primary amine to form the succinimide.³² This reaction is accomplished by mixing the reactants and heating them to remove water and force succinimide formation.

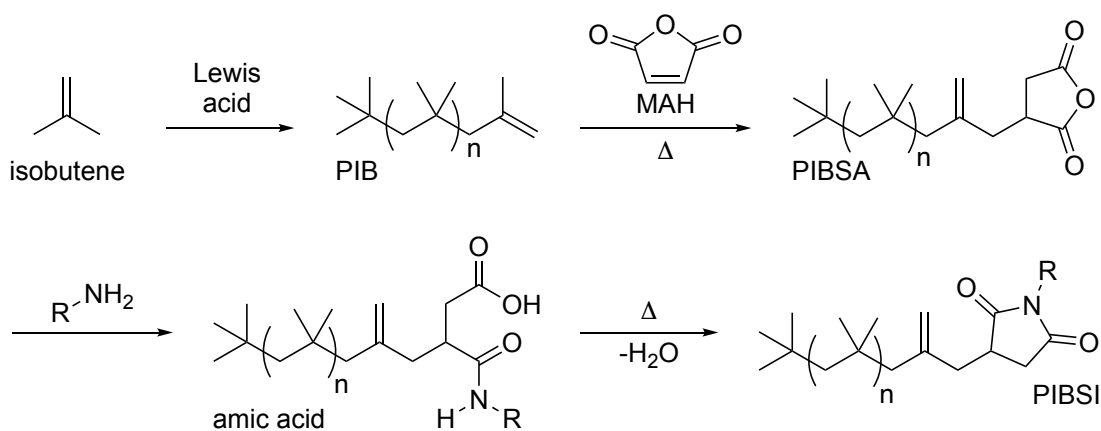


Figure 1.11 – The general procedure for the synthesis of PIBSI dispersants where R is usually a polyamine.

1.3.1.1 PIB and PIBSA synthesis

The intermediate in PIBSI dispersant synthesis, PIBSAs (Figure 1.12), can be themselves used to stabilise emulsions.^{34,35} Due to their industrial importance, the synthesis of PIBSAs has received some attention in the literature over the last two decades.^{36–38}

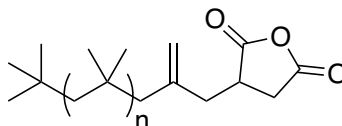


Figure 1.12 – Polyisobutenyl succinic anhydride (PIBSA).

PIBSAs are formed by the reaction of MAH with PIB, which is achieved industrially by two main methods. The first method uses PIB produced through AlCl_3 catalysed cationic polymerisation of isobutene. PIB formed by this route has a poorly defined structure due to frequent branching reactions occurring during its production. This forms tri- and tetra-substituted alkenes which are less reactive due to steric hindrance.³⁹

To produce sites reactive to MAH the PIB is first reacted with chlorine gas, losing two moles of HCl .²² This generates 1,3 dienes that will react with MAH via Diels-Alder addition (Figure 1.13).²² This chlorination route allows the use of lower reaction temperatures for MAH addition which saves energy and minimises thermal PIB degradation.¹³ However, residual chlorine in the dispersant makes it the major contributor of chlorine to the final engine oil lubricant,⁴⁰ which was cause for concern as it represented a viable route to release chlorinated compounds into the environment. Consequently, a chlorine-free alternative route was developed.¹³

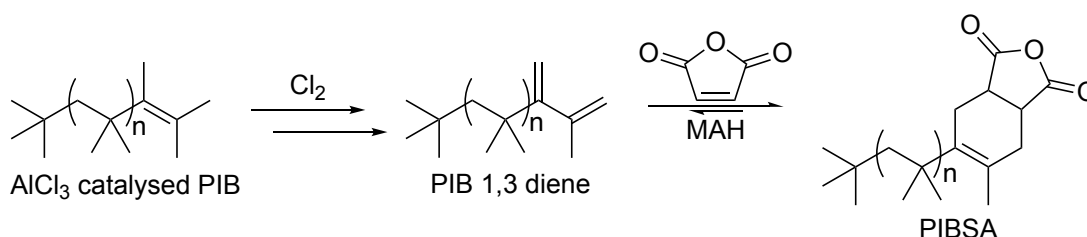


Figure 1.13 – Formation of PIBSAs by PIB chlorination and subsequent Diels-Alder MAH addition.

The second method to produce PIBSAs uses PIB produced by BF_3 catalysed cationic polymerisation of isobutene.¹³ When BF_3 is used to catalyse isobutene polymerisation it produces PIB with a more defined structure where the residual alkene is always located on

the terminating isobutene unit (Figure 1.14).¹³ This is because BF_3 does not facilitate the carbocation rearrangements and β scission reactions that give AlCl_3 PIB its poorly defined structure.³⁹ Further improvement of this reaction by the development of more efficient catalysts for isobutene polymerisation has received attention in the literature in the last decade.^{41–46}

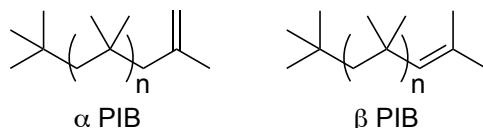


Figure 1.14 – The two major alkene isomers of commercial polyisobutene produced by BF_3 catalysed polymerisation of isobutene.⁴⁷

When the terminating alkene is the vinylidene structure, known as α PIB, it can be reacted with MAH via the Alder-ene reaction to yield PIBSA (Figure 1.15).²² The reaction is typically conducted at 200–240 °C and under pressure to prevent MAH evaporation.³² This approach gives a desirable chlorine-free product and the high uniformity of the starting material— $\sim 85\%$ α PIB—gives a more uniform product. However, work by the Lubrizol Corporation—one of the largest producers of dispersants by the chlorination method—suggests reducing lubricant chlorine levels does not impact tailpipe emissions and may increase overall product emissions due to the higher reaction temperatures, making the chlorine-free method more energy intensive.⁴⁸ Despite higher energy costs, the chlorine-free route remains in use in industry due to its more uniform products and the benefit of not handling chlorine on an industrial scale.

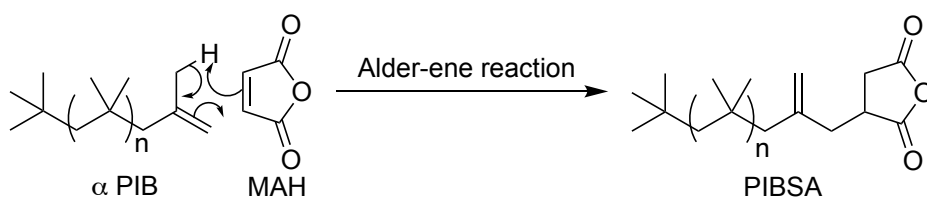


Figure 1.15 – PIBSA formation by the Alder-ene addition of maleic anhydride (MAH) to vinylidene terminated PIB.

Industrially, the reaction of MAH with PIB is not generally under sophisticated control. As a result, a second equivalent of MAH can add to the alkene of a PIBSA molecule. This forms a double-headed bis-PIBSA, and such products were observed by Harrison *et al.* in 2002 using electron spray ionisation - mass spectrometry (ESI-MS). While the exact structures are yet to be determined, the molecular weights indicated PIB molecules with two succinic

anhydride groups attached (Figure 1.16). While their existence has been demonstrated, the impact of bis-PIBSAs on dispersant performance has not yet been explored.

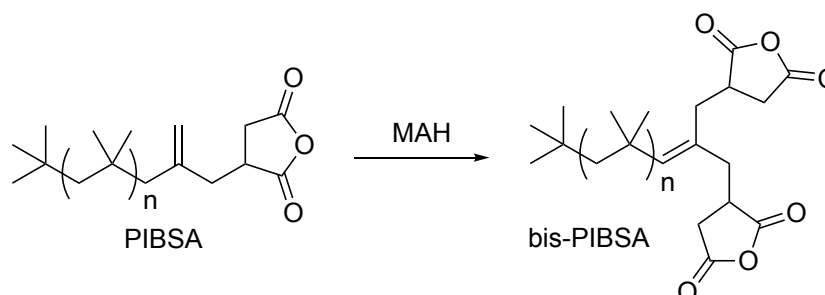


Figure 1.16 – The formation of a bis-PIBSA by addition of MAH to PIBSA.

1.3.1.2 Amines

Once the PIBSA is produced it can be reacted with a primary amine to form a succinimide. Instead of a mono-amine, polyethylene amines such as tetraethylenepentamine (TEPA) (Figure 1.17) are used to form the dispersant hydrophile.¹³ The amine gives the dispersant its soot-binding ability and using polyamines increases the number of interactions.

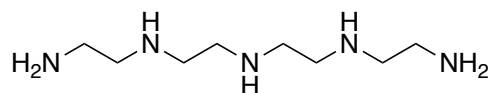


Figure 1.17 – Tetraethylenepentamine.

Acid-base reactions of the amine with acidic sites on the surfaces of sludge, soot and carbon black bind to the dispersant surface.^{49,50} This reaction is exothermic (60 kJ mol^{-1}), binding the dispersant strongly to the surface.^{49,50} The more nitrogens present in the head group, the higher the number of interactions, further strengthening the binding. Commercial-grade polyamines contain a wide range of structures, including branched amines and piperazines.⁵¹ This can affect dispersant interactions as piperazines do not bind as strongly as linear amines,⁴⁹ however the actual performance effect of this during use is unknown.

1.3.2 Impact of dispersant structure

While the structure in Figure 1.10 represents the ideal structure of average commercial PIBSIs, many alterations have been attempted. In 1992 Bartha *et al.* investigated the effect of increasing the number of PIB chains attached to an amine on thermal stability and soot

dispersion.⁵² While bis-PIBSIs were more thermally stable than mono-PIBSIs, the latter were more effective dispersants.⁵² They also found substituting the PIB tail for polyethylene significantly reduced thermal stability of the dispersant.⁵²

Higher molecular weight PIBSIs provide greater steric stabilisation and this is reflected in dispersing performance.^{53,54} This can be taken further by the development of high molecular weight polymeric dispersants that show improved sludge handling performance.⁵⁵⁻⁵⁷

Modifications of the amine have also been pursued. Phosphorous esters can impart an antioxidant (AO) effect⁵⁸ and using PIBSIs to incorporate boron into the lubricant^{59,60} improves wear performance. Using the dispersant to dissolve graphene into the lubricant also has wear benefits.⁶¹

Nassar *et al.* coupled a dispersant amine with a phenol that allowed the dispersant to behave as an AO due to the labile phenol hydrogen.⁶² Other amine modifications include reaction with ethylene carbonate, however this proved to decrease dispersancy.³⁷

Dispersants for more general use do not need aminic head groups. Oxygen-containing head groups are used as jet fuel detergents^{63,64} and aromatic head groups for crude oil dispersion.⁶⁵⁻⁶⁷ However, the strong binding of basic amines to acidic sites is key to engine oil dispersants.

1.3.3 Dispersant interactions

Engine oil lubricants are complex mixtures of functional additives that are in themselves complex mixtures. Therefore it is vital not to think of a lubricant as a homogeneous liquid of ideally-solvated non-interacting molecules. Instead, the inherent insolubility of some additives, their molecular interactions, and the heterogeneity of the lubricant should be taken into account. One of the components that is most interactive in a lubricant is the dispersant. This aspect of their behaviour constitutes the most studied area of dispersant chemistry.

In the first instance, dispersants interact with themselves. In 1991 Ganc and Nagarajan determined that, at concentrations above 0.02 g cm^{-3} in decane, PIBSIs form spherical inverse micelles with well-solvated loosely packed tails.⁶⁸ The data fitted the closed association model where all PIBSI molecules were in micelles and no monomers were present. The micelles

formed were approximately 60 Å in diameter and contained 19 PIBSI molecules at 25 °C, which decreased to 9 molecules at 65 °C. While this temperature range is appropriate for the blending of additive packages and fully-formulated lubricants, it is not representative of the oil during use where temperatures of 115–180 °C are achieved.^{69,70}

This aggregation can be useful for dispersant characterization. In 2008 Pucci *et al.* showed aggregation-induced luminescence of PIBSAs could be used to determine the anhydride content of the PIBSA.⁷¹ In 2014 Pirouz *et al.* showed that fluorescence quenching by dispersant secondary amines could be used to characterise dispersants as the quenching scaled with amine size.⁷² The bulk measurements can help us to understand the average molecule in a sample of PIBSI dispersant, however it does not help characterise individual structures or the range of structures present within the sample.

1.3.3.1 Dispersants with zinc dialkyldithiophosphate (ZDDP) antiwear agents

Antiwear agents are added to reduce the wear suffered by mechanical parts, increasing the lifetime of the engine. Due to their high performance to cost ratio, zinc dialkyldithiophosphates (ZDDPs) (Figure 1.18) are the main antiwear agent used.⁷³ Initially patented as an antioxidant and corrosion inhibitor in the 1940s, its antiwear properties emerged as the performance demands on engines increased.⁷³ Antiwear agents deposit a hard wearing layer, known as a tribofilm, on engine components that provides physical protection. Initiated both by high engine temperatures (above 100 °C) and mechanical rubbing, ZDDPs decompose to form hard polyphosphate films approximately 100 nm thick.⁷³ These hard films are resistant to wear which protects metal surfaces of the engine.

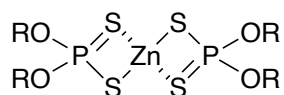


Figure 1.18 – The general structure of zinc dialkyldithiophosphate (ZDDP) where R is an alkyl chain.⁷³

Beyond single-component systems, the majority of studies on dispersant interactions focus on ZDDP. Early work by Vipper *et al.* in 1972 showed a synergistic effect on solubility for mixed systems of PIBSI and ZDDP in oil.⁷⁴ Later work by the same group using conductivity measurements confirmed the dispersant and ZDDP interaction.⁷⁵ The nature of the reaction became more clear in the 1990s. Harrison *et al.* reported ³¹P nuclear magnetic resonance

(NMR) spectroscopy studies of dispersant and ZDDP interactions.⁷⁶ They showed dispersant amines can act as bidentate ligands at the zinc atom of ZDDP (Figure 1.19). However, unlike in model amines, dispersant amines were unable to displace the sulfur ligands on zinc which was attributed to the steric bulk of the dispersant tail. This work was later supported by Kapur *et al.*⁷⁷

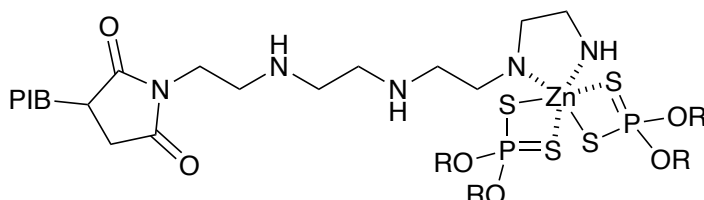


Figure 1.19 – The dispersant/ZDDP complex proposed by Harrison *et al.*⁷⁶

The impact of this interaction was reported by Bartha *et al.* who suggested it was stronger with larger amines and this caused a decrease in the antiwear performance of ZDDP.⁷⁸ The work following on from this is in general agreement as to the negative impacts of dispersants on ZDDP performance.^{59,60,79–83} Due to dispersants binding to surfaces faster than ZDDP, growth of the ZDDP tribofilm can be interrupted. A fully formed ZDDP film can be degraded by dispersant, but not under purely thermal conditions.⁶⁰

1.3.3.2 Dispersants with molybdenum dithiocarbamate (MoDTC) friction modifiers

As their name suggests, friction modifiers (FMs) change the sliding characteristics of surfaces, lowering friction. As with many other lubricant additives, FMs take the form of surfactants. The two most common structures are oleamide and glycerol monooleate (Figure 1.20). The polar head binds the surfaces and the apolar tails organise on the surface, forming a densely packed layer which protects the surface.

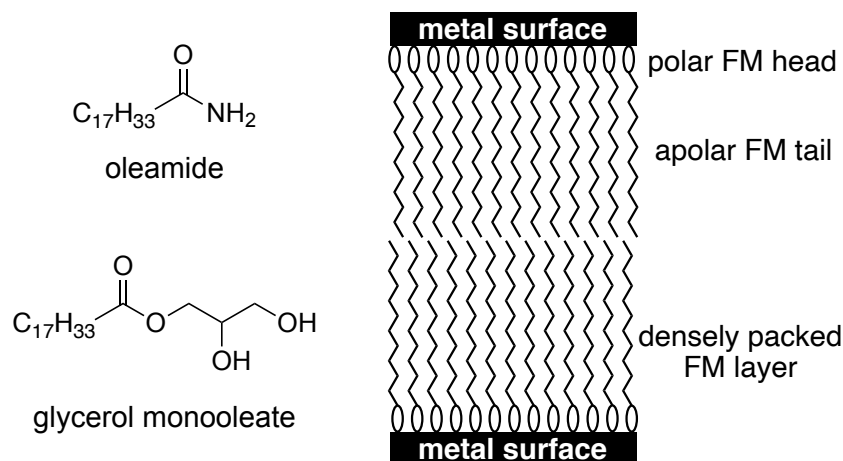


Figure 1.20 – Two of the most common friction modifiers—oleamide and glycerol monooleate—and a representation of how they would arrange on a metal surface to prevent contact and reduce friction.

Inorganic friction modifiers are also used in engine oil lubricants, the most common being molybdenum dithiocarbamate (MoDTC) (Figure 1.21). MoDTC works by thermally decomposing to form layers of MoS_2 on metal surfaces.⁸⁴ These layers can move over each other easily, greatly reducing friction.

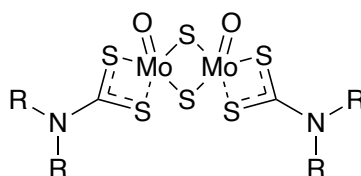


Figure 1.21 – The general structure of molybdenum dithiocarbamate (MoDTC) where R is an alkyl chain.⁸⁵

PIBSI dispersants have also been found to interact with MoDTC friction modifiers. As with ZDDP, amines coordinate to the metal centre in the bulk lubricant.^{86,87} Unhindered amines can form stable complexes that prevent decomposition to form tribofilms on surfaces. The amines found in PIBSIs do coordinate but less strongly, delaying deposition of the tribofilm which can lead to increased wear in bench tests.⁸⁸

1.3.3.3 Dispersants with detergents

Detergents are used to clean the engine and prevent deposits, improving fuel efficiency and engine lifetime. Compared to dispersants, detergents have a more conventional soap-like structure (Figure 1.22). The surfactant anion is usually the conjugate base of alkyl benzenesulfonic acid, alkylphenol, alkylsalicylic acid or a long-chain carboxylic acid.⁸⁹

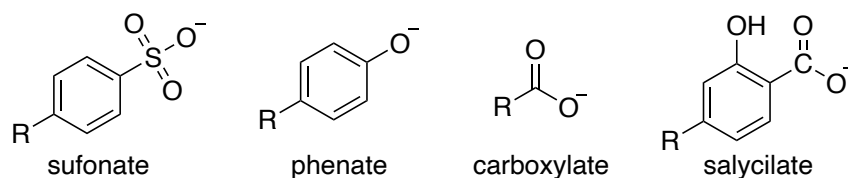


Figure 1.22 – The four main detergent anions used in engine oil lubricants. R is an alkyl chain. For sulfonates, R = 15–30 carbon atoms. For phenates, R = 5–30 carbon atoms. For salicylates and carboxylates, R = 12–30 carbon atoms.

By reacting the acid with a metal oxide or hydroxide, the corresponding salt is formed where the metal cation is usually Ca^{2+} , Mg^{2+} , Ba^{2+} or Na^+ .⁸⁹ When this reaction progresses stoichiometrically, a neutral detergent is yielded. When an excess of metal is used, along with CO_2 , metal carbonates are formed which remain suspended in detergent micelles (Figure 1.23). These dispersants with higher levels of carbonate are known as “over-based” detergents and they are used to neutralise acids formed by lubricant oxidation, which reduces engine corrosion.⁸⁹

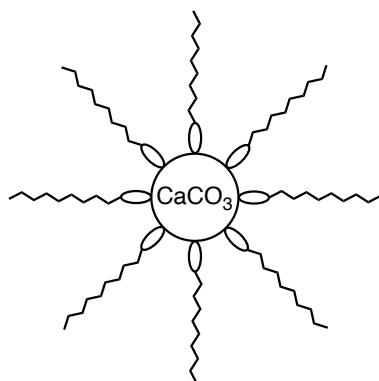


Figure 1.23 – A representation of an over-based detergent colloid, where calcium carbonate is suspended in a detergent inverse micelle.

Dispersants interact with detergents. Detergents exist in hydrocarbon media as colloidal particles with a basic carbonate core with detergent molecules on the surface, stabilising the base in an inverse micelle. Papke *et al.* showed that dispersants interact strongly with these colloidal particles, irreversibly binding to the surface.⁹⁰ This was later attributed to

dispersants first rapidly binding through physisorption to the colloid surface then slowly hydrolysing due to the presence of a base to yield a strongly binding amic-acid.⁹¹

Further work showed the interaction between polymeric succinimide dispersants and over-based calcium aryl sulfonate detergents was also strong.⁹² The interaction increased the high temperature (100 °C) viscosity by 50%, whereas cold-temperature viscometerics were unaffected. Papke *et al.* found pre-blending the detergent with a conventional PIBSI dispersant prevented this reaction,⁹² presumably as the PIBSI had strongly bonded with all available detergent colloids, preventing the polymeric dispersant interacting.

Clearly, additives in lubricant oils interact strongly depending on their structure. However, work by Kapur *et al.* showed that, in terms of wear performance, dispersant/detergent/ZDDP interactions had no impact.⁹³

1.4 Autoxidation

Autoxidation of the lubricant is one of the reasons dispersants are needed, as the polar products form sludge which have negative performance impacts. The high temperatures in the internal combustion engine promote autoxidation which produces the sludge, and limits the lifetime of the lubricant.^{69,70} The majority of the oil within the engine has a long residence time in the engine oil sump where temperatures remain relatively low (below 120 °C).⁹⁴ However, as the lubricant circulates throughout the engine it comes into contact with hotter areas. The main area where the lubricant gets hot is in the piston rings, where the temperature has been measured to range from 115–180 °C.^{69,70} A small volume ($\approx 0.4 \text{ cm}^3$) of lubricant spends around 60 seconds in this environment before 88% of it returns to the cooler sump and the remaining 12% is lost to the combustion chamber.⁹⁵

In this environment, the temperature and oxygen-rich atmosphere combine to degrade the lubricant. This process, whereby oxygen initiates and perpetuates a degradation cycle, is known as autoxidation. Oxygen in the atmosphere is found in its molecular form, O_2 , which has six paired electrons in bonding orbitals and, because of Hund's rule, two unpaired electrons in an antibonding orbital. This gives an overall bond order of two, makes oxygen paramagnetic, and means oxygen can behave as a diradical. Whilst an oxygen molecule is a relatively stable radical, O_2 can initiate autoxidation by abstracting a hydrogen atom from hydrocarbons.^{96–98}

A simplified reaction scheme is shown in Figure 1.24 and is discussed in greater detail in Chapter 4. First, a labile hydrogen is abstracted from a lubricant hydrocarbon by O_2 .⁹⁶⁻⁹⁸ The alkyl radical then reacts with oxygen, entering a chain reaction.⁹⁶⁻⁹⁸ The radical is oxidised to form an alkyl peroxy radical that then forms an alkyl peroxide by hydrogen abstraction, regenerating more carbon-centred radicals.⁹⁶⁻⁹⁸ Through this cycle, a low level of initiation can propagate and multiply to result in a high level of oxidation.

Various oxygen-containing products such as alcohols, aldehydes and carboxylic acids are produced through oxidation.⁹⁹ Further radical reactions form lactones, and primary oxidation products can also react by non-radical routes such as in ester formation.⁹⁹ Alternatively after hydrogen abstraction, an alkyl radical can react with another alkyl radical in a recombination reaction, forming a dehydrodimer.¹⁰⁰ Dehydrodimers are double the molecular weight of the starting material and therefore contribute to viscosity increase during oxidation. All these reactions contribute to the wide variety of products that can form from simple alkyl starting materials, meaning determining and predicting autoxidation mechanisms and products is complex.

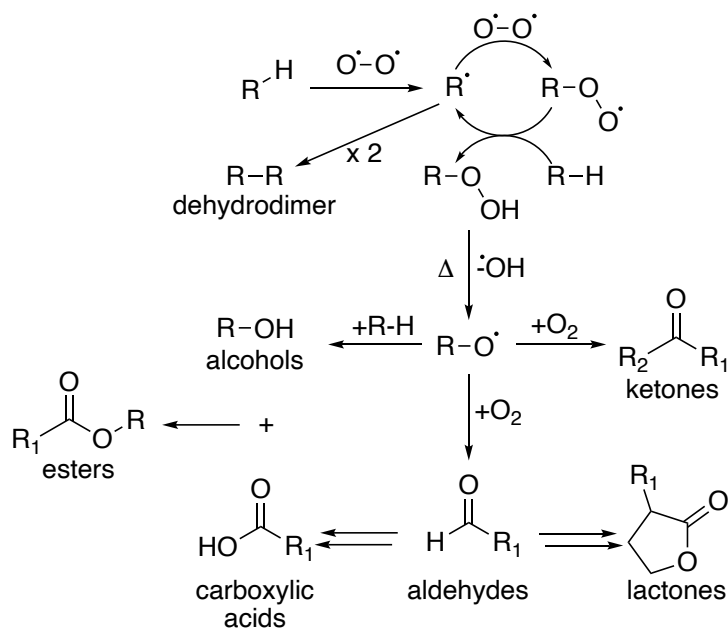


Figure 1.24 – A simplified reaction mechanism for the autoxidation of alkanes to yield various oxygen containing products.

Autoxidation is the main factor limiting the lifetime of an engine oil lubricant. Therefore it is important to understand its mechanisms in order to develop higher performance lubricants that also maintain their initial performance for as long as possible. Initial work applying

hydrocarbon autoxidation mechanisms to the field of lubricants was conducted by Jensen and Korcek^{101–107} from 1979 to the mid 1990s, and by Blaine and Savage in the early 1990s.^{108–110} The work centred on the autoxidation of linear hydrocarbons (*n*-hexadecane) at engine-relevant temperatures of 160–180 °C. In this, they found the primary products to be alkyl peroxides. However, at the high temperatures in an engine, peroxides degrade to form other products like alcohols, aldehydes and acids.

This work used linear hydrocarbons to model lubricant oils however synthetic base oils are branched in nature and mineral oils are even more complex. This is relevant to autoxidation because the rate of initial hydrogen abstraction is dependent on the C–H bond dissociation enthalpy (BDE). Bonds with the lowest BDE are the most likely to be broken and BDE is dependent on the stability of the resultant radical. Stability of carbon-centred radicals increases from primary to secondary to tertiary. Therefore, in a branched alkane system, hydrogens on a tertiary carbon are the most reactive.

This was demonstrated by Stark *et al.* who used pristane and squalane (Figure 1.25) as model base oils for autoxidation studies.⁹⁹ When oxidised at 170 °C, hydrogens on pristane tertiary carbons were 15 times more reactive than hydrogens on secondary carbons and 16 of the 23 products identified were derived from reactions occurring at tertiary carbons. The work of Stark *et al.* demonstrated the significant impact of just a small structural change to the substrate and how chemical mimics for studying autoxidation must accurately represent the system they are modelling.

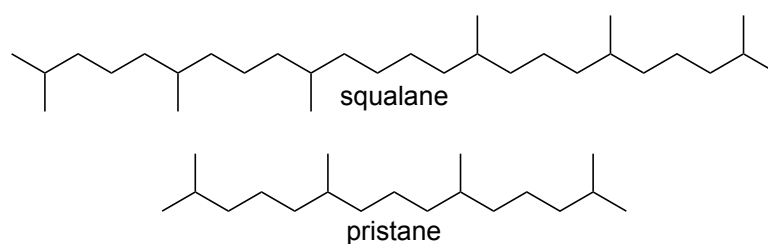


Figure 1.25 – Squalane (2,6,10,15,19,23-hexamethyltetracosane) and pristane (2,6,10,14-tetramethylpentadecane).

The products formed through autoxidation affect the lubricant quite detrimentally. The simplest performance impact is the corrosive effect of acidic autoxidation products.¹³ Formulators can combat this with corrosion inhibitors, or with “over-based” detergents which neutralise acids (see Section 1.3.3.3).¹³ The total lubricant basicity is measured by the total base number (TBN). Throughout a lubricant’s lifetime, the TBN decreases and its

counterpart—total acid number (TAN)—increases. When the TBN is too low and the TAN is too high, lubricant performance decreases to the point where it needs replacing.

The other major effect of autoxidation is viscosity increase.¹³ As a result of oxidation, the viscosity of the lubricant increases which increases friction and decreases fuel economy. In an extreme case, oxidation products and lubricant viscosity increase can stop the lubricant from flowing around the engine, starving components of lubricant and causing catastrophic wear.

1.4.1 Antioxidants

Antioxidants (AOs) are added to reduce autoxidation, extending lubricant lifetime. They broadly fall into two categories, radical scavenging and peroxide destroying AOs. Residual sulfur in the base oil, and ZDDP prevent autoxidation by destroying peroxides, disrupting the chain mechanism of autoxidation.¹¹¹ Phenolic and aminic (Figure 1.26) radical scavenging antioxidant additives donate a hydrogen atom to a reactive lubricant-derived radical (Figure 1.27), stopping autoxidation.

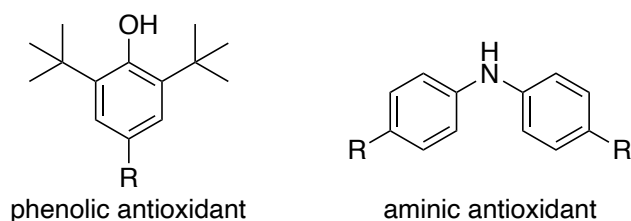


Figure 1.26 – The general structures of phenolic and aminic antioxidants where R is an alkyl chain.

The phenolic antioxidant donates the phenolic hydrogen and the aminic AO donates the aminic hydrogen. This quenching prevents the lubricant radical reacting further; due to the high stability of the resultant AO radical, it does not participate in further autoxidation.

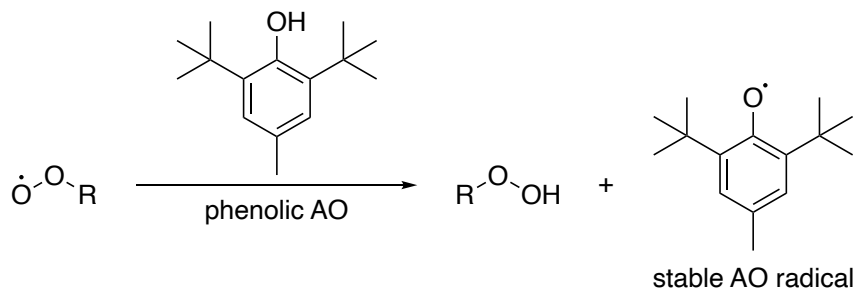


Figure 1.27 – Quenching of an alkyl radical by the antioxidant BHT.

The aromatic structure of the resultant radical is highly resonance stabilised (Figure 1.28). In butylated hydroxytoluene (BHT) and similar phenolic antioxidants, *tert*-butyl groups offer additional steric stabilisation of the radical.¹¹¹

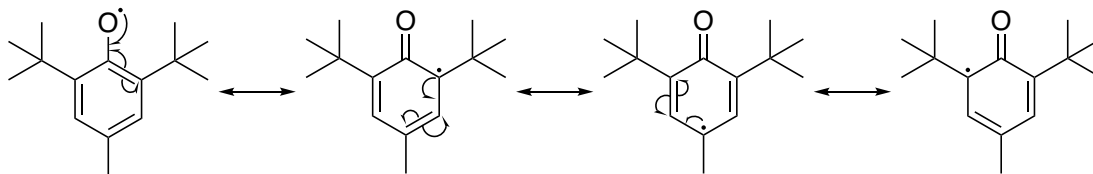


Figure 1.28 – Resonance stabilisation of the BHT radical.

Not only do aminic antioxidants quench reactive radicals through hydrogen donation, they are thought to catalytically prevent oxidation. The nitrogen atom can be oxidised to a nitroxyl radical that destroys peroxides through the Denisov cycle. One molecule of aminic antioxidant has been reported to destroy up to 40 radicals.¹¹² The Denisov cycle is discussed in greater detail in Section 5.3.

1.5 Dispersants and autoxidation

To date, very little is known about dispersants and autoxidation despite their inherent interconnected properties and dispersants' importance for lubricant performance. In fact, to the best of the author's knowledge there is only one study that looks at the effect of autoxidation on dispersants.¹¹³ In 1981 T. R. Erdman, working for the Chevron Research Company, synthesised a range of PIBSI dispersants with ¹⁴C tags. The tags were either located on the succinimide or on the amine (Figure 1.29).

Erdman tracked the concentrations of ¹⁴C during an engine test. Samples were taken from the bulk lubricant throughout the test and deposits that formed on various engine components during the test were analysed at the end of the test. Erdman concluded that because concentrations of ¹⁴C were approximately the same across different areas of the engine regardless of dispersant type, the dispersant had not degraded during use. This was claimed despite the observation of amide-containing "lacquers" that were attributed to PIBSI degradation and have also been observed in other studies.^{114,115} What this work actually shows is that the dispersant did not degrade at a site between the ¹⁴C labels on the succinimide and the amines. However, it is not proof that it did not degrade outside of this area. This is significant because the alkene that joins the tail to the head was not covered

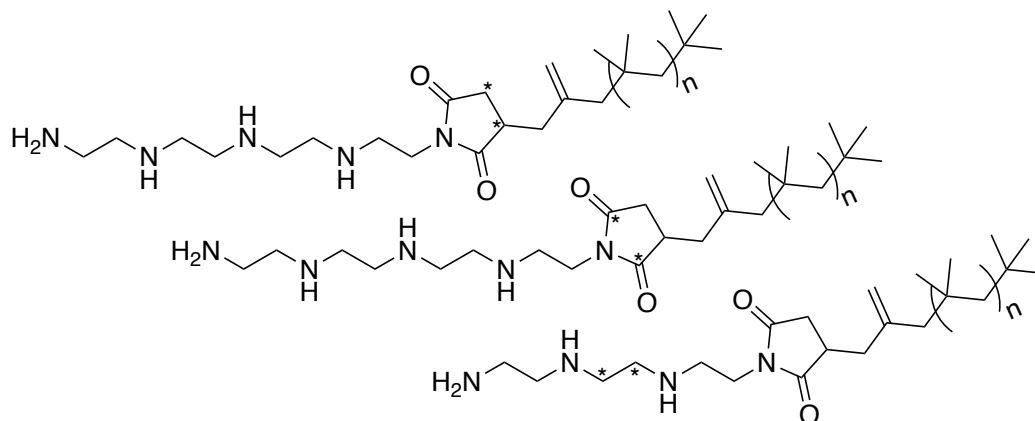


Figure 1.29 – The three ^{14}C labelled PIBSIs studied by Erdman.¹¹³ * denotes the labelling sites.

by this study but alkenes are known to oxidise rapidly due to their relatively labile allylic hydrogens.¹¹⁶ Therefore, more work is needed to determine the actual effect autoxidation has on the PIBSI dispersant structure and the effect this has on lubricant and engine performance.

1.6 Project aims

The previous work on PIBSIs described above covers their synthesis and their interactions in lubricants. The majority of this work is done on “fresh” dispersants and lubricants that have not seen operating conditions in an engine. No previous work has tried to determine mechanisms behind dispersant autoxidation, a phenomenon that is known to occur by the observation of amide lacquers.^{114,115} By determining how dispersants break down, the weak points within the dispersant structure can be highlighted which would facilitate the design of new dispersants without such weaknesses. In this thesis dispersants and autoxidation are combined with a view to understand how dispersants behave during use and how this might impact the performance of the lubricant.

Chapter 2 gives the experimental procedures used in this work. Chapter 3 explores some serendipitous surfactant synthesis, where the role of radicals in the synthesis of PIBSA for use in PIBSI dispersants was investigated. This novel behaviour showed just how complex the seemingly simple synthesis of dispersants can be, and shows how the poorly characterised mixtures of compounds in a commercial dispersant are not suitable for

determining autoxidation mechanisms. To address this, a high purity chemical mimic or model for PIBSI dispersants has been synthesised and studied. The purity and structure of the mimic allowed its autoxidative degradation mechanisms to be determined through product studies relying on gas chromatography - electron ionisation - mass spectrometry (GC-EI-MS) and gas chromatography - flame ionisation detector (GC-FID). The work is reported in Chapter 4 and was published in 2019.¹¹⁷ To build on this work, the chemical mimic was altered to include secondary and tertiary amines, as found in PIBSI dispersants. This is reported in Chapter 5.

The work in this thesis sheds light on the interesting mechanisms behind both dispersant synthesis and their degradation during use. Through this increased understanding, more durable and higher performing dispersants and lubricants can be developed.

Chapter 2

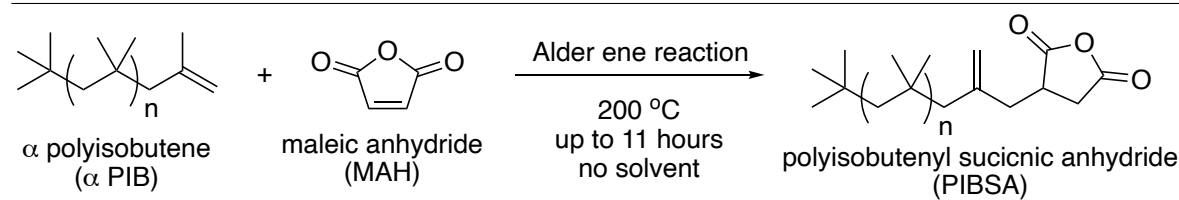
Experimental

This experimental chapter is split into sections describing the sample preparation and synthesis conducted in each results chapter of this thesis. This is followed by a description of the analytical techniques used across all three chapters. Finally, a list of all materials used in this work is provided.

2.1 Experimental procedures supporting Chapter 3

The reaction of polyisobutene (PIB) and maleic anhydride (MAH) to form polyisobutenyl succinic anhydrides (PIBSAs) (Scheme 2.1) was initially investigated in PIBSA synthesis A, described below, using a comparable experimental set up to that used by Balzano *et al.*³²

Scheme 2.1 The formation of PIBSA by the Alder ene reaction of MAH with the terminal alkene of α PIB.



The initial experiment was conducted on a 20 g scale in a two-piece glass flask under one atmosphere of argon with stirring—an equivalent set up to Balzano *et al.* Samples were taken to monitor conversion and yield to determine the optimum reaction time for PIBSA yield and purity. This was followed by a scaled up reaction at 100 g, the same scale used by Balzano *et al.*, to produce a larger quantity of PIBSA for further experiments. Due to unexpected results suggesting the occurrence of different reaction chemistry, the reaction was then scaled down to 500 mg and modified to allow the use of air sensitive techniques in PIBSA synthesis B and C to determine reaction mechanism. The full list of materials used can be found in Table 2.7.

The PIB was supplied by Afton Chemical Ltd with an number averaged molecular weight (M_N) of 950 g mol⁻¹. Further characterisations of molecular weight and distribution were not attempted because the relatively low molecular weight was below the calibration limit for the available gel permeation chromatograph which would give unreliable results. As such, the stoichiometry reported within this section should not be taken as absolute. This is because a polymer distribution bias, such as a higher concentration of small low molecular weight oligomers, could skew the expected concentration of double bonds, relative to which MAH

quantities were calculated. To improve upon this work, more-accurate determination of the alkene content of the polymer could be attempted by assessing the iodine value, such as in the ASTM International, formerly known as American Society for Testing and Materials (ASTM) D1541 method using the Rosenmund-Kuhnhehn reagent.

2.1.1 PIBSA synthesis A

Samples were prepared on a 20 mg and a 100 g scale in a 250 cm³ two-piece glass flask equipped with overhead stirring. The flask was charged with PIB (see Table 2.1) and heated to 200 °C, with stirring, under argon. MAH (1.0 eqv., see Table 2.1) was added. When indicated in Chapter 3, maleic acid (MA) was added. The reaction was held at 200 °C with stirring under one atmosphere of argon for up to 11 hours. Samples were taken at regular intervals for analysis by nuclear magnetic resonance (NMR) spectroscopy and attenuated total reflection - Fourier transform - infrared (ATR-FT-IR) spectroscopy.

Table 2.1 – Parameters used in PIBSA synthesis A. **purified by sublimation.

Rxn.	PIB/(g, mol)	MAH/(g, mol, eqv.)	MA/(g, mol, eqv.)	time/h
1	20, 0.021	2.06, 0.021, 1.0	-	11.0
2	100, 0.105	10.32, 0.105, 1.0	-	5.0
3	20, 0.021	2.06, 0.021, 1.0 **	-	5.0
4	20, 0.021	2.06, 0.021, 1.0	0.122, 0.001, 0.05	5.0

2.1.2 PIBSA synthesis B

PIBSA synthesis B was designed to test the effect of a radical scavenging antioxidant (AO) on the production of different PIBSA structures, discussed further in Chapter 3.

A single-necked 25 cm³ round bottom flask was charged with PIB (500 mg, 5.26×10^{-4} mol) and MAH (1 to 4 mol eqv.). When required, tri-*tert*-butylphenol (13.8 mg, 2.4×10^{-5} mol 0.05 eqv.) was added as a radical scavenger. The flasks were evacuated and backfilled with argon three times and held under one atmosphere of argon at 200 °C with magnetic stirring (350 RPM) for five hours. The samples were cooled to room temperature and crude samples taken for analysis by ¹H-NMR spectroscopy.

2.1.3 PIBSA synthesis C

PIBSA synthesis C experiments were designed to determine radical initiator source within the PIBSA synthesis system, discussed further in Chapter 3. Five protocols were investigated.

C1: A single-necked 25 cm³ glass round bottom flask was charged with PIB (500 mg, 5.26×10^{-4} mol) and MAH (51.5 mg, 5.26×10^{-4} mol, 1 eqv.). The flasks were evacuated and backfilled with argon three times (later referred to as passive degassing). The flask was held under one atmosphere of argon with magnetic stirring (350 RPM) at 200 °C for five hours. After cooling to room temperature, the crude product was analysed by ¹H-NMR spectroscopy.

C2: PIB (≈ 2.5 g) was dissolved in *n*-hexane (≈ 20 cm³) and passed through a plug of activated basic alumina. The resultant sample was concentrated under a reduced pressure of air to yield alumina-purified PIB. A single-necked 25 cm³ glass round bottom flask was charged with alumina-purified PIB (500 mg, 5.26×10^{-4} mol) and MAH (51.5 mg, 5.26×10^{-4} mol, 1 eqv.). The flasks were evacuated and backfilled with argon three times. The flask was held under an argon atmosphere with magnetic stirring (350 RPM) at 200 °C for five hours. After cooling to room temperature, the crude product was analysed by ¹H-NMR spectroscopy.

C3: PIB (500 mg, 5.26×10^{-4} mol) was dissolved in *n*-pentane (5 cm³) in a single-necked 25 cm³ glass round bottom flask. MAH (51.5 mg, 5.26×10^{-4} mol, 1 eqv.) was added before the flask was sealed and freeze pump thaw (FPT) degassed for three cycles. The temperature was increased to 50 °C while magnetically stirring (350 RPM) and under a flow of argon to evaporate the solvent (≈ 10 minutes). The flask was placed under an argon atmosphere and heated with magnetic stirring (350 RPM) to 200 °C for 5 hours. After cooling to room temperature, the crude product was analysed by ¹H-NMR spectroscopy.

C4: PIB (500 mg, 5.26×10^{-4} mol) was dissolved in *n*-pentane (5 cm³) and filtered through a plug of activated basic alumina into a single-necked 25 cm³ glass round bottom flask. MAH (51.5 mg, 5.26×10^{-4} mol, 1 eqv.) was added before the flask was sealed and FPT degassed for three cycles. The temperature was increased to 50 °C while magnetically stirring (350 RPM) and under a flow of argon to evaporate the solvent (≈ 10 minutes). The flask was placed under an argon atmosphere and heated with magnetic stirring (350 RPM) to 200 °C for 5 hours. After cooling to room temperature, the crude product was analysed by ¹H-NMR spectroscopy.

C5: PIB (500 mg, 5.26×10^{-4} mol) was dissolved in *n*-pentane (5 cm³) and filtered through a plug of activated basic alumina into a single-necked 25 cm³ glass round bottom flask. MAH (51.5 mg, 5.26×10^{-4} mol, 1 eqv.) and di-*tert*-butyl peroxide (5 μ L, 4 mg, 2.74×10^{-5} mol, 5 mol%) was added before the flask was sealed and FPT degassed for three cycles. The temperature was increased to 50 °C while magnetically stirring (350 RPM) and under a flow of argon to evaporate the solvent (\approx 10 minutes). The flask was placed under an argon atmosphere and heated with magnetic stirring (350 RPM) to 200 °C for 5 hours. After cooling to room temperature, the crude product was analysed by ¹H-NMR spectroscopy.

2.1.4 Bis-PIBSA formation under radical conditions

A single-necked 25 cm³ round bottom flask was charged with PIBSA 3 (500 mg, 4.8×10^{-4} mol) and MAH (138 mg, 14.4×10^{-4} mol, 3 mol eqv.). The flasks were evacuated and backfilled with argon three times and held under one atmosphere of argon at 200 °C with magnetic stirring (350 RPM) for five hours. The samples were cooled to room temperature and crude samples taken for analysis by ¹H-NMR spectroscopy.

2.1.5 Bis-PIBSA formation under Alder ene conditions

A single-necked 25 cm³ round bottom flask was charged with PIBSA 3 (500 mg, 4.8×10^{-4} mol) and MAH (184 mg, 19.2×10^{-4} mol, 4 mol eqv.). Tri-*tert*-butylphenol (13.8 mg, 2.4×10^{-5} mol, 0.05 eqv.) was added as a radical scavenger. The flasks were evacuated and backfilled with argon three times and held under one atmosphere of argon at 200 °C with magnetic stirring (350 RPM) for five hours. The samples were cooled to room temperature and crude samples taken for analysis by ¹H-NMR spectroscopy.

2.1.6 Itaconic anhydride addition to PIB

A single-necked 100 cm³ round bottom flask was charged with PIB (10 g, 10.5 mmol) and itaconic anhydride (IAH) (1.177 g, 10.5 mmol, 1.0 mol eqv.). When required, tri-*tert*-butylphenol (138 mg, 5.25×10^{-4} mol, 0.05 eqv.) was added as a radical scavenger. The flasks were evacuated and backfilled with argon three times and held under one atmosphere of argon at 200 °C while magnetically stirring (350 RPM) for five hours. The

samples were cooled to room temperature and crude samples of the dark brown product were taken for analysis by ^1H -NMR spectroscopy.

2.1.7 Styrene-assisted MAH addition to PIB

A single-necked 100 cm³ round bottom flask was charged with PIB (10 g, 10.5 mmol) and MAH (1.03 g, 10.5 mmol, 1.0 mol eqv.). Styrene (1.09 g, 10.5 mmol, 1.0 mol eqv.) was added and the flask was evacuated and backfilled with argon three times. The flask was held under one atmosphere of argon and heated to 140 °C with magnetic stirring (350 RPM). Within three minutes the previously clear colourless solution had turned white and opaque. After 30 minutes, a white solid had formed and the reaction was aborted.

2.1.8 PIBSA analysis

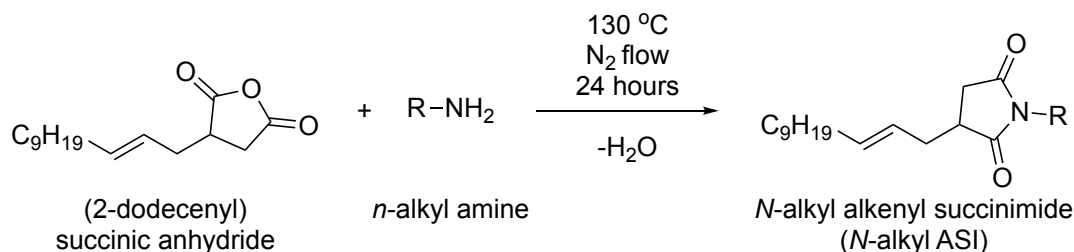
The crude products were analysed by ATR-FT-IR spectroscopy to confirm succinic anhydride formation and by ^1H -NMR spectroscopy to calculate yield, conversion and selectivity. Alkene protons were integrated relative to PIB geminal dimethyl protons which were assumed to remain constant due to their low reactivity. For structural determination, samples were purified to remove unreacted PIB prior to analysis using a micro-scale K60 silica column. A plugged glass Pasteur pipette was loaded with K60 silica and wetted with *n*-hexane. The product (200 mg) was dissolved in a minimum of *n*-hexane and loaded onto the micro column. Unreacted PIB was eluted by flushing the column with 100% *n*-hexane. To elute the PIBSA product, the solvent system was changed to 5% EtOAc in *n*-hexane. The sample was concentrated *in vacuo* and dissolved in CDCl_3 for analysis by ^1H , ^{13}C , ^1H - ^1H correlation spectroscopy (COSY), distortionless enhancement by polarization transfer (DEPT)-135 and heteronuclear multiple quantum coherence (HMQC) NMR spectroscopy.

2.2 Experimental procedures supporting Chapter 4

2.2.1 General *N*-alkyl alkenyl succinimide (ASI) synthesis procedure

N-alkyl alkenyl succinimides (ASIs) were synthesised following Scheme 2.2 as described below.

Scheme 2.2 The synthesis of *N*-alkyl alkenyl succinimides (ASIs) where R ranges from *n*-propyl to *n*-heptyl.

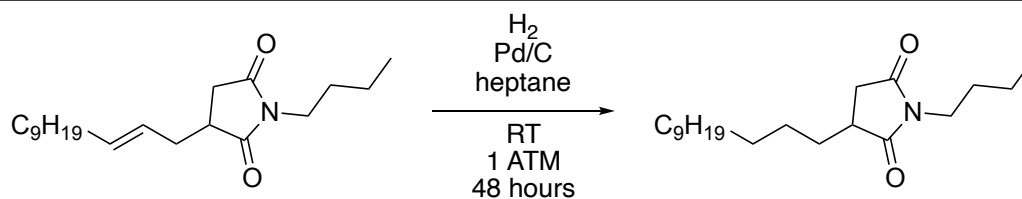


A three-necked 125 cm^3 round bottom flask was charged with (2-dodecenyl)succinic anhydride (4.00 g, 15 mmol) which was then melted at $60\text{ }^\circ\text{C}$ under a flow of nitrogen with stirring. An *n*-alkyl amine was added (16.5 mmol, 1.1 eq.) and the resultant mixture heated to $130\text{ }^\circ\text{C}$ for 24 hours with magnetic stirring (250 RPM) under a flow of nitrogen (0.04 L min^{-1}). Succinimide formation was confirmed by ATR-FT-IR and the crude product was purified by flash column chromatography on K60 silica gel by elution with 20% ethyl acetate in petroleum spirit ($40\text{--}60\text{ }^\circ\text{C}$). ASI dispersant analogues were prepared with *n*-propyl, *n*-butyl, *n*-pentyl, *n*-hexyl and *n*-heptyl amines to yield the corresponding *N*-alkyl ASI. Clear colourless liquids were afforded for all *N*-alkyl ASIs in good yields with at least 98% purity as determined by gas chromatography - flame ionisation detector (GC-FID). The purified product was characterised by $^1\text{H-NMR}$ spectroscopy, gas chromatography - electron ionisation - mass spectrometry (GC-EI-MS) and electron spray ionisation - mass spectrometry (ESI-MS), see Appendix Chapter 7.

2.2.2 *N*-butyl ASI hydrogenation

N-butyl ASI was hydrogenated following Scheme 2.3 and the procedure described below.

A 500 cm^3 round bottom flask was charged with *N*-butyl ASI (4.0 g), 1% Pd on carbon (0.39 g, 0.3% (mol/mol) Pd) and *n*-heptane (200 cm^3). The resultant mixture was placed under a hydrogen atmosphere and magnetically stirred (250 RPM) for 48 hours at room temperature

Scheme 2.3 The hydrogenation of *N*-butyl ASI using palladium on carbon.

and pressure. The crude product was filtered through celite and purified by flash column chromatography on K60 silica gel using 20% ethyl acetate in petroleum spirit (40–60 °C) affording a white solid in good yields with 98% purity by GC-FID. The purified product, H_2 -*N*-butyl ASI, was characterised by 1H -NMR spectroscopy, GC-EI-MS and ESI-MS, see Appendix Chapter 7.

2.2.3 Neat *N*-alkyl ASI autoxidation

A three-necked 125 cm³ round bottom flask was heated to 170 °C under a flow of oxygen (0.04 L min⁻¹). The *N*-alkyl ASI (3.0 g) was added and held at 170 °C for 180 minutes with magnetic stirring (375 RPM). The liquid temperature was monitored using a K-type thermocouple. Samples (0.15 g) were taken at regular intervals and analysed by GC-FID and GC-EI-MS. A schematic of the reaction apparatus is shown in Figure 2.1.

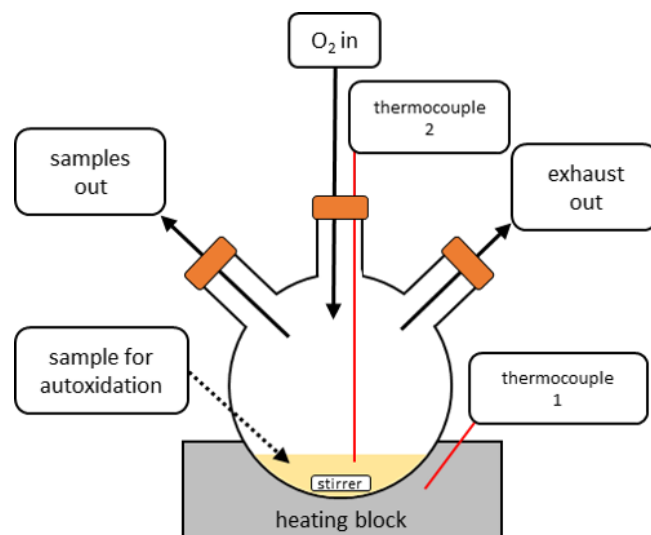


Figure 2.1 – A schematic of the experimental set up used for neat ASI autoxidation.

2.2.4 *N*-alkyl ASI autoxidation in squalane

A stainless steel (EN BS 304) reactor with a 55 cm³ internal volume was heated to 170 °C under a flow of oxygen (0.04 L min⁻¹). A sample of ASI dissolved in squalane (10 cm³, 5% w/w, Figure 2.2) was injected via a cannula. The temperature of the sample reached equilibrium in under two minutes, during which time autoxidation was assumed to be negligible. The mixture was held at 170 °C for 90 minutes with stirring (375 rpm). The liquid temperature was measured using a K-type thermocouple. Samples (0.3 cm³) were taken at regular intervals and analysed by quantitative GC-FID.⁹⁹ Ageing experiments were conducted in triplicate and analysed once by GC-FID from which mean and standard error were calculated. A schematic of the reaction set up is shown in Figure 2.3.

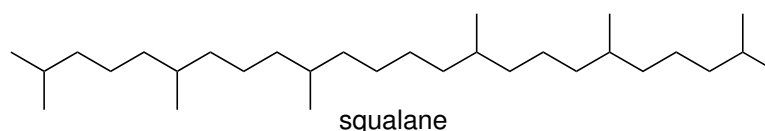


Figure 2.2 – 2,6,10,15,19,23-hexamethyltetracosane (C₃₀H₆₂) commonly known as squalane.

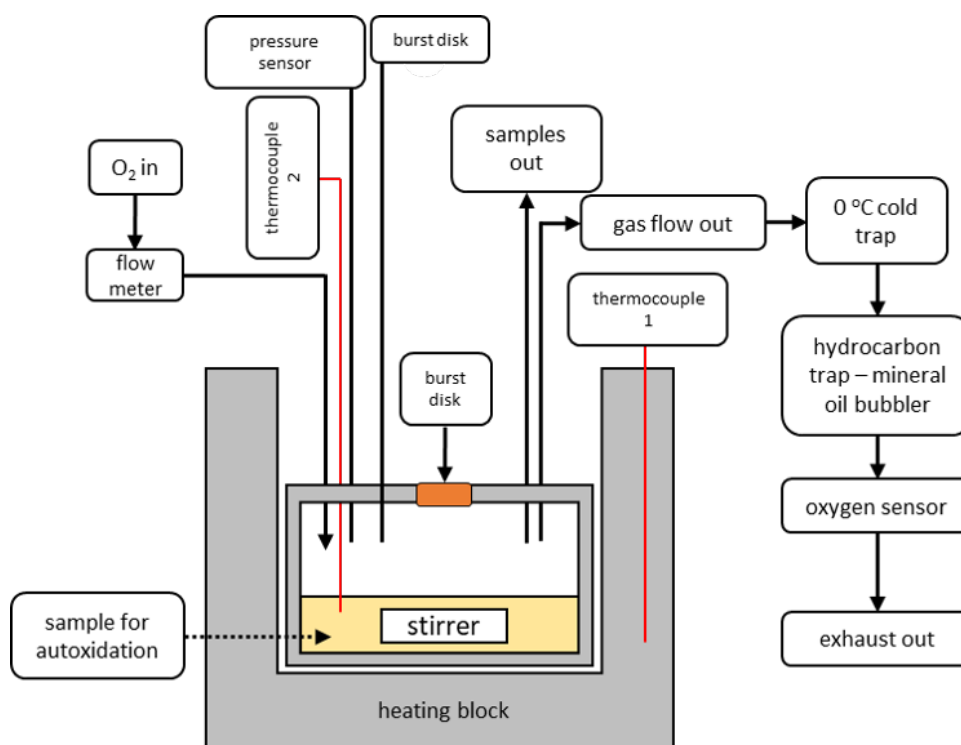


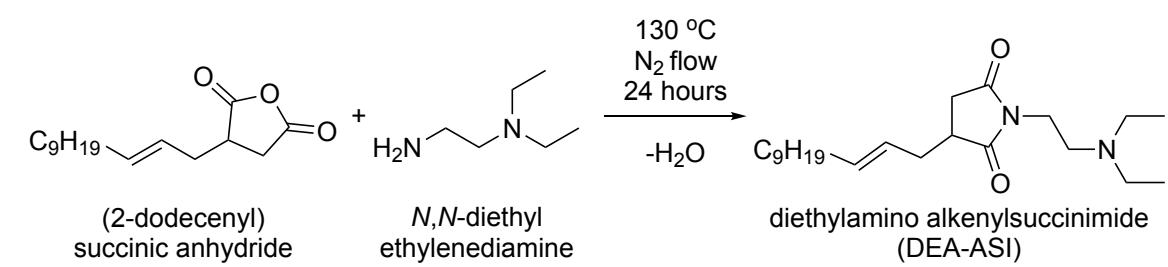
Figure 2.3 – The experimental set up used for ASI autoxidation in squalane.

2.3 Experimental procedures supporting Chapter 5

2.3.1 Diethylamino alkenyl succinimide (DEA-ASI) synthesis

Diethylamino alkenyl succinimide (DEA-ASI) was synthesised following Scheme 2.4 and the procedure described below.

Scheme 2.4 The synthesis of diethylamino alkenyl succinimide (DEA-ASI).

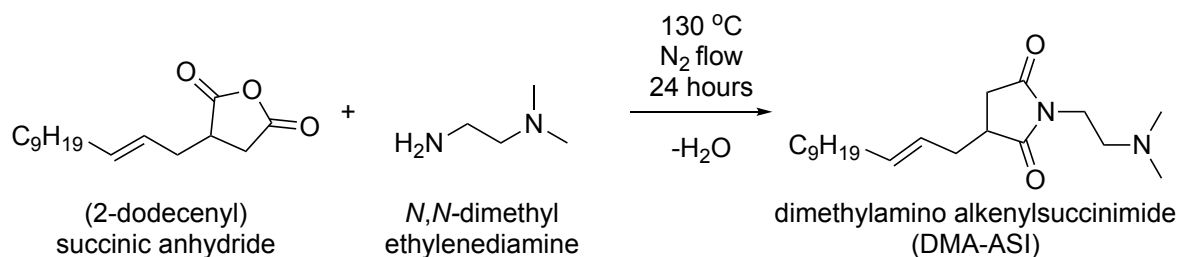


A three-necked 125 cm³ round bottom flask was charged with (2-dodecenyl)succinic anhydride (10.00 g, 37.5 mmol) which was then melted at 60 °C under a flow of nitrogen (0.04 L min⁻¹) with magnetic stirring (250 RPM). *N,N*-diethylethylenediamine was added (5.17 g, 44.5 mmol, 1.2 eq.) and the resultant mixture heated to 130 °C for 24 hours with stirring under a flow of nitrogen. Succinimide formation was confirmed by ATR-FT-IR and the crude product was purified by flash column chromatography on K60 silica gel by elution using ethyl acetate with 1% triethylamine. A clear straw-yellow liquid was afforded in good yields with at least 95% purity determined by GC-FID. The purified product contained a mix of *cis* and *trans* isomers with a slight dominance of the *trans* isomer. The exact ratio of isomers could not be determined due to co-elution of the two GC peaks. The purified product was characterised by ¹H-NMR spectroscopy and ESI-MS, see Appendix Chapter 7.

2.3.2 Dimethylamino alkenyl succinimide (DMA-ASI) synthesis

Dimethylamino alkenyl succinimide (DMA-ASI) was synthesised following Scheme 2.5 and the procedure described below.

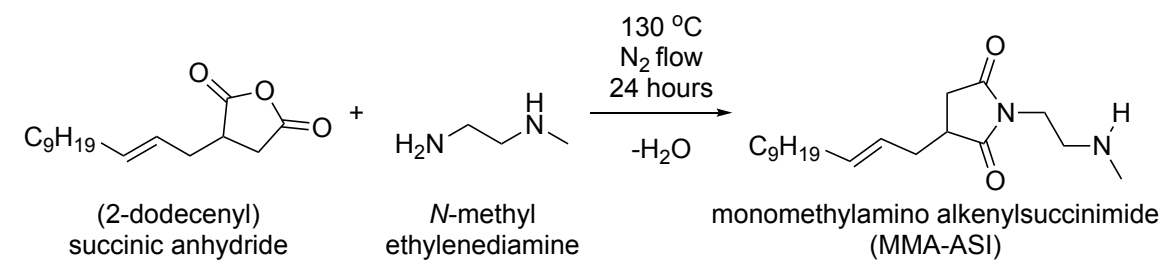
A three-necked 125 cm³ round bottom flask was charged with (2-dodecenyl)succinic anhydride (10.00 g, 37.5 mmol) which was then melted at 60 °C under a flow of nitrogen (0.04 L min⁻¹) with stirring. *N,N*-dimethylethylenediamine was added (3.92 g, 44.5 mmol,

Scheme 2.5 The synthesis of dimethylamino alkenyl succinimide (DMA-ASI).

1.2 eq.) and the resultant mixture heated to 130 °C for 24 hours with stirring under a flow of nitrogen. Succinimide formation was confirmed by ATR-FT-IR and the crude product was purified by flash column chromatography on K60 silica gel by elution using acetone with 1% triethylamine. A clear straw-yellow liquid was afforded in good yields with at least 95% purity determined by GC-FID. The purified product contained a mix of *cis* and *trans* isomers with a slight dominance of the *trans* isomer. The exact ratio of isomers could not be determined due to co-elution of the two GC peaks. The purified product was characterised by ¹H-NMR spectroscopy and ESI-MS, see Appendix Chapter 7.

2.3.3 Monomethylamino alkenyl succinimide (MMA-ASI) synthesis

Monomethylamino alkenyl succinimide (MMA-ASI) was synthesised following Scheme 2.6 and the procedure described below.

Scheme 2.6 The synthesis of monomethylamino alkenyl succinimide (MMA-ASI).

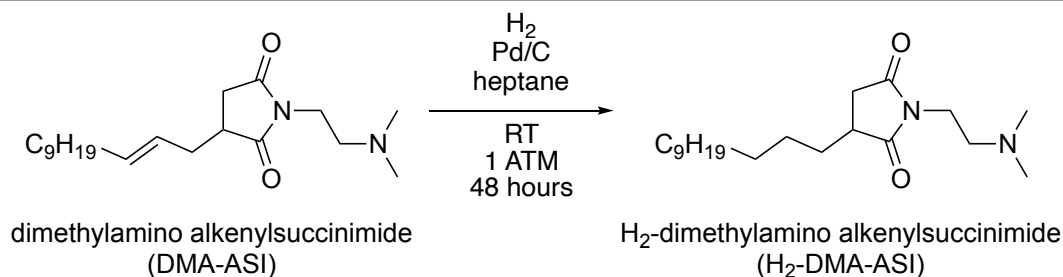
A three-necked 125 cm³ glass round bottom flask was charged with (2-dodecenyl)succinic anhydride (10.00 g, 37.5 mmol) which was then melted at 60 °C under a flow of nitrogen (0.04 L min⁻¹) with magnetic stirring (250 RPM). *N*-methylethylenediamine was added (3.30 g, 44.5 mmol, 1.2 eq.) and the resultant mixture heated to 130 °C for 24 hours with magnetic stirring (250 RPM) under a flow of nitrogen (0.04 L min⁻¹). Succinimide formation was confirmed by ATR-FT-IR and the crude product was purified by flash

column chromatography on K60 silica gel by elution using acetone with 1% triethylamine. A clear straw-yellow liquid was afforded in poor yields (<10%) with at least 95% purity determined by GC-FID. The purified product contained a mix of cis and trans isomers with a slight dominance of the trans isomer. The exact ratio of isomers could not be determined due to co-elution of the two GC peaks. The purified product was characterised by $^1\text{H-NMR}$ spectroscopy and ESI-MS, see Appendix Chapter 7.

2.3.4 Dimethylamino alkenyl succinimide (DMA-ASI) hydrogenation

Dimethylamino alkenyl succinimide (DMA-ASI) was hydrogenated following Scheme 2.7 and the procedure described below.

Scheme 2.7 The hydrogenation of dimethylamino alkenyl succinimide (DMA-ASI).



A 50 cm³ round bottom flask was charged with DMA-ASI (600 mg, 1.78 mmol), 10% Pd on carbon (3.78 g, 5% (mol/mol) Pd) and *n*-heptane (30 cm³). The resultant mixture was placed under a hydrogen atmosphere and magnetically stirred (250 RPM) for 48 hours at room temperature and pressure. The crude product was filtered through celite and concentrated *in vacuo* affording a clear liquid in good yields with at least 95 % purity by GC-FID. The purified product, H₂-DMA-ASI, was characterised by $^1\text{H-NMR}$ spectroscopy and ESI-MS, see Appendix Chapter 7.

2.3.5 Amino ASI autoxidation in squalane

Amino ASIs were oxidised in squalane following the same procedure as used previously for alkyl ASIs. The only change was the pre-heating of the MMA-ASI containing sample to ensure full ASI dissolution.

A stainless steel (EN BS 304) reactor with a 55 cm³ internal volume was heated to 170 °C under a flow of oxygen (0.04 L min⁻¹). A sample of amino ASI dissolved in squalane (10 cm³, 5% w/w) was injected via a cannula. Prior to injection the solution of 5% MMA-ASI

in squalane was heated to 80 °C to ensure homogeneity. The temperature of the sample reached equilibrium in under two minutes, during which time autoxidation was assumed to be negligible. The mixture was held at 170 °C for 90 minutes with magnetic stirring (375 rpm). The liquid temperature was measured using a K-type thermocouple. The oxygen concentration in the exhaust gases was monitored using a Teledyne Analytical Instruments R17-A oxygen sensor. Samples (0.3 cm³) were taken at regular intervals and analysed by quantitative GC-FID.⁹⁹ Ageing experiments were conducted in triplicate and analysed once by GC-FID from which average values were calculated. A schematic of the reaction set up is shown in Figure 2.3.

2.3.6 Performance testing of diethylamino ASI using industry-standard tests

A large quantity (\approx 130 g) of diethylamino ASI (DEA-ASI) was synthesised and purified following the below procedure. This product was then evaluated for oxidation performance using two standard industrial tests. Fully formulated lubricant oils were tested using the Coordinating European Council (CEC) L-109-14 and ASTM D 7097 thermo-oxidation engine oil simulation test (TEOST) tests following the official test procedures.^{118,119} The ASTM D 7097 test was conducted by Afton Chemical Ltd and the CEC L-109-14 was conducted at a third party commercial testing facility.

2.3.6.1 Large scale diethylamino ASI (DEA-ASI) synthesis

A 500 cm³ round bottom flask was charged with (2-dodecenyl)succinic anhydride (104.6 g, 392.6 mmol) which was then melted at 60 °C under a flow of nitrogen with stirring. *N,N*-diethylethylenediamine added (50.2 g, 432 mmol, 1.1 eq.) and the resultant mixture heated to 130 °C for 24 hours with stirring under a flow of nitrogen. Succinimide formation was confirmed by ATR-FT-IR. The crude product was purified using short-path vacuum distillation (Kugelrohr distillation) at 300 °C and 2 mbar pressure. Clear straw yellow liquid was afforded in good yield (130 g, 90%) at 92% purity as a mixture of cis/trans alkene isomers, determined by GC-FID. The purified product was characterised by ¹H-NMR spectroscopy, GC-EI-MS and ESI-MS, see Appendix Chapter 7.

2.4 Analysis

2.4.1 Gas chromatography with flame ionisation detection (GC-FID)

GC-FID samples were analysed on one of three GCs. Results in Chapter 3 were collected using a Shimadzu GC-17a gas chromatograph. Results in Chapter 4 were collected using a Shimadzu GC-17a and an Agilent 6890 gas chromatograph. Results in Chapter 5 were collected using an Agilent 7890 gas chromatograph. All GCs were calibrated prior to use, and the calibration regularly checked and updated after machine maintenance to ensure reliability and accuracy. Calibrations were performed using authentic standards and the effective carbon number (ECN) method, discussed later. Samples were not derivatised prior to quantitation. Samples were diluted in ethyl acetate to ensure appropriate viscosity and concentration.

2.4.1.1 Shimadzu GC-17a gas chromatograph

Samples were analysed using a Shimadzu GC-17a gas chromatograph with a flame ionisation detector. The capillary column was a Phenomenex ZB-5HT inferno (30 m x 0.25 mm x 0.25 μm) with a 5% diphenyldimethyl polysiloxane stationary phase and a 5 m length of integral guard column. Chromatography parameters are shown in Table 2.2. Quantitative GC samples were prepared by dissolving the accurately weighed sample (0.1 g, 4 significant figures) in ethyl acetate (1.00 cm^3).⁹⁹

Table 2.2 – The parameters used for Shimadzu GC-17a GC-FID analysis.

Parameter	Condition	Units
Carrier gas	Helium	-
Sample solvent	Ethyl acetate	-
Flow rate	2.0	mL min^{-1}
Injector temperature	370	$^{\circ}\text{C}$
Injection volume	1.0	μL
Split ratio	10:1 or 2:1	-
Initial column temperature	50 (1 minute hold)	$^{\circ}\text{C}$
Ramp rate	5	$^{\circ}\text{C min}^{-1}$
Final column temperature	350 (20 minute hold)	$^{\circ}\text{C}$
Detector temperature	370	$^{\circ}\text{C}$
Total analysis time	86	min

2.4.1.2 Agilent 6890 gas chromatograph

Samples were analysed using an Agilent 6890 gas chromatograph with a flame ionisation detector. The capillary column was a Restek Rxi-5HT (30 m x 0.25 mm x 0.25 μm) with a 5% diphenyldimethyl polysiloxane stationary phase. Chromatography parameters are shown in Table 2.3. Quantitative GC samples were prepared by dissolving the accurately weighed sample (0.1 g, 4 significant figures) in ethyl acetate (1.00 cm^3).⁹⁹

Table 2.3 – The parameters used for Agilent 6890 gas chromatograph GC-FID analysis.

Parameter	Condition	Units
Carrier gas	Helium	-
Sample solvent	Ethyl acetate	-
Flow rate	2.0	mL min^{-1}
Injector temperature	340	$^{\circ}\text{C}$
Injection volume	0.5	μL
Split ratio	15:1	-
Initial column temperature	50 (1 minute hold)	$^{\circ}\text{C}$
Ramp rate	5	$^{\circ}\text{C min}^{-1}$
Final column temperature	340 (1 minute hold)	$^{\circ}\text{C}$
Detector temperature	340	$^{\circ}\text{C}$
Total analysis time	60	min

2.4.1.3 Agilent 7890 gas chromatograph

Samples were analysed using an Agilent 7890 gas chromatograph with a flame ionisation detector. The capillary column was a Restek Rxi-5HT (30 m x 0.25 mm x 0.25 μm) with a 5% diphenyldimethyl polysiloxane stationary phase. Chromatography parameters are shown in Table 2.4. Quantitative GC samples were prepared by dissolving the accurately weighed sample (0.1 g, 4 significant figures) in ethyl acetate (1.00 cm^3).⁹⁹

Table 2.4 – The parameters used for Agilent 7890 gas chromatograph GC-FID analysis.

Parameter	Condition	Units
Carrier gas	Helium	-
Sample solvent	Ethyl acetate	-
Flow rate	2.0	mL min ⁻¹
Injector temperature	340	°C
Injection volume	0.5	μL
Split ratio	50:1	-
Initial column temperature	50 (1 minute hold)	°C
Ramp rate	5	°C min ⁻¹
Final column temperature	340 (1 minute hold)	°C
Detector temperature	360	°C
Total analysis time	60	min

2.4.1.4 GC-FID Calibration

By GC-FID, the concentrations of squalane and *N*-butyl ASI were determined by calibration to external standards. For other compounds where external calibration to authentic standards was not possible, compounds were quantified by the effective carbon number (ECN) method.¹²⁰ The ECN method takes advantage of the linear relationship between the amount of “burnable” carbon within a molecule, and its FID response.

To calibrate using the ECN method, first traditional calibration curves of concentration vs response must be determined for a range of high-purity standards. In this work, a range of alkanes from decane (C₁₀) to pristane (C₁₉) were used. The alkanes were dissolved in squalane (C₃₀) which provided another data point. Alkanes were used for the calibration points in this study because compounds found in lubricant samples are predominantly hydrocarbon based and so should show similar behaviour to the analytical standards.

The linear response factors for the compounds were determined, factoring in analyte purity. An example of the calibration used in this work can be found in Figure 2.4. Once response factors have been determined, they were plotted against the effective carbon number of the compound. The carbon number is calculated from the contributions of the constituent atoms of a compound. Atomic contributions are shown in Table 2.5.¹²¹ This allows response factor to be plotted against effective carbon number (Figure 2.4, bottom right) to give a linear fit. After the structure of an unknown analyte was determined, its effective carbon number was

calculated and the graph used to calculate a reliable estimate of the GC response factor for the analyte. This method is a simple, low-expense, method to determine the concentrations of compounds for which analytical standards are unavailable.

Table 2.5 – Atomic contributions to effective carbon number.¹²¹

Atom	Type	ECN contribution
C	aliphatic	1
C	aromatic	1
C	olefinic	0.95
C	carbonyl	0
C	primary alcohol	-0.5
O	secondary alcohol	-0.75
N	primary amine	-0.5
N	secondary amine	-0.75
N	tertiary amine	-0.25

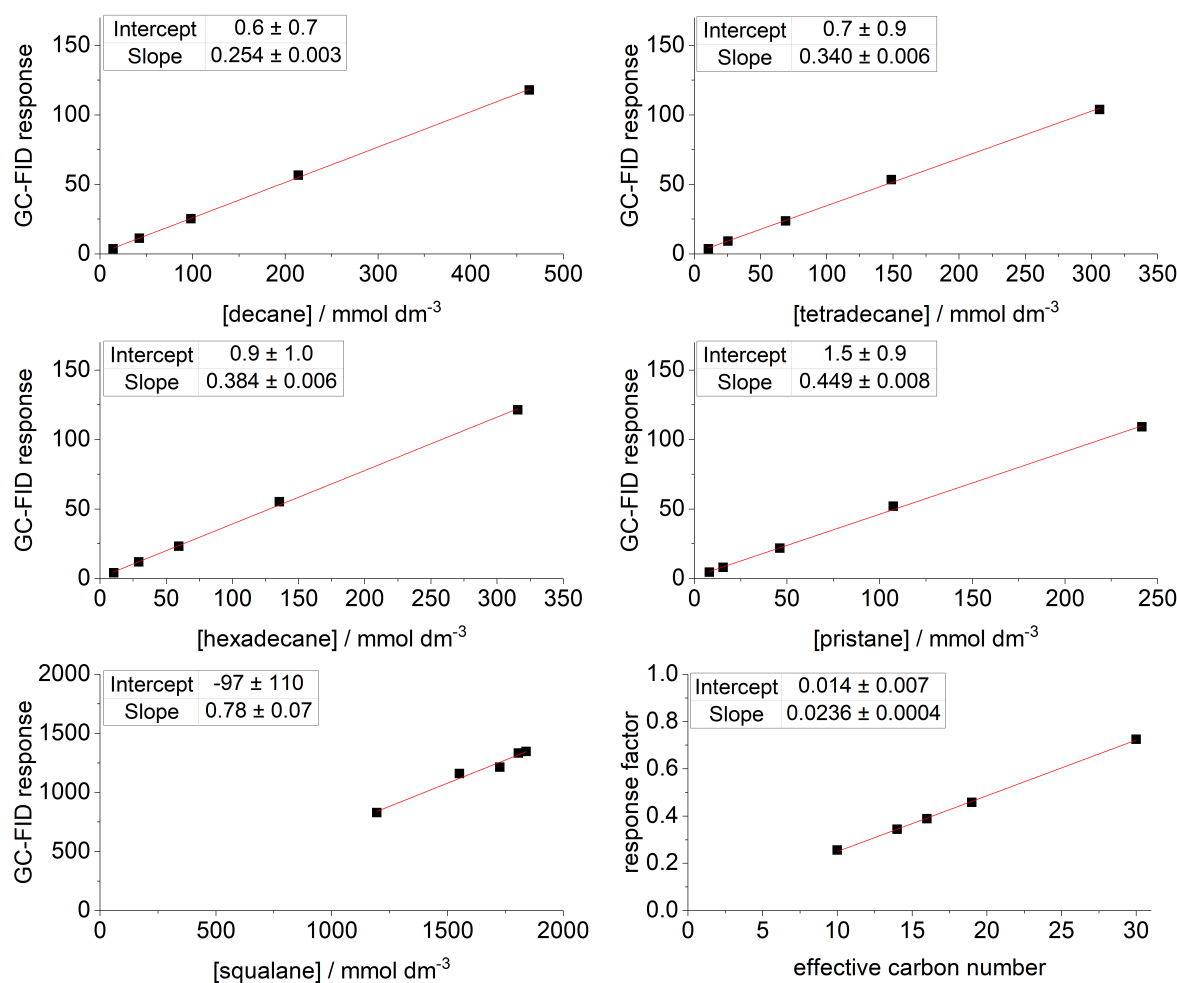


Figure 2.4 – An example of the calibration curves produced in this work along with the graph of response factor against effective carbon number (bottom right). Gradients and intercepts are shown with standard error. All intercept values are within two standard errors. The ECN calibration standard error is $\pm 1.5\%$.

2.4.2 Gas chromatography electron ionisation mass spectrometry (GC-EI-MS)

2.4.2.1 Unit mass GC-EI-MS

A Perkin-Elmer Clarus 500 gas chromatograph coupled to a Clarus 560-S electron ionisation (EI) mass spectrometer (MS) was used to gather unit mass resolution data in positive ion mode. Chromatography parameters are shown in Table 2.6. The column was a Restek Rxi-5HT capillary column with a 5% diphenyldimethyl polysiloxane stationary phase. The 30 m column had a 0.25 mm internal diameter and a film thickness of 0.25 μm . Where

possible products were identified by comparison of experimental data to National Institute of Standards and Technology (NIST) library data. Where reliable matches could not be found, fragment ions were assigned and discussed later.

Table 2.6 – The parameters used for gas chromatography - electron ionisation - mass spectrometry (GC-EI-MS) analysis.

Parameter	Condition	Units
Carrier gas	Helium	-
Sample solvent	Ethyl acetate	-
Flow rate	2.0	mL min ⁻¹
Injector temperature	340	°C
Detector temperature	340	°C
Split ratio	30:1	-
Initial column temperature	50 (1 minute hold)	°C
Ramp rate	5	°C min ⁻¹
Final column temperature	340 (1 minute hold)	°C
Total analysis time	60	min

2.4.2.2 Accurate mass GC-EI-MS

Samples were analysed using an Agilent 7890 gas chromatograph using a Phenomenex ZB5-MS plus column (30 m x 0.25 mm x 0.25 µm) coupled to a Waters GTC Premier time of flight (ToF) mass analyser in positive mode. The oven had an initial temperature of 50 °C for one minute with a 5 °C min⁻¹ ramp to 340 °C and hold for 11 minutes. The EI source was held at 70 eV. Samples were analysed at both a 20:1 and a 2:1 split ratio to give good resolution of both high and low concentration analytes respectively. The ToF was calibrated to authentic mass standards and accurate mass defect was calculated relative to these standards and is reported in ppm. The Root Mean Squared error of the mass analyser was determined to be ≈ 10 ppm.

2.4.2.3 GC-MS sample derivatisation

Silylation was used to functionalise hydroxyl group containing species and identify structural isomers in Chapter 4.¹²²⁻¹²⁴ The sample (100 mg) was stirred in ethyl acetate (1 cm³) with *N,O*-bis(trimethylsilyl) trifluoroacetamide / 1% trimethylsilyl chloride (500 µL) at 50 °C for 3 hours before being injected in to the GC-EI-MS, following the same analysis conditions used for non-derivatised samples.

Acetonide derivatisation was used to functionalise vicinal diol containing species in Chapter 4.^{125,126} The sample (100 mg) was stirred in anhydrous acetone (5 cm³) with anhydrous CuSO₄ (500 mg) at 50 °C for 3 hours. The sample was filtered and concentrated under a flow of nitrogen before being injected into the GC-EI-MS, following the same analysis conditions used for non-derivatised samples. Compounds that did not contain hydroxyl functionality were characterised from samples prior to derivatisation and so their structures were unaffected by the heat, solvent, and reagents used in the derivatisation steps.

2.4.3 Electrospray ionisation mass spectrometry

The sample (≈ 1 mg) was dissolved in ethyl acetate (1 cm³) and an aliquot (0.1 cm³) was diluted further in methanol (1 cm³) and injected (1 μ L) into an Agilent 1260 infinity liquid chromatograph with a 50:50 methanol/water mobile phase. The analyte was detected using a Bruker Compact time of flight mass spectrometer in positive mode with internal calibration using sodium formate between m/z 90 and 1178. Resolution was ≈ 12600 with mass errors <3 ppm.

2.4.4 Attenuated total reflectance Fourier transform infrared spectroscopy

A Perkin Elmer Spectrum Two spectrometer was used to collect IR spectra. Four scans between 4000–650 cm⁻¹ at a 4 cm⁻¹ resolution were averaged to produce the final spectrum. The blank diamond crystal was used as the reference.

2.4.5 Nuclear magnetic resonance spectroscopy

In a general procedure, samples were analysed in CDCl₃ using a JEOL ECS 400 MHz spectrometer at 25 °C. Eight scans were collected for each ASI sample and 32 scans for PIBSA samples to improve the signal to noise ratio. Chemical shifts were calculated relative to CDCl₃.

2.4.6 Rheometry

Samples of *N*-butyl ASI before and after bulk phase autoxidation at 170 °C for 3 hours were analysed using a Brookfield R/S plus cone and plate rheometer at 20 °C using C50-1 and C25-2 spindles for low and high viscosity samples respectively. Data was recorded every second and smoothed using a 10-point moving average.

2.4.7 Oxygen consumption estimation

Throughout the oxidation reactions, the concentration of oxygen in the exhaust gases was measured a Teledyne Analytical Instruments R17-A oxygen sensor. The sensor generates an oxygen-concentration-dependent voltage using zirconium dioxide Nernst cell. From the measured voltage, the percentage concentration of oxygen by volume ($[O_2]\%$) and the quantity of oxygen consumed during the reaction was calculated. The fraction of O_2 consumed (δO_2) at a given time ($t = x$) was calculated and expressed as a percentage by Equation 2.1 .

$$\delta O_2 (t=x) = \frac{[O_2]_{(t=0)} - [O_2]_{(t=x)}}{100} \quad (2.1)$$

Using the gas flow rate (Q) and δO_2 , the volume of O_2 (V) consumed in a given amount of time Δt was calculated by Equation 2.2.

$$V/dm^3 = Q/dm^3 s^{-1} \cdot \Delta t/s \cdot \delta O_2 \quad (2.2)$$

δO_2 was used to estimate the moles (n) of O_2 consumed using the ideal gas law (Equation 2.3). The temperature used for calculations was the laboratory temperature during the reaction. The pressure was assumed to be standard atmospheric pressure (101.3 kilopascals).

$$n = \frac{pV}{RT} \quad (2.3)$$

where: n = moles

p = pressure / pascals

V = volume / dm^3

R = gas constant / $\text{J K}^{-1} \text{mol}^{-1}$

T = temperature / K

The total oxygen consumed at $t = x$ was estimated by integrating n with respect to time (x) using Equation 2.4. Integrating across the whole experiment, where x typically equals 90 minutes, yielded $\text{O}_2(\text{total})$.

$$\text{O}_2(\text{total}) = \int_0^x n dx \quad (2.4)$$

Figure 2.5 shows the raw O_2 data collected through an oxidation experiment, along with the estimated trend in O_2 consumption. The small O_2 consumption between $t = 0$ and $t = 5$ minutes is attributed to degassing of atmospheric nitrogen, released by the sample under stirring in an O_2 rich environment. Calculations did not account for this initial $[\text{O}_2]$ concentration decrease as this represented an insignificant amount relative to $\text{O}_2(\text{total})$.

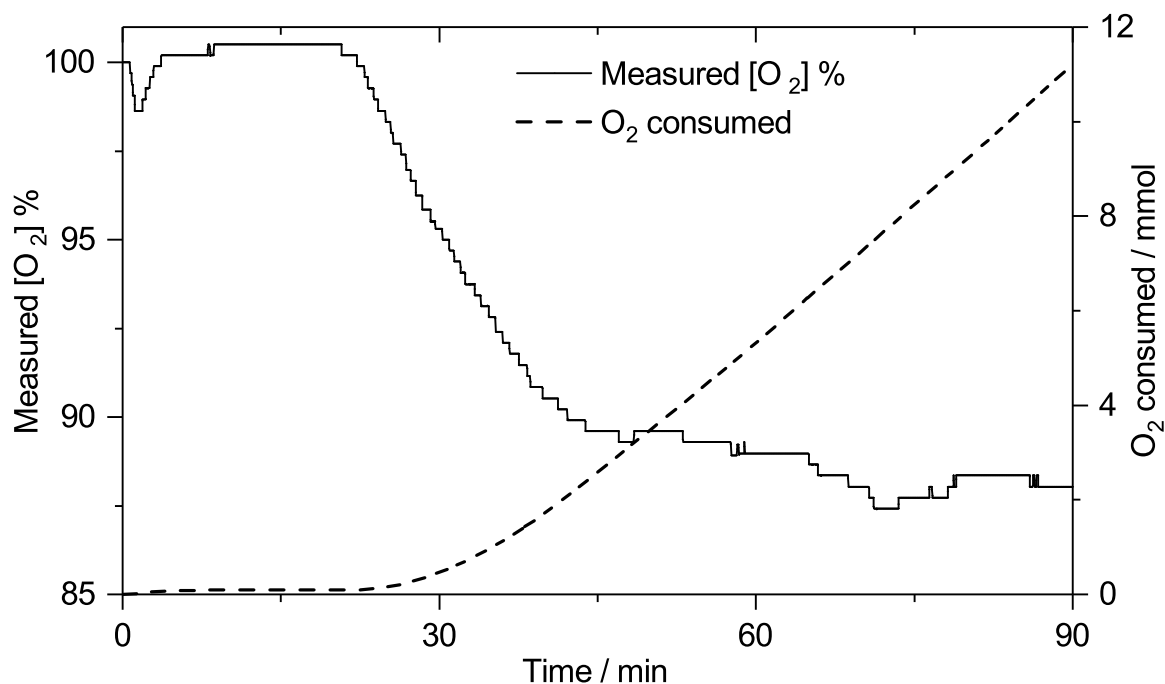


Figure 2.5 – An example of the oxygen concentration and consumption during the oxidation of a model lubricant.

2.5 Materials

Table 2.7 – Materials used in this project.

Material	Supplier	Comments
alumina	Honeywell Fluka	aluminium oxide, activated, basic, Brockmann I
argon	BOC	99.9%
<i>n</i> -butylamine	Sigma Aldrich	99.5%
2-dodecen-1-yl succinic anhydride	Sigma Aldrich	95.0%
ethyl acetate	Sigma Aldrich	99.7%
helium	BOC	99.9%
<i>n</i> -heptane	ACROS Organics	99.0%
<i>n</i> -heptylamine	ACROS Organics	99.0%
<i>n</i> -hexane	Sigma Aldrich	97.0%
<i>n</i> -hexylamine	Sigma Aldrich	99.0%
maleic anhydride	Sigma Aldrich	99.0%
maleic acid	Alfa Aesar	98.0%
nitrogen	BOC	99.9%
<i>N,N</i> -diethylethylenediamine	Sigma Aldrich	99.0%
<i>N,N</i> -dimethylethylenediamine	Sigma Aldrich	95.0%
<i>N</i> -methylethylenediamine	Alfa Aesar	95.0%
oxygen	BOC	99.9%
palladium on activated carbon	Sigma Aldrich	10% Pd
palladium on activated carbon	Sigma Aldrich	1% Pd
<i>n</i> -pentane	Fischer Scientific	99.0%
<i>n</i> -pentylamine	Sigma Aldrich	99.0%
petroleum ether 40–60 °C	Sigma Aldrich	-

polyisobutene	Afton Chemical Ltd.	950 g mol ⁻¹ M _N , 85% α-PIB, 10% β-PIB, 5% unassigned alkene isomers (by ¹ H-NMR spectroscopy)
<i>n</i> -propylamine	Sigma Aldrich	98.0%
K60 silica gel (flash) (35-70)	Sigma Aldrich	-
styrene	Sigma Aldrich	99%
triethylamine	Sigma Aldrich	99.5%
2,4,6-tri- <i>tert</i> -butylphenol	Sigma Aldrich	98.0%

Chapter 3

The role of radicals in the synthesis of polyisobutenyl succinic anhydrides

3.1 Introduction

Discussed in more detail previously in Section 1.3, a key step in the synthesis of polyisobutenyl succinimide (PIBSI) dispersants is the addition of maleic anhydride (MAH) to polyisobutene (PIB) to form polyisobutenyl succinic anhydrides (PIBSAs) (Figure 3.1). The addition occurs via the Alder-ene reaction when vinylidene-terminated α PIB is used.

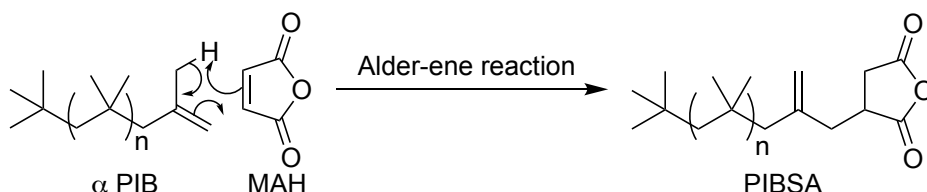


Figure 3.1 – PIBSA formation by the Alder-ene addition of maleic anhydride (MAH) to vinylidene terminated PIB.

In 2012 several 1D and 2D nuclear magnetic resonance (NMR) spectroscopy techniques were used by Balzano *et al.* to characterise Alder-ene addition products of MAH to PIB with a high α alkene content.³² The *exo* and *endo* products, PIBSA 1 and 2 respectively (Figure 3.2), were the expected products of MAH addition to the α PIB isomer (Figure 1.14).¹²⁷ An unexpected third product (PIBSA 3) with a pendant vinylidene group was also observed and, after 21 hours at 200 °C with a 1:1 PIB:MAH ratio, significant quantities of this product were produced.³²

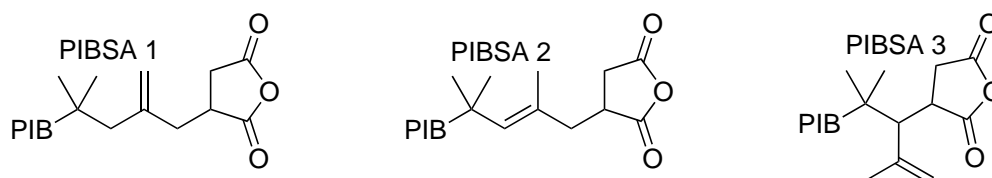


Figure 3.2 – The three major PIBSA isomers characterised by Balzano *et al.*³²

The structure of PIBSA 3 was determined by Balzano *et al.* and its formation attributed to the Alder-ene addition of MAH to the *endo*-alkene of beta (β) PIB, which was present in low concentrations ($\approx 10\%$) in the starting material.¹²⁸ In this chapter, the mechanism for PIBSA 3 formation has been investigated and a novel alternative mechanism is proposed.

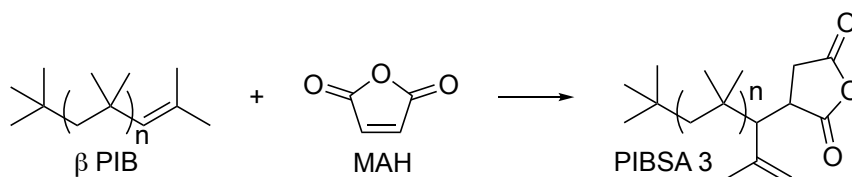


Figure 3.3 – Formation mechanism of PIBSA 3 proposed by Balzano *et al.*³²

3.2 Results

3.2.1 Conventional PIBSA synthesis

Initially, this work aimed to replicate the synthesis reported by Balzano *et al.* to produce 100 g of PIBSA for further degradation experiments. A PIBSA product of the highest possible purity was desired. Therefore, a smaller scale reaction (20 g, 21 mmol) was performed for eleven hours, with sampling, to find the optimum reaction time where yield and selectivity was high. Each sample was analysed by $^1\text{H-NMR}$ spectroscopy for PIB conversion, PIBSA yield, and PIBSA selectivity.

Conversion was defined as the amount of PIB that was consumed. Yield was defined as the amount of PIBSA formed relative to the maximum possible quantity that could form, assuming one PIBSA molecule forms per PIB molecule. Selectivity was defined as the amount of consumed PIB that reacted via a specific route relative to the total amount of PIB consumed by all reactions.

The PIB conversion data is shown in Figure 3.4. It shows α PIB was consumed from the beginning of the reaction whereas the concentration of β PIB remained stable at its initial level throughout. PIBSA yields and selectivities are shown in Figure 3.5. PIBSA yield increased steadily throughout the reaction, concurrent with α PIB consumption, to reach a maximum yield of 35%. Selectivity for PIBSA products increased from 35% to 55% in the first three hours, before steadily decreasing for the rest of the reaction reaching approximately 40% after eleven hours.

The reaction gave an acceptable balance between yield and selectivity after five hours and so a 100 g scale reaction was performed for 5 hours, without sampling. The $^1\text{H-NMR}$ spectrum of the crude product is shown in Figure 3.6, along with spectra of polyisobutene and the 20 g scale PIBSA product. NMR spectroscopy signal assignments were taken from Balzano *et al.*³²

Significant differences in the relative concentrations of each PIBSA product (1, 2 and 3) were observed. On the 20 g scale, PIBSA 3 was the major product whereas PIBSA 1, as expected and previously reported, was the major product of the 100 g scale reaction. The PIB conversion, PIBSA yield and PIBSA selectivity data is shown in Table 3.1.

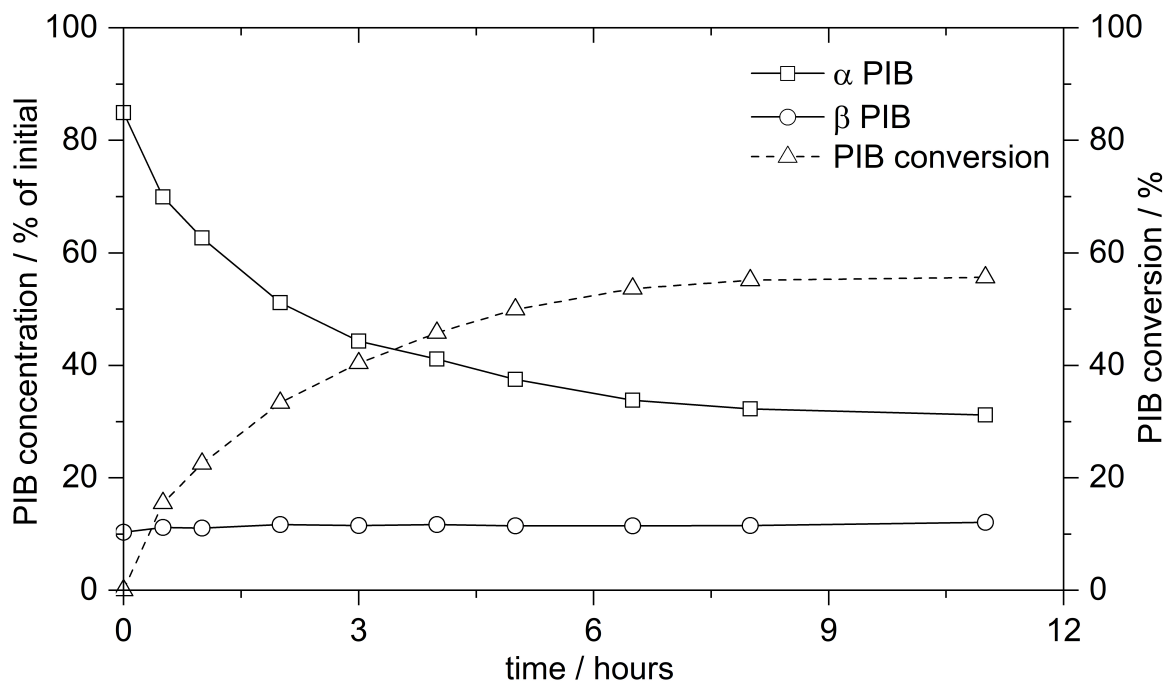


Figure 3.4 – The concentration of PIB and its conversion during the reaction of PIB and MAH on a 20 g scale at 200 °C with a 1:1 MAH:PIB ratio.

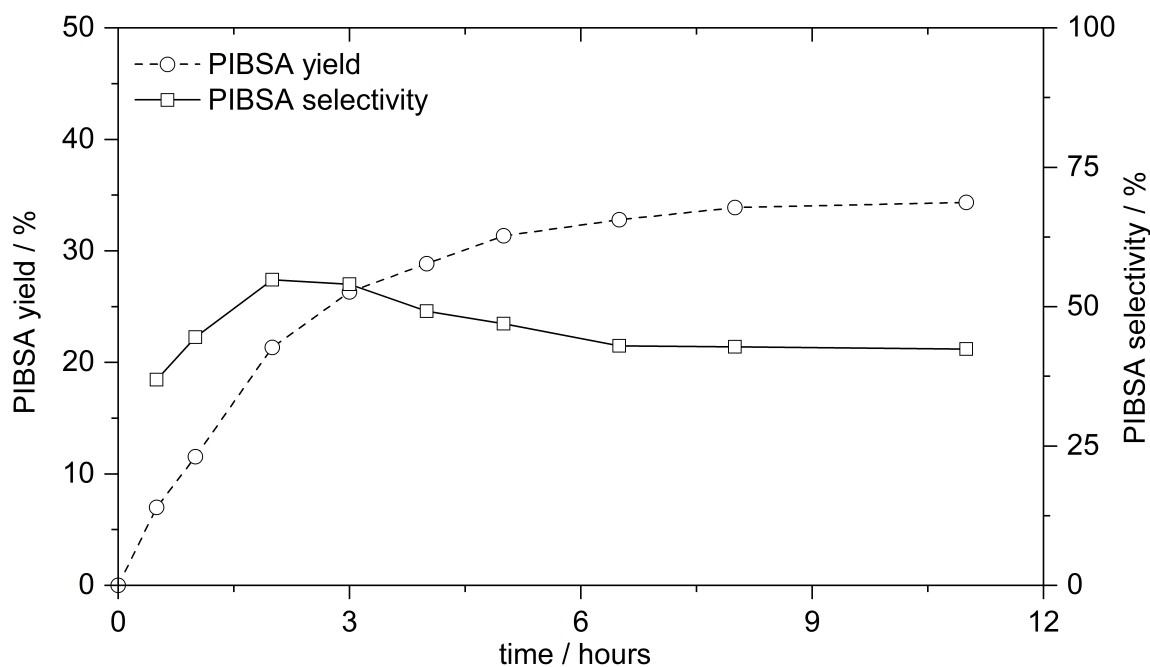


Figure 3.5 – The PIBSA yield and PIBSA selectivity during the reaction of PIB and MAH on a 20 g scale at 200 °C with a 1:1 MAH:PIB ratio.

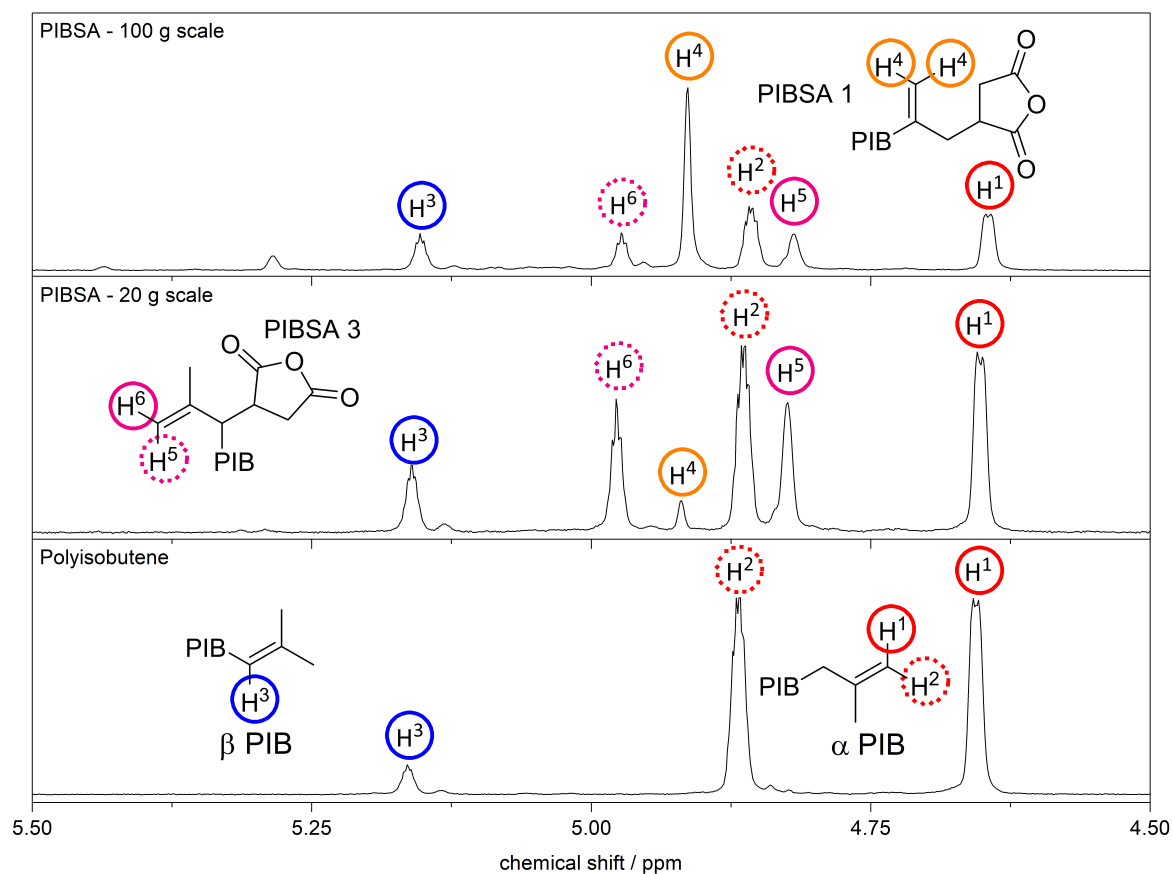


Figure 3.6 – A comparison of the alkene region (4.5–5.5 ppm) of the ¹H-NMR spectra of polyisobutene (bottom), PIBSA synthesised on a 20 g scale (middle) and PIBSA synthesised on a 100 g scale (top).

Table 3.1 – PIB conversion, PIBSA yields and PIBSA selectivities for the three PIBSA isomers from the 20 and 100 g PIBSA synthesis reactions.

Rxn. Scale / g	PIB conversion / %	PIBSA yield / %				PIBSA selectivity / %			
		1	2	3	Total	1	2	3	Total
20.0	50.0	1.7	0.0	21.2	22.9	3.5	0.0	42.4	45.8
100.0	66.9	21.6	3.8	10.9	36.3	32.3	5.7	16.3	54.3

While Balzano *et al.* did not report absolute conversions, yields and selectivities, comparisons were made for this study by examining the ratio of the three products. This is shown in Table 3.2. Products synthesised on the 100 g scale had an approximately comparable (but not identical) distribution as reported by Balzano *et al.* where 60% of the PIBSA product was the PIBSA 1 isomer. In contrast at the 20 g scale, the major product was PIBSA 3 at 93%.

Table 3.2 – PIBSA product distributions calculated from Balzano *et al.* and from this work.

Experiment	Reaction time	PIBSA distribution / %		
		1	2	3
Balzano <i>et al.</i>	4 hours	70	19	11
This work, 100 g scale	5 hours	60	10	30
This work, 20 g scale	5 hours	7	0	93

To confirm the structure of PIBSA 3, the crude product was purified using a silica micro-column. The sample was loaded as a solution in hexane and unreacted PIB was eluted using pure hexane. The PIBSA products were eluted using 5% (v/v) EtOAc in hexane and concentrated *in vacuo*. The resultant, purified, PIBSA was analysed by various one- and two-dimensional NMR spectroscopy techniques (^1H , ^{13}C , ^1H - ^1H correlation spectroscopy (COSY), heteronuclear multiple quantum coherence (HMQC) and distortionless enhancement by polarization transfer (DEPT) 135, see Appendix 7.1.1). DEPT-135 was used to determine the number of protons attached to a carbon and HMQC gave information on which carbon a proton was attached to. ^1H - ^1H COSY shows which protons are coupled together, allowing determination of spatial relationships. From this, complete assignments of the ^1H and ^{13}C spectra can be made and the structure can be determined. The NMR spectroscopy evidence supported the PIBSA 3 structure proposed by Balzano *et al.*

The substantial disparity in product distributions upon simply changing the reaction scale suggests PIBSA 3 does not form by the Alder-ene mechanism proposed by Balzano *et al.*³² Therefore, the mechanism of PIBSA 3 formation was investigated further.

3.2.2 PIBSA 3 synthesis via radical addition

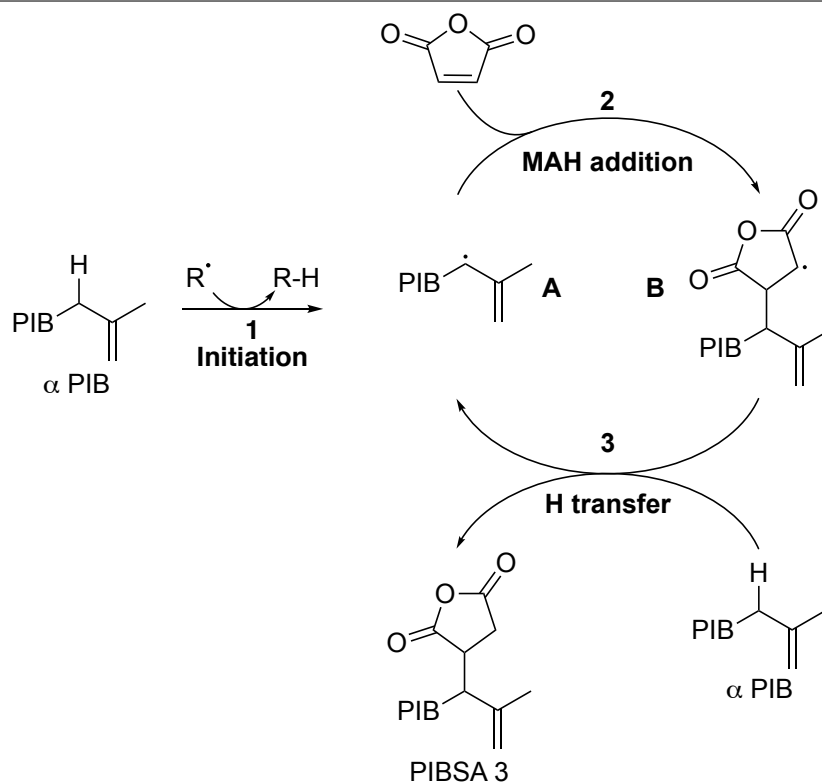
The main difference between the 100 g and 20 g reaction system was the volume of the reactor head space. Both reactions used the same apparatus; a 250 cm³ two-piece glass flask

equipped with an overhead stirrer. Therefore, the 20 g reaction had approximately 100 cm³ extra head space (80 g PIB at 0.8 g cm⁻³). While efforts were made to remove air from the reactor, flasks equipped with overhead stirrers are inherently difficult to manage for air and moisture sensitive chemistry. Therefore, the reaction with larger head space may have had higher volumes and concentrations of O₂ and H₂O present.

Water could impact the reaction by hydrolysing MAH to maleic acid (MA) which could alter reactivity. To test this, samples were prepared on the 20 g scale using MAH as received from the supplier, MAH purified by sublimation, or MAH with additional MA (5 mol %). This had no significant effect on PIBSA 3 yield (see Appendix Figure 7.3).

It was examined if O₂ could affect PIBSA 3 yields by initiating a radical addition of MAH to PIB. Scheme 3.1 shows the proposed mechanism. A carbon-centred radical (**A**) formed by the abstraction of a labile secondary (2°) allylic hydrogen from α PIB could add to MAH, forming radical **B** on the succinic anhydride ring. PIBSA 3 forms by the transfer of a labile hydrogen, likely from α PIB. Such radical addition is used in polymer functionalisation, typically by reactive extrusion using heat and radical initiators to introduce succinic anhydride sites to substrates like polypropene, natural rubber and polyethene.^{129–131}

Scheme 3.1 The mechanism proposed for PIBSA 3 formation by radical induced MAH addition to α PIB.



To test this hypothesis, the reaction was scaled down to 500 mg to allow the effective use of air sensitive techniques. In addition, the effect of a radical scavenging antioxidant (2,4,6-tri-*tert*-butylphenol, Figure 3.7) was investigated. Theoretically, the labile hydroxyl hydrogen atom of the antioxidant (AO) would quench any reactive radical species, minimising PIBSA 3 formation.

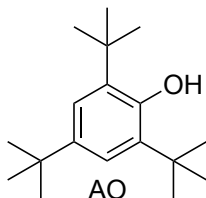


Figure 3.7 – 2,4,6-tri-*tert*-butylphenol, a radical scavenging antioxidant (AO).

The reaction was studied under three sets of conditions; under an argon atmosphere, under argon with a radical scavenging AO present, and under air. All reactions were conducted at atmospheric pressure for 5 hours at 200 °C and the crude product was analysed by ¹H-NMR spectroscopy.

The ¹H-NMR spectra of the crude products are shown in Figure 3.8. The change of experimental set up from 100 g to 500 mg altered the reaction selectivity. Under argon on a 500 mg scale, a 4:1 MAH:PIB molar ratio yielded all three PIBSAs with a ratio of 50:10:40 for PIBSAs 1, 2 and 3 respectively. When the AO was added, no PIBSA 3 was produced and PIBSAs 1 and 2 were produced in a 80:20 ratio. The addition of an AO completely stopped the formation of PIBSA 3, strongly supporting the hypothesis that PIBSA 3 forms by a radical mechanism.

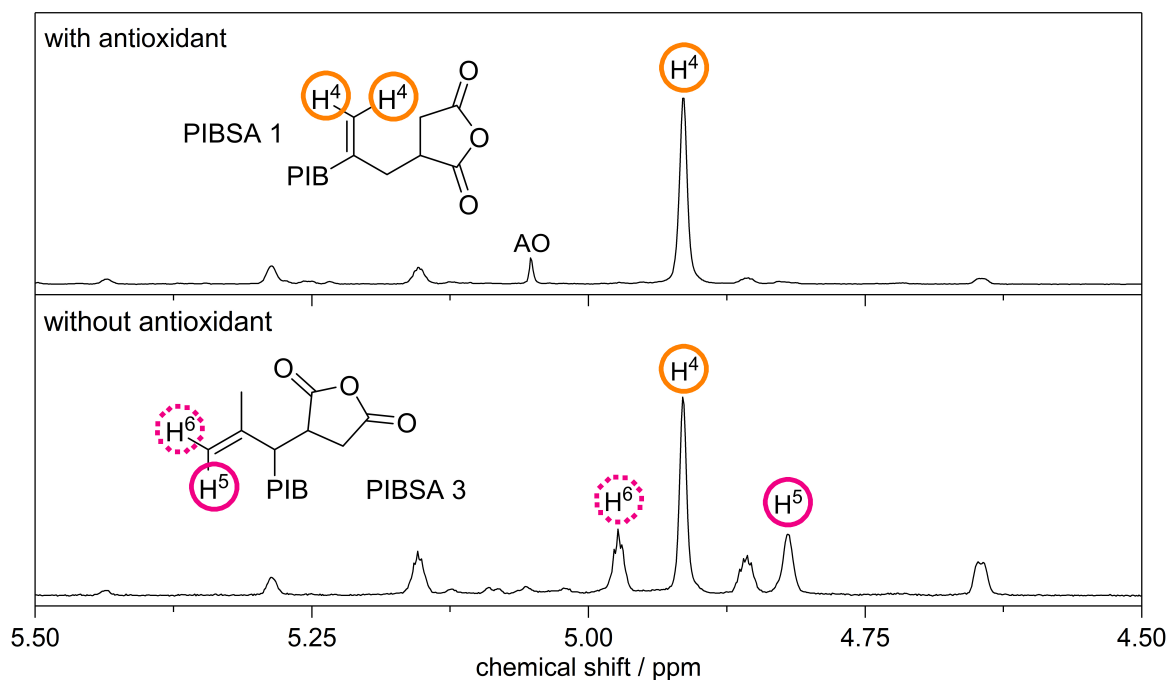


Figure 3.8 – NMR spectra in the alkene region (4.5–5.5 ppm) of PIBSA synthesised on a 500 mg scale under argon for five hours, either with (top) or without (bottom) a radical scavenging antioxidant (2,4,6-tri-*tert*-butylphenol).

3.2.3 Radical initiator source

With results suggesting the importance of radicals in the formation of PIBSA 3, efforts were made to determine the source of the radical initiator. The initiator was thought likely to be either trace levels of molecular oxygen or alkyl hydroperoxide contaminants within the PIB starting material.

PIB is a viscous material which slows gas exchange at the liquid/gas interface. Unless sufficiently stirred, oxygen below the PIB surface cannot exchange with the inert atmosphere above. Therefore, simply exchanging the atmosphere above the PIB surface for an inert gas, as was done in this work and by Balzano *et al.*, could be inadequate.

Alternatively, trace levels of peroxides can form in the starting material over time in storage. Species with labile hydrogens slowly react with oxygen eventually forming alkyl hydroperoxides. At the high temperatures used in PIBSA synthesis (200 °C), peroxides homolyse¹³² to form highly reactive alkoxy ($R-O\cdot$) and hydroxyl ($\cdot OH$) radicals which could initiate radical reactions.

Two techniques were developed to determine the source of the radical initiator. Further efforts were made to exclude oxygen from the 500 mg system prior to reaction using freeze pump thaw (FPT) degassing.¹³³ To mitigate the effect of high PIB viscosity trapping oxygen, the starting materials were first dissolved in n-pentane. The resultant mixture was thoroughly degassed using FPT degassing, replacing the atmosphere for nitrogen and removing all traces of oxygen. The pentane was then removed under a flow of nitrogen with stirring and gentle heating to 40 °C.

To remove peroxides from the system, PIB was dissolved in pentane and passed through a micro-column of activated basic alumina prior to FPT degassing. Activated aluminas are effective for removing peroxides from organic substrates.¹³⁴

The ¹H-NMR spectra in Figure 3.9 show the products of five different reaction procedures which are summarised in Table 3.3. A low MAH:PIB ratio of 1:1 was chosen as this most selectively yielded the PIBSA 3 product.

Experiment 1 (top) was the standard procedure where PIB was used as received and the system was passively degassed by exchange of the atmosphere for an inert gas (nitrogen or argon). This experiment was repeated four times giving an average PIBSA 3 yield of 14.8% with a standard error of ±0.8%. This error is assumed to be applicable to other experiments which were only conducted once.

Experiment 2 shows the result of removing peroxides using alumina prior to the reaction and using the same passive degassing technique was used as in experiment 1. The yield of PIBSA 3 here was 15.1%, showing no statistically significant difference from experiment 1.

In experiment 3, the PIB was dissolved in pentane and FPT degassed, but no effort was made to remove peroxides. PIBSA 3 was still produced, but with a lower yield of 4.2%.

In experiment 4, PIB was dissolved in pentane and passed through an alumina micro-column and FPT degassed prior to the reaction. This method stopped production of PIBSA 3 with a yield 0.0% at a detection limit of 0.1% while maintaining production of a low level of the non-radical product PIBSA 1, as seen in experiments 1–3.

In experiment 5, after peroxides were removed using alumina, di-*tert*-butyl peroxide (5 μL, 4 mg, 5 (mol/mol)%) was added before FPT degassing. The addition of a peroxide increased the yield of PIBSA 3 to 39.6%.

This set of experiments demonstrated that the production of PIBSA 3 could be initiated by both the homolysis products of alkyl hydroperoxides and by trace levels of molecular oxygen. The procedure was challenging to replicate, indicating the sensitivity of the system to the smallest trace of radical initiator.

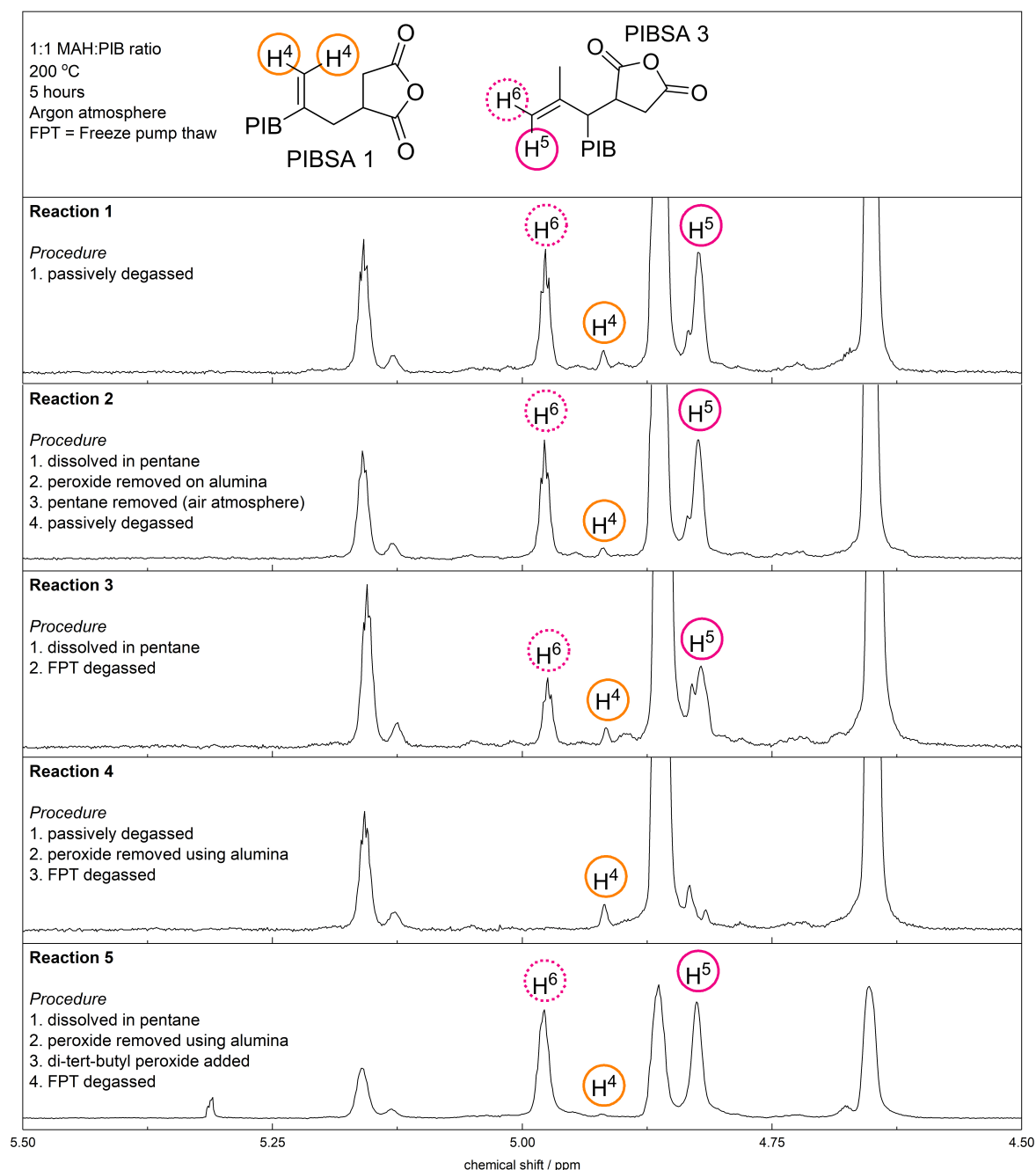


Figure 3.9 – The crude ^1H -NMR spectra from five different 500 mg scale PIBSA synthesis reactions using a 1:1 PIB:MAH ratio. Corresponding procedures and PIBSA 3 yields are reported in Table 3.3.

Table 3.3 – The yield of PIBSA 3 under five different reaction conditions, calculated from the $^1\text{H-NMR}$ spectra in Figure 3.9. The synthesis was conducted at 200 °C for 5 hours using a 1:1 PIB:MAH ratio. *Average value from four reactions with standard error, FPT = freeze pump thaw.

Reaction	Procedure	PIBSA 3 yield / %
1	1. passively degassed	14.8 ± 0.8 *
2	1. dissolved in pentane	15.1
	2. peroxide removed on alumina	
	3. pentane removed (air atmosphere)	
	4. passively degassed	
3	1. dissolved in pentane	4.2
	2. FPT degassed	
4	1. dissolved in pentane	0.0
	2. peroxide removed using alumina	
	3. FPT degassed	
5	1. dissolved in pentane	39.6
	2. peroxide removed using alumina	
	3. di- <i>tert</i> -butyl peroxide added	
	4. FPT degassed	

3.2.4 Competing PIB loss mechanisms

3.2.4.1 PIB loss through evaporation

During the 100 g and 20 g scale reactions, significant levels of condensation were observed on the reactor lid. The clear and colourless liquid was analysed by attenuated total reflection - Fourier transform - infrared (ATR-FT-IR) spectroscopy and found to have absorbance bands similar to PIB but with far higher intensity of vinylic signals—notably the vinylidene C–H out-of-plane bend at 890 cm^{-1} .¹³⁵ This suggested the condensate was low mass oligomers of PIB. As PIB conversion was calculated from the alkene signals relative to alkyl signals, evaporation of lower than average weight oligomers contributed to observed PIB conversion during PIBSA synthesis.

The evaporation of low mass oligomers was also significant on the 500 mg scale. Under all the of the conditions studied, the selectivity for PIBSA products was never greater than 75%.

To test if evaporation was limiting selectivity, gas chromatography - electron ionisation - mass spectrometry (GC-EI-MS) was used to characterise, and gas chromatography - flame ionisation detector (GC-FID) to quantify, low mass oligomers present within PIB. Suitable analytical standards could not be purchased to confirm PIB structures. Instead, using

Kugelrohr short path distillation, low mass oligomers of PIB were isolated and characterised using GC-EI-MS. Oligomers were isolated to protect the mass spectrometry equipment from high mass oligomers.

From this data, the structure and mass of each GC peak was determined, see Appendix (Section 7.1.3, page 177) for characterisation. When PIB (as received) was analysed by GC-FID, individual α and β PIB oligomers of mass up to 600 g mol^{-1} could be reliably observed and quantified. Above 600 g mol^{-1} , peaks were broad with poor shape. The $\alpha:\beta$ ratio also changed due to lower than expected concentrations of the α isomer. This suggested, due to high oven temperatures and a long hold at high temperature, on column degradation was occurring and so data for compounds above 600 g mol^{-1} was deemed unreliable. The chromatogram is shown in Figure 3.10 and the retention times and corresponding molecular weights are shown in Table 3.4.

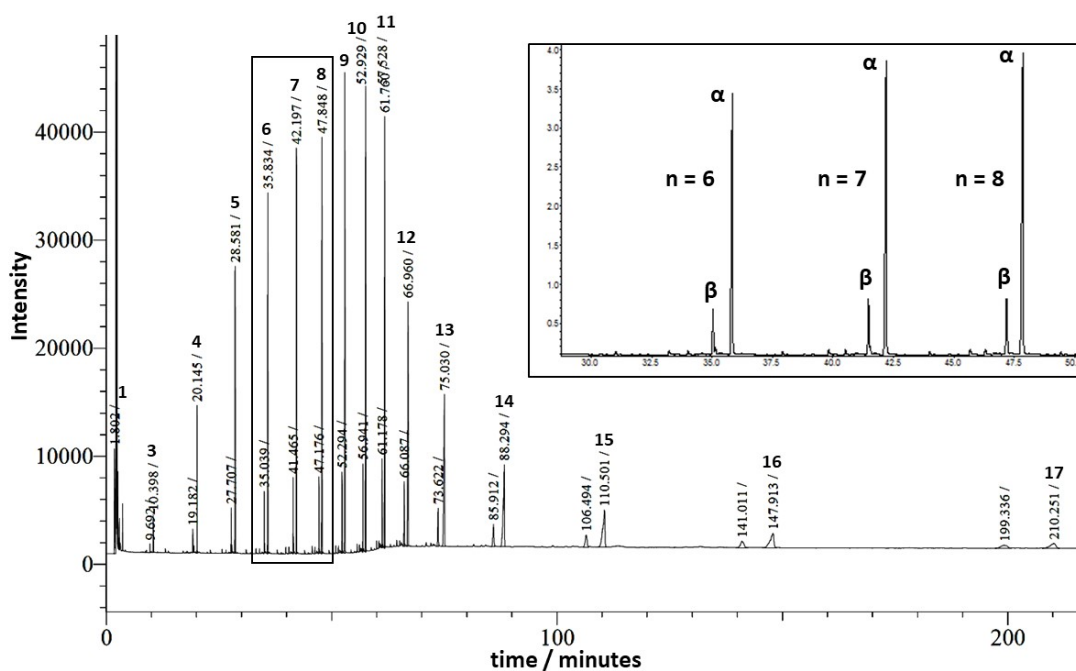


Figure 3.10 – A GC-FID chromatogram of $M_n = 950 \text{ g mol}^{-1}$ PIB with peaks labelled according to the number of isobutene units in the oligomer. Inset; an expansion of the chromatogram between 30 and 50 minutes denoting the number of isobutene units and the alkene isomer (α or β).

Table 3.4 – GC-FID retention times (R_t) the corresponding number of isobutene units and mass of the oligomer. Di-isobutene (2 isobutene units) was not observed.

R_t / minutes	Units of isobutene	mass / g mol^{-1}
1.8	1	56
n/a	2	112
10.5	3	168
20.2	4	224
28.7	5	280
35.9	6	336
42.3	7	392
47.9	8	448
53.0	9	504
57.6	10	560
61.8	11	616
67.1	12	672
75.2	13	728
88.6	14	784
111.1	15	840
148.8	16	896
212.5	17	952

To test the evaporation hypothesis PIB was heated to 200 °C for 5 hours. This was performed under argon with an AO present to prevent autoxidation. The liquid product was characterised by $^1\text{H-NMR}$ spectroscopy and GC-FID. By $^1\text{H-NMR}$ spectroscopy, 17% loss of the PIB alkene was observed.

The concentrations of PIB oligomers as a percentage of their original concentration in the starting material are shown in Figure 3.11. A decrease in the concentration of PIB oligomers lighter than 350 g mol^{-1} was observed. As the mass of the oligomer decreased, so did its concentration, following the trend in boiling point. The concentrations of oligomers above 350 g mol^{-1} did not significantly alter due to heating. This suggests that the loss of PIB by evaporation of light oligomers was significant, accounting for around 17% of the total PIB conversion during a 500 mg scale reaction for 5 hours. The concentration of isobutene observed also decreased but unexpectedly remained higher than that of tri-isobutene. This suggests some thermal degradation of PIB occurred during heating.

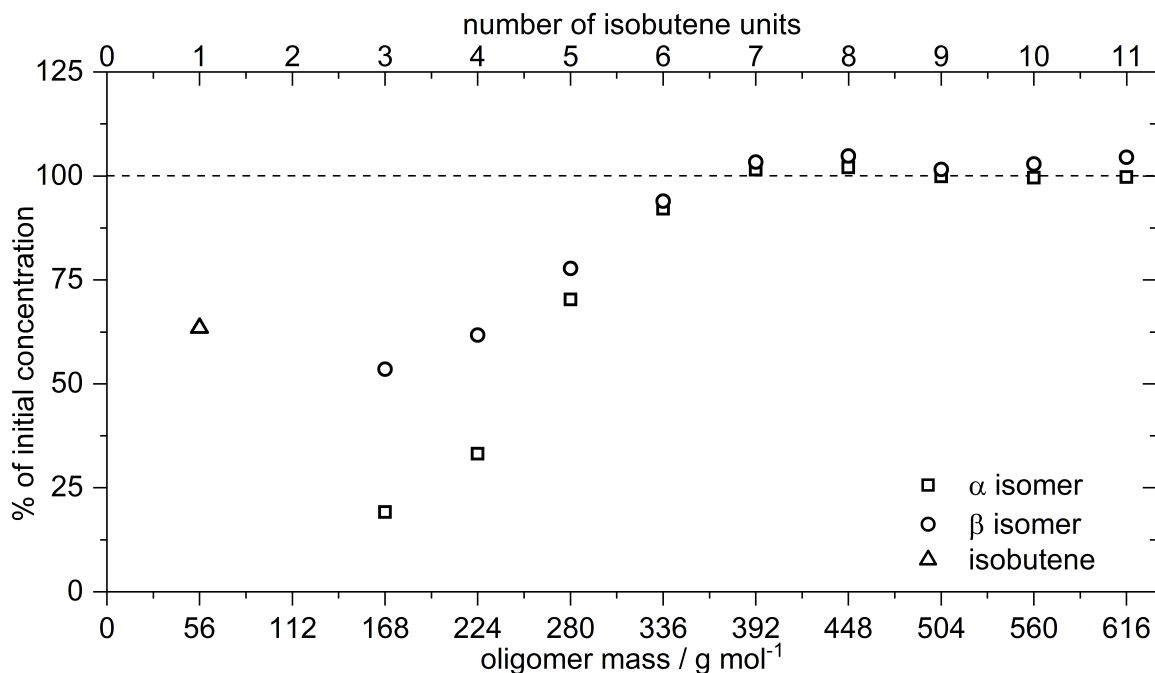


Figure 3.11 – The concentrations of α and β PIB oligomers after heating of a 500 mg sample at 200 °C for 5 hours with an antioxidant present. Concentrations were determined by GC-FID and are reported relative to their concentration in PIB before heating.

3.2.4.2 PIB conversion through autoxidation

The highest selectivity for PIBSA products was observed when a radical scavenging AO was present and the lowest when the reaction was completed under air. This decreased selectivity is attributed to competing autoxidation reactions, evidence for which can be seen in the NMR spectra. Control experiments of PIB stirred under argon for five hours were conducted, both with and without a radical scavenging AO.

Without AO present, two peaks could be observed at 3.18 and 3.75 ppm. Such signals were previously reported for the autoxidation of high mass (1.4 and 0.5 MDa) PIB by Pazur *et al.* in 1997.¹³⁶ They were attributed to primary (1°) and secondary (2°) alcohols respectively (Figure 3.12), arising from autoxidation at 1° and 2° carbon sites within PIB. The alcohols were observed in the NMR spectra of the PIBSA products synthesised in this work whenever radical sources were present. The alcohol at 3.18 ppm can also be seen in data presented by Balzano *et al.* where it remained unassigned. The 3.75 ppm peak was outside of the spectral ranges presented by Balzano *et al.*

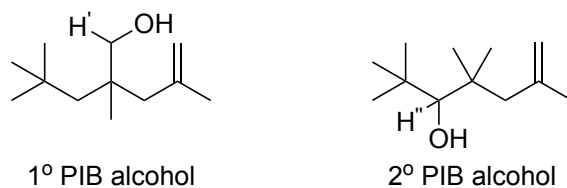


Figure 3.12 – 1° and 2° PIB alcohols observed by $^1\text{H-NMR}$ spectroscopy with resonances at 3.18 (H') and 3.75 (H'') ppm respectively.¹³⁶

Without AO present, the composition of PIB also changed in favour of the more thermodynamically stable β isomer. Measured by $^1\text{H-NMR}$ spectroscopy, the ratio of α : β :unassigned alkene structures changed from 85:10:5 to 73:20:7 due to heating. When an antioxidant was present, no changes in PIB isomer composition or PIB oxidation products were observed.

When analysed by GC-FID, the α PIB concentration decreased which corresponded to a β PIB concentration increase. Similar to Figure 3.11, α PIB oligomers of mass $<350 \text{ g mol}^{-1}$ also showed a decrease in concentration correlating to the oligomer boiling point. The exception being α tri-isobutene, which increased to 130% of its original value after heating. The concentration of isobutene observed increased to double its starting value.

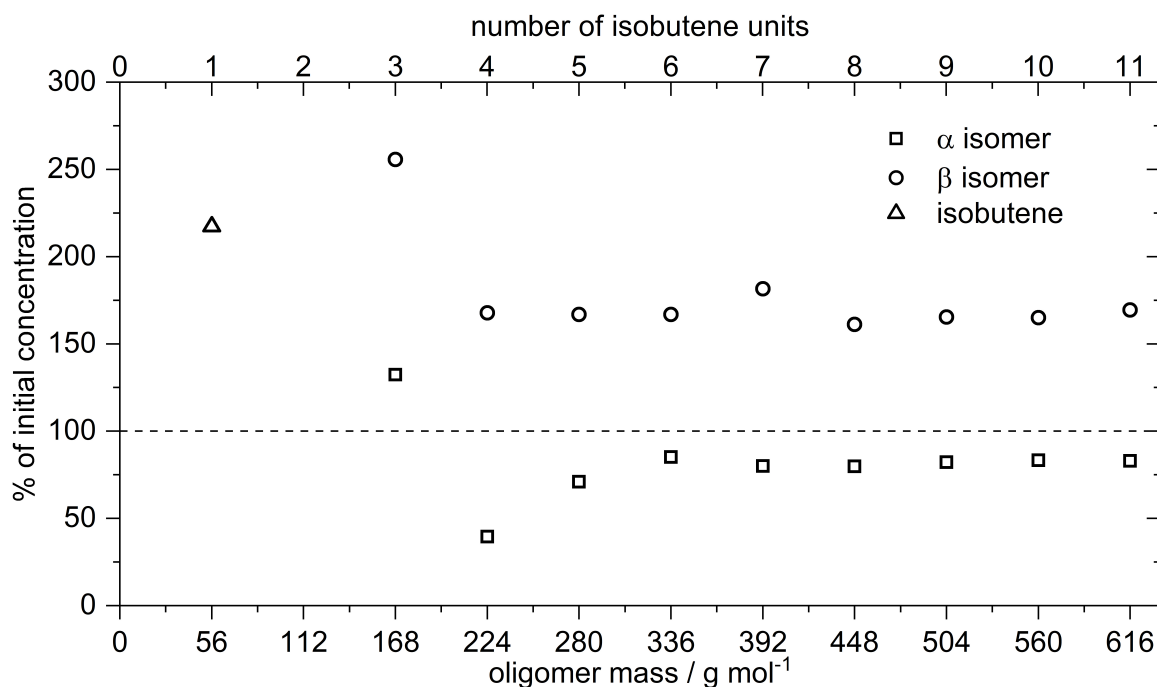


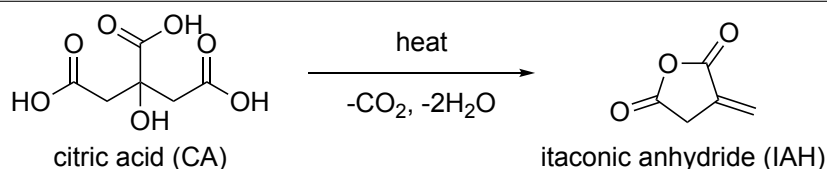
Figure 3.13 – The concentrations of α and β PIB oligomers after heating to 200°C for 5 hours under argon without AO. Concentrations were determined by GC-FID and are reported relative to their concentration prior to heating.

3.2.5 Further PIBSA synthesis results

3.2.5.1 Itaconic anhydride as an alternative to maleic anhydride

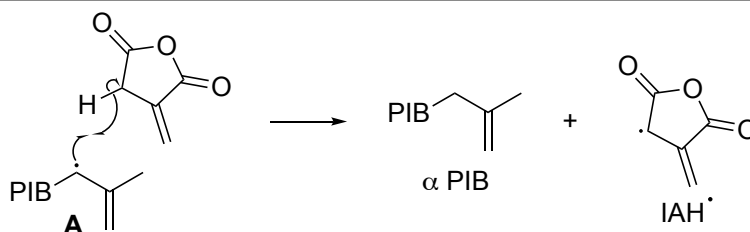
The use of itaconic anhydride (IAH) as a greener alternative to MAH was also examined. Synthesised from citric acid (CA) in a thermal decarboxylation and dehydration reaction (Scheme 3.2), IAH represents a renewable alternative to petrochemically derived MAH.¹³⁷ IAH was used in place of MAH under conditions shown to promote either Alder-ene addition or radical addition, however no functionalisation of PIB with IAH was observed in either reaction. IAH isomerised to the more thermodynamically stable citraconic anhydride (CAH) which also did not react with PIB to form PIBSAs.

Scheme 3.2 The formation of itaconic anhydride (IAH) by the thermal dehydration and decarboxylation of bioderivable citric acid (CA).



The non-reaction through Alder-ene addition can be attributed to the more electron rich enophile compared to MAH. The absence of radical addition is attributed to the relative bond strengths within IAH. Hydrogens α to the carbonyl in IAH are stabilised both by resonance with the alkene, and the carbonyl. Therefore, they represent a source of labile hydrogens that can add to PIB radicals, favoured over C–C coupling through the alkene. This destroys PIB radicals, preventing any further reaction (Scheme 3.3).

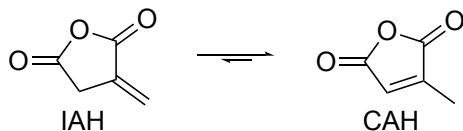
Scheme 3.3 The proposed reaction between PIB radicals and IAH. Instead of adding to the IAH double bond, the radical **A** abstracts a labile allylic IAH hydrogen.



Low levels of radical species are required to initiate this reaction, therefore only a small amount of IAH can be consumed by acting as an antioxidant. IAH readily isomerises to the more stable CAH (Scheme 3.4). CAH formation was shown by comparing ¹H-NMR

spectroscopy signals from the crude PIBSA product to a known sample of CAH. This is the likely mechanism by which IAH is consumed, giving 100% IAH conversion. There was no evidence of CAH adding to PIB through either Alder-ene or radical addition, however the reaction with commercial CAH was not investigated. Therefore, due to its lack of reactivity towards PIB alkenes, the use of IAH as an alternative to MAH was not pursued.

Scheme 3.4 The conversion of itaconic anhydride (IAH, left) to citraconic anhydride (CAH, right). The equilibrium lies in favour of the more thermodynamically stable CAH.



3.2.5.2 Styrene assisted MAH addition

The addition of styrene to the radical-initiated addition of MAH on to aliphatic polymers has been shown to increase the amount of MAH added to the polymer.^{138–144} Increased MAH addition rates is thought to happen through a MAH/styrene charge transfer complex.^{145,146} However, when tested in this work, a tacky white solid formed immediately upon styrene addition which was assumed to be a styrene/MAH copolymer without addition to PIB occurring. No further experiments were conducted due to time constraints.

3.2.5.3 The formation of bis-PIBSAs

The industrial production of PIBSAs is known to produce low levels of bis-PIBSAs, where a second equivalent of MAH has added to a PIBSA molecule as shown in Figure 3.14. The main evidence for their formation is reported by Harrison *et al.*³⁹ who—using ESI-MS—observed a series of ions corresponding to bis-PIBSA. However, full structural analysis of these species is yet to be undertaken and therefore their formation mechanism is unknown.

Bis-PIBSAs could form from MAH addition to PIBSA 1, 2 or 3, or possibly from another low-concentration, unidentified PIBSA species. The pendant vinylidene group in PIBSA 3 shows the lowest steric hindrance compared to the alkene in PIBSAs 1 and 2 and is therefore is a good candidate for the Alder-ene addition of MAH. Predicted products are shown in Figure 3.14.

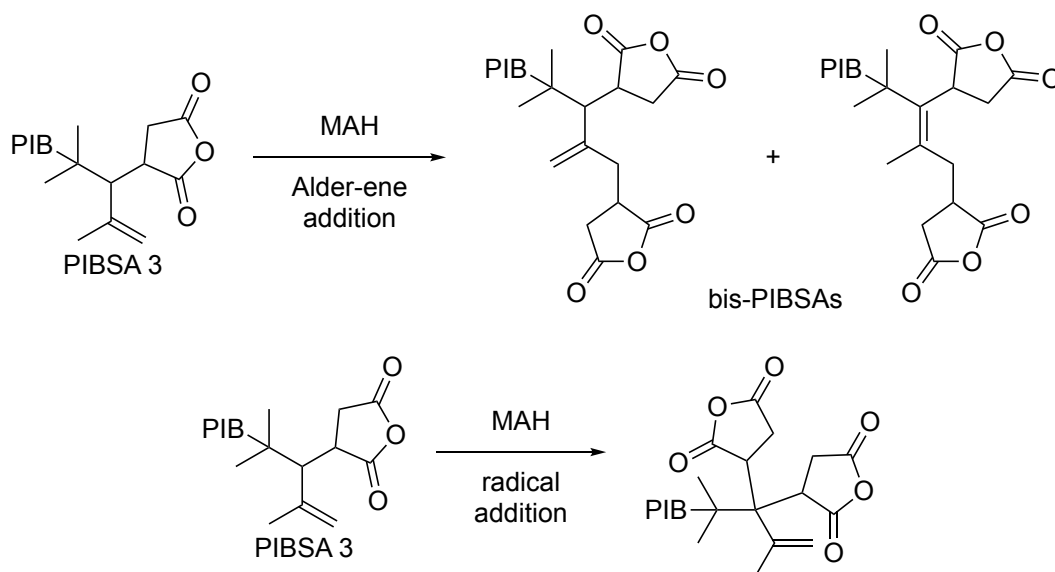


Figure 3.14 – The possible reaction of MAH with PIBSA 3 by the Alder-ene and radical addition pathways.

The addition of MAH to PIBSA 3 was attempted on a 500 mg scale. PIBSA 3 was purified using a silica column to remove unreacted PIB from the crude PIBSA product. This product was then reacted under both Alder-ene addition and radical addition promoting conditions. The reaction of PIB with MAH on the 500 mg scale was optimised for yield and selectivity for either the Alder-ene (PIBSAs 1 & 2) or radical products (PIBSA 3).

Table 3.5 shows PIB conversions and selectivity for the Alder-ene and radical addition of MAH to PIB. The optimised conditions (reaction 4 and 7) were used to promote the Alder-ene and radical addition respectively. However, no significant consumption of, or products from addition to, PIBSA 3 were observed by $^1\text{H-NMR}$ spectroscopy.

Table 3.5 – A table of reaction conditions (MAH:PIB ratio and AO concentration) for the reaction of PIB and MAH on a 500 mg scale. PIB conversion and PIBSA selectivities are shown, and the optimum conditions for Alder-ene addition (rxn. 4) and radical addition (rxn. 7) are shown in bold.

Rxn.	MAH:PIB	AO / mol %	PIB conversion / %	PIBSA selectivity / %			
				1	2	3	total
1	1.0	5.0	27.9	1.5	0.0	0.0	1.5
2	2.0	5.0	32.4	14.7	2.2	0.0	16.9
3	3.0	5.0	69.1	41.7	8.4	0.0	50.1
4	4.0	5.0	83.1	47.4	11.8	0.0	59.2
5	1.0	0.0	42.1	0.6	0.0	23.3	23.9
6	2.0	0.0	50.0	3.8	0.4	25.6	29.8
7	3.0	0.0	81.3	7.0	0.7	24.4	32.0
8	4.0	0.0	82.7	19.0	3.4	15.6	38.0

3.3 Discussion

Polyisobutenyl succinic anhydrides (PIBSAs) comprise a wide range of structures three of which, shown in Figure 3.15, were characterised by NMR spectroscopy by Balzano *et al.* in 2012.³²

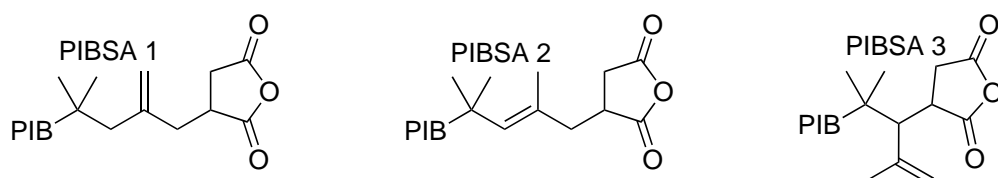


Figure 3.15 – The three main PIBSA isomers characterised by Balzano *et al.*³²

PIBSAs are reported to form by the Alder-ene addition of MAH to the terminal vinylidene alkene of α polyisobutene and PIBSAs 1 and 2 are consistent with this mechanism.

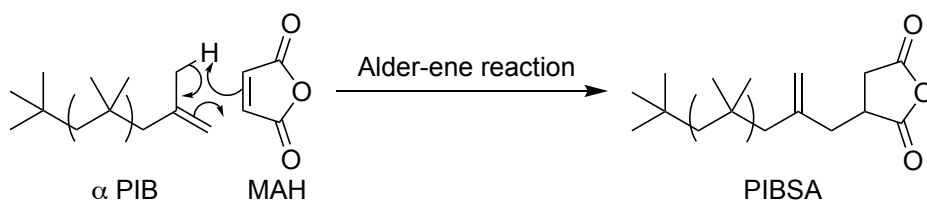


Figure 3.16 – PIBSA 1 formation by the Alder-ene addition of maleic anhydride (MAH) to vinylidene terminated PIB.

The PIBSA 3 structure was novel and its formation was attributed to the Alder-ene addition of MAH to the β PIB isomer (Figure 3.17).³²

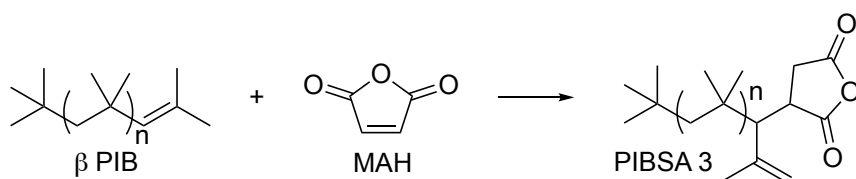


Figure 3.17 – The formation of PIBSA 3 by Alder-ene addition of MAH to β PIB proposed by Balzano *et al.*³²

In this work, the composition of PIBSA showed dependence on the reaction scale. Using similar apparatus and scale (100 g PIB) to Balzano *et al.* yielded comparable results to those previously reported. However, when the same apparatus was used on a 20 g scale, the reaction strongly favoured the PIBSA 3 product. The Alder-ene mechanism could not account for the dependence of selectivity on reaction scale. Therefore, an alternative reaction

mechanism to convert PIB to PIBSA 3 was explored.

In this work the concentration of β PIB changed negligibly during the reaction (Figure 3.4, page 56). α PIB was consumed from the start suggesting it is the reactive species, not β PIB. Arguably, α PIB could convert to β PIB and immediately react to form PIBSA 3. If this were the case we would expect both measurable consumption of the 10% of β PIB initially present and for an increase in β PIB concentration to be associated with increased reactivity.

In 2005, Pucci *et al.*¹²⁸ reported that using Lewis acid catalysts (RuCl_3 and SnCl_2), known to promote Alder-ene reactions,¹⁴⁷ reduced PIBSA yields due to the conversion of α to β PIB. Therefore, β PIB is not the reactive species.

A radical mechanism was proposed for converting α PIB to PIBSA 3 (Scheme 3.1, page 59). This was tested by the addition of a radical scavenging AO in to the reaction mixture. The addition of AO stopped the formation of PIBSA 3, supporting a radical mechanism.

The full proposed reaction mechanism is shown in Figure 3.18 and discussed below, separated into the three main steps:

1. Initiation
2. MAH addition
3. Hydrogen transfer

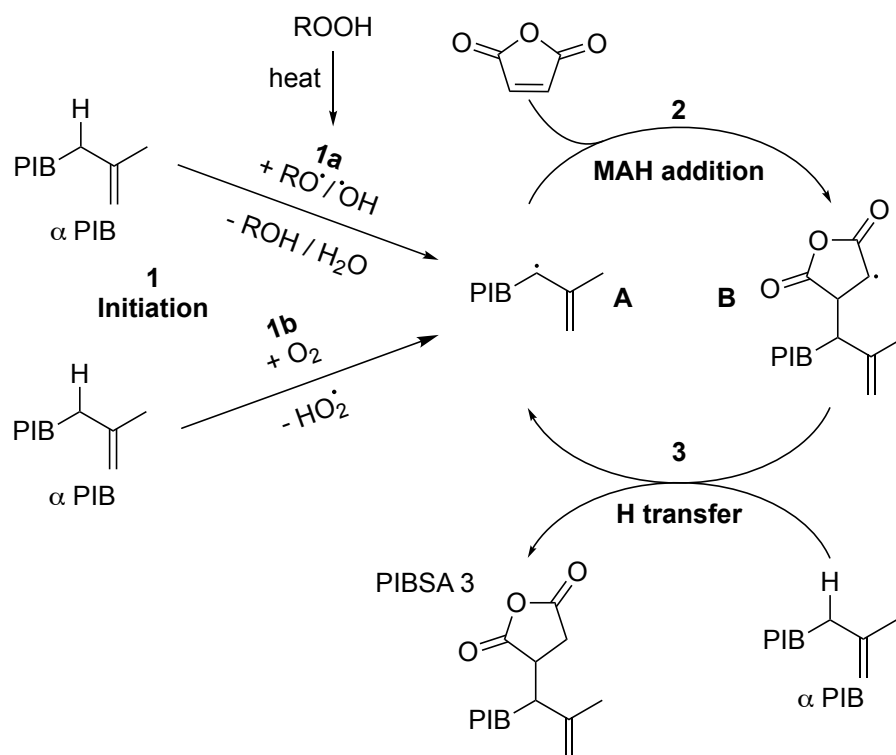
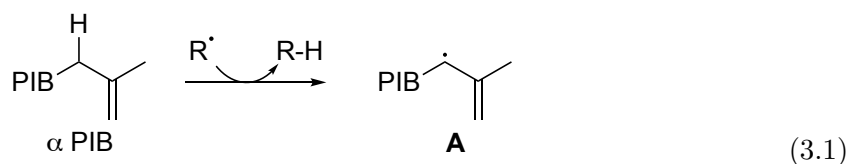


Figure 3.18 – The proposed radical chain mechanism for PIBSA 3 formation from α PIB initiated by O_2 or radical products of thermal peroxide homolysis.

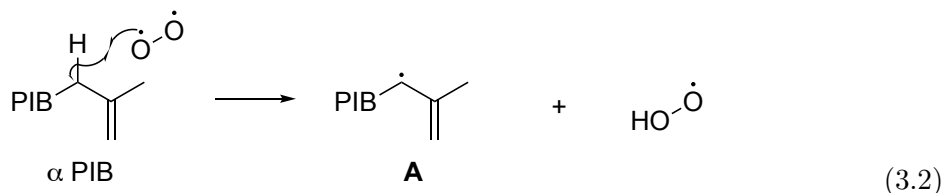
3.3.1 Initiation

The first step of the proposed mechanism is the abstraction of a relatively labile 2° allylic hydrogen from α PIB which generates radical **A**, a carbon-centred 2° allylic PIB radical (Reaction 3.1). This initial abstraction could plausibly occur by reaction with trace levels of molecular oxygen or by the homolysis products of alkyl hydroperoxide impurities present within PIB.

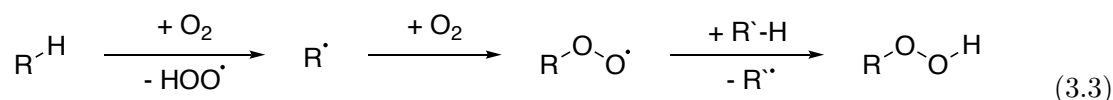


To determine the source of radical initiator, various experiments were conducted where peroxides were removed and/or oxygen was rigorously excluded from the reaction vessel. The data (Table 3.3, page 64), suggested that both peroxides and all traces of molecular oxygen must be removed in order to prevent radicals forming in the system. The addition of

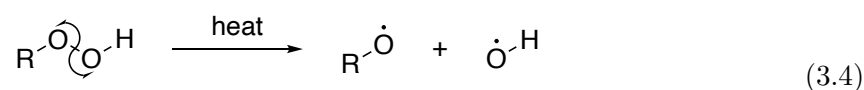
a peroxide dramatically increased PIBSA yields to 40%, further supporting the role of peroxides and radicals. Molecular oxygen contains two unpaired electrons and so it can be described as a di-radical, allowing it to initiate radical chemistries (Reaction 3.2).



The other plausible source of radicals is alkyl hydroperoxides, formed by slow autoxidation during material storage with oxygen present (Reaction 3.3). This is a chain reaction where alkyl radicals are regenerated during the peroxide formation step. This allows the reaction to propagate with a low level of initiation.



At 200 °C, the temperature of PIBSA synthesis, alkyl hydroperoxides homolyse to form alkoxy ($\text{R}-\text{O}^\bullet$) and hydroxyl ($^\bullet\text{OH}$) radicals which can react further (Reaction 3.4).¹³²



Once formed, the reactive radical initiator can abstract a labile hydrogen atom. The abstraction site and rate depends on the C–H bond dissociation enthalpy (BDE) which depends on the stability of the resultant radical. The more stable the radical, the lower the C–H BDE and the higher the rate of abstraction. Selected relevant BDEs can be found in Table 3.6.

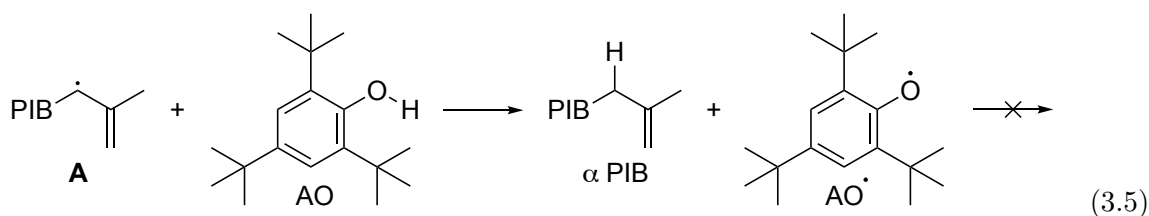
Within its main chain PIB contains 1°, 2°, and quaternary (4°) aliphatic carbons. On the alkene terminus there are allylic and vinylic carbons. α PIB contains a 2° allylic and a 1° allylic carbon whereas β PIB contains two 1° allylics. The other hydrogens in the reaction system are the vinylics of MAH.

Table 3.6 – Selected bond dissociation enthalpies (BDEs).

Bond	Type	BDE / kJ mol ⁻¹	Reference
CH ₃ CH ₂ -H	1° aliphatic C-H	423	116
(CH ₃) ₂ CH-H	2° aliphatic C-H	413	116
(CH ₃) ₃ C-H	3° aliphatic C-H	404	116
H ₂ C=C-CH ₂ -H	1° allylic C-H	361	148
H ₂ C=C-CRH-H	2° allylic C-H	345	148
H ₂ C=C(H)-H	vinyl C-H	463	116
H-CH ₂ CHO	α acetyl C-H	393	116
(CH ₃) ₃ CO-OH	peroxide O-O	196	116
2,4,6-(CH ₃) ₃ PhO-H	antioxidant O-H	340	149

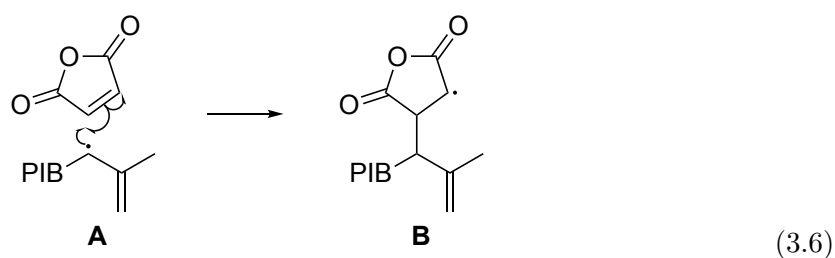
Radical **A** would be the most stable radical possible in the system (Figure 3.18), unless an AO is present, the C-H BDE of a secondary allylic hydrogen is lowest in the system and therefore its hydrogen abstraction rate the fastest. This means radical **A** will be the dominant initial chain carrier in this reaction.

The BDE of the 2° allylic C-H (345 kJ mol⁻¹) is higher than the BDE of the AO phenolic O-H (340 kJ mol⁻¹). Therefore, when a radical scavenging AO is present it reacts with radical **A**, forming PIB and a highly stabilised AO radical (Reaction 3.5). This prevents any further reactions, stopping the production of PIBSA 3 as shown in this work (Figure 3.8, page 61).

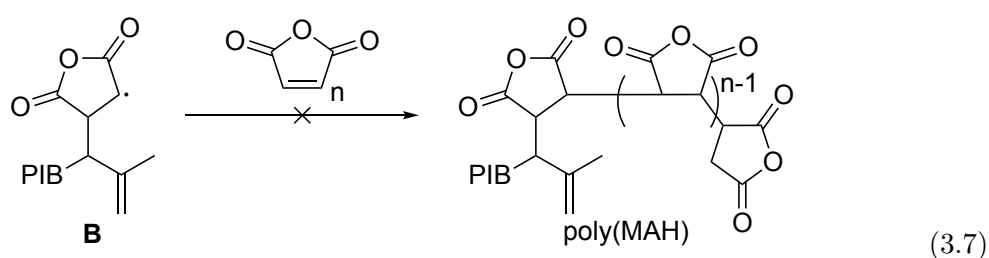


3.3.2 MAH addition

As radical **A** is the most stable radical possible in this system it is unlikely to react away by abstracting a hydrogen. It is proposed that radical **A** adds to the alkene of MAH, forming a C-C bond to the anhydride ring and a new radical intermediate (radical **B**), where the radical is centred on the succinic anhydride (SAH) ring (Reaction 3.6). Such radical addition is common in the radical-initiated “grafting” of MAH and other alkene-containing functionalisation agents to polymers in a process called reactive extrusion.¹⁵⁰

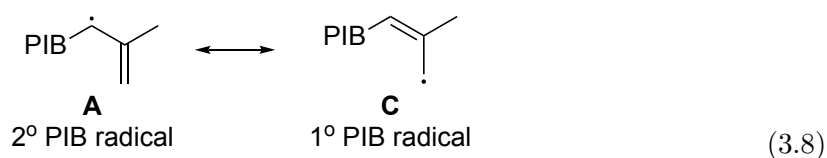


Radical **B** could theoretically react with further equivalents of MAH, forming a short chain of poly(MAH).

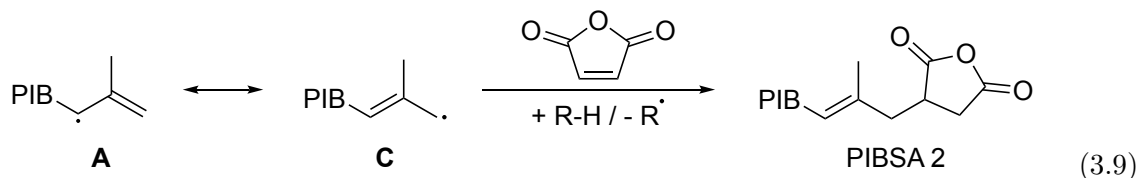


However, no evidence for this was observed. This could be because the reaction temperature (200 °C) was above the ceiling temperature for poly(MAH). The ceiling temperature of a polymer is where the rate of polymerisation and depolymerisation are equal. Above this temperature, the monomer is favoured over the polymer. MAH concentrations in this work ranged between 0.8 and 3.5 mol dm⁻³ and, as a 5 mol dm⁻³ solution in benzene, MAH does not polymerise at temperatures above 145 °C.¹⁵¹ Also, work by Russell in 1995 showed, when possible, hydrogen abstraction is preferred over MAH polymerisation, even at reaction temperatures below ceiling temperature.¹⁵²

Radical **A** is not a localised radical as drawn but is delocalised through two resonance structures (Reaction 3.8). Therefore, the spin density can also centre on the 1° allylic carbon (radical **C**) and reactions can occur at both sites.

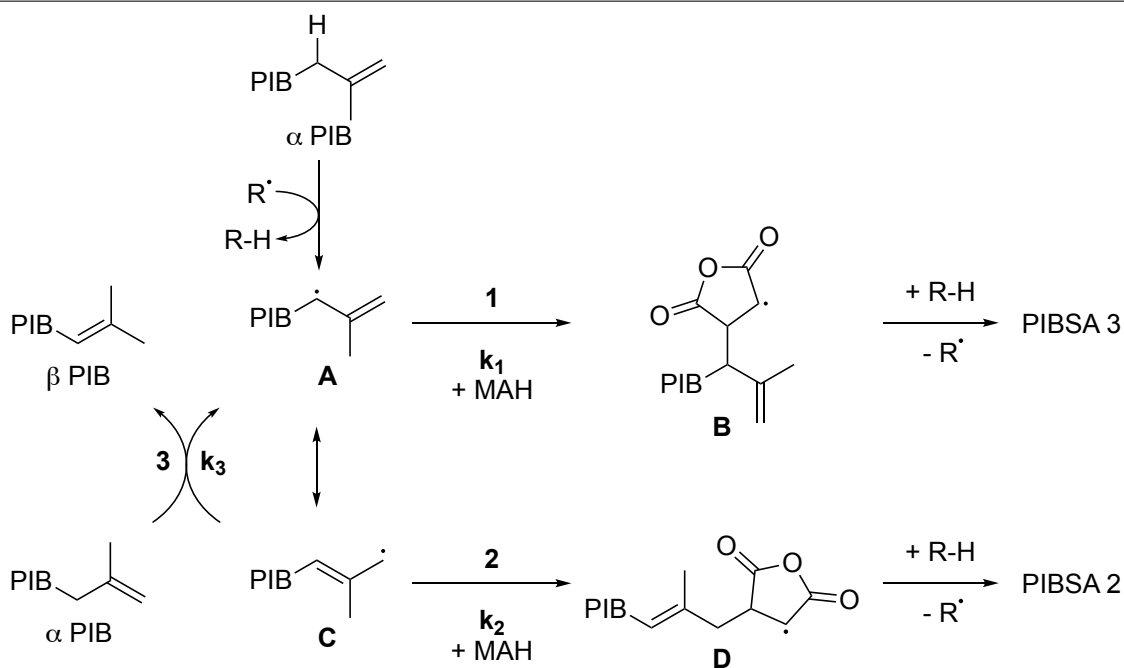


The reaction of MAH with radical **C** would yield the PIBSA 2 structure (Reaction 3.9).



However, under radical conditions, PIBSA 3 was always the dominant product. PIBSA 2 was only ever observed in low concentrations regardless of the presence of an AO and boosting the radical reaction by adding a peroxide initiator did not increase the concentration of PIBSA 2 observed (Figure 3.9, Page 63). This suggests MAH addition to radical **C** is not a significant reaction pathway. This is because of three main factors, depicted in Scheme 3.5.

Scheme 3.5 The potential reaction routes of the 2° and 1° allylic PIB radicals to form PIBSAs 2 and 3.



Firstly, the lower C–H BDE (345 kJ mol^{-1}) means radical **A** is more stable than radical **C** (361 kJ mol^{-1} , Table 3.6, page 3.6). Therefore, the radical **A** is the more dominant of the two resonance forms and so MAH is more likely to react at this site, forming PIBSA 3.

Secondly, the rate of MAH addition radical **A** (k_1 , Scheme 3.5) is higher than for MAH addition radical **C** (k_2) to form radical **D**. This is because electron-donating R groups increase

the nucleophilicity of a carbon-centred radical, increasing its reaction rate with electron poor alkenes such as MAH.¹⁵³ For a carbon-centred radical, adding a second stabilising alkyl group results in a near ten-fold increase in the rate of radical addition to electron poor alkenes.^{154,155}

Thirdly, radical **C** has two competing reaction routes. If **C** does not react with MAH, it can react by abstracting a relatively labile hydrogen atom from a second equivalent of α PIB, generating β PIB and regenerating radical **A**. Such behaviour has been demonstrated in this work (Figure 3.13, page 68) where α PIB was converted to β PIB under radical promoting conditions. This reaction reduces the proportion of radical **C** reacting to form PIBSA while simultaneously increasing PIBSA 3 production through radical **A**.

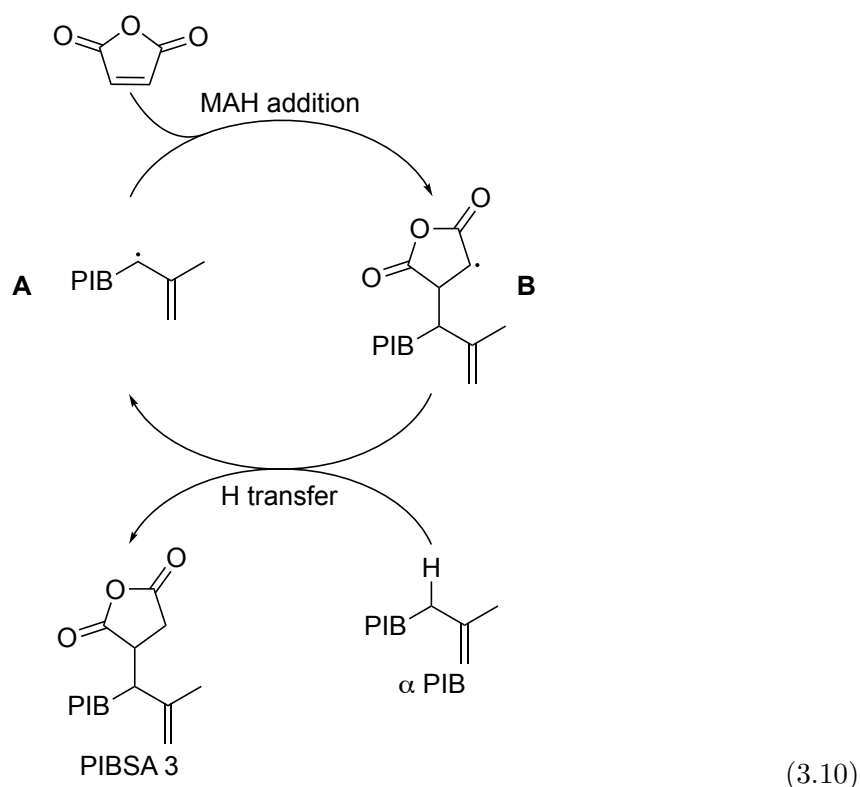
These three factors combine to give a highly selective radical route to solely yield PIBSA 3.

3.3.3 Hydrogen transfer

To complete the synthesis of PIBSA 3, the succinic anhydride radical formed in Reaction 3.6 must then abstract a labile hydrogen atom. Due to the low levels of initiator present in the system, this step must form part of a chain reaction to propagate further production of PIBSA 3.

In this work, 5 mol% of AO reacted to stop all PIBSA 3 production by donating a hydrogen to reactive radical species, preventing their further reaction. Therefore, as the AO reacts stoichiometrically, there must be fewer than 0.05 equivalents of radical species within the system. As PIBSA 3 yields far greater than 5% were achieved, the mechanism must involve a chain reaction that regenerates reactive radical species. Furthermore, when just 5 mol% of *di-tert*-butyl peroxide radical initiator were added, PIBSA 3 yields more than doubled from 15 to 40% (Table 3.3, page 64), supporting a chain reaction.

This chain reaction can be propagated by transfer of an allylic hydrogen from a second equivalent of α PIB to radical **B** (Reaction 3.10). This is possible due to radical **B** being 48 kJ mol⁻¹ less stable than radical **A** (see α acetyl C–H, Table 3.6). Such transfer forms PIBSA 3, while regenerating radical **A**, propagating the chain reaction.

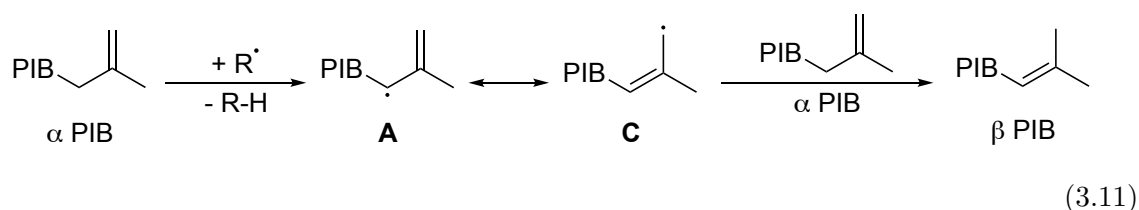


3.3.4 Competing reactions during PIBSA synthesis

In this work, the selectivity for PIBSA (both Alder-ene and radical products) was never 100%. The highest selectivity achieved was around 75% suggesting other competing PIB loss mechanisms were active. It was shown through $^1\text{H-NMR}$ spectroscopy and GC-FID that PIB autoxidation and the evaporation of low mass PIB oligomers were the likely competing mechanisms of PIB conversion.

The thermal degradation of PIB was reported by Pazur *et al.* in 1997.¹³⁶ Various aldehydes, ketones, alcohols and alkenes were observed, all attributed to initial oxidation on the PIB chain. Using high mass PIB (0.42 and 1.4 MDa) gave low signal to noise for effects of oxidation at the vinyl terminus. By using low mass (950 g mol^{-1}) PIB in this work, changes in the vinyl terminus could be observed.

The most important observation was the decrease in α PIB concentration with a concurrent increase in β PIB concentration. The ratio of α : β :unassigned alkene structures changed from 85:10:5 to 73:20:7 when measured by $^1\text{H-NMR}$ spectroscopy. It is proposed that isomerisation is induced by hydrogen abstraction to form radical **A** (Reaction 3.11).



The resonance form of the **A**, radical **C**, contains the endo-alkene of β PIB and a 1° allylic radical. Radical **C** is less stable than radical **A** and **C** abstracts a hydrogen from a second equivalent of α PIB. This forms β PIB while regenerating radical **A**, propagating the chain reaction.

As the β PIB isomer has been shown to be unreactive with regards to forming PIBSAs and dispersants, such loss of α PIB would be detrimental to the overall dispersant yield. Globally, approximately 600,000 tonnes of PIB are converted into lubricant additives annually.¹⁵⁶ Therefore, small gains in reaction yield and selectivity would give a large volume waste reduction.

3.3.5 Comparison with industrial PIBSA

In this work, PIBSAs were synthesised at 200 °C for five hours. This is the upper temperature limit for atmospheric pressure reactions due to the boiling point of MAH (202 °C). To increase yields in the commercial process, higher temperatures are used along with higher pressures to prevent MAH evaporation. Therefore, the products of the commercial synthesis will likely be different.

A $^1\text{H-NMR}$ spectroscopy comparison in the alkene region of a lab sample (100 g scale synthesis) with a commercial sample is shown in Figure 3.19. The commercial sample was synthesised using the same $\text{Mn} = 950 \text{ g mol}^{-1}$ PIB as used in this work. In the commercial sample, the yield of PIBSA 1 is high and PIBSA 2 can also be observed in reasonable quantities. Various other unidentified alkene species can be seen with a broad range of chemical shifts. α PIB has undergone almost complete conversion whereas β PIB is still present in significant quantities. Small quantities of PIBSA 3, the radical product, can be observed in the commercial sample. This shows radical chemistry involved in the formation of PIBSA 3 is applicable to the industrial process.

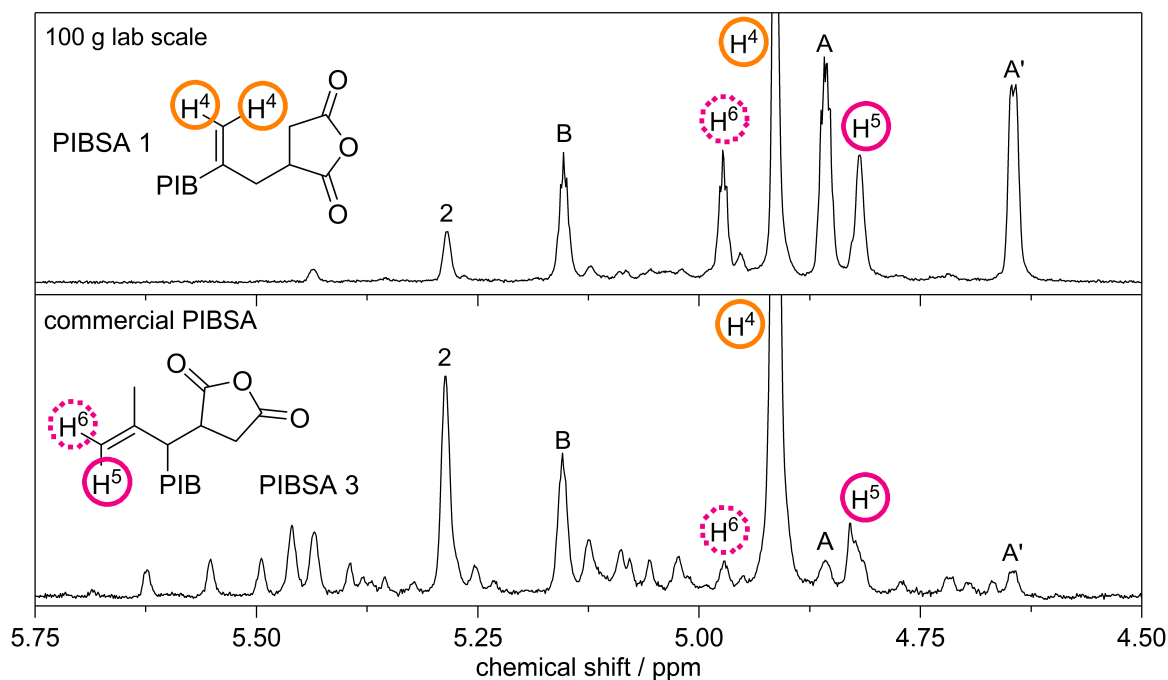


Figure 3.19 – A comparison of the ¹H-NMR spectra of lab synthesized PIBSA (top) with a commercial sample of comparable molecular weight (bottom) in the region showing alkene protons (4.5–5.5 ppm). PIBSA 1 (H⁴) and PIBSA 3 (H⁵ and H⁶) are shown, along with known proton signals from PIBSA 2 (2), α PIB (A and A') and β PIB (B).

Figure 3.20 shows a comparison of the two samples in the region where succinic anhydrides are observed. The commercial sample is more complex in this region. The spectrum is crowded with an uneven baseline whereas the lab synthesised sample has more clearly defined peaks with a more even baseline. The extra signals and poor baseline of the commercial sample may arise from low levels of unidentified anhydride species, similar to the extra peaks in the alkene region.

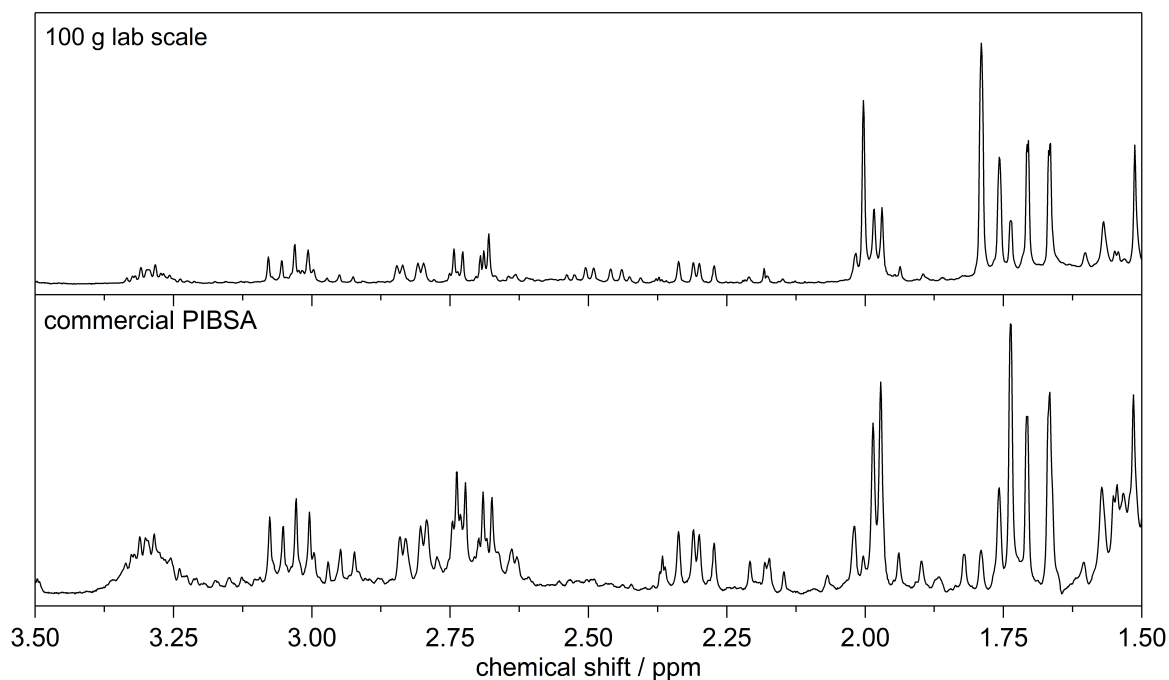


Figure 3.20 – A comparison of the ^1H -NMR spectra of lab synthesized PIBSA (top) with a commercial sample of comparable molecular weight (bottom) in the region showing succinic anhydride protons (1.5–3.5 ppm).

3.3.6 Implications for industry

Having shown how the smallest trace of reactive radical species can dramatically change the PIBSA product distribution, some implications for industry can be inferred. The difference in chemical structure between PIBSA 1 and 3 is small (Figure 3.15, page 72). When these are used to make dispersants, the small structure change in a large molecule should not impact the amphiphilicity and hence dispersancy should be comparable.

However, the formation of PIBSA 3 requires the presence of reactive radical species that can also participate in damaging side reactions, such as PIB autoxidation and α to β PIB conversion. To produce a consistent product with a predictable performance level, it is important to control reactive radical species and doing so would minimise the production of PIBSA 3. As such the level of PIBSA 3 in a commercial sample, monitored quickly and easily by ^1H -NMR spectroscopy, could be used as a proxy to monitor radical levels during the reaction.

Radical side reactions should be minimised and at industrial scale, minimising oxygen entrainment is relatively simple due to the use of closed-loop systems and large reactors

with low surface area to volume ratios. The main challenge presented by this scale is viscosity. Due to the viscous nature of both the starting materials and products, materials are often stored at high temperatures ($>100\text{ }^{\circ}\text{C}$) to maintain pumpability. Therefore if unchecked, radical chemistry could have a significant effect due to the time and temperature of material storage.

Also of concern for industrial chemistry is scale-up from bench to plant and the use of small scale bench reactions for research and development. Equipment type and scale differ greatly between these applications. As has been shown in this work, simply changing the scale from 20 to 100 g had a significant impact on the product distribution. Extra care should be taken on the lab scale to ensure control of oxygen levels and the generation of radicals in order to replicate the commercial process as closely as possible.

The author recommends the routine use of radical scavenging antioxidants in both lab and commercial PIBSA synthesis. This would help to ensure consistency across batches and across reaction scales, improving product quality and hastening research and development. AOs are not expected to be harmful at any stage of the PIBSI synthesis, nor should residual AO be damaging to the finished lubricant where AOs are already present. PIBSA 3 formation is sensitive to just the smallest trace of radical species. Therefore its formation, observed quickly by $^1\text{H-NMR}$ spectroscopy, could be used as a diagnostic tool to determine the presence of radicals within a system and to monitor batch-to-batch consistency.

3.4 Conclusion

The work presented in this chapter has shed new light on the mechanisms behind the synthesis of polyisobutenyl succinic anhydrides (PIBSAs), an important product for automotive lubricants. It was found that an unusual PIBSA structure (PIBSA 3) previously identified by Balzano *et al.* did not in fact form by the Alder-ene addition of maleic anhydride (MAH) to polyisobutene (PIB) as previously proposed.³² Instead, the importance of radical species in the formation of PIBSA 3 has been shown and a radical chain mechanism proposed to account for its formation.

The mechanism involves the addition of MAH to α PIB. It is initiated by either trace levels of molecular oxygen or by hydroxyl ($\bullet\text{OH}$) and alkoxy ($\text{R-O}\bullet$) radicals from alkyl

hydroperoxide homolysis. These radical species selectively abstract a labile 2° allylic hydrogen from α PIB to form radical **A** which then adds to the alkene of MAH. The resultant radical (**B**) abstracts a labile hydrogen from a second equivalent of α PIB, generating the stable PIBSA 3 product and regenerating **A**. By this mechanism, PIBSA 3 yields of up to 20% were achieved. When a radical initiator was added yields increased to 40%.

This mechanism introduces another process variable into laboratory and commercial scale PIBSA synthesis. These radical chain mechanisms must be controlled in order to improve product consistency and to prevent unwanted side reactions such as the conversion of reactive α PIB to the unreactive β isomer. This could be achieved by the addition of an antioxidant to break the chain reaction. Adding a radical scavenger at an early stage would both stabilise the starting material and ensure that only consistent Alder-ene PIBSA products were produced.

Chapter 4

The autoxidation of alkenyl succinimides—mimics for PIBSI dispersants

4.1 Introduction

Dispersants, like polyisobutenyl succinimides (PIBSIs) (Figure 4.1), are used in engine oil lubricants to mitigate the negative impacts of lubricant autoxidation, sludge, and soot.^{18,19} However, beyond a single publication in 1981,¹¹³ little is known about how autoxidation impacts dispersants. Understanding the behaviour of dispersants during use, particularly how they degrade by autoxidation, is critical to developing new, more robust dispersants.

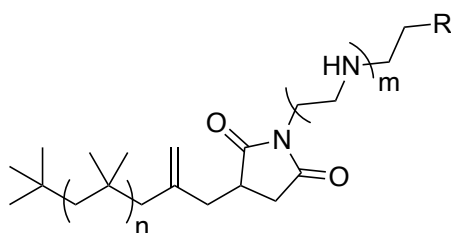


Figure 4.1 – The idealised structure of a polyisobutenyl succinimide dispersant where n is typically 16-60, m is typically 3 and $R = \text{NH}_2$ or alkenyl succinimide.³²

Autoxidation mechanisms are often determined by product studies where the products from the autoxidation of a substrate are characterised and logical formation routes proposed. Because of the complexity of autoxidation reactions leading to a multitude of products, a chemically pure and well-characterised substrate must be used to be certain of the parent structure of a degradation product. Commercial dispersants have a general functionality but can have a very broad range of structures due to polyisobutene (PIB) polydispersity, ethylene amine type and purity, and process variables. Therefore the characterisation of PIBSI dispersants and their autoxidation products would be challenging. Linking a degradation product to a specific starting molecule to infer its formation mechanism in product studies would be prohibitively complex. Instead of studying PIBSI dispersants directly, high purity chemically equivalent model compounds, alkenyl succinimides (ASIs), were developed for use in product studies. The most studied ASI in this chapter was *N*-butyl alkenyl succinimide (Figure 4.2).

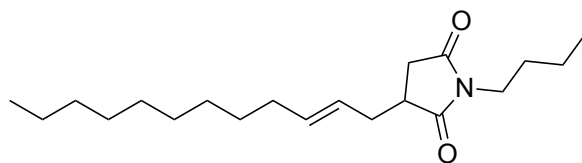


Figure 4.2 – *N*-butyl ASI, the main alkenyl succinimide studied in this chapter.

In PIBSI dispersants, the alkene is located β to the succinimide group and so ASIs containing an analogous alkene- β -succinimide moiety were investigated (Figure 4.3). The previous study into dispersant autoxidation by Erdman did not take into account the alkene which, due to the highly labile allylic hydrogens, is vulnerable to autoxidation.¹¹³

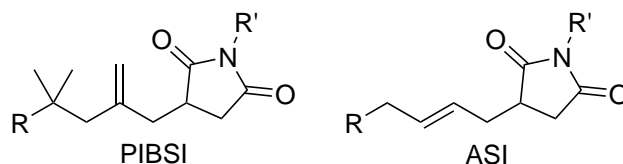


Figure 4.3 – A comparison between the structures of PIBSI dispersants and ASI model dispersants.

ASIs containing a C₁₂ *n*-alkyl tail could be synthesised in a single step from readily available starting materials whereas low molecular weight ASIs with a PIB-like tail and an equivalent alkene structure cannot be synthesised easily from readily available starting materials. Their high purity and low molecular weight (<400 Da) make ASIs and their autoxidation products suitable for analysis by gas chromatography (GC) coupled to mass spectrometry (MS) for characterisation and flame ionisation detector (FID) for quantification. A detailed study of the autoxidation of ASI dispersant mimics is reported here, with major products identified and quantified and formation mechanisms discussed. By finding the main degradation mechanisms of ASIs, the breakdown pathways and products involved in PIBSI autoxidation can be predicted and implications for lubricant performance inferred.

4.2 Results

4.2.1 ASI autoxidation products

N-butyl ASI (Figure 4.4, R = *n*-butyl) was the main dispersant mimic studied in this work.

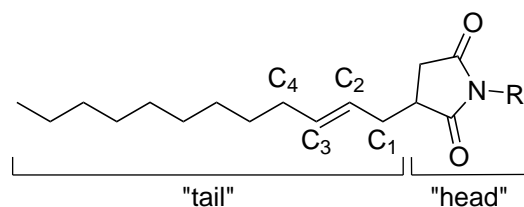


Figure 4.4 – The labelling system for ASIs, R = *n*-propyl to *n*-heptyl.

It had a favourable GC retention time where it did not overlap with a well-understood base oil mimic (squalane, $C_{30}H_{62}$, Figure 4.5) or its autoxidation products.⁹⁹ This allowed its concentration in a model lubricant to be accurately monitored, which is discussed later.

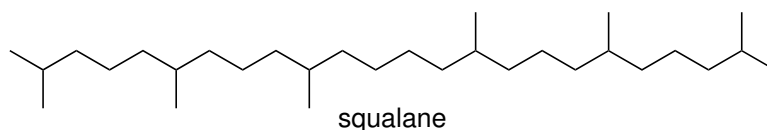


Figure 4.5 – 2,6,10,15,19,23-Hexamethyltetracosane ($C_{30}H_{62}$) commonly known as squalane.

When a solution of ASI in squalane was oxidised using pure oxygen, ASI degradation products could not be observed due to the low initial concentration of ASI (5% w/w). To enable identification of ASI degradation products, neat ASI was oxidised at 170 °C over a period of 3 hours with sampling. 170 °C is representative of temperatures a lubricant is subjected to during use, and gave a rate of degradation that was practical to investigate experimentally.^{69,70} Samples of oxidised neat ASI were analysed by GC and in total 15 products were identified using gas chromatography - electron ionisation - mass spectrometry (GC-EI-MS) and quantified using gas chromatography - flame ionisation detector (GC-FID).

Figures 4.6 and 4.7 show the GC-FID chromatograms resulting from the liquid phase autoxidation of neat *N*-butyl ASI at 170 °C for 30 minutes. From this, twelve products were observed and characterised. A further three products were observed and characterised after oxidation for 180 minutes. Products were characterised using GC-EI-MS and fragment ion assignments are discussed later.

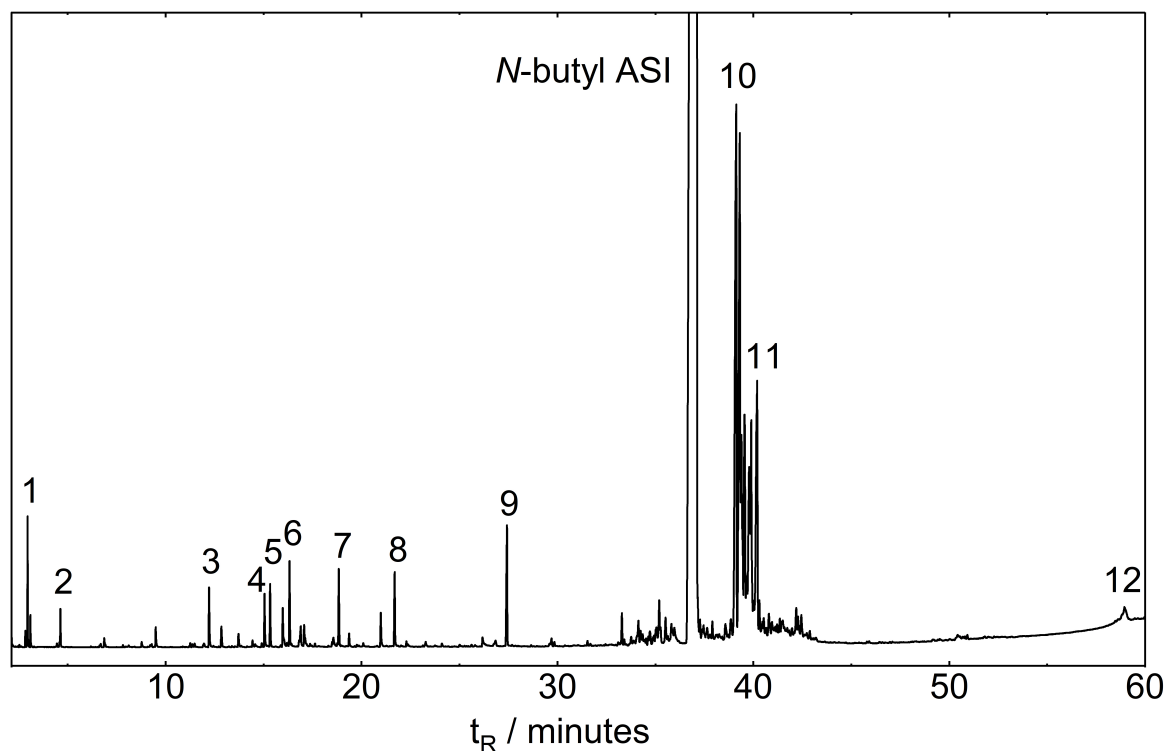


Figure 4.6 – A GC-FID chromatogram of oxidised *N*-butyl ASI (autoxidation at 170 °C for 30 minutes) showing degradation products (**1-9**), unreacted *N*-butyl ASI, oxygenated ASI products **10** and **11**, and the *N*-butyl ASI dehydromer (**12**).

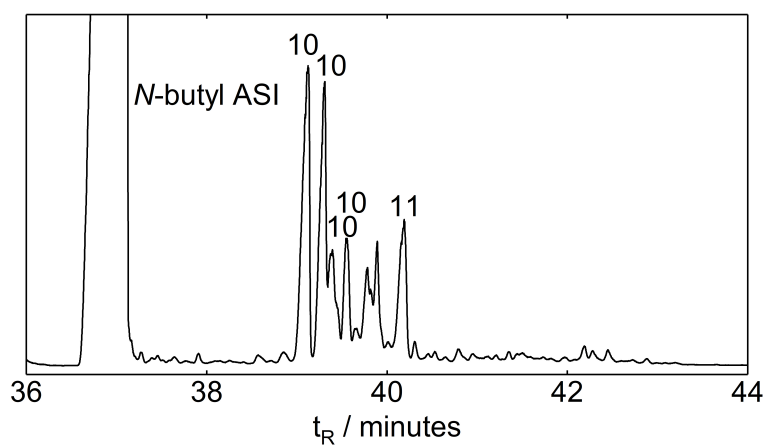


Figure 4.7 – An expansion of the GC-FID chromatogram in Figure 4.6 showing unreacted *N*-butyl ASI and oxygenated ASI products **10** and **11**.

After the sample was oxidised for 30 minutes, a series of degradation products (**1-9**) with a significantly lower retention time than *N*-butyl ASI were observed. These result from the cleavage of C-C bonds in the ASI structure. A cluster of four peaks and a single peak (**10** and **11**, Figure 4.7) with a higher retention time than *N*-butyl ASI were characterised as oxygenated ASI products. These products contain the complete *N*-butyl ASI carbon skeleton with increased functionality through the addition of oxygen.

A comparatively broad peak (**12**) was observed with a significantly higher retention time than the starting material. It was characterised as a dehydrodimer of *N*-butyl ASI, where two molecules of *N*-butyl ASI have dimerised by a recombination reaction, eliminating two hydrogen atoms and forming a covalent bond (Reaction 4.1).



As shown by Figures 4.8 and 4.9, when *N*-butyl ASI was oxidised for a longer time ($t > 60$ minutes), two further degradation products (**13** and **14**) and a third oxygenated ASI product (**15**) were also observed making a total of 15 observed products.

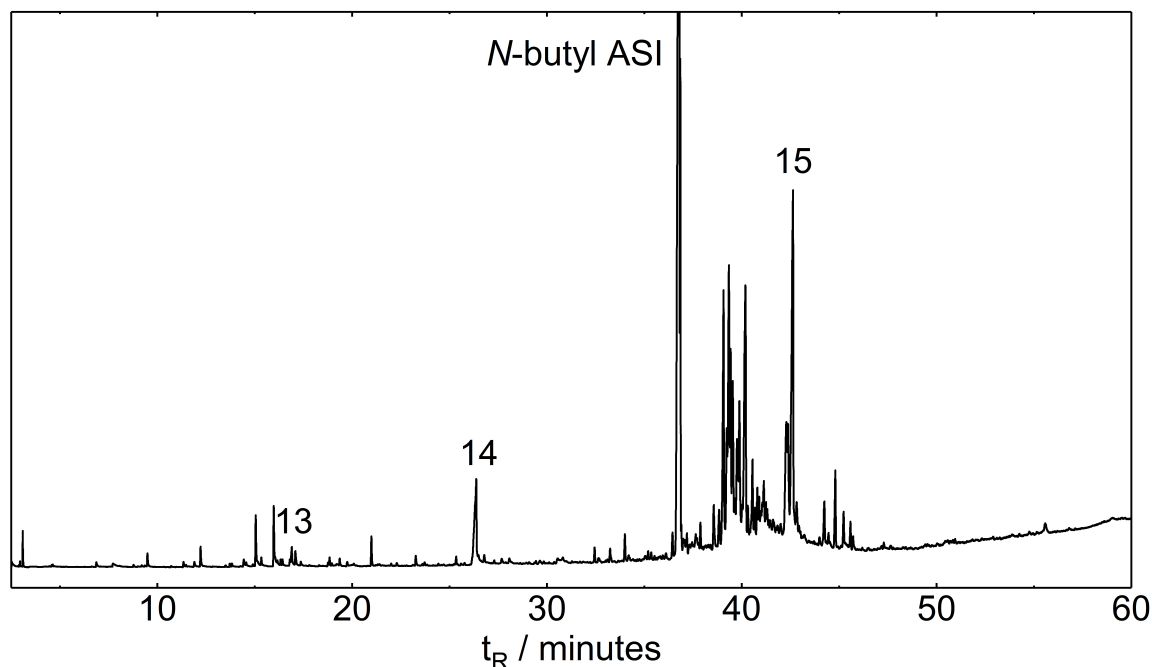


Figure 4.8 – A GC-FID chromatogram of oxidised *N*-butyl ASI (autoxidation at 170 °C for 180 minutes) showing degradation products **13** and **14**, unreacted *N*-butyl ASI and oxygenated ASI product **15**.

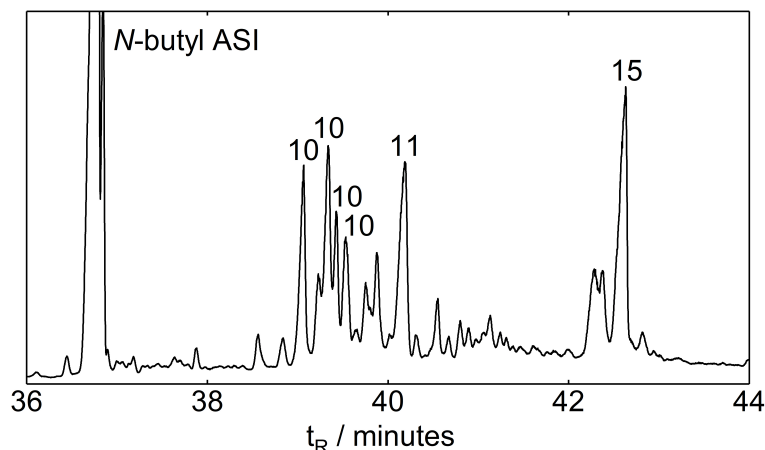


Figure 4.9 – An expansion of the GC-FID chromatogram in Figure 4.8 showing unreacted *N*-butyl ASI and oxygenated ASI products **10**, **11** and **15**.

To aid product assignment, a series of dispersant analogues with varying *N*-alkyl chain lengths (*n*-propyl to *n*-heptyl) were prepared and oxidised under the same conditions. Figure 4.10 shows the GC-FID traces of *N*-propyl to *N*-heptyl ASIs oxidised for 30 minutes at 170 °C. ASIs were prepared with the same C₁₂ “tail” and therefore fragment species with the same retention times (**1**, **2**, **3**, **6** and **7**) contained the ASI “tail” but not the *N*-alkyl chain from the “head” group. Species originating from the succinimide “head” group (**4***, **5***, **8*** and **9***) showed progressively longer retention times with longer *N*-alkyl chains. The retention times of all functionalised ASI products increased with increasing *N*-alkyl chain length.

A total of fifteen products of *N*-butyl ASI autoxidation at 170 °C were characterised by accurate mass GC-EI-MS. Table 4.1 gives the structures identified. Regioisomers of functionalised ASI products and their formation mechanisms are discussed with respect to the numbering in Figure 4.4.

The EI spectra of fragments originating solely from the “tail” of *N*-butyl ASI (**1**, **2**, **3**, **6**, **7** and **13**) were readily characterised by reference to the National Institute of Standards and Technology (NIST) database (see Appendix, Chapter 7). *N*-butyl succinimide (**4**) was also characterised in this way. Where NIST database matches could not be found (**5**, **8**, **9**, **10**, **11**, **12**, **14** and **15**) accurate mass measurements of the molecular ion were used to determine chemical formulae and fragment ions were used to determine structure. Silylation and acetonide derivatisation were used to confirm the presence of hydroxyl groups and identify regioisomers. Assignments are reported and discussed below.

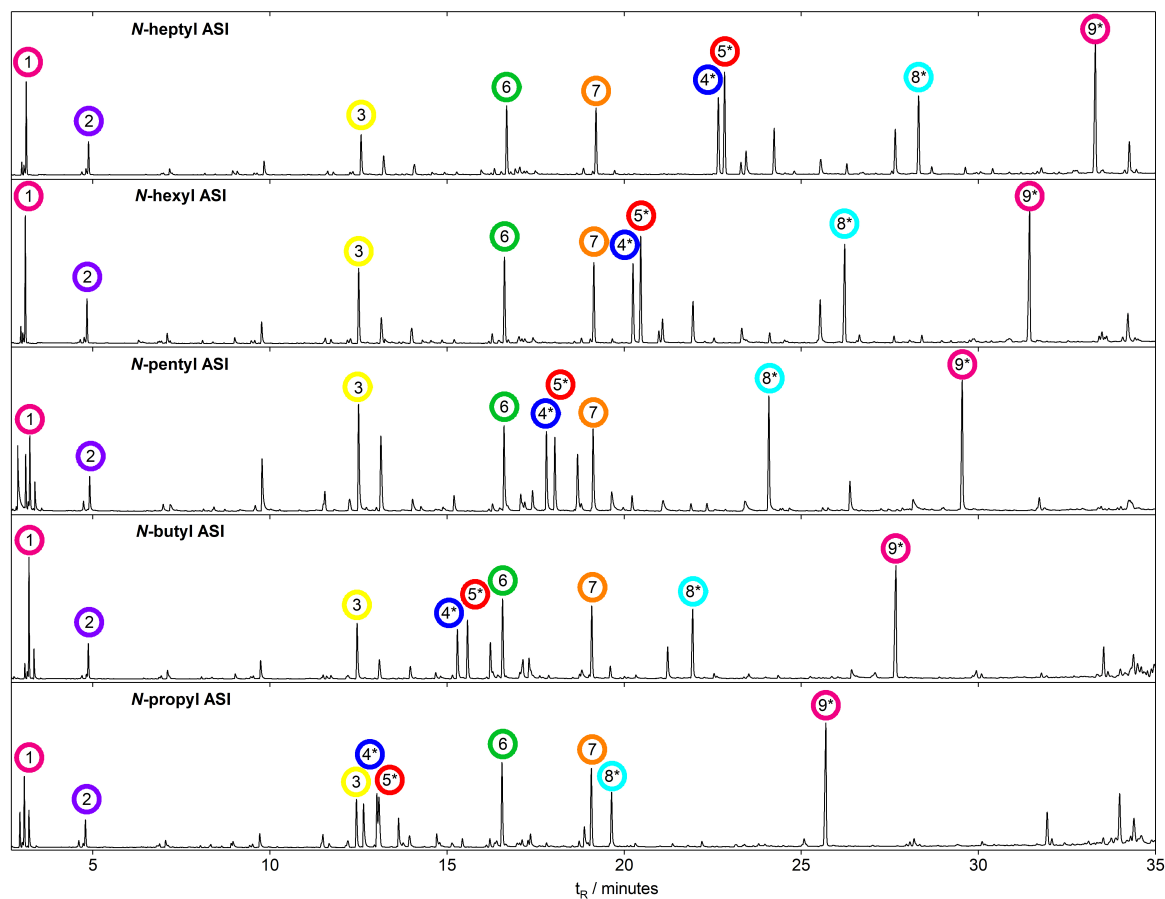


Figure 4.10 – GC-FID chromatograms of oxidised ASIs (*N*-propyl to *N*-heptyl, 170 °C, 30 minutes) between 0 and 35 minutes. Species with equivalent retention times (1, 2, 3, 6 and 7) originate from the ASI “tail”. Species originating from the succinimide “head” group (4*, 5*, 8* and 9*) show increasing retention time with increasing *N*-alkyl chain lengths.

Table 4.1 – Identified products from the autoxidation of *N*-butyl ASI at 170 °C. ^a Identified by comparison to the NIST database. ^b EI-MS fragment assignments made and discussed later. ^c Silylated derivative observed. ^d Acetonide derivative observed.

Peak	Name	Structure
1 ^a	octane	
2 ^a	nonane	
3 ^a	decanal	
4 ^a	<i>N</i> -butyl succinimide	
5 ^b	3-methyl <i>N</i> -butyl succinimide	
6 ^a	undec-2-enal	
7 ^a	dodec-2-enal	
8 ^b	succinimide aldehyde	
9 ^b	α,β -unsaturated succinimide aldehyde	
10 ^{b,c}	<i>N</i> -butyl ASI alcohol e.g. C ₄ <i>N</i> -butyl ASI alcohol	
11 ^b	C ₄ <i>N</i> -butyl ASI ketone	

Table 4.1 – Identified products from the autoxidation of *N*-butyl ASI at 170 °C. ^a Identified by comparison to the NIST database. ^b EI-MS fragment assignments made and discussed later. ^c Silylated derivative observed. ^d Acetonide derivative observed.

Peak	Name	Structure
12 ^b	<i>N</i> -butyl ASI dehydrodimer e.g. C ₄ -C ₄ <i>N</i> -butyl ASI dehydrodimer	
13 ^a	<i>n</i> -decanoic acid	
14 ^{b,c}	succinimide acid	
15 ^{b,c,d}	C ₂ ,C ₃ <i>N</i> -butyl ASI diol	

4.2.2 Characterisation of novel compounds from *N*-butyl ASI autoxidation

4.2.2.1 Product 5 - 3-Methyl, *N*-butyl ASI

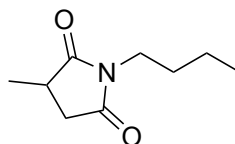


Figure 4.11 – The structure of product **5**, 3-methyl, *N*-butyl succinimide.

Peak **5** in Figure 4.6 was characterised as $C_9H_{15}NO_2$ with -4.7 ppm mass error, within the 10 ppm root mean square (RMS) error calculated for the equipment. EI fragment ions for peak **5** can be found in Table 4.2. It showed an analogous EI fragmentation pattern to *N*-butyl succinimide (**4**) studied by Duffield *et al.*¹⁵⁷ *N*-butyl succinimide shows fragments resulting from fragmentation at each carbon position of the *n*-butyl chain, yielding a series of diagnostic fragments. EI fragments of peak **5** were of equivalent intensity but 14 Da heavier than fragments from **4**, suggesting an additional methylene unit. Observation of the full and sequential fragmentation of the *n*-butyl chain for peak **5** suggested the additional CH_2 unit was located on the succinimide, not the *n*-butyl chain. From this information, peak **5** was identified as 3-methyl, *N*-butyl succinimide (Figure 4.11).

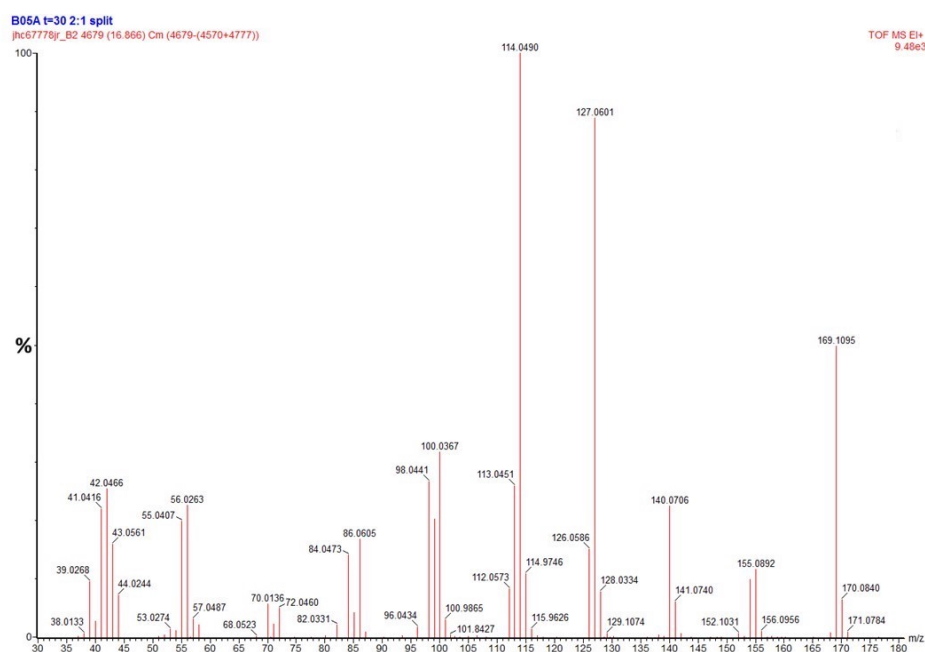
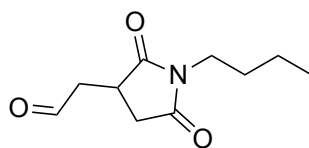


Figure 4.12 – The EI mass spectrum of product **5**, 3-methyl, *N*-butyl succinimide.

Table 4.2 – Fragment ion assignments for product **5**, 3-methyl *N*-butyl succinimide.

m/z	Ion	m/z	Ion
169		155	
140		127	
114		99	
98		86	
56		55	

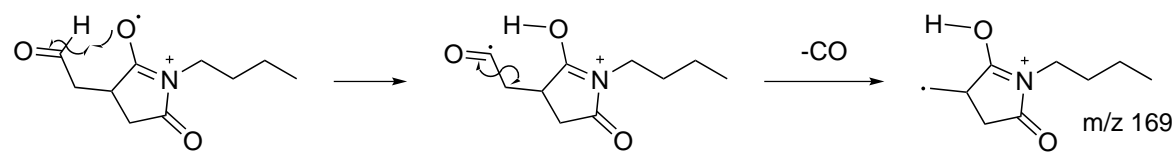
4.2.2.2 Product **8** - succinimide aldehyde

**Figure 4.13** – The structure of product **8** - succinimide aldehyde

Peak **8** was characterised as a succinimide containing aldehyde with the formula $C_{10}H_{15}NO_3$ to 7.6 ppm mass error, within the 10 ppm RMS error for the equipment. The presence of the complete *N*-butyl chain was confirmed by a fragmentation sequence analogous to peak **4**. Prominent fragments at m/z 169 and m/z 153 were attributed to aldehyde functionality. The m/z 169 fragment was consistent with the formula $C_9H_{15}NO_2^{+\bullet}$ (4.7 ppm mass error)

representing the loss of CO ($M^{+\bullet} - 28$). The suggested mechanism for its formation during EI-MS analysis is shown in Scheme 4.1. Initiated by ionisation of the nitrogen and resonance of the resultant radical to a succinimide carbonyl, hydrogen transfer from the aldehyde followed by α -cleavage could eliminate CO and generate the odd electron ion with m/z 169.

Scheme 4.1 The proposed EI-MS fragmentation of the succinimide aldehyde (**8**) by loss of CO.



The m/z 153 fragment was consistent with $C_8H_{11}NO_2$ with 9.8 ppm mass error. The proposed mechanism of formation is analogous to that determined by Christiansen *et al.*,¹⁵⁸ where ionisation of the aldehyde initiates γ -hydrogen transfer to the aldehyde oxygen, followed by inductive cleavage to eliminate C_2H_4O and yield the odd electron succinimide ion with m/z 153 (Scheme 4.2).

Scheme 4.2 The proposed EI-MS fragmentation of the succinimide aldehyde (**8**) to lose C_2H_4O .

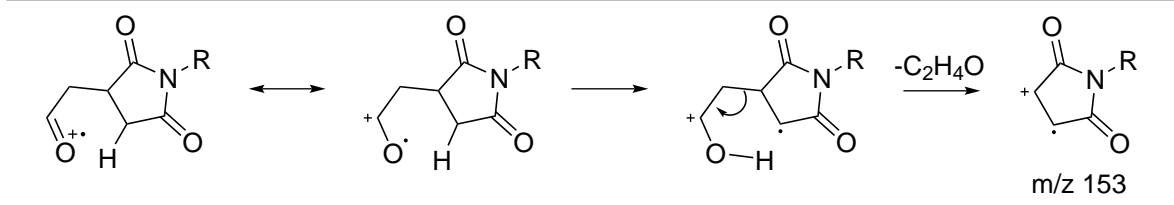


Table 4.3 – Fragment ion assignments for product **8**, succinimide aldehyde.

m/z	Ion	m/z	Ion
197		182	
169		168	
155		153	

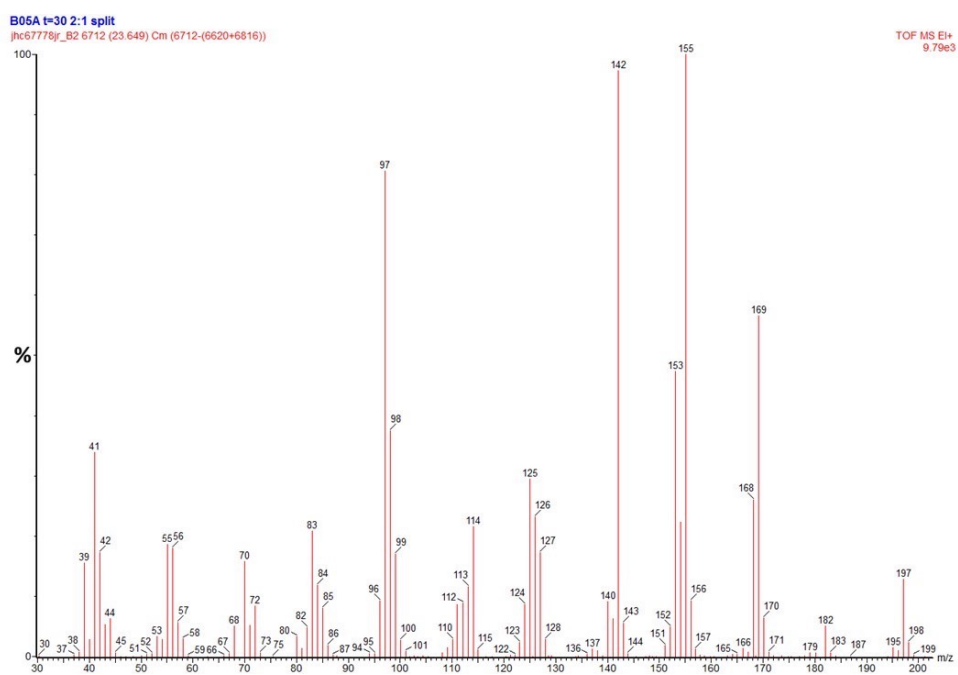
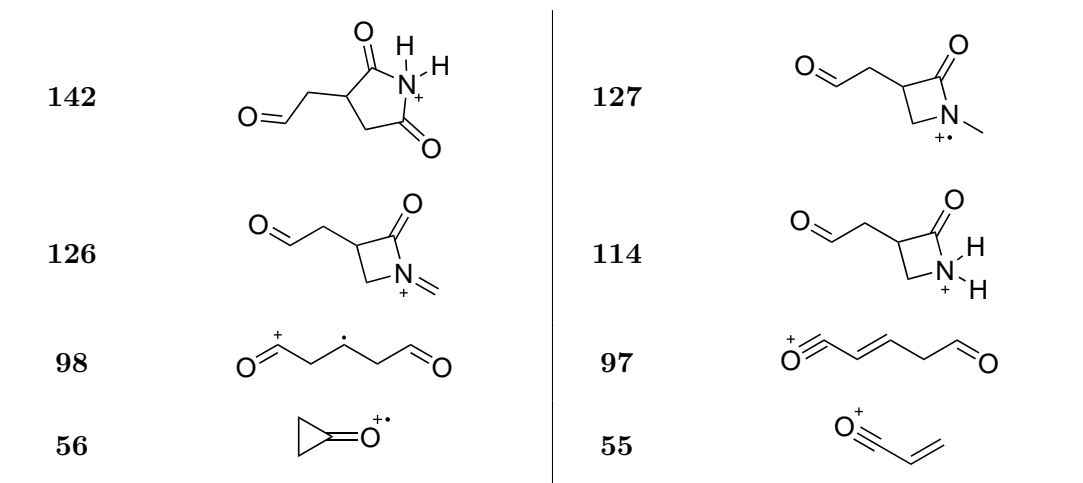


Figure 4.14 – An EI mass spectrum of the succinimide aldehyde, product **8**.

4.2.2.3 Product 9 - α,β -unsaturated succinimide aldehyde

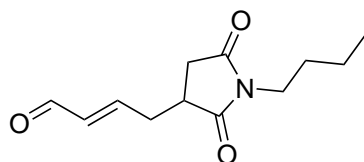


Figure 4.15 – The structure of the α,β -unsaturated succinimide aldehyde, product **9**.

Peak **9** was characterised with the formula $C_{12}H_{17}NO_3$ with -5.4 ppm mass error, within the 10 ppm RMS error for the equipment. A fragment ion with m/z 194 corresponds to the loss of CHO suggesting the presence of an aldehyde. The base peak at m/z 153 was assigned to the *N*-butyl succinimide radical cation, consistent with the aldehyde functionality not being on the *N*-butyl chain. It is thought that the m/z 153 fragment forms by an equivalent mechanism to the m/z 153 ion observed for peak **8**. The formula of peak **9** has a ring double bond equivalents (RDBE) value¹⁵⁹ of five. With the contribution from three carbonyls and a succinimide ring summing to four, the fifth RDBE is attributed to an alkene. Fragment ions consistent with *N*-butyl succinimide were observed, which is consistent with the α,β -unsaturated succinimide aldehyde structure **9**.

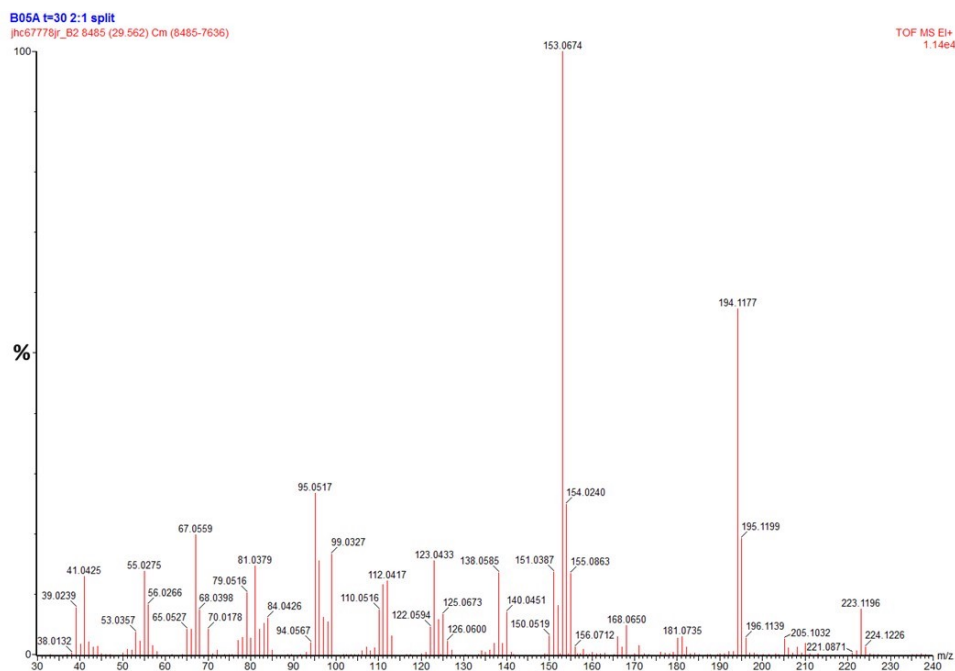


Figure 4.16 – The EI mass spectrum of the α,β -unsaturated succinimide aldehyde, product **9**.

Table 4.4 – Fragment ion assignments for product **9**, α,β -unsaturated succinimide aldehyde.

m/z	Ion	m/z	Ion
223		194	
194		181	
168		153	

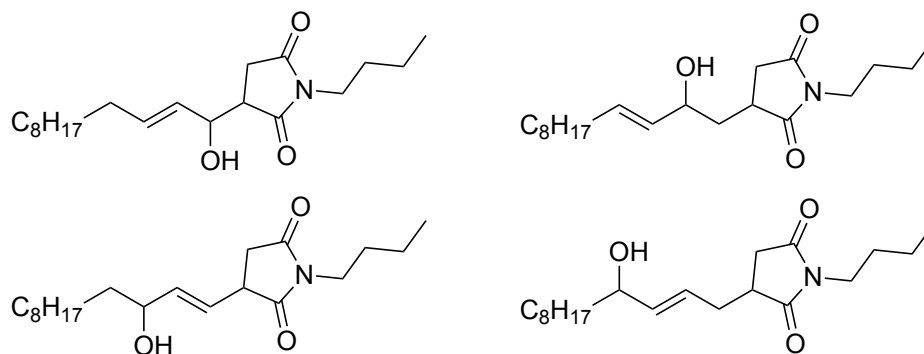
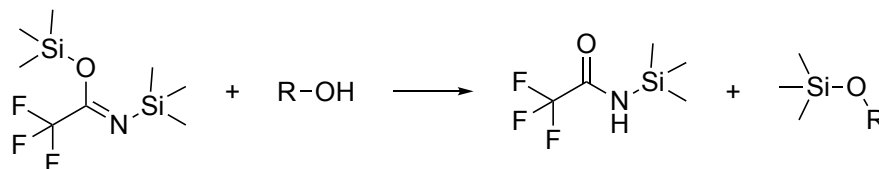
4.2.2.4 Product 10 - *N*-butyl ASI alcohol

Figure 4.17 – The four isomers of product **10**, *N*-butyl ASI alcohol, observed in this work.

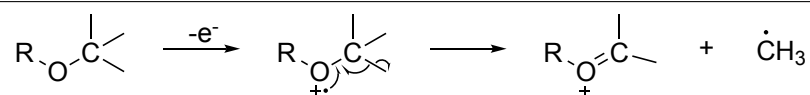
When *N*-butyl ASI ($C_{20}H_{35}NO_2$) was oxidised at 170 °C, a cluster of four distinct peaks (**10**, Figure 4.7) with GC retention times of ca. 39 minutes were observed. The peaks were identified as $C_{20}H_{35}NO_3$ with a -2.1 ppm mass error, suggesting the addition of one oxygen atom to *N*-butyl ASI. Silylation, as described in Section 2.4.2.3 on Page 47, was used to further characterisation. Hydroxyl groups in alcohols and carboxylic acids readily form trimethylsilyl (TMS) esters (Scheme 4.3), whereas ketones and aldehydes do not react.

Scheme 4.3 Silylation of alcohol groups using *N,O*-bis(trimethylsilyl)trifluoroacetamide (BSTFA).



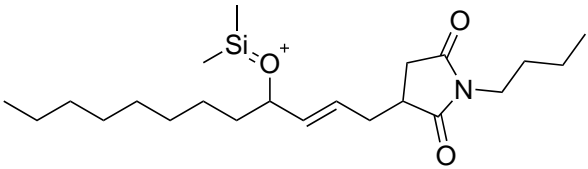
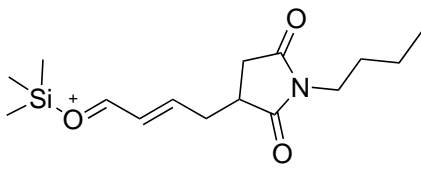
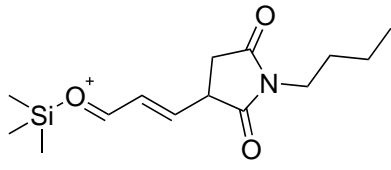
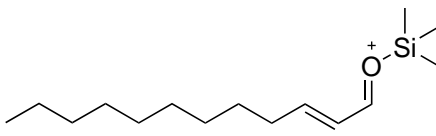
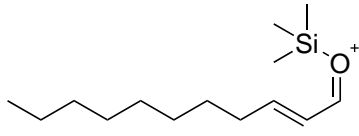
The resultant silyl ether or ester shifts GC retention time and produces distinctive EI-MS fragments. Silylation is also useful for determining the molecular ion of alcohols and carboxylic acids, particularly those of high molecular weight which would otherwise dehydrate during analysis, destroying the molecular ion. TMS derivatives readily fragment by loss of CH_3^\bullet to give a strong $[M-15]^+$ peak, allowing determination of molecular weight for the parent compound (Scheme 4.4).

Scheme 4.4 EI fragmentation of a silyl ether forming a stable silyl cation and eliminating $\bullet CH_3$



In the case of peak **10**, silylation caused the peaks to shift to a longer retention time confirming alcohol functionality. The predictable fragmentation of silyl-ethers allowed assignment of the alcohol regioisomers. Silyl ethers of allyl alcohols preferentially expel the more stable alkyl radical fragment over the vinylic radical fragment, yielding an unsaturated silyl cation. The four silylated alcohols co-eluted on GC, however prominent fragment ions from the four alcohol isomers could still be observed (Figure 4.18). Fragments with m/z 296, 282, 255 and 241 were assigned to the most stable fragments of silyl ethers of allyl alcohols in the C₄, C₃, C₁ and C₂ positions respectively (Table 4.5). This is consistent with the formation of four major allylic alcohol species (Figure 4.17) during the initial stages of *N*-butyl ASI autoxidation.

Table 4.5 – EI-MS fragment ion assignments for silylated *N*-butyl ASI alcohols (**10**).

m/z	Ion	Parent Isomer
394		C ₁ C ₂ C ₃ C ₄
296		C ₄
282		C ₃
255		C ₁
241		C ₂

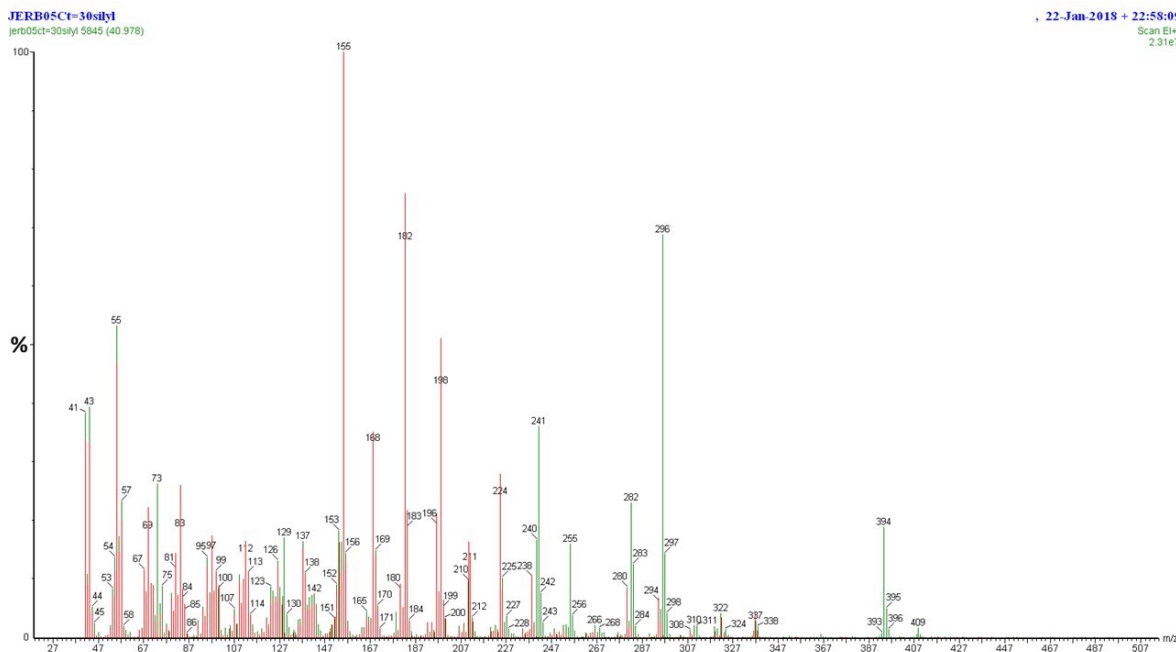


Figure 4.18 – An EI-MS spectrum of the four co-eluting silylated *N*-butyl ASI alcohols (green) overlaid with a spectrum from the *N*-butyl ASI alcohol (**10**, red).

4.2.2.5 Product 11 - *N*-butyl ASI ketone

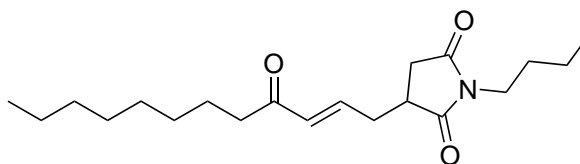


Figure 4.19 – The structure of the C_4 *N*-butyl ASI ketone, product **11**.

A single, asymmetric, GC peak (**11**) was observed and was consistent with the formula $C_{20}H_{33}NO_3$ (-2.1 ppm mass error). This formula represents addition of oxygen to *N*-butyl ASI and the elimination of two hydrogen atoms. This is consistent with ketone formation whilst maintaining the ASI structure. No other significant GC peaks with a nominal mass of 335 Da (*N*-butyl ASI mass ion + 14) were identified. The peak asymmetry suggested the partial coelution of multiple ketone products which was confirmed by changes observed in the mass spectra collected across the peak.

Nitrogen containing compounds complicate EI fragmentation analysis as, without a known nitrogen content, fragment ions cannot be assigned as odd or even electron species. To aid assignments, oxidised *N*-propyl ASI was analysed. EI fragments originating from the

succinimide “head” of *N*-propyl ASI had 14 Da lower m/z values than equivalent fragments originating from *N*-butyl ASI. Solely “tail” derived fragments had the same m/z values for both *N*-propyl and *N*-butyl ASI. Using this to determine nitrogen content allowed assignment of odd and even electron fragments from the *N*-butyl ASI ketone (**11**), see Table 4.6. Most of the mass spectra collected from peak **11** were complicated by coelution. However, the earliest eluting portion of the peak yielded clear and simple spectra with prominent fragments at m/z 194, 222 and 237. Comparison to the equivalent *N*-propyl ASI ketone showed the three ions contain nitrogen.

The EI fragmentation of allylic ketones was studied by Bowles *et al.* who showed fragmentation occurred by either α cleavage or inductive cleavage at the carbonyl.¹⁶⁰ The McLafferty rearrangement was not observed by Bowles *et al.* due to an absence of γ -hydrogens. However, the McLafferty rearrangement is applicable to the γ -hydrogen-containing compounds, peak **11**. The fragment ions are consistent with the C₄ isomer of the *N*-butyl ASI ketone, shown in Figure 4.19. The base peak at m/z 194 originates from inductive cleavage at the carbonyl and an m/z 222 fragment from α -cleavage. The m/z 237 ion forms by the McLafferty rearrangement. The coelution of other ketone regioisomers prevented their definitive characterisation.

Table 4.6 – A summary of the fragment ions of the C₄ *N*-propyl ASI ketone and the C₄ *N*-butyl ASI ketone (**11**), their region of origin, and electronic character.

m/z		Origin	Electronic Character
<i>N</i> -propyl ASI ketone	<i>N</i> -butyl ASI ketone		
321	335	M ^{+•}	Odd
224	238	Head	Even
223	237	Head	Odd
208	222	Head	Even
180	194	Head	Even
154	168	Head	Even
141	155	Head	Odd
95	95	Tail	Even
67	67	Tail	Even

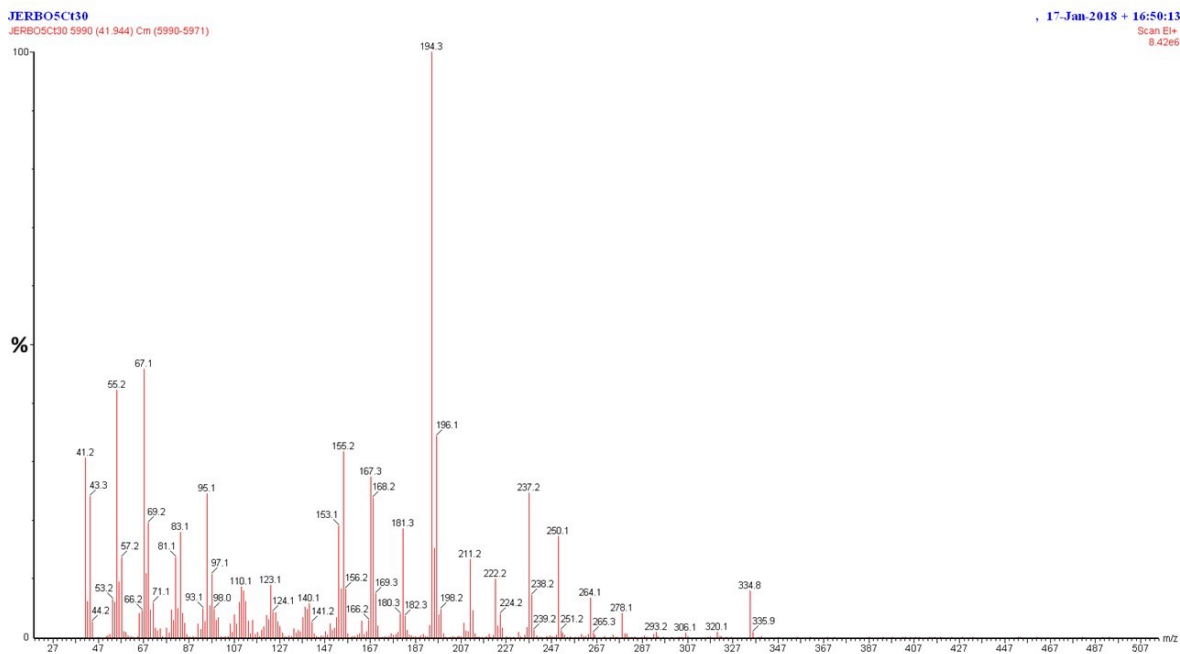


Figure 4.20 – An EI mass spectrum of the C₄ N-butyl ASI ketone (**11**).

Table 4.7 – EI-MS fragment ion assignments for the C₄ N-butyl ASI ketone (**11**).

m/z	Ion
335	
237	
222	
194	

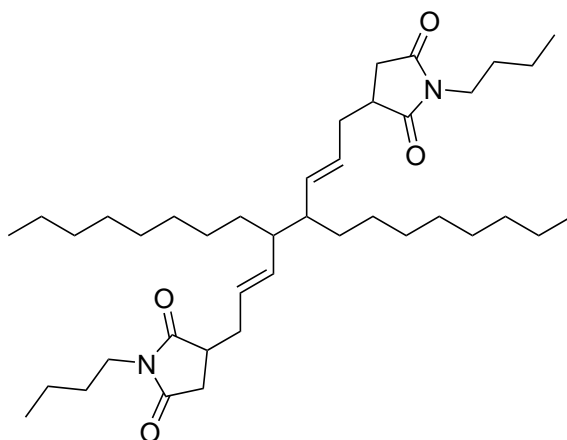
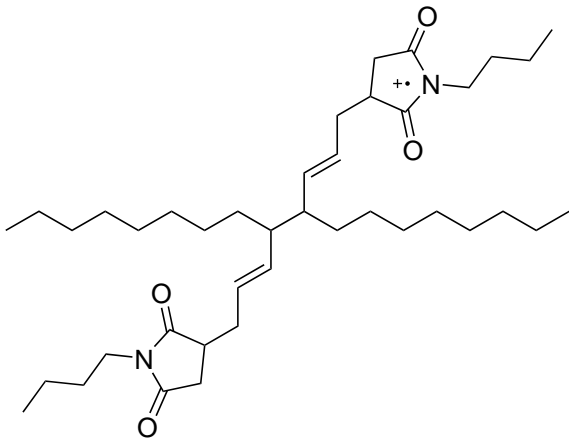
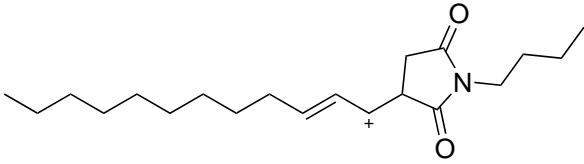
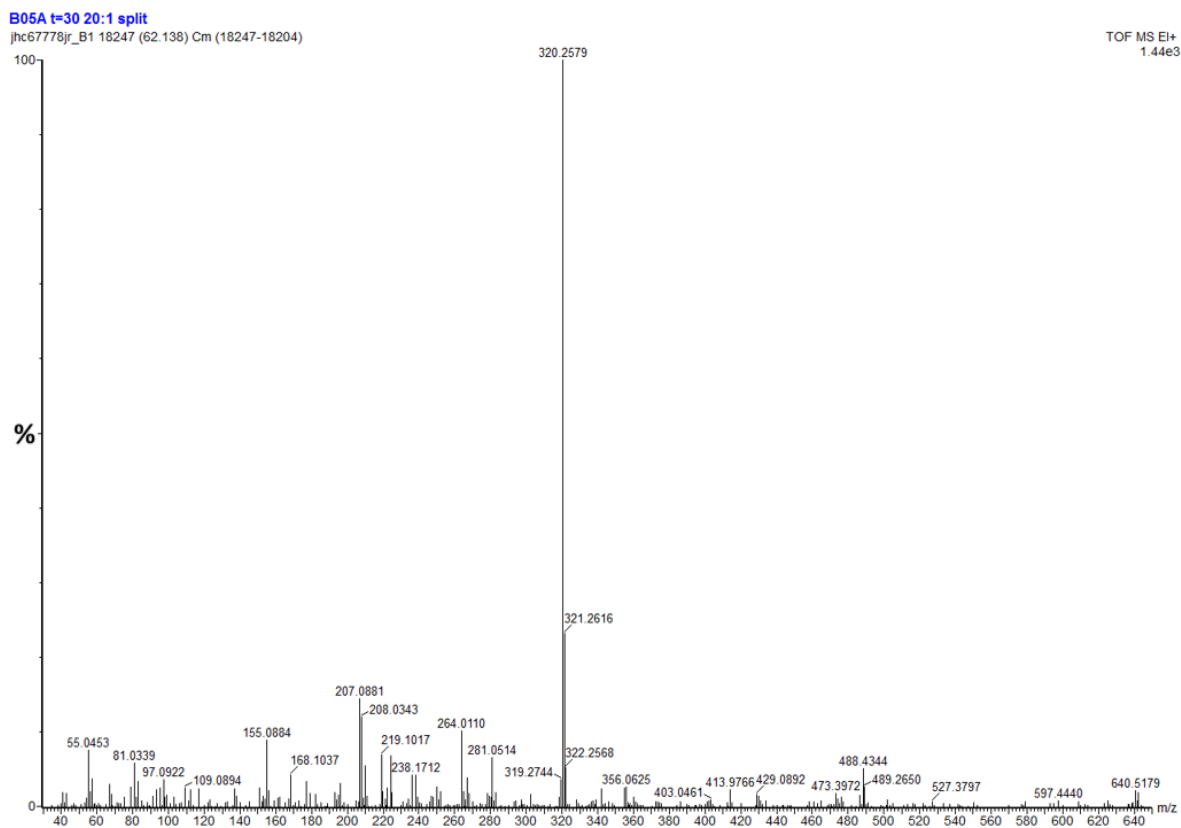
4.2.2.6 Product **12** - *N*-butyl ASI dehydrodimer

Figure 4.21 – The C₄-C₄ *N*-butyl ASI dehydrodimer, an example structure for the one of the possible *N*-butyl ASI dehydrodimers.

A comparatively broad peak (**12**) with high retention time and formula C₄₀H₆₈N₂O₄ was observed (mass error of 0.0 ppm). Representing exactly half the mass of the molecular ion, the most significant fragment had the formula C₂₀H₃₄NO₂ (-1.6 ppm mass accuracy). This peak is likely a true fragment of **12** and not simply a doubly-charged M²⁺• ion. The M+1 isotope peak of a doubly-charged M²⁺• ion would be expected at m/z = 320.5. However, the data showed a singly-charged M+1 isotope peak of with m/z = 321 derived from the M⁺• ion. These observations were consistent with the formation of a dehydrodimer; two times the mass of *N*-butyl ASI minus two hydrogen atoms. The broad peak suggests multiple regioisomers of the dimeric species were formed but not resolved by GC.

Table 4.8 – EI-MS fragment ion assignments for the *N*-butyl ASI dehydrodimer.

m/z	Ion
640	
320	

**Figure 4.22** – An EI mass spectrum of the *N*-butyl ASI dehydrodimer with its molecular ion at m/z 640 and strong base peak at m/z 320.

4.2.2.7 Product 14 - succinimide acid

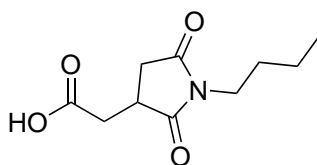


Figure 4.23 – The structure of the succinimide acid (**14**).

Peak **14** was tentatively assigned as the succinimide acid structure shown in Figure 4.23. The GC peak showed shark fin behaviour, which is characteristic of carboxylic acid groups. The chemical formula determined by accurate mass MS is consistent with the formula $C_{10}H_{15}NO_4$ with an accuracy of -8.9 ppm. However, the mass spectrum (Figure 4.25) was complex, and assignment of fragment ions was challenging. The peak readily formed the silylated derivative, confirming the presence of an OH group and confirming the mass of the molecular ion (Figure 4.26).

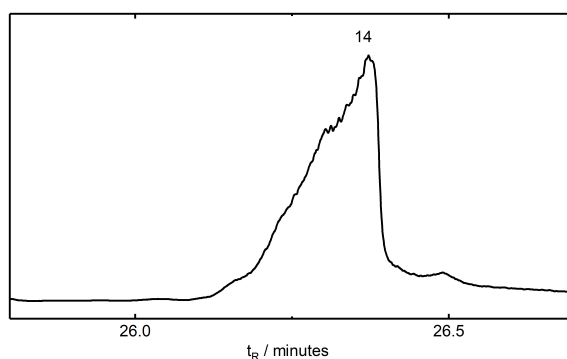


Figure 4.24 – An expansion of the GC chromatogram showing the shark fin behaviour of peak **14** which is consistent with the elution of a highly polar species, such as a carboxylic acid, on a comparatively non-polar GC column.

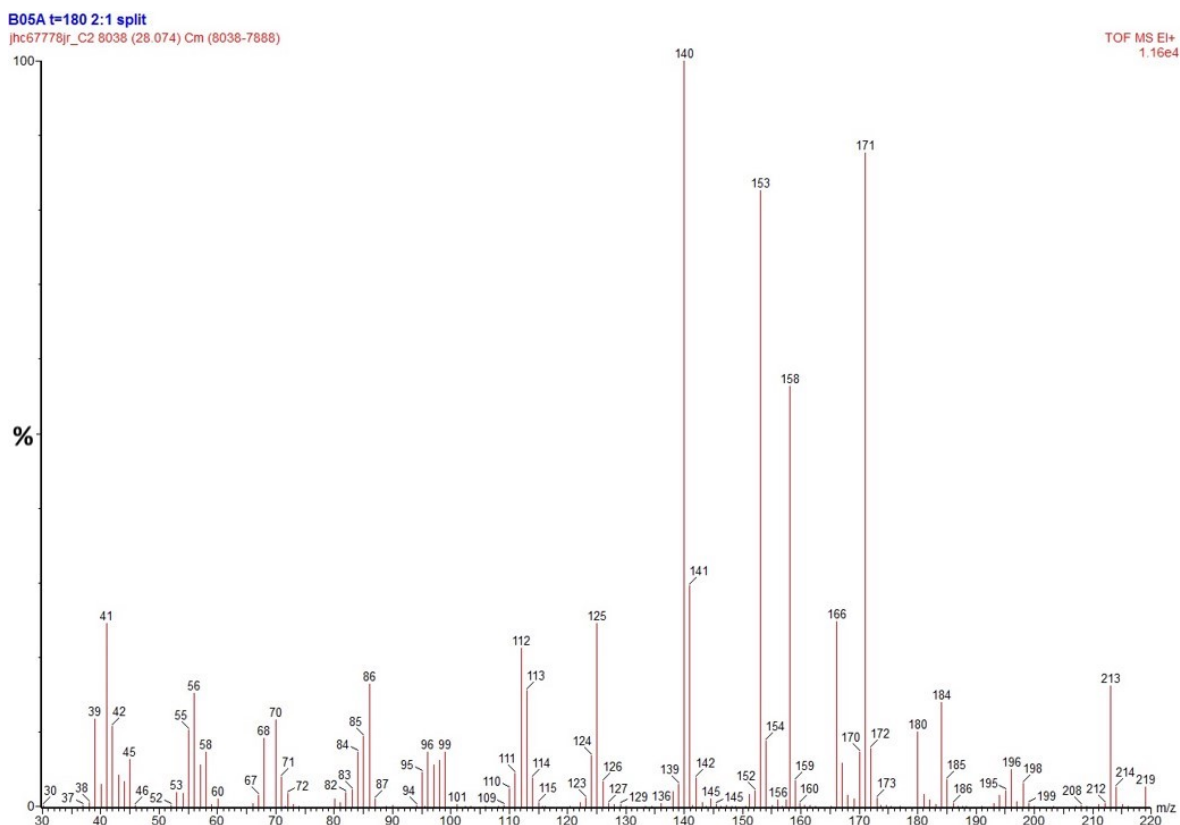


Figure 4.25 – The EI mass spectrum of the succinimide acid (14).

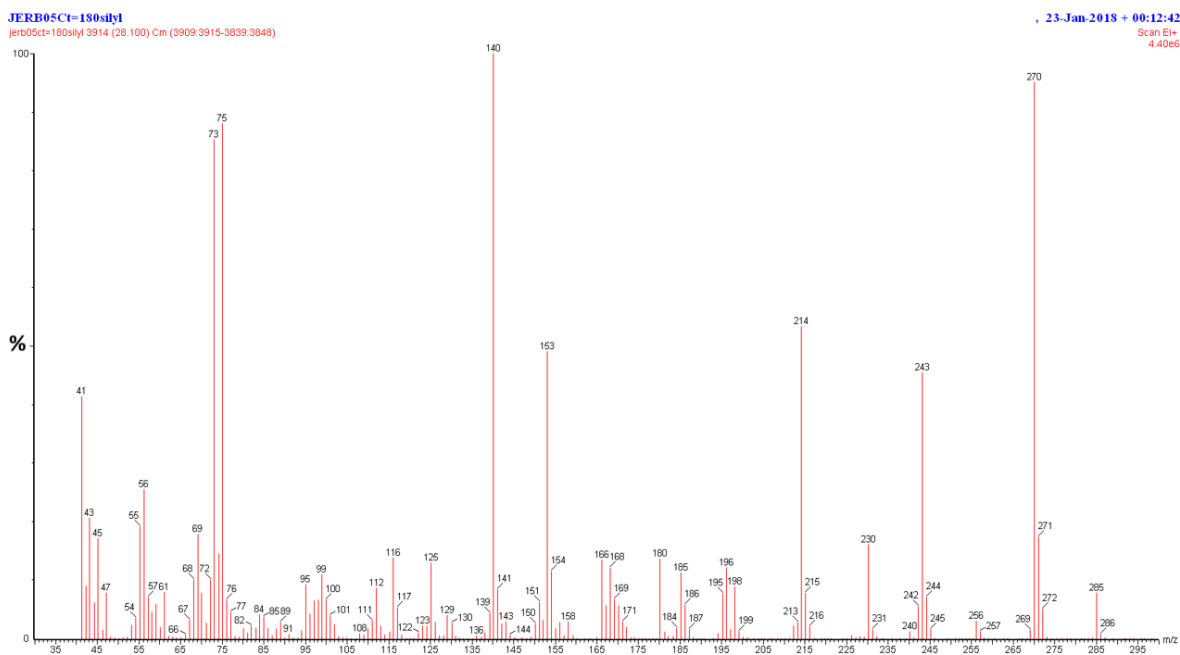
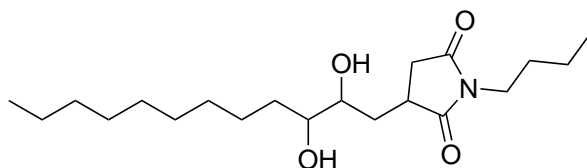


Figure 4.26 – The EI mass spectrum of the silyl ester derivative of the succinimide acid (14).

4.2.2.8 Product 15 - C₂,C₃ *N*-butyl ASI diolFigure 4.27 – C₂,C₃ *N*-butyl ASI diol (**15**).

The peak **15** was identified as the formula C₂₀H₃₇NO₄ (2.0 ppm mass error), consistent with the addition of two oxygen and two hydrogen atoms to the *N*-butyl ASI structure, most likely from the formation of two alcohols and reduction of the alkene. The molecular ion and its structure were confirmed by acetonide and silylation derivatisation. Upon reaction with acetone (Scheme 4.5), **15** formed the acetonide derivative as shown by the diagnostic MS fragments in Figure 4.28 and Table 4.9, confirming the presence of two alcohol groups in the form of a vicinal diol.

Scheme 4.5 The formation of a cyclic acetal by the reaction of a vicinal diol with acetone. When used to derive vicinal diols for mass spectrometry this is called acetonide derivatisation.

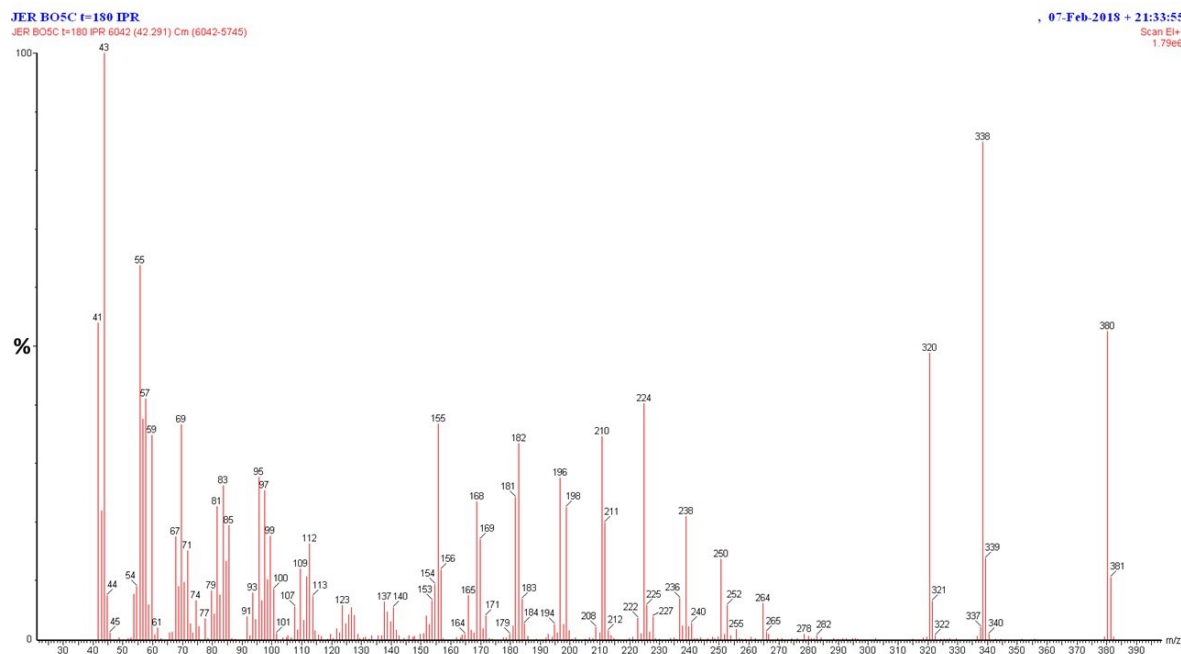
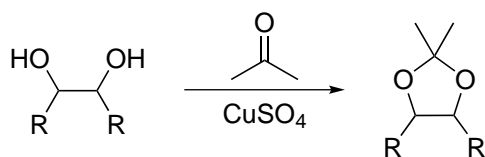
Figure 4.28 – The EI mass spectrum of the acetonide derivative of the C₂,C₃ *N*-butyl ASI diol (**15**).

Table 4.9 – EI-MS fragment ion assignments for the acetonide derivative of the C₂,C₃ *N*-butyl ASI diol (**15**).

m/z	Ion
395	
380	
338	
320	

When silylated, the diol formed two mono substituted TMS ethers, where one alcohol was silylated, and one disubstituted TMS ether, where both alcohols were silylated. The silylated compounds resolved by GC, allowing the mass spectra to be analysed. The diagnostic EI fragmentation of the TMS ethers¹²² (Figure 4.29 and Table 4.10) showed the regioisomer to be the C₂,C₃ *N*-butyl ASI diol (**12**).

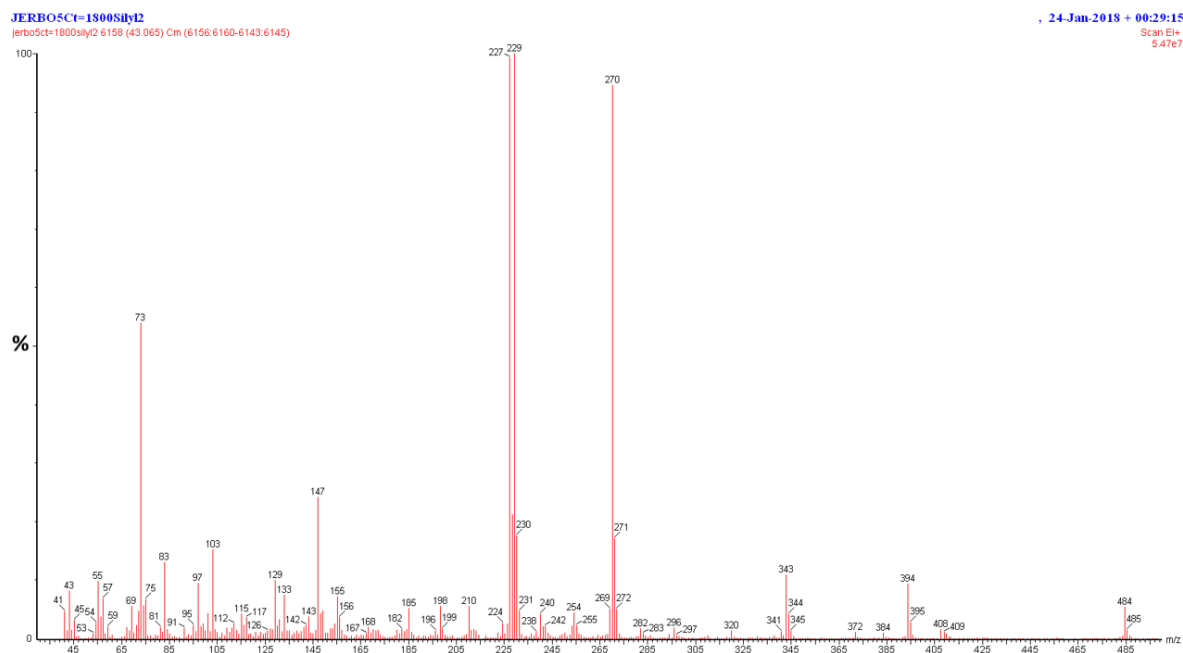


Figure 4.29 – The EI mass spectrum of the bis-silylated C₂,C₃ *N*-butyl ASI diol (**15**).

4.2.3 Product distribution

Autoxidation products of *N*-butyl ASI were quantified by GC-FID from samples taken during the three-hour reaction. Concentrations were determined using the effective carbon number (ECN) method.¹²⁰ The concentrations of oxygenated ASI-products are shown in Figure 4.30. While the *N*-butyl ASI alcohol (**10**) and *N*-butyl ASI ketone (**11**) concentrations increased from t_0 , the C_2, C_3 *N*-butyl ASI diol (**15**) was only observed after 60 minutes. The concentration of the *N*-butyl ASI alcohol (**10**) decreased after 90 minutes. The concentrations of individual degradation products and the dehydrodimer were also determined and are shown in Figure 4.31. All products increased in concentration from the beginning of the reaction (t_0) reaching a maximum at around 60 minutes before steadily decreasing for the last two hours of reaction.

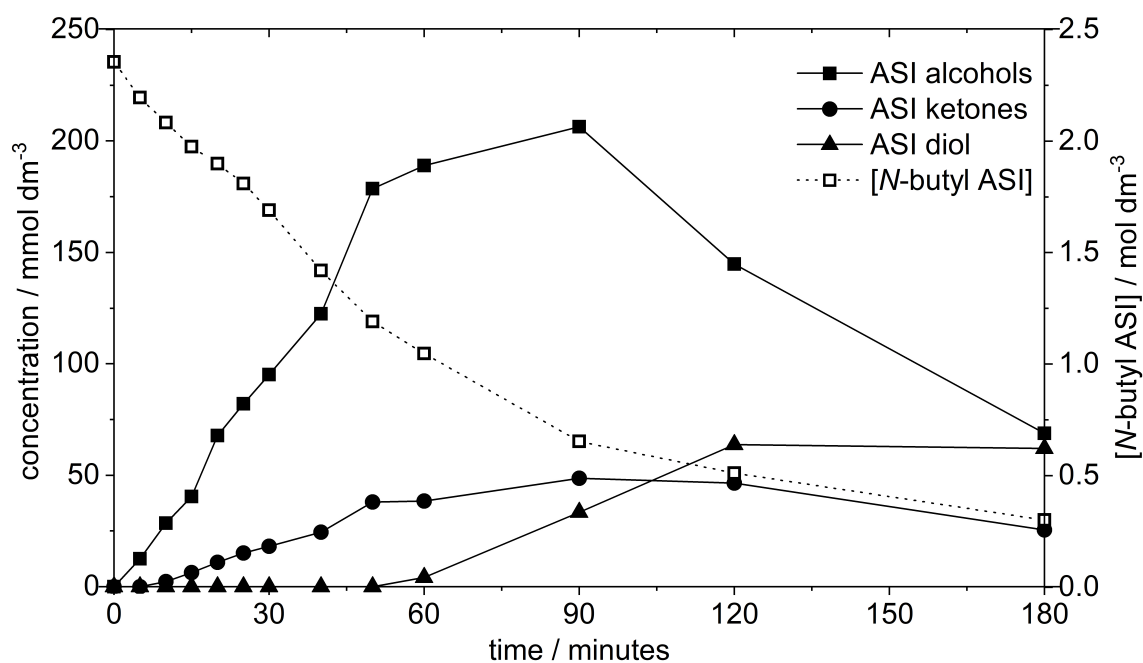


Figure 4.30 – The concentration *N*-butyl ASI alcohols, (**10**), *N*-butyl ASI ketone (**11**) and the C_2, C_3 *N*-butyl ASI diol (**15**) during the autoxidation. The concentration of *N*-butyl ASI is also shown.

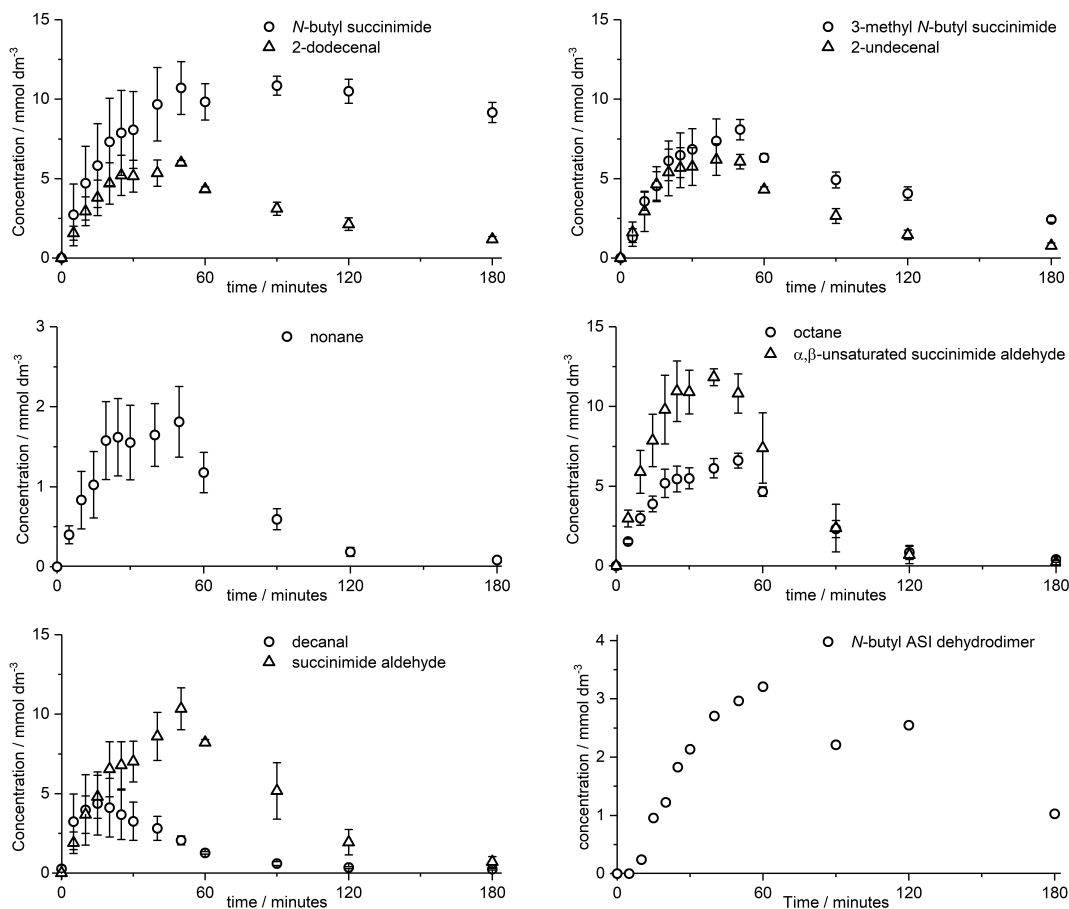


Figure 4.31 – The concentrations of the primary degradation products of *N*-butyl ASI and the *N*-butyl ASI dehydrodimer. Error bars of standard error are also shown.

Reaction selectivities were also calculated, defined as the proportion of reacted material that goes on to form a certain product or group of products. The data from one experiment is given in Figure 4.32. The selectivity was calculated for the sum of the ASI degradation products, those with GC retention times lower than *N*-butyl ASI, and for the sum of the oxygenated ASI products, the products observed with GC retention times higher than *N*-butyl ASI. As the structures of all observed peaks had not been determined, molar concentrations could not be readily calculated. Therefore, selectivity was calculated based on the GC-FID peak areas for all observed peaks.

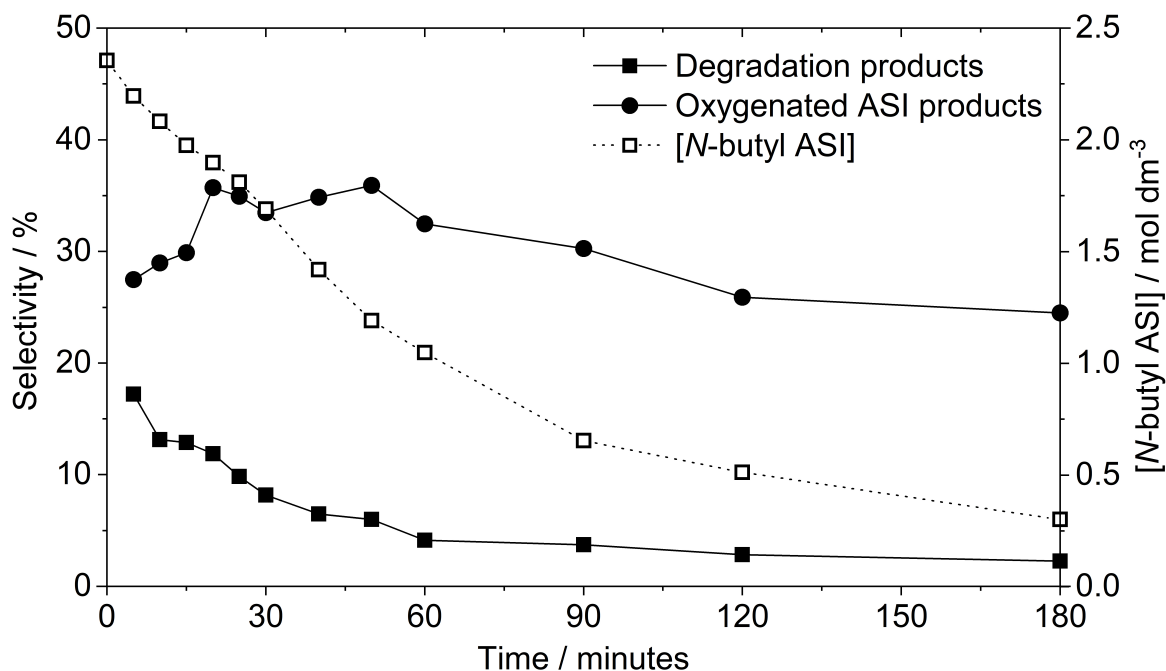


Figure 4.32 – The selectivity for all observed degradation products and all observed oxygenated ASI products. The concentration of *N*-butyl ASI is also shown.

Early in the reaction (five minutes), the selectivity for *N*-butyl ASI forming degradation products was 17%, decreasing to 4% by 60 minutes. The selectivity for oxygenated ASI products increased from 27% early in the reaction to a maximum of 36% at 50 minutes, after which it decreased to a low of 24% by the end of the reaction.

At the start of the reaction, the liquid sample contained pure *N*-butyl ASI which was also monitored by GC-FID. As the reaction progressed, the sum of the peak areas for *N*-butyl ASI and all the observed products noticeably decreased, with a selectivity for products that were observable by GC-FID of 44% early in the reaction (at five minutes), decreasing to 27% by the end of the three hour reaction. This is attributed to the formation of high molecular weight and high polarity species that were not detectable due to very low volatility at the maximum GC temperature (340 °C).

4.2.4 Viscosity increase on autoxidation

The dynamic viscosity of *N*-butyl ASI before and after autoxidation at 170 °C for three hours was measured at shear rates between 50 and 750 s⁻¹. Prior to autoxidation, *N*-butyl ASI showed Newtonian behaviour with a low and shear-independent viscosity of 0.06 Pa s. After autoxidation, the sample viscosity at a shear rate of 50 s⁻¹ was 17.6 Pa s, a 300-fold increase. The sample showed reversible shear thinning behaviour with the viscosity decreasing to 14.4 Pa s when the shear rate was ramped to 750 s⁻¹. After a hold period of five minutes when no shear force was applied, the sample showed the same shear thinning behaviour for a second and third shear cycle (Figure 4.33). This indicates that intermolecular bonds contribute significantly to the viscosity increase, such as hydrogen bonds formed between alcohol containing oxidation products.

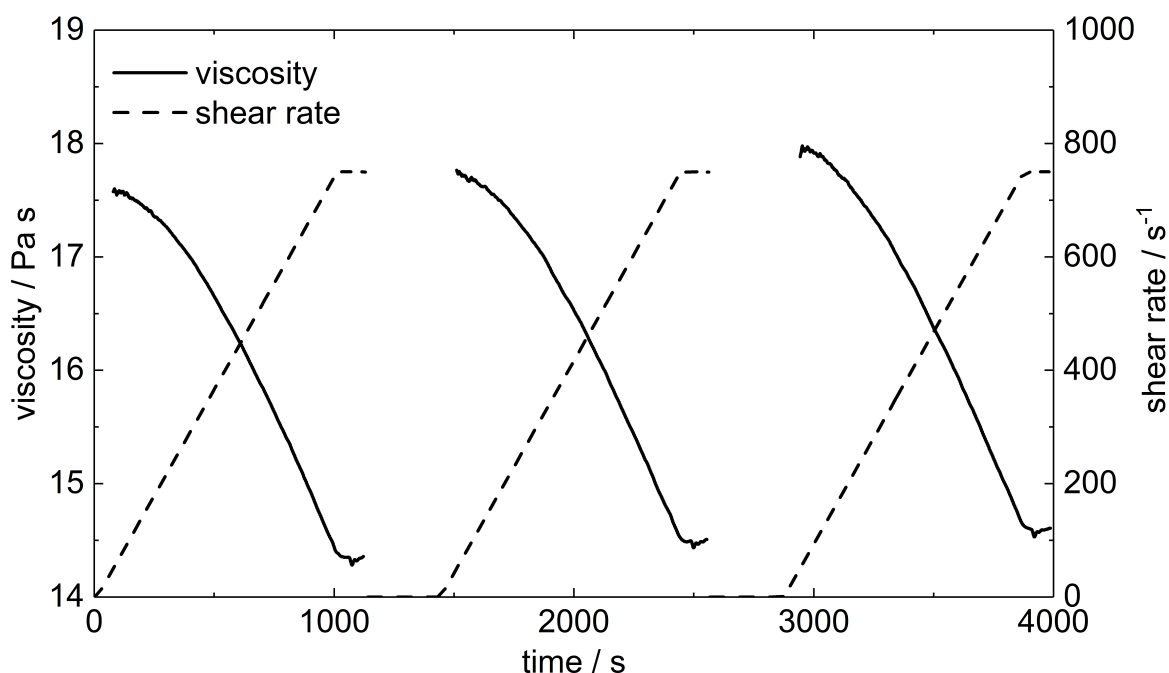


Figure 4.33 – The dynamic viscosity behaviour of *N*-butyl ASI after autoxidation at 170 °C for three hours. Three cycles are shown with shear rates between 50 s⁻¹ and 750 s⁻¹.

4.2.5 ASI autoxidation in a model base oil

The autoxidative stability of two ASIs in a lubricant oil mimic (squalane) was tested at 170 °C using a steel reactor with a continuous oxygen flow following a previously described procedure.⁹⁹ A control experiment of pure squalane oxidised under the same conditions was

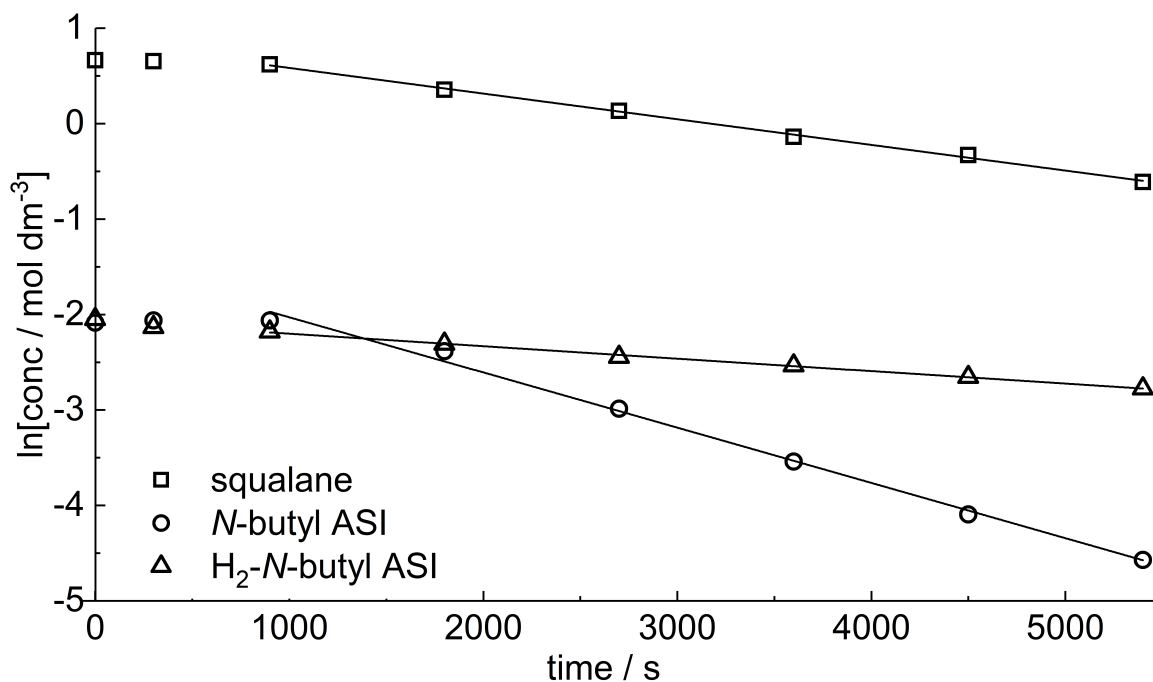


Figure 4.34 – The natural logarithm of squalane, *N*-butyl ASI and H₂-*N*-butyl ASI concentrations during autoxidation at 170 °C. The data for squalane concentrations is from the autoxidation of squalane with no ASI present. Pseudo-first order rate constants were calculated from the linear fit after the 15-minute induction period.

also conducted. The decay rate of both squalane and the ASI dispersant mimic was measured for 5% (w/w) solutions of either *N*-butyl ASI or H₂-*N*-butyl ASI, its hydrogenated analogue, in squalane. The concentrations were representative of dispersants in commercial lubricants⁶ and were monitored by GC-FID, shown in Figure 4.34. By GC-FID, squalane and its degradation products did not coelute with the ASI peak allowing accurate monitoring of their concentration throughout the reaction.

After an induction period of 15 minutes the decay of both ASIs and squalane was approximately first order; to quantify the rates of reaction, pseudo-first order rate constants were calculated (Table 4.34). Volatile species were condensed at 0 °C from the reactor exhaust gases and analysed by GC-MS (See Appendix Section 7.2.3). Squalane and the ASIs were not observed and so losses of these molecules can be solely attributed to autoxidative breakdown, with no significant contribution from evaporative losses.

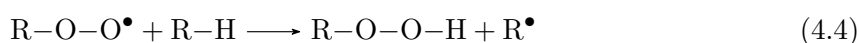
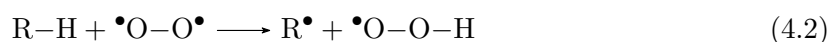
Table 4.11 – The pseudo first order rate constant of squalane, *N*-butyl ASI and H₂-*N*-butyl ASI decay at 170 °C. Ageing experiments were conducted in triplicate from which the average and standard error was calculated.

sample	pseudo-first order rate constant / 10 ⁻⁴ s ⁻¹		
	squalane	<i>N</i> -butyl ASI	H ₂ - <i>N</i> -butyl ASI
squalane	2.79 ± 0.07	-	-
5% (w/w) <i>N</i> -butyl ASI in squalane	2.69 ± 0.05	6.15 ± 0.10	-
5% (w/w) H ₂ - <i>N</i> -butyl ASI in squalane	2.67 ± 0.07	-	1.31 ± 0.06

4.3 Discussion

4.3.1 ASI autoxidation mechanisms

The products observed indicate ASI autoxidation mechanisms are comparable with those observed in hydrocarbon autoxidation^{99,101,104,108–110,161–164} which is initiated by the abstraction of labile hydrogen atoms by molecular oxygen (Reaction 4.2). The resultant carbon-centred radicals (R•) can react with oxygen forming alkyl peroxy radicals (Reaction 4.3).¹⁰¹ These abstract a hydrogen atom from another molecule to form alkyl peroxides and regenerating R• in a chain reaction (Reaction 4.4).¹⁰⁵



The hydroperoxides formed by Reaction 4.4 are the primary non-radical product of hydrocarbon autoxidation however, at the elevated temperatures used in this study, peroxides readily decompose forming hydroxyl and alkoxy radicals (Reaction 4.5).¹⁰⁶



4.3.1.1 Products from alkoxy radical formation

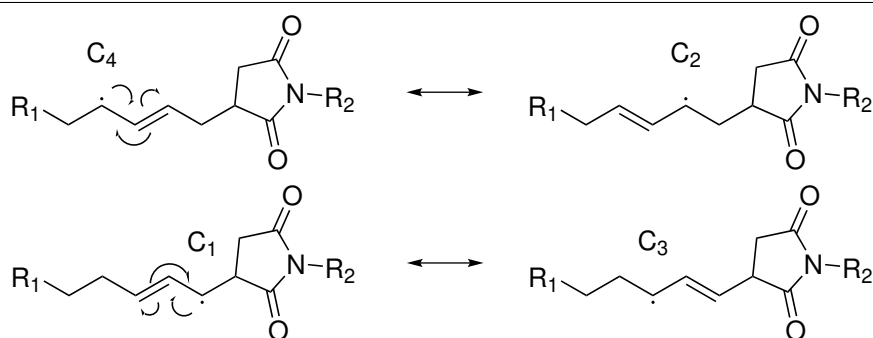
Hydrogen abstraction by alkoxy radicals forms alcohols (Reaction 4.6) while regenerating alkyl radicals as part of the autoxidation chain reaction.



Four isomers of the *N*-butyl ASI alcohol (**10**) were observed and fully characterised in this work. The alcohol within these structures was allylic in nature, positioned at either C₁, C₂, C₃ or C₄ (Figure 4.4). No other alcohol isomers were observed, showing autoxidation was initiated by highly specific abstraction of allylic hydrogens. This can be explained by the C–H bond dissociation enthalpy (BDE), where by a lower BDE due to the higher stability of the formed radical give a higher rate of abstraction.^{164–166} BDE and carbon-centred radical stability increases in the order primary < secondary < tertiary < allylic.¹¹⁶

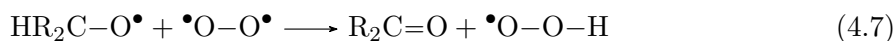
In this work, allylic alcohols were the major products observed from ASI autoxidation which is consistent with allylic hydrogens at C₁ and C₄ (Figure 4.4) being the dominant site of hydrogen abstraction. After abstraction, the resultant radicals at C₁ and C₄ can shift spin density to the C₃ and C₂ positions (Scheme 4.6), as previously observed for the autoxidation of mono-unsaturated lipids.¹⁶⁷ Hence, there are four radical sites to react further; C₁, C₂, C₃ and C₄.

Scheme 4.6 The resonance stabilisation of radicals generated in the C₁ and C₄ positions transferring spin density to the C₃ and C₂ positions respectively.



Via Reactions 4.2, 4.3, 4.4 and 4.5, alkoxy radicals are selectively formed at C₁, C₂, C₃ and C₄ sites. Hydrogen abstraction by alkoxy radicals (Reaction 4.6) forms the corresponding allylic alcohol, which is consistent with the four observed isomers of the *N*-butyl ASI alcohol

(10). The C₄ *N*-butyl ASI ketone (11) can also form through alkoxy radical intermediates.⁹⁹ Abstraction of hydrogen by molecular oxygen from an alkoxy radical in the allylic C₄ could form the ketone and a hydroperoxy radical by Reaction 4.7.



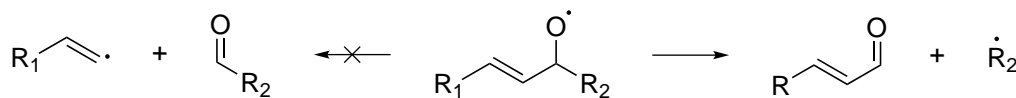
The C₄ *N*-butyl ASI ketone was the only ketone containing product characterised, however its GC peak (11) showed evidence for the co-elution of multiple ketone isomers. From the *N*-butyl ASI alcohol (10), there is evidence for the formation of alkoxy radicals at the C₁, C₂, C₃ and C₄ sites. All alkoxy radical isomers could form the ketone and so the uncharacterised ketone products are likely C₁, C₂ and C₃ ketone isomers.

For the formation of degradation products, the major cleavage mechanism is thought to be α cleavage of alkoxy radicals (Reaction 4.8) and the products observed all resulted from alkoxy radical formation at C₁, C₂, C₃ and C₄ sites.¹⁰⁴



The α cleavage of allylic alkoxy radicals is preferential, cleaving the C-C bond β to the alkene to yield an α,β -unsaturated aldehyde and a comparatively stable alkyl radical, opposed to the less stable vinylic radical from cleavage of the bond α to the alkene (Scheme 4.7).¹⁶⁸

Scheme 4.7 The preferential cleavage of an α,β -unsaturated alkoxy radical.

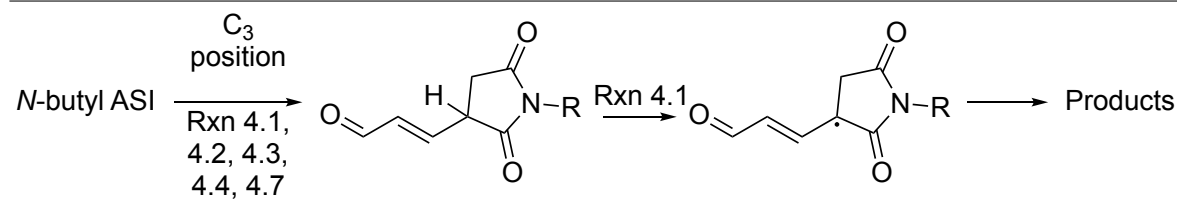


Hydrogen abstraction by the resultant alkyl radical fragment (R_2^\bullet in Scheme 4.7) to yield the corresponding alkane (Reaction 4.9) accounts for the formation of octane (1), nonane (2), *N*-butyl succinimide (4) and 3-methyl, *N*-butyl-succinimide (5).



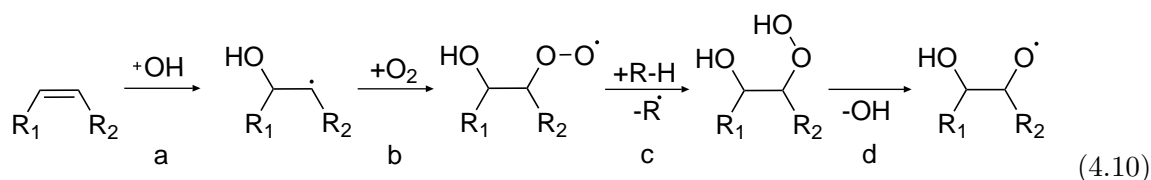
The major primary fragment products observed arose from the α cleavage of C_1 to C_4 alkoxy radicals however, the α,β -unsaturated aldehyde fragment expected to form from α cleavage of a C_3 alkoxy radical (Scheme 4.8) was not observed. The resultant succinimide fragment would contain an allylic tertiary carbon that would have a low C-H BDE, making this species highly reactive to oxidation and therefore it was not observed.

Scheme 4.8 The formation and subsequent degradation of the expected product of alkoxy radical α cleavage at the C_3 position of *N*-butyl ASI.

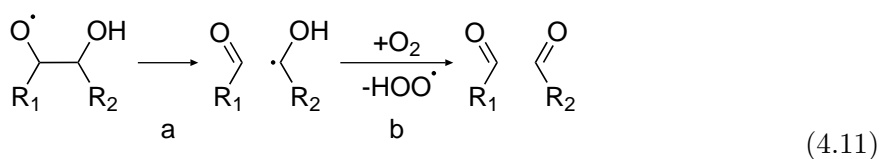


4.3.1.2 Hydroxyl radical addition to the alkene

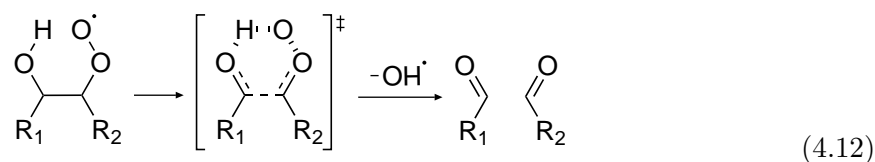
Decanal (**3**), succinimide aldehyde (**8**) and the C_2,C_3 *N*-butyl ASI diol (**15**) cannot be attributed to initial abstraction of allylic hydrogens. Degradation products **3** and **8** represent cleavage across the ASI alkene and the C_2,C_3 *N*-butyl ASI diol (**15**) represents oxidation of the C_2 and C_3 carbons. Their formation is consistent with direct hydroxyl radical ($\bullet\text{OH}$) addition to the alkene. Upon addition of ($\bullet\text{OH}$) to the alkene, a carbon-centred radical is generated α to the newly formed alcohol (Reaction 4.10a). Addition of oxygen to the alkyl radical yields an α -hydroxy peroxy radical (Reaction 4.10b). This species can abstract hydrogen (Reaction 4.10c) and upon homolysis of the resultant peroxide (Reaction 4.10d), an α -hydroxy alkoxy radical is formed.¹⁶⁹



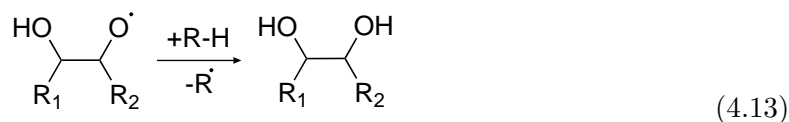
By Reaction 4.11, the α -hydroxy alkoxy radical would yield decanal (**3**) and succinimide aldehyde (**8**) through cleavage.¹⁷⁰



An alternative mechanism for aldehyde formation by $\bullet\text{OH}$ addition to alkenes is possible. The Waddington mechanism (Reaction 4.12) involves the decay of the α -hydroxy peroxy radical through a cyclic six-membered transition state. Simultaneous α -cleavage eliminates a hydroxyl radical yielding two aldehydes.¹⁷¹



Conventional lubricant degradation mechanisms would suggest the formation of carboxylic acids as a major secondary oxidation product, formed via the further oxidation of highly reactive aldehydes to carboxylic acids.⁹⁹ In the later stages of *N*-butyl ASI oxidation, small concentrations of two carboxylic acids were identified. A carboxylic acid containing succinimide and *n*-decanoic acid (peaks **13** and **14** respectively). These are consistent with the oxidation of an aldehyde containing succinimide and decanal (peaks **3** and **8** respectively). The formation of the C_2, C_3 *N*-butyl ASI diol (**15**) can be accounted for by Reaction 4.13 where hydrogen is abstracted by the α -hydroxy alkoxy radical formed in Reaction 4.10.



When *N*-butyl ASI was oxidised both decanal (**3**) and succinimide aldehyde (**8**) were observed in the initial stages of the reaction whereas the C_2, C_3 *N*-butyl ASI diol (**15**) was only observed after 60 minutes. Formation of the diol involves an intermolecular hydrogen abstraction and therefore, to compete with a comparatively rapid cleavage reaction, a source of sufficiently labile hydrogen atoms is required. The delayed formation of the C_2, C_3 *N*-butyl ASI diol (**15**) suggests the hydrogen donated to the α -hydroxy alkoxy radical is unlikely to be donated by

a second equivalent of *N*-butyl ASI. Instead, a source of sufficiently labile hydrogens must accumulate noticeably to compete with decay by fragmentation, such as aldehydes.

4.3.1.3 Recombination

The formation of the *N*-butyl ASI dehydrodimer (**12**) is attributed to recombination of two carbon-centred ASI radicals (Reaction 4.14), a known radical termination mechanism in liquid phase autoxidation of model lubricants.¹⁰⁰ Recombination of any of the four allylic radical isomers would yield 10 different dehydrodimer regioisomers which is consistent with the broad GC peak observed.



The reaction selectivity—the proportion of material reacting via a certain pathway—suggested the formation of high molecular weight and high polarity species, unobservable by GC, to be a major radical termination route (Figure 4.32). However, the concentration of the *N*-butyl ASI dehydrodimer (**12**) plateaued at a low concentration early in the reaction suggesting it reacted further. The tertiary hydrogens of the *N*-butyl ASI dehydrodimer (**12**) are highly labile, promoting rapid further oxidation of the *N*-butyl ASI dehydrodimer (**12**), yielding products of relatively high mass and polarity that would be unobservable by GC.

4.3.1.4 Mechanism overview

This work has found significant evidence that the autoxidation of ASIs is highly specific, reacting only at allylic sites or at the alkene itself. The overall mechanism for the formation of the observed products of ASI autoxidation is shown in Figure 4.35. In summary, all of the observed autoxidation products can be accounted for by chemical mechanisms following from either hydroxyl radical addition to the double bond, or abstraction of the allylic hydrogen atoms adjacent to the double bond, thus demonstrating the controlling influence of the double bond in the degradation of alkenyl succinimides, and by extension, of commercial polyisobutenyl succinimide dispersants. The succinimide group or the long alkane tail do not noticeably contribute to degradation.

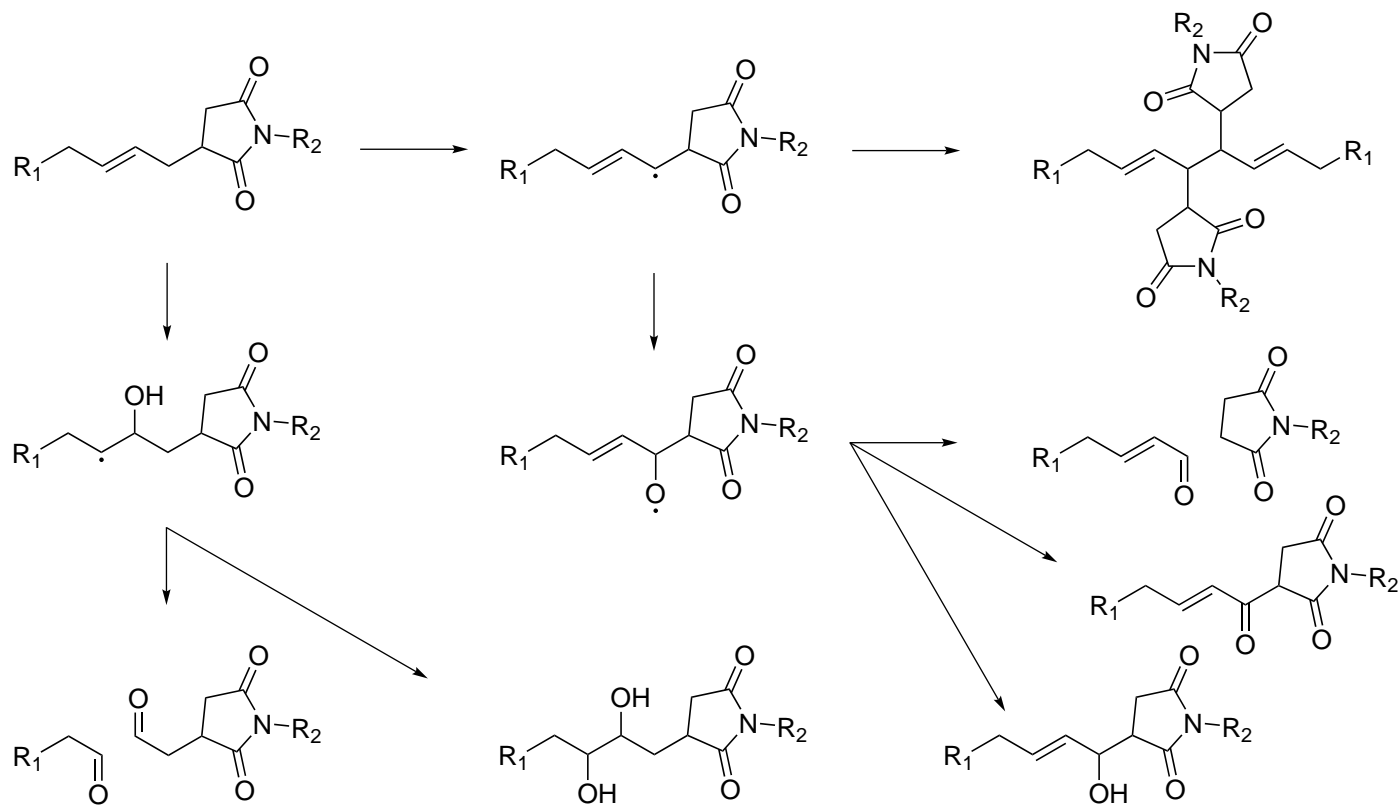


Figure 4.35 – The mechanism for ASI autoxidation showing the three major routes to the thirteen primary products identified of ASI autoxidation.

4.3.1.5 Relative reactivities

The reactivity of *N*-butyl ASI and its hydrogenated analogue, H₂-*N*-butyl ASI, was examined relative to a model base oil, squalane. Both squalane and ASIs followed first order decay when oxidised at 170 °C. Shown in Table 4.11, the pseudo-first order rate constant for the decay of *N*-butyl ASI was 2.3 times higher than that of squalane. Studied previously by Stark *et al.*, squalane primarily reacts by abstraction of hydrogens located on one of the six tertiary carbons.⁹⁹ This work has shown ASIs preferentially react by abstraction of one of four hydrogens at allylic sites. Therefore, ASI allylic hydrogens are approximately 3.5 times more reactive to autoxidative degradation at 170 °C than tertiary hydrogens in a model lubricant.

This means, in real lubricant formulations, the dispersant will decay noticeably quicker than the lubricant base oil. By way of comparison, the induction period for liquid phase autoxidation of *n*-octane, which contains only primary and secondary hydrogen atoms, is approximately twice as long as for 2-methylheptane (one tertiary as well as six secondary hydrogens),¹⁶⁴ which supports the suggestion that a comparatively low proportion of hydrogen atoms with a lower bond strength can have a noticeable effect on the rate of autoxidation of a molecule. To confirm the importance of the alkene in ASI autoxidation, the alkene of *N*-butyl ASI was hydrogenated. After hydrogenation its decay rate constant decreased by 80%, showing the importance of the alkene for dispersant autoxidation and that hydrogenation could be an effective way to improve the oxidative stability of PIBSI dispersants.

4.3.1.6 Viscosity increase

The viscosity of *N*-butyl ASI increased 300-fold after oxidation at 170 °C for three hours, suggesting the formation of high molecular weight and/or high polarity species. This viscosity increase is attributed to the *N*-butyl ASI dehydrodimer and its subsequent autoxidation products; higher polarity species and higher order polymers than the dehydrodimer that were not detectable by GC (Figure 4.32).

The oxidised ASI also showed non-Newtonian behaviour, whereby the viscosity decreased as shear force increased (Figure 4.33). This shear thinning was reversible; when the shear force was stopped for five minutes, the viscosity increased back to its original value. Reversibility

suggests the shear thinning effect was due to breaking intermolecular bonds, such as hydrogen bonds between alcohol groups. Bonds are reformed as the shear force decreases, increasing the viscosity back to the original value. As well as high polarity species, high molecular weight products likely also contribute to the large viscosity increase upon ASI autoxidation.

4.3.1.7 Implications for PIBSI dispersant degradation during use in engine lubricants

When the mechanisms of ASI autoxidation are applied to PIBSI dispersants used in commercial automotive engine lubricants, several significant performance impacts can be inferred. Dispersants are used to solubilise polar oxidation products derived from lubricant autoxidation, known as sludge, and soot from incomplete fuel combustion that would otherwise agglomerate within the lubricant. Soot agglomeration and sludge formation alters the rheology of a fluid. Lubricants with high soot and sludge loading exhibit shear-thinning non-Newtonian behaviour due to shear forces breaking up intermolecularly bonded agglomerates, as was observed for oxidised *N*-butyl ASI. The amphiphilic structure of a PIBSI dispersant aids soot and sludge dispersion which prevents agglomerates from forming. Not only does this give Newtonian rheology, but also mitigates the negative performance impacts of soot and sludge on mechanical wear and fuel economy.¹⁸

The fragmentation of PIBSI dispersants via the α cleavage or hydroxyl radical addition mechanisms demonstrated in this work have severe performance implications. Site-specific cleavage of the polar head group from the apolar tail would render the dispersant ineffective. Not only does this reduce the concentration of active dispersant, but cleavage liberates the polar head group into the lubricant which, being insoluble in the lubricant base oil, would agglomerate and contribute to the sludge formation it is designed to prevent. Therefore, fragmentation would have a significant and detrimental impact on both dispersant performance and lubricant rheology. Recombination of radicals to yield the ASI dehydrodimer, and subsequent reactions to form heavier and more polar species, is suggested to be a significant oxidation pathway for ASI autoxidation and can account for the observed 300-fold viscosity increase at low shear rates.

In a lubricant oil, allylic carbon-centred radicals formed by hydrogen atom abstraction can also self-react to form the ASI dehydrodimer, or react with other carbon-centred radicals,

formed, for example, by hydrogen abstraction from the base oil, to form heavier and often more polar species. Evidence suggests this to be a significant oxidation pathway for bulk ASI oxidation, leading to a viscosity increase which can increase mechanical friction, decrease fuel economy, and increase CO₂ emissions.

The selectivity for the three major decay routes—recombination, oxygenation, and degradation—is likely to be dependent on the lubricant formulation. For instance, a source of labile hydrogens such as a radical scavenging antioxidant (AO) would donate hydrogen atoms to alkoxy and carbon centred PIBSI radicals, limiting their decay by α cleavage and recombination respectively. Through its rapid degradation, the addition of PIBSI dispersants to a lubricant increases its radical forming ability and therefore reduces its lifetime. Formulators can mitigate this by increasing the AO concentration but this would come at an additional cost.

4.4 Conclusion

Alkenyl succinimides (ASIs) have been studied as chemical models for the autoxidation of polyisobutenyl succinimide (PIBSI) dispersants. The initial radical attack was shown to be site specific, either by abstraction of resonance-stabilised allylic hydrogen atoms or hydroxyl radical addition to the alkene. Allylic ASI alcohols, ASI ketones, and seven degradation products were characterised and attributed to alkoxy radical formation. The formation of an ASI diol was attributed to the initial addition of a hydroxyl radical to the alkene and subsequent addition of oxygen, hydrogen abstraction, and hydroxyl radical elimination. This forms a hydroxy-alkoxy radical, which can then abstract a hydrogen atom to form the diol. Two aldehydes can also be accounted for by \bullet OH addition to the alkene followed by α cleavage of the hydroxy-alkoxy radical. The recombination of carbon-centred ASI radicals is thought to be a major product forming route, with high molecular weight products contributing to a 300-fold shear dependent viscosity increase. Allylic ASI hydrogens were found to be 3.5 times more reactive (at 170 °C) than tertiary hydrogens of squalane, a lubricant oil mimic. Degradation of PIBSI dispersants would negatively impact their dispersing performance and PIBSI dehydrodimers would increase lubricant viscosity, harming fuel economy and CO₂ emissions.

Chapter 5

Amine-containing alkenyl succinimide dispersant mimics

5.1 Introduction

Chapter 4 discussed the autoxidation of alkenyl succinimides (ASIs) as chemical mimics for commercial polyisobutenyl succinimide (PIBSI) dispersants. ASIs are a simplified version of PIBSI dispersants, retaining some of the key chemical characteristics such as the succinimide and the alkene, and their relative positions. High ASI purity coupled with an appropriate molecular weight allowed the autoxidation mechanisms and products of ASIs to be determined through product studies. *N*-butyl ASI (Figure 5.1) was the main structure studied.

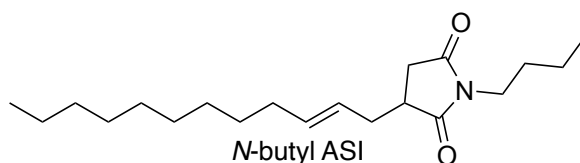


Figure 5.1 – *N*-butyl ASI, the main dispersant mimic studied in Chapter 4.

The focus of the study in Chapter 4 and its associated publication was on the succinimide and alkene structures within PIBSI dispersants.¹¹⁷ The polyethylene amine hydrophile attached to the succinimide nitrogen was simplified to an *n*-alkyl chain as it was assumed the aminic nitrogens would not be significantly reactive. This allowed an oil-soluble & low mass mimic to be readily synthesised at high enough purity for product studies. This approach allowed thorough characterisation of ASI autoxidation products, giving insights into reaction mechanisms. It was determined that the autoxidation of alkyl ASIs was dominated by reactions at the alkene and allylic sites.

In this chapter, the model was expanded to cover four new ASIs containing aminic hydrophiles, known as amino ASIs, shown in Figure 5.2. They contain the same alkenyl tail and succinimide linker as before but the head group has an aliphatic aminic nitrogen. This brings the ASI model closer to commercial PIBSI dispersants that rely on alkyl tails for oil-solubility and aminic head groups for soot-binding ability, connected by a succinimide.

The structures diethylamino alkenyl succinimide (DEA-ASI) and dimethylamino alkenyl succinimide (DMA-ASI) contained a single tertiary amine with either two ethyl or two methyl groups attached respectively. This was done to assess the impact of tertiary amines and the impact of hydrogens α to aminic nitrogens. Hydrogenated DMA-ASI (H₂-DMA-ASI) was used to assess the impact of the alkene on autoxidation. Finally, monomethylamino alkenyl succinimide (MMA-ASI) was used to investigate the effect of the

secondary aminic N–H. This chapter is an investigation into the autoxidation of amino ASIs in model lubricants and the performance of DEA-ASI in two industry-standard oxidation tests.

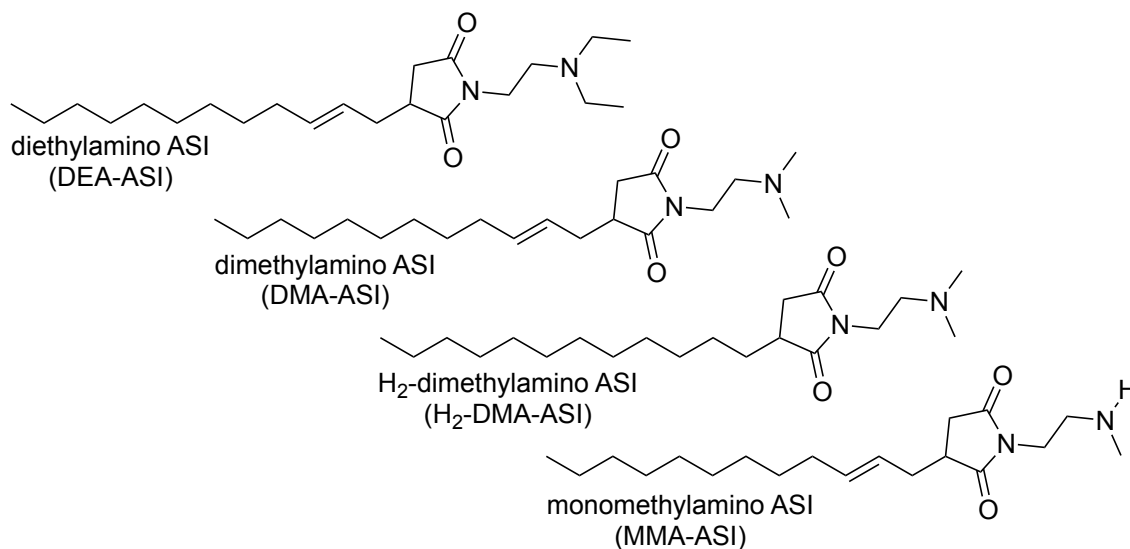


Figure 5.2 – The amine-containing ASIs studied in this chapter—diethylamino ASI (DEA-ASI), dimethylamino ASI (DMA-ASI), H₂-dimethylamino ASI (H₂-DMA-ASI) and monomethylamino ASI (MMA-ASI).

5.2 Results

5.2.1 Amino ASI autoxidation in a model lubricant

The autoxidation of three amino ASIs was investigated in a model lubricant where the ASI was dissolved in a model base oil (squalane, Figure 5.3). This followed the same procedure used in Chapter 4. A 5% (w/w) solution of the ASI in squalane, a base oil mimic, was injected to a steel reaction vessel held at 170 °C. The solution was held at this temperature, with stirring and under a flow of pure oxygen, for 90 minutes and samples were taken at regular intervals.

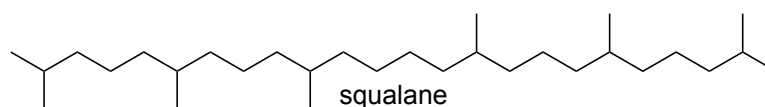


Figure 5.3 – 2,6,10,15,19,23-Hexamethyltetracosane (squalane, C₃₀H₆₂), the model base oil used in this study.

One procedural change was made for the oxidation of MMA-ASI. Due to its insufficient solubility in squalane at room temperature, the mixture was pre-heated to 80 °C to yield a clear and homogenous solution prior to its injection into the reactor. The low solubility of MMA-ASI also prevented its reliable quantification by gas chromatography - flame ionisation detector (GC-FID).

The concentration of oxygen in the exhaust gases was measured during the reaction, as described in Chapter 2 (Page 49). Samples of the lubricant taken throughout the reaction were analysed by GC-FID to determine the concentration of squalane and the amino ASIs. Oxidation products of the amino ASI were characterised using high resolution gas chromatography - electron ionisation - mass spectrometry (GC-EI-MS).

5.2.1.1 Oxygen consumption

During the autoxidation reaction, oxygen was flowed across the stirred substrate held at 170 °C for 90 minutes. After passing through a cold trap and scrubbing to remove hydrocarbon soluble compounds, the concentration of oxygen in the exhaust gas was measured. During autoxidation the concentration of oxygen in the exhaust gases decreases due to the production of other gases, namely CO and CO₂. From the decrease in oxygen concentration, the quantity of oxygen consumed can be estimated, as described in the experimental section (section 2.4.7 page 49). As a benchmark, when 5% *N*-butyl ASI was oxidised in squalane, the amount of oxygen consumed was approximately the same as when pure squalane was oxidised (Figure 5.4).

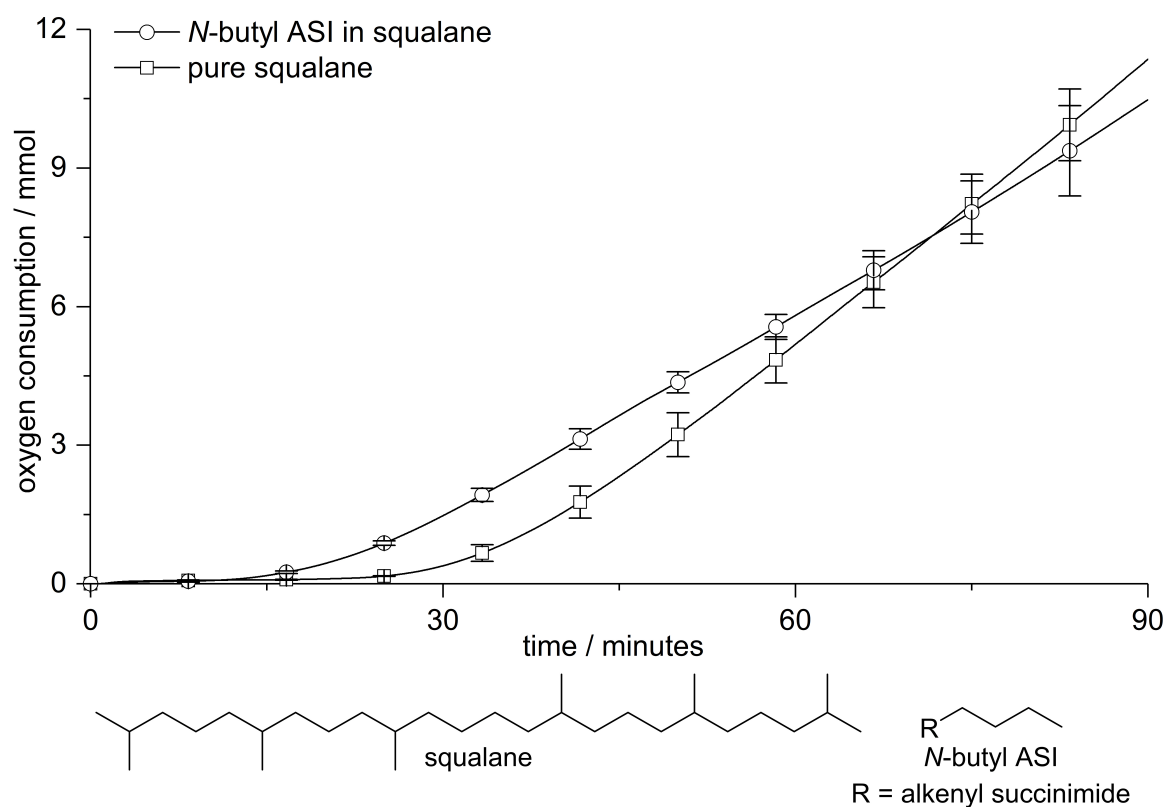


Figure 5.4 – Oxygen consumption from the autoxidation of squalane and a 5% (w/w) solution of *N*-butyl ASI in squalane at 170 °C for 90 minutes. The data are an average of three experiments with error bars of one standard deviation.

When amino ASIs were oxidised in squalane, different behaviour was observed. Shown by Figure 5.5, amino ASIs reduced oxygen consumption and that reduction of oxygen consumption was dependent on the amine structure. The secondary-amine-containing MMA-ASI showed oxygen was consumed after 30 minutes, like with pure squalane, but the amount of oxygen consumed was nearly a third of the value for pure squalane. The tertiary-amine-containing DMA-ASI showed a low level of oxygen was consumed from the start of the reaction. This low level was maintained for the whole 90 minutes, ultimately reaching a tenth of the level observed for pure squalane. When DEA-ASI was used, no measurable oxygen was consumed for the duration of the 90 minute reaction.

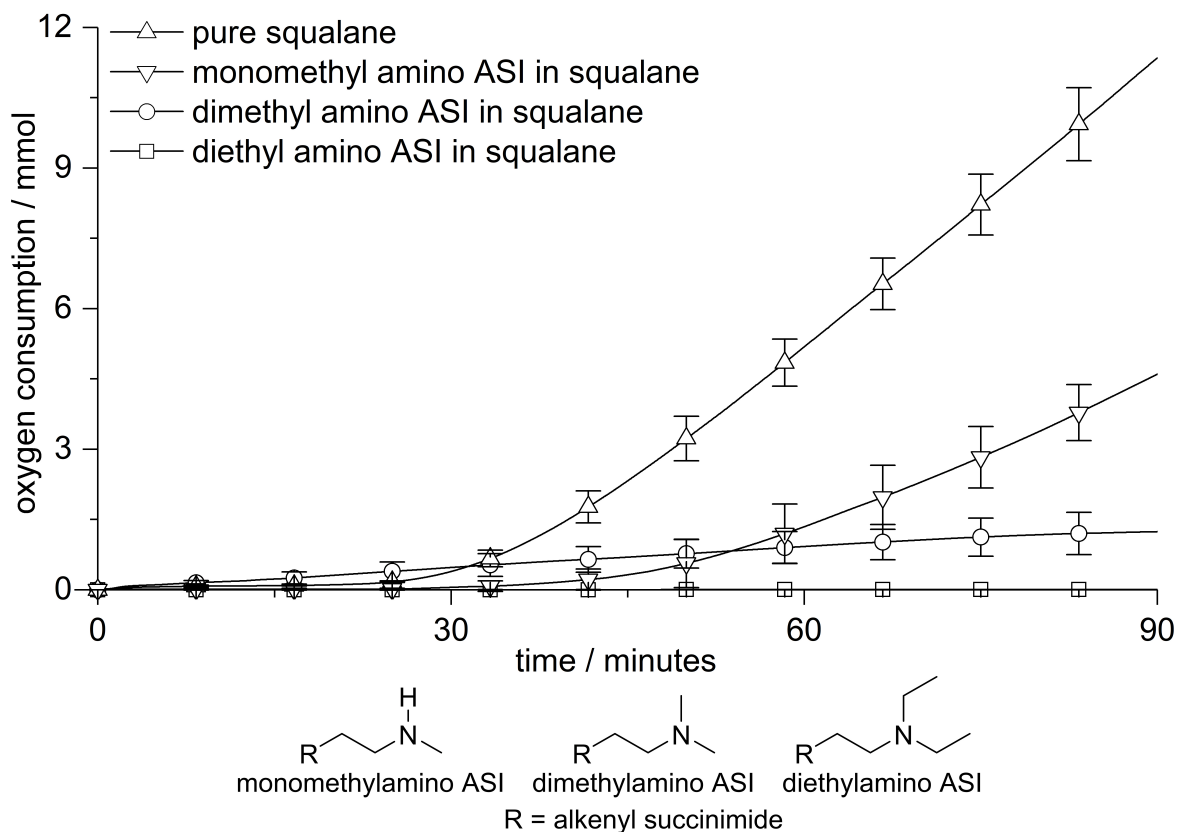


Figure 5.5 – Oxygen consumption from the autoxidation of squalane and 5% (w/w) solutions of three amino ASIs (MMA-ASI, DMA-ASI and DEA-ASI) in squalane oxidised at 170 °C for 90 minutes. The data shown are an average of three experiments with error bars of one standard deviation.

To test the effect of the alkene, which was previously shown to be crucial for ASI autoxidation, the alkene of DMA-ASI was hydrogenated to yield H₂-dimethylamino ASI (H₂-DMA-ASI, Figure 5.2, Page 133). When this was oxidised in squalane, there was no measured oxygen consumption for the duration of the reaction (Figure 5.6). This contrasts the low level of oxygen consumed during DMA-ASI autoxidation.

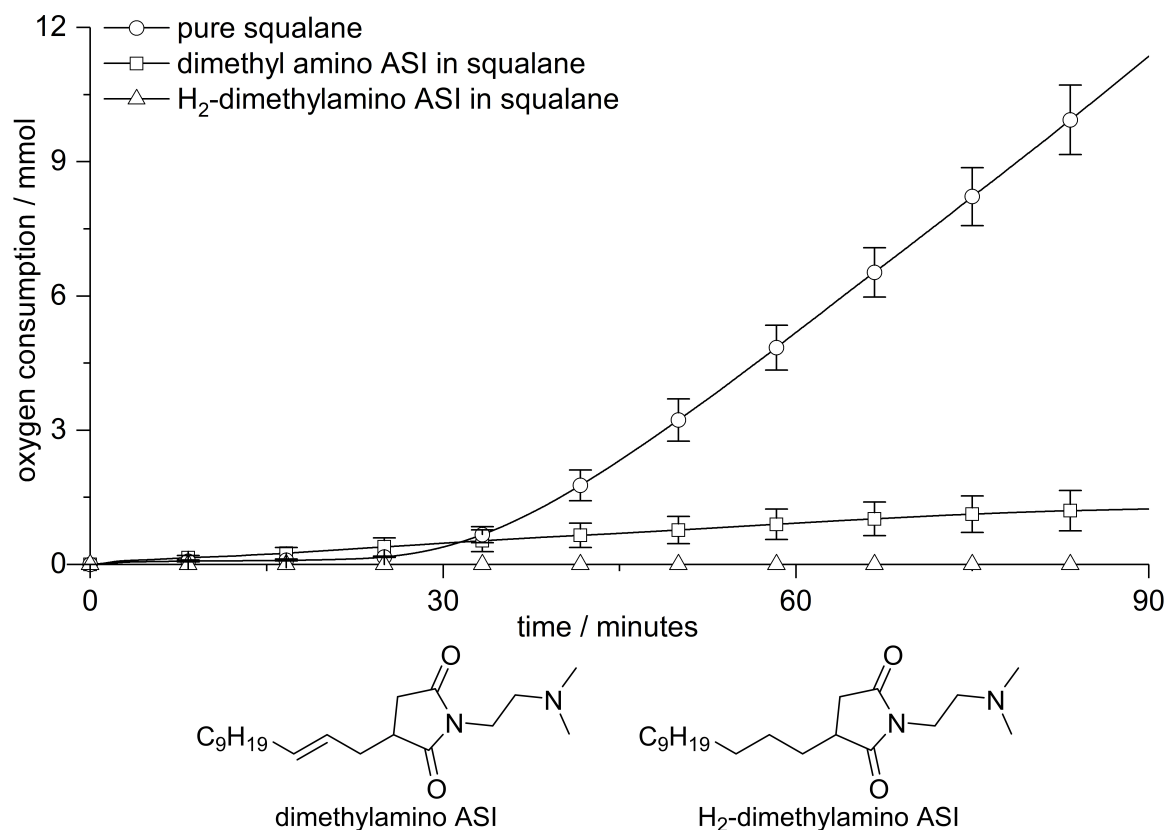


Figure 5.6 – Oxygen consumption from the autoxidation of squalane and 5% (w/w) solutions of DMA-ASI and H₂-DMA-ASI in squalane oxidised at 170 °C for 90 minutes. The data shown are an average of three experiments with error bars of one standard deviation except for H₂-DMA-ASI which is from a single experiment.

The oxygen consumption data suggests incorporating amines in the ASI structure imparts antioxidant functionality to the ASI. The strength of antioxidant functionality was dependent on the structure. The more hindered the amine, the stronger the antioxidant effect. Alkene hydrogenation further reduced the level of oxygen consumption.

5.2.1.2 GC-FID

Samples were taken throughout the autoxidation of the model lubricants for analysis by GC-FID. By comparing these with a chromatogram from the autoxidation of pure squalane, significant differences can be observed. Chromatograms from samples collected after 90 minutes of autoxidation at 170 °C are shown in Figure 5.7. For comparison, results from pure squalane are also shown (Figure 5.7 A). In the autoxidation of pure squalane, large

concentrations of oxidation products can be clearly seen. At a higher GC retention time, squalane alcohols can be seen and at lower retention times, fragment alkanes, alkenes, ketones and lactones are present.⁹⁹ When amino ASIs DEA-ASI or DMA-ASI were present (Figure 5.7 B and C respectively) at 5% (w/w) concentrations, squalane degradation products were highly suppressed. The same was true when H₂-DMA-ASI was oxidised (Figure 5.8 B). When MMA-ASI was oxidised (Figure 5.8 C), significant amounts of squalane degradation products were observed.

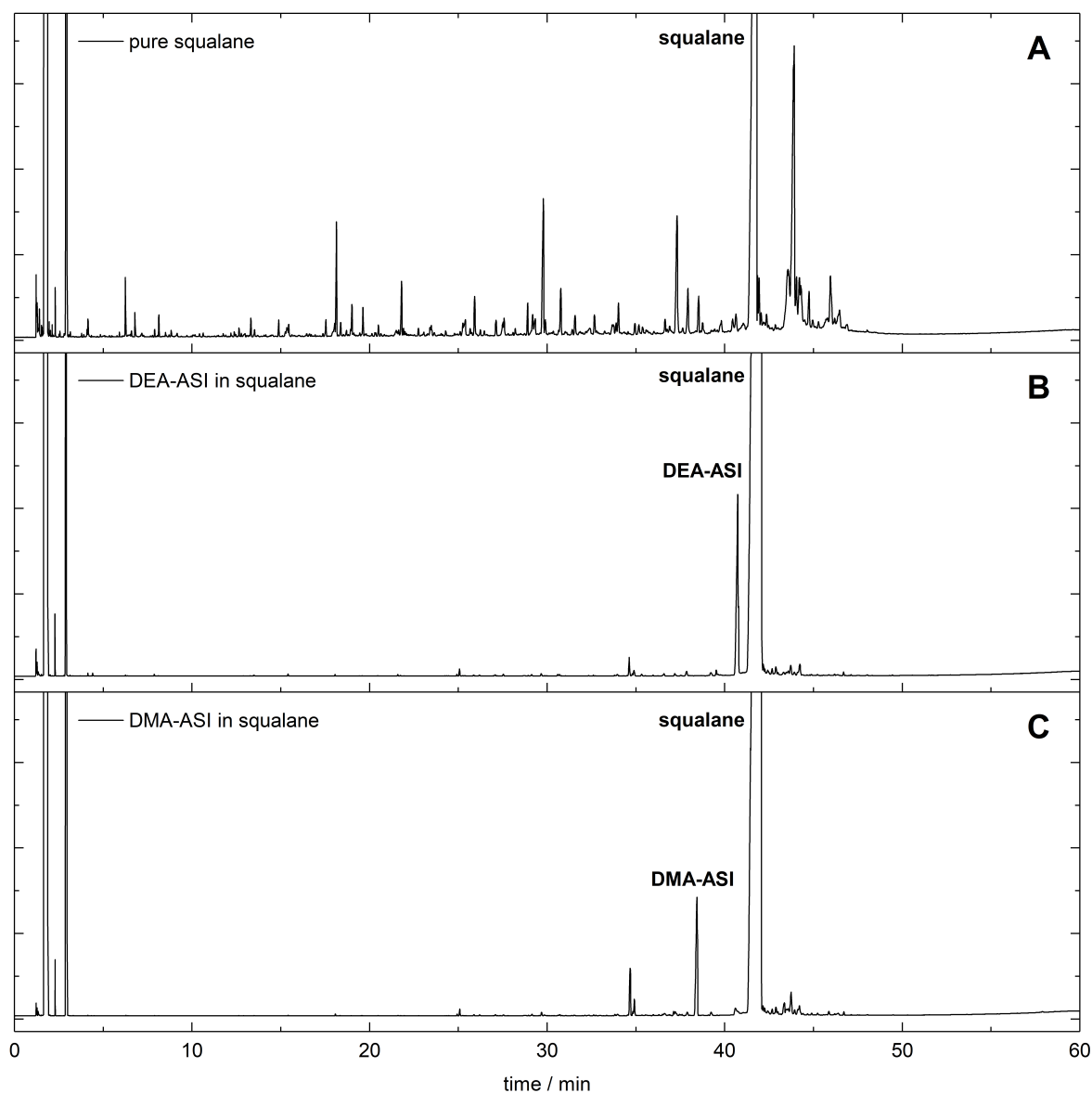


Figure 5.7 – GC-FID traces of model lubricants oxidised for 90 minutes at 170 °C. The figure shows the 90 minute traces for pure squalane (top), 5% (w/w) DEA-ASI in squalane (middle) and 5% (w/w) DMA-ASI in squalane (bottom). Samples were analysed at the same concentration and are presented at the same scale to allow visual, qualitative, comparison.

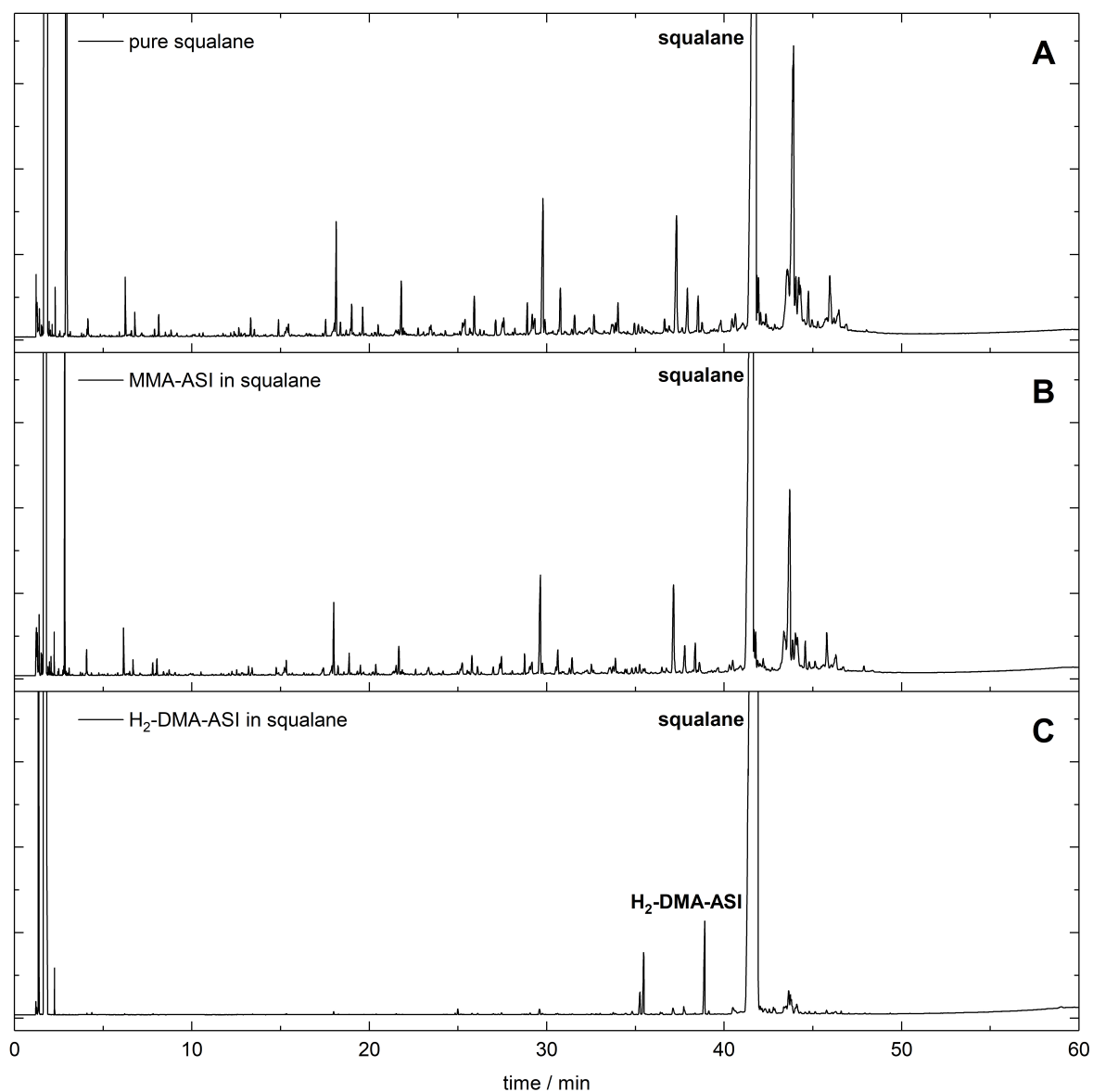


Figure 5.8 – GC-FID traces of model lubricants oxidised for 90 minutes at 170 °C. The figure shows the 90 minute traces for pure squalane (top), 5% (w/w) MMA-ASI in squalane (middle) and 5% (w/w) H₂-DMA-ASI in squalane (bottom). Samples were analysed at the same concentration and are presented at the same scale to allow visual, qualitative, comparison.

From the GC-FID, the concentrations of both squalane and the amino ASIs could be monitored. Figure 5.9 shows the concentration of DMA-ASI and DEA-ASI during autoxidation. The data for *N*-butyl ASI from Chapter 4 is also shown for comparison. The concentration of MMA-ASI could not be accurately monitored by GC-FID due to the poor solubility of MMA-ASI in squalane giving unreliable quantitation.

The concentration of the reference compound, *N*-butyl ASI, remained constant for the first 15 minutes before decreasing for the rest of the 90 minute reaction, reaching a final concentration of approximately 10% of its initial value. In contrast to this, the concentration of DMA-ASI decreased at a slow and steady rate from the start of the reaction reaching approximately half its initial value. The concentration of the diethyl analogue, DEA-ASI, remained unchanged for the duration of the reaction, within the error for the measurement.

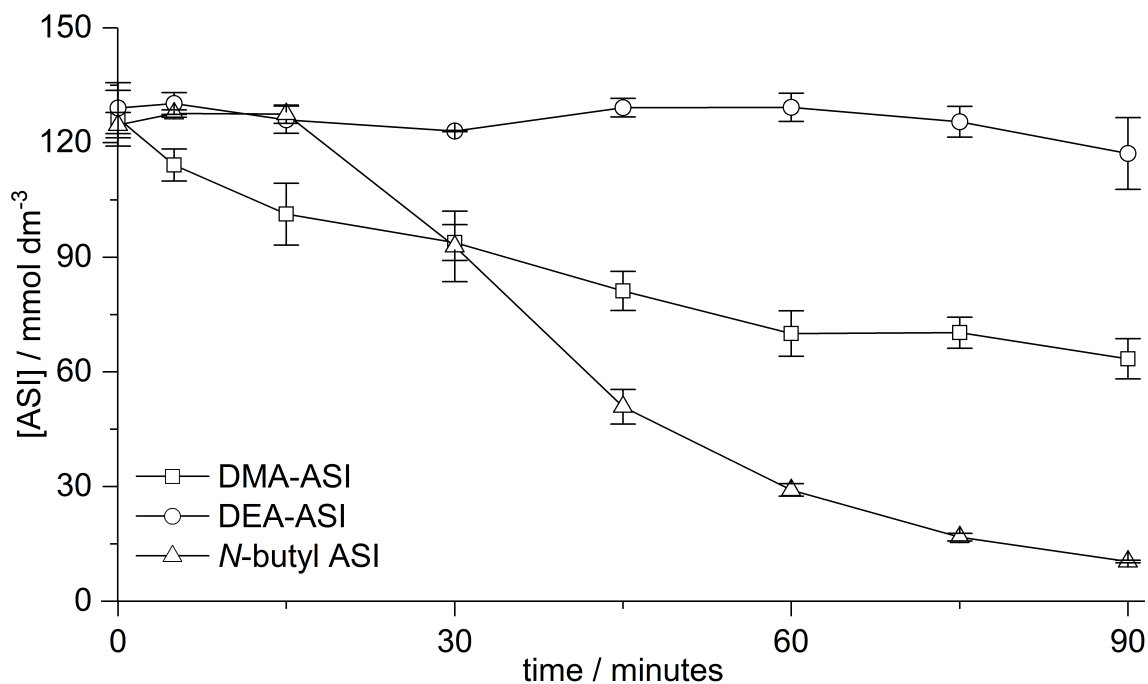


Figure 5.9 – The concentrations of DMA-ASI and DEA-ASI during the autoxidation of a 5% amino ASI solution in squalane at 170 °C for 90 minutes. The trend for *N*-butyl ASI (from Chapter 4) is shown for comparison. MMA-ASI could not be reliably quantified due to solubility issues. Experiments were conducted in triplicate from which averages and standard errors were calculated.

Figure 5.10 shows the concentration of squalane throughout the autoxidation of the model lubricants. The concentration of squalane oxidised without an ASI present is also shown. The squalane concentration remained constant within error for the first 15 minutes, before steadily decaying for the rest of the reaction to approximately 10% of its initial value. This mirrored the behaviour of *N*-butyl ASI shown in Figure 5.9.

The concentration of squalane during the reaction with MMA-ASI was monitored and this showed similar behaviour to the autoxidation of pure squalane. The concentration of squalane during the reaction with DMA-ASI and DEA-ASI present showed little change from its value at the start of the reaction.

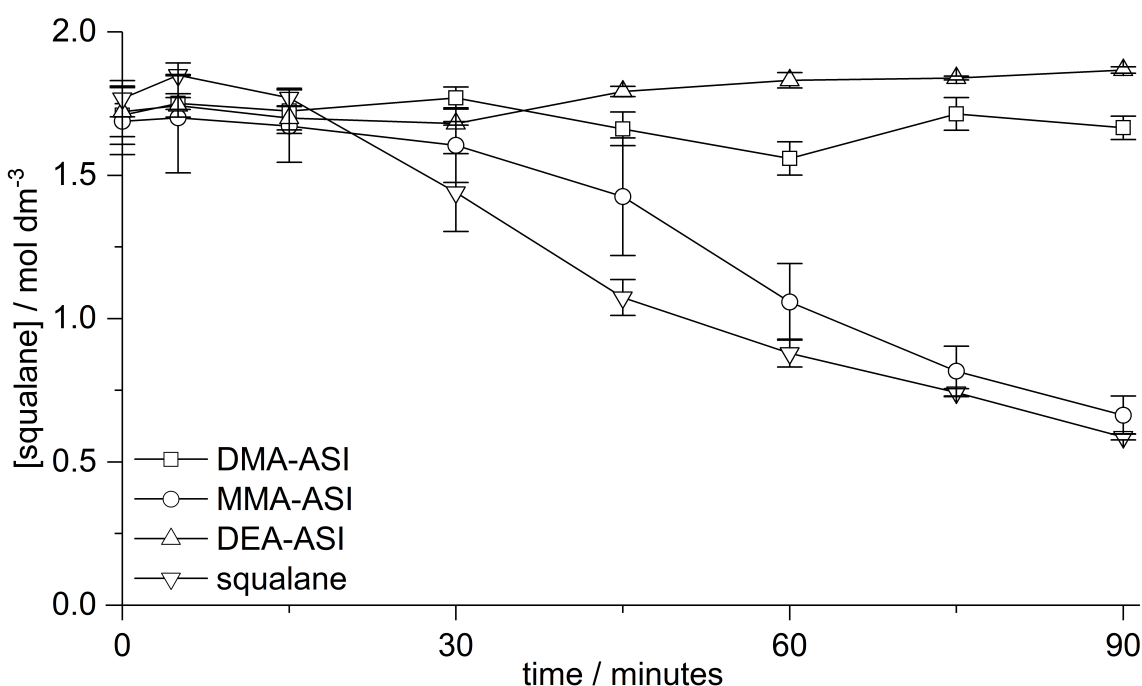


Figure 5.10 – The concentration of squalane during the autoxidation of a 5% solution of amino ASI in squalane at 170 °C for 90 minutes. The trend for the autoxidation of pure squalane is also shown for comparison. Experiments were conducted in triplicate from which averages and standard errors were calculated.

A single experiment was conducted where H₂-DMA-ASI was oxidised as a 5% (w/w) solution in squalane following the same procedure and analysed by GC-FID. Figure 5.11 shows the concentration of H₂-DMA ASI as well as DMA-ASI. Compared to the alkene containing DMA-ASI, H₂-DMA ASI decayed more rapidly. Figure 5.12 shows the trend for squalane concentration where both DMA-ASI and H₂-DMA ASI showed similar behaviour with no significant change in squalane concentration.

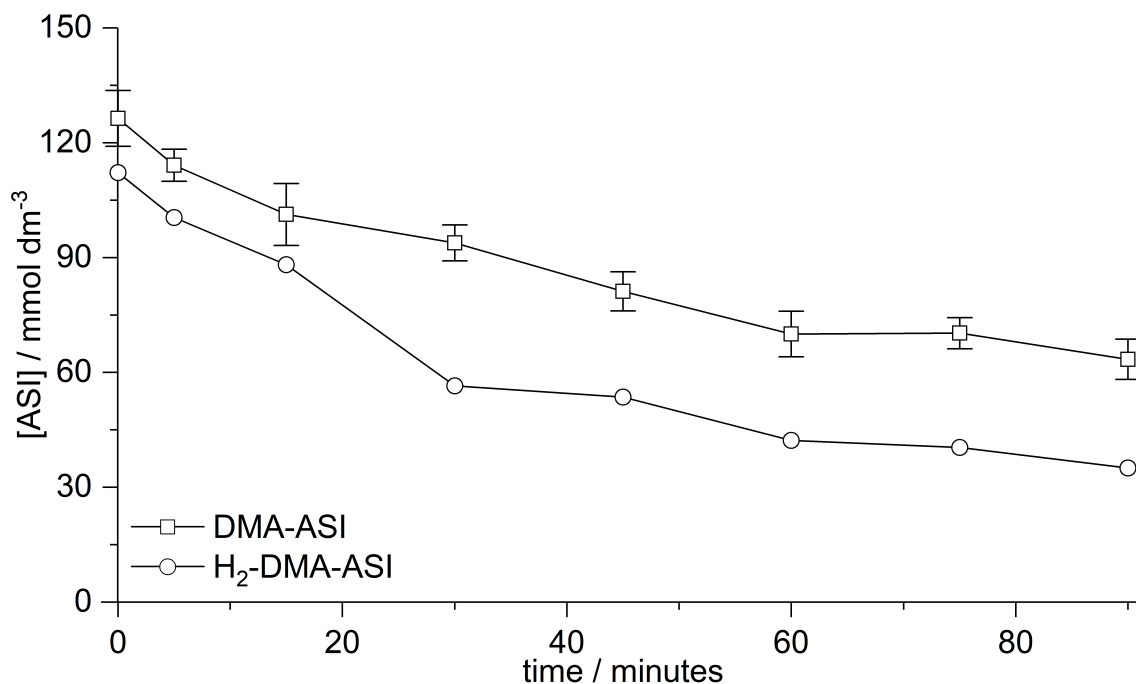


Figure 5.11 – The concentrations of DMA-ASI and H₂-DMA-ASI during the autoxidation of a 5% amino ASI solution in squalane at 170 °C for 90 minutes. The autoxidation of DMA-ASI was conducted in triplicate from which averages and standard errors were calculated. Data for H₂-DMA-ASI was collected from a single experiment.

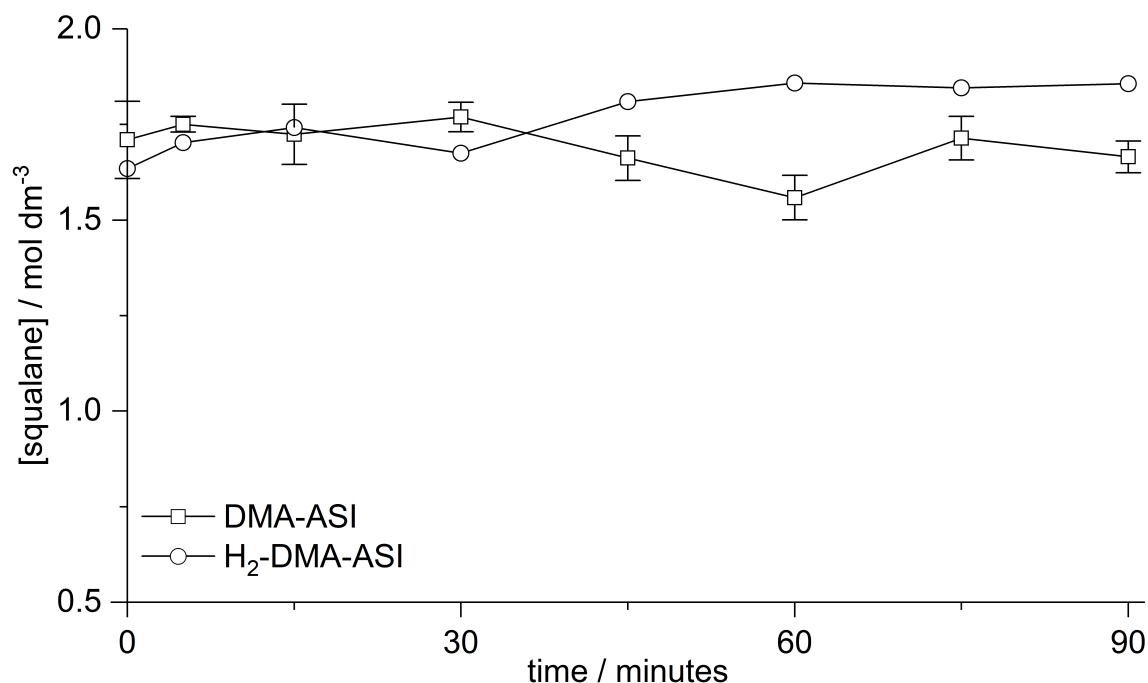


Figure 5.12 – The concentration of squalane during the autoxidation of a 5% amino ASI solution in squalane at 170 °C for 90 minutes. The autoxidation of DMA-ASI was conducted in triplicate from which averages and standard errors were calculated. Data for H₂-DMA-ASI was collected from a single experiment.

5.2.1.3 Amino ASI autoxidation products

When DMA-ASI and DEA-ASI were oxidised, they decayed via highly selective pathways to yield two common and identifiable autoxidation products. When H₂-DMA-ASI was oxidised, it also selectively decayed, yielding two autoxidation products that were related to those observed for DMA- and DEA-ASI. As shown in Figure 5.13, all four of these products had GC retention times in the same region as, but slightly lower than, the parent amino ASI.

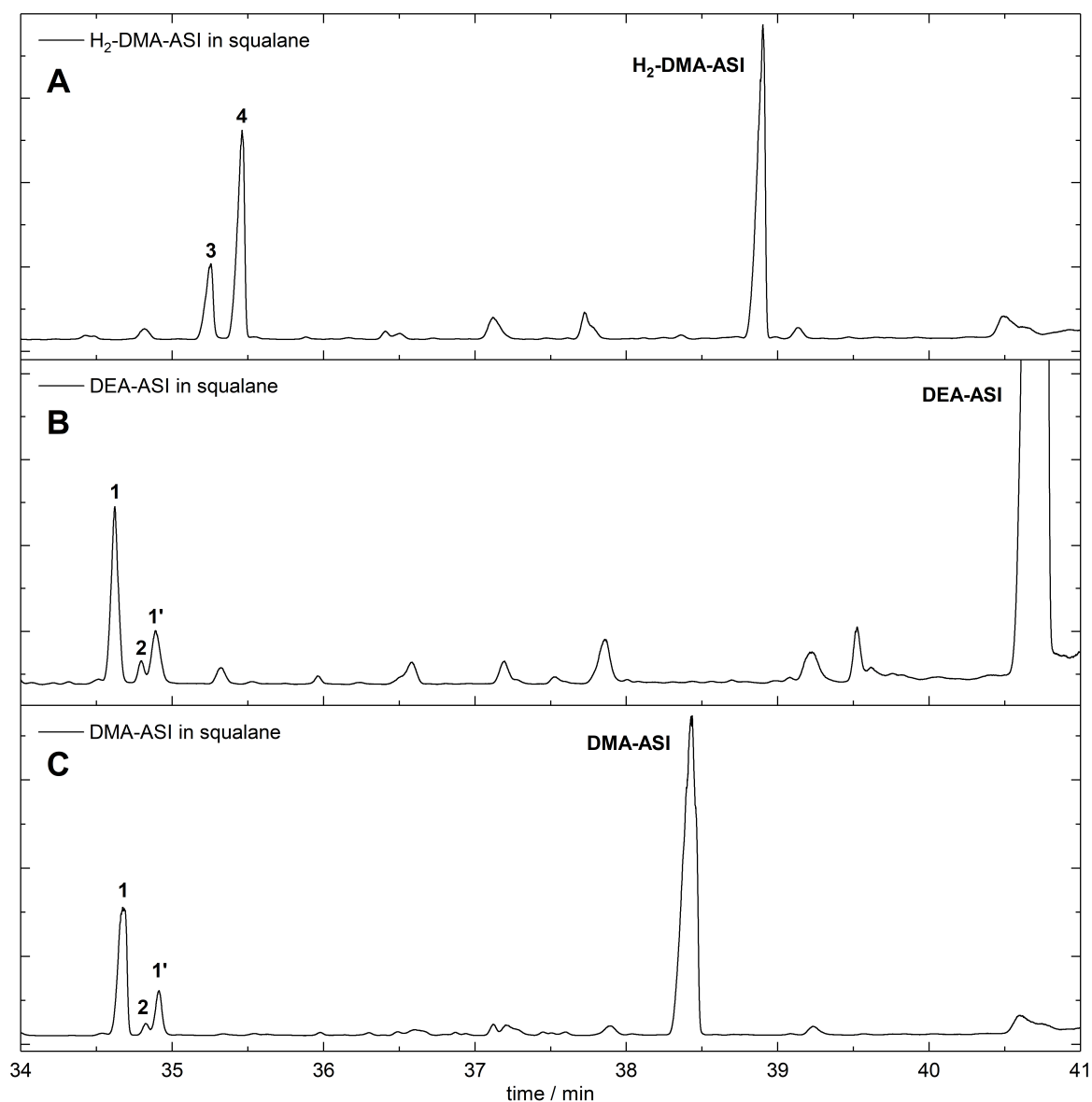


Figure 5.13 – A zoomed view of the chromatograms in Figures 5.7 and 5.8 (pages 138 and 139) showing the four major amino ASI autoxidation products, 1/1', 2, 3 and 4.

Alkene-containing ASIs (DMA- and DEA-ASI) produced two major products. **1** and **1'** which were alkene isomers and product **2**. These products had the same retention times regardless of their parent ASI structure. H₂-DMA-ASI yielded two products (**3** and **4**) which had retention times slightly higher than products **1/1'** and **2**. The four products did not correspond to any of the alkyl ASI degradation products observed in Chapter 4, suggesting they resulted from reactions at the amine.

The degradation products were characterised using high resolution GC-EI-MS. Prior to analysis, unreacted squalane was removed using a silica micro-column to protect the mass spectrometry (MS) equipment. The chemical formula of the peaks was calculated from the observed molecular ion and is shown in Table 5.1. Data from DMA-ASI showed compounds **1** and **1'** had the same mass ion with a composition of C₁₈H₂₉NO₂. Despite the GC-FID suggesting DEA-ASI was not consumed, the same peaks were observed for DEA-ASI, albeit at a lower intensity. Two peaks, representing the two alkene isomers, were observed because the amino-ASIs could not be purified to yield single isomers (unlike the alkyl ASIs used in Chapter 4).

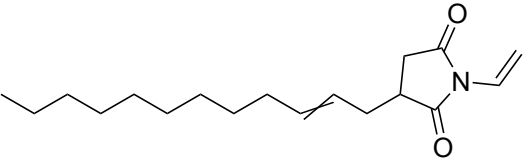
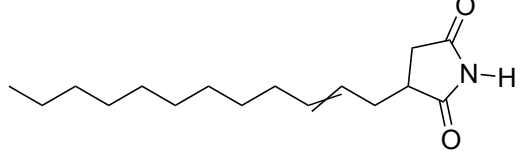
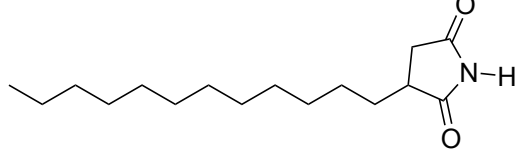
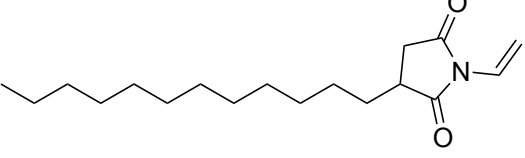
A single peak (**4**) with the mass of peak **1** plus two daltons was observed for the hydrogenated analogue H₂-DMA-ASI, suggesting an analogous structure and that the hydrocarbon tail was present and intact in products **1/1'** and **4**. This chemical formula, and the observation of the same degradation products for both DMA-ASI and DEA-ASI, suggests the product forms by loss of the aminic nitrogen and its attached carbon chains. With a ring double bond equivalents (RDBE) value¹⁵⁹ of five, the only plausible structures for peaks **1**, **1'** and **4** are the structures shown in Table 5.2 with an alkene having formed α to the succinimide nitrogen. Product **1** is likely the *trans* alkene isomer due to its higher concentration in the starting material, however this cannot be confirmed by GC-EI-MS.

Product **2** had a chemical formula of C₁₆H₂₇NO₂ and this was identical for DMA-ASI and DEA-ASI. The product from the hydrogenated analogue, product **3**, had the same formula plus two hydrogens, indicating the presence of the intact alkyl tail in the structure. Product **2** has a RDBE value of 4, and product **3** has a value of 3. The products likely formed by reaction at the aminic head group. To yield a structure of the appropriate formula, the whole head group must be cleaved at the succinimide nitrogen, leaving a single hydrogen in its place, as shown in Table 5.2. Only a single alkene isomer of product **2** was observed, likely due to its low concentration.

Table 5.1 – Accurate mass data for amino ASI degradation products **1**, **1'**, **2**, **3** and **4**.

Peak	m/z (measured)	m/z (calculated)	Mass accuracy / ppm	Chemical Formula
1	291.21701	291.21983	-7.8	C ₁₈ H ₂₉ NO ₂
1'	291.21656	291.21983	-9.4	C ₁₈ H ₂₉ NO ₂
2	265.20046	265.20418	-12.0	C ₁₆ H ₂₇ NO ₂
3	267.21542	267.21983	-16.5	C ₁₆ H ₂₉ NO ₂
4	293.22986	293.23548	-17.3	C ₁₈ H ₃₁ NO ₂

Table 5.2 – The structures of compounds **1/1'**, **2**, **3** and **4**.

Peak	formula	structure
1/1'	C ₁₈ H ₂₉ NO ₂	
2	C ₁₆ H ₂₇ NO ₂	
3	C ₁₆ H ₂₉ NO ₂	
4	C ₁₈ H ₃₁ NO ₂	

The degradation products were quantified using GC-FID. Due to their analogous structures, products **1**, **1'** and **4** likely formed by the same reaction mechanism—the same can be said for products **2** and **3**. The compounds are grouped together as such.

Figure 5.14 shows the concentrations of **1** and **4** throughout the 90 minute autoxidation at 170 °C. **1** and **4** were produced in the same quantities, up to 24 mmol dm⁻³, for DMA-ASI and H₂-DMA-ASI suggesting the alkene played no part in its formation. DEA-ASI produced just 3 mmol dm⁻³ of **1**. The data from DMA-ASI had sufficient signal to noise to allow calculation of selectivity for the formation of product **1/1'**. Averaged over the 90 minutes, the proportion of decayed DMA-ASI reacting to form **1/1'** was 37±2%, which is remarkably high selectivity for an autoxidative degradation product.

Figure 5.15 shows the concentration of **1'** for DMA- and DEA-ASI. **1'** started at a non-zero concentration (2 mmol dm^{-3}) due to co-elution with an impurity in squalane and therefore absolute concentrations are unreliable. However, the difference between DMA- and DEA-ASI can be observed with DMA-ASI producing significant quantities (6 mmol dm^{-3}) of **1'**, whereas DEA-ASI produced a negligible quantity of **1'**.

Figure 5.16 shows the concentrations of **2** and **3**. As with the other products, DMA-ASI produced more (2 mmol dm^{-3}) of **2** than DEA-ASI (0.5 mmol dm^{-3}). Interestingly, the hydrogenated analogue H₂-DMA-ASI produced far higher concentrations of **3** (11 mmol dm^{-3}) compared to the production of **2** by the alkene-containing DMA-ASI. This suggests alkene functionality can play a role in the formation of product **2**.

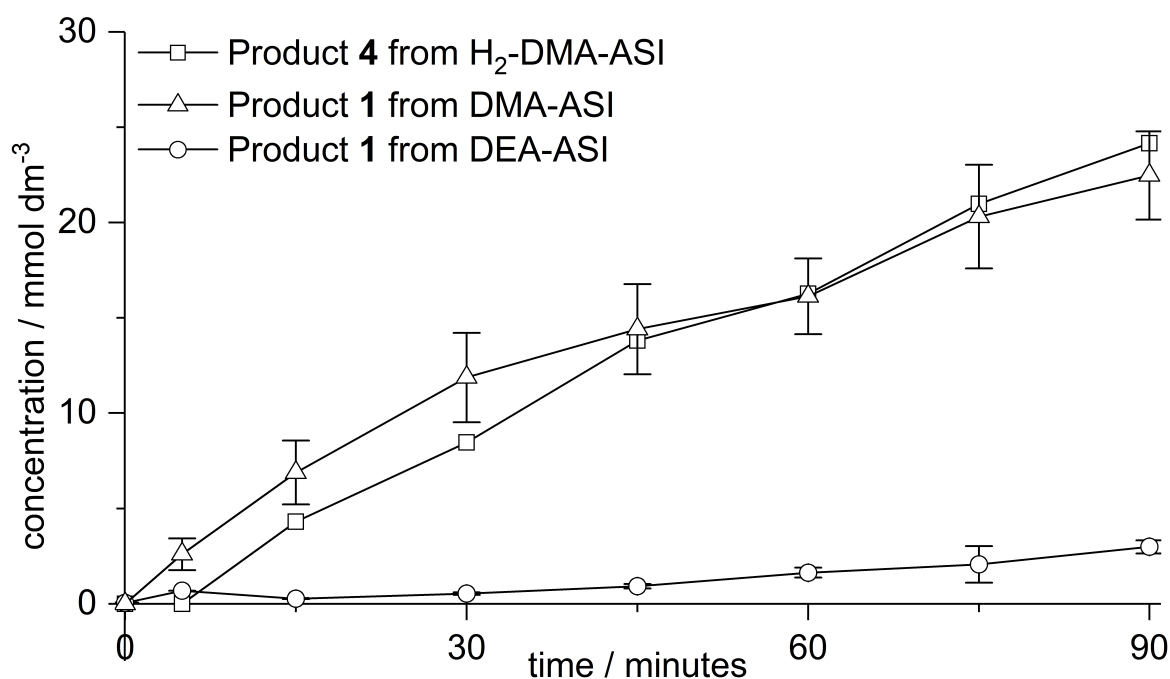


Figure 5.14 – The concentrations of products **1** and **4** during the autoxidation of alkyl ASIs (DMA-, DEA-, and H₂-DMA-ASI) as a 5% (w/w) solution in squalane. Values for DMA-ASI and DEA-ASI are averages of triplicate data with standard error bars shown. H₂-DMA-ASI data is from a single experiment.

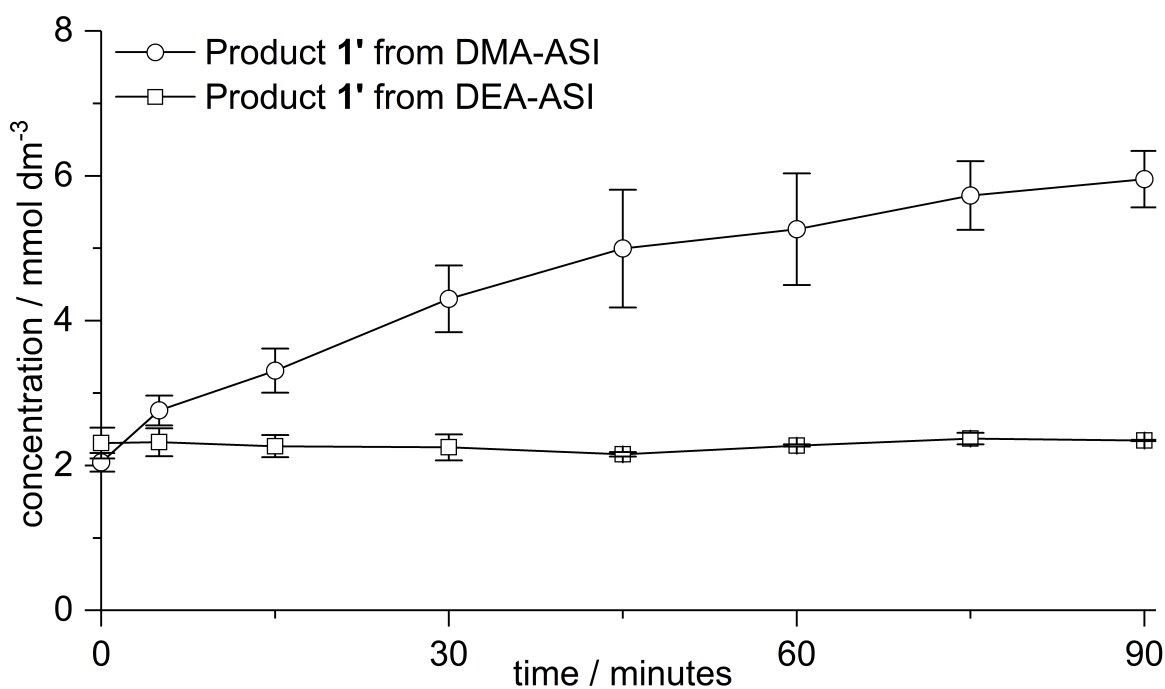


Figure 5.15 – The concentration of product 1' during the autoxidation of DMA-ASI and DEA-ASI as 5% (w/w) solutions in squalane. Values are averages of triplicate data with standard error bars shown. Co-elution with an impurity from squalane resulted in a non-zero value at $t = 0$ minutes.

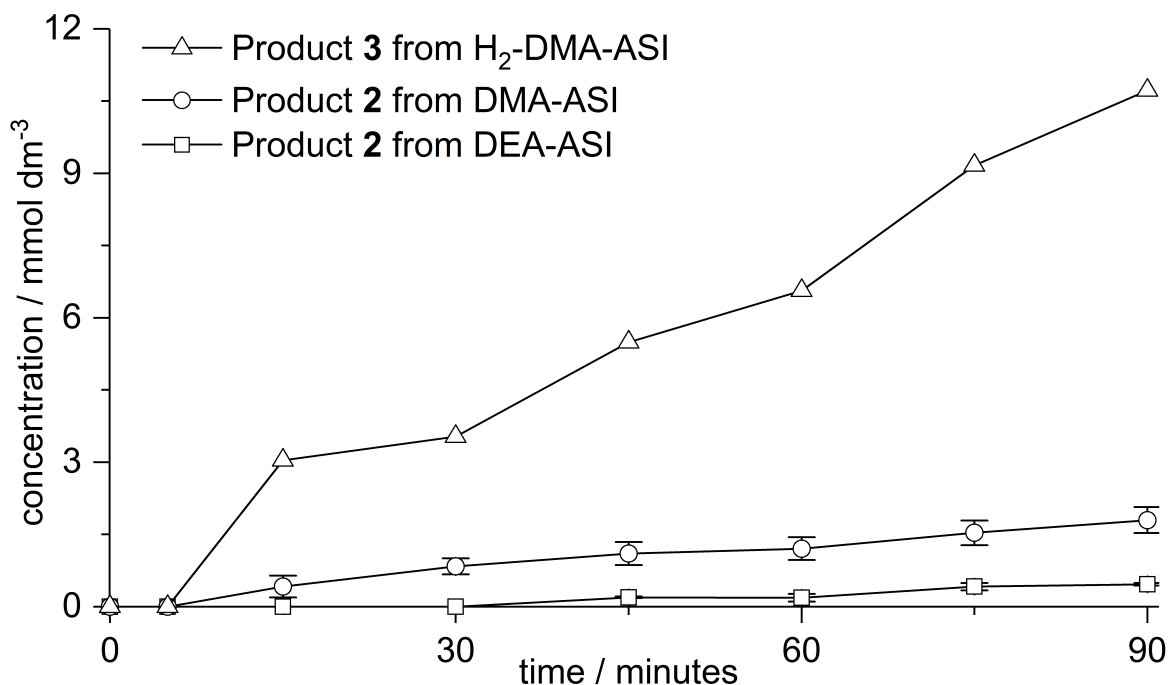


Figure 5.16 – The concentrations of products 2 and 3 during the autoxidation of alkyl ASIs (DMA-, DEA-, and H₂-DMA-ASI) as a 5% (w/w) solution in squalane. Values for DMA-ASI and DEA-ASI are averages of triplicate data with standard error bars shown. H₂-DMA-ASI data is from a single experiment.

GC-FID and GC-MS evidence suggests that adding amine functionality into an ASI dispersant mimic imparts antioxidant behaviour and that behaviour depends on the amine structure. DMA-ASI was consumed from the start of autoxidation by a mechanism that prevented autoxidation of squalane. DEA-ASI showed a stronger antioxidant effect, whereby minimal consumption of the ASI prevented all squalane oxidation, suggesting a catalytic mechanism. Degradation products of the amino ASIs indicate the nature of the chemistry occurring due to the aminic nitrogen and provide clues to the antioxidant mechanism, discussed later.

5.2.2 Oxidation in a real lubricant

Having shown the most promising antioxidant behaviour, diethylamino ASI (DEA-ASI) was taken forward for commercial oxidation testing. A sample of DEA-ASI was prepared and used as an antioxidant (AO) additive in a commercial automotive lubricant oil. This was compared to a baseline formulation, with no AO, and to formulations containing 1 and 2% of diphenylamine (DPA)—a commercially used amine-containing antioxidant.

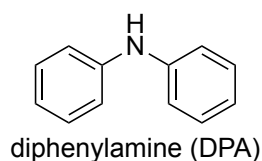


Figure 5.17 – Diphenylamine (DPA).

The composition of the fluids used is shown in Table 5.3. Blends were formulated around a commercial additive package that included PIBSI dispersants and zinc dialkyldithiophosphate (ZDDP) dissolved at 9.9% (w/w) in a group II base oil. Additional components of a viscosity modifier and a pour point depressant were added to produce a fully functional automotive lubricant. AO components were added on an equal % (w/w) basis. This did not factor in DPA having approximately half the molecular weight of DEA-ASI. Therefore at equal % (w/w) concentrations, DPA was present at approximately double the molar concentration of DEA-ASI.

Table 5.3 – The lubricants used for oxidation testing of DEA-ASI with an AO free baseline blend and diphenylamine (DPA) blends for comparison.

Component	% (w/w) of blend		
	Baseline blend	DPA blend	ASI blend
Group II base oil	79.4	78.4 to 77.4	79.2 to 77.4
Viscosity modifier	10.5	10.5	10.5
Commercial additive package	9.9	9.9	9.9
Pour point depressant	0.2	0.2	0.2
Diphenylamine	0.0	1.0 or 2.0	0.0
DEA-ASI	0.0	0.0	0.2 to 2.0

The lubricant samples were subjected to two standard industrial oxidation tests. The first test, the Coordinating European Council (CEC) L-109-14, is used commercially for measuring bulk oxidation.¹¹⁸ A small volume of lubricant is diluted with biodiesel (7% w/w) and subjected to ageing at 150 °C under a flow of air and in the presence of a catalyst for 216 hours (nine days). Samples are taken throughout and analysed for kinematic viscosity measured at 100 °C (KV_{100}) and by attenuated total reflection - Fourier transform - infrared (ATR-FT-IR) spectroscopy. As oxidation progresses, radical recombination and the formation of more polar products increase the viscosity of the fluid. Carbonyl containing compounds like acids, aldehydes, ketones and lactones also form during oxidation. Carbonyls produce a prominent infrared (IR) absorbance band around 1700 cm^{-1} , the absorbance intensity of which can be used as a measure of the degree of oxidation.

The viscosity data from the CEC L-109-14 are shown in Figure 5.18. It shows that all lubricants, after dilution with 7% biodiesel, had the same viscosity of 11.4 cSt. After 72 hours the baseline formulation showed the lowest viscosity, and the DPA containing formulations the highest. However, this differentiation was minimal.

A clear difference between the formulations was shown at the end of the nine day test period. The baseline formulation, with no AO, produced the highest viscosity sample at 52 cSt. The addition of 1% ASI yielded a slight decrease relative to the baseline formulation to 49 cSt and 2% ASI further decreased the end of test viscosity to 36 cSt. Both 1% and 2% DPA reduced the end of test viscosity to under 17 cSt, showing it to be more effective than DEA-ASI for mitigating oxidative viscosity increase.

The oxidation by IR data is shown in Figure 5.19. The formulations containing ASI followed the same shaped curve as the baseline formulation but at a lower value indicating lowered oxidation levels. The value was lower at 2% compared to 1%. The DPA containing formulations showed a flatter curve and both performed similarly. At the end of test, DPA containing formulations gave a similar result to the 2% ASI formulation.

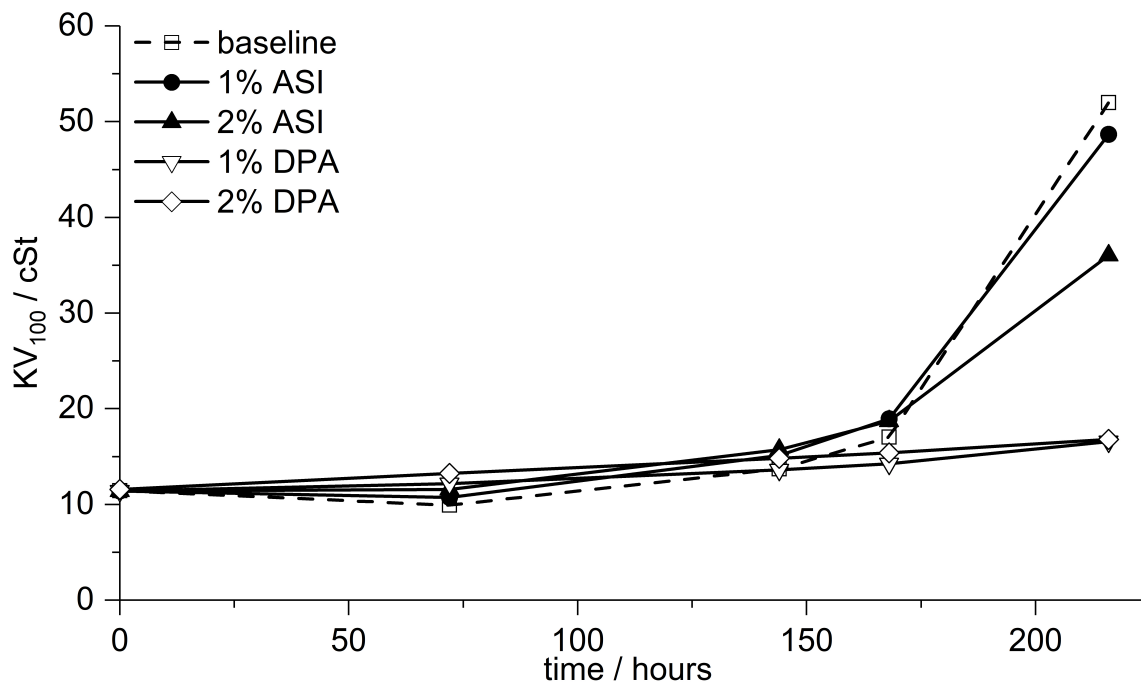


Figure 5.18 – The trend of kinematic viscosity at 100 °C (KV_{100}) over time for samples from the CEC L-109-14 oxidation test. The formulations tested were baseline, 1 and 2% DPA and 1 and 2% DEA-ASI.

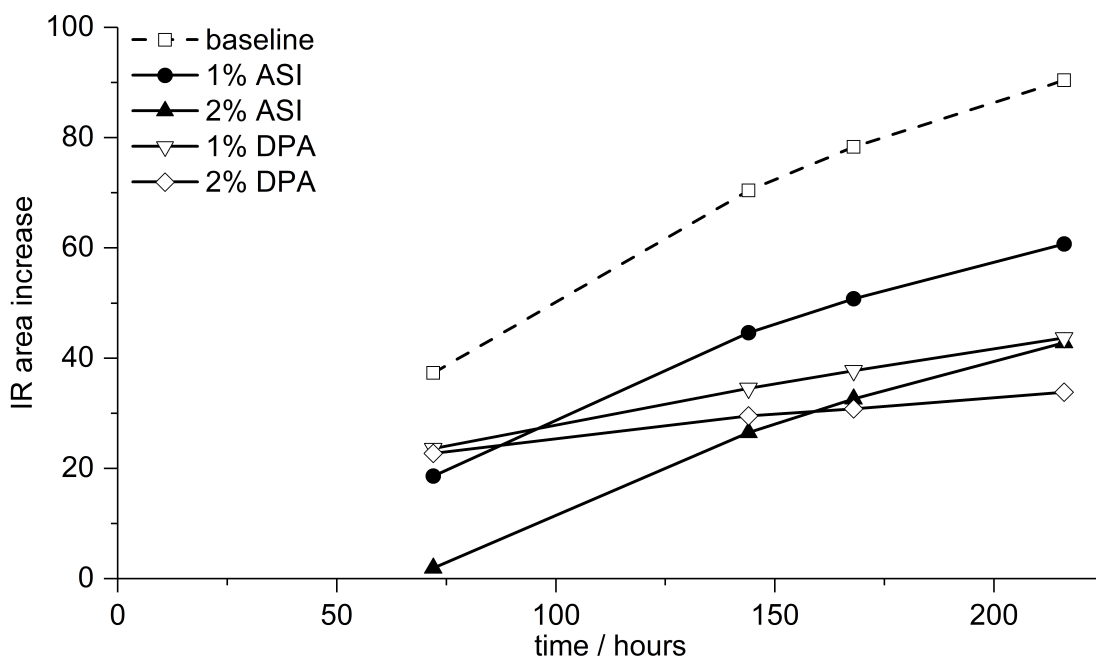


Figure 5.19 – The trend of oxidation by IR carbonyl area increase over time for samples from the CEC L-109-14 oxidation test. The formulations tested were baseline, 1 and 2% DPA and 1 and 2% DEA-ASI.

In the thermo-oxidation engine oil simulation test (TEOST) test, the lubricant sample is circulated over a resistively-heated steel rod for 24 hours.¹¹⁹ The mass of the rod is measured before and after the test and the mass gain is attributed to deposit formation from lubricant degradation. The results are reported in mg of deposit formed and are shown in Figure 5.20.

The baseline formulation, with no AO, was tested twice and formed on average 35 mg of deposit during the 24 hour test. Addition of DPA, as expected, reduced deposit formation to an average of 21 and 14 mg for 1 and 2% DPA formulations respectively. Formulations containing 1 and 2% ASI were tested twice yielding average values of 35 and 42 mg, equivalent to or higher than the baseline value of 35 mg. Formulations with between 0.2 and 0.8% ASI were tested once and showed a non-linear response to ASI concentration. At either end of this concentration range, deposit quantities equivalent to the baseline fluid were recorded. However, at 0.4 and 0.6% ASI, 22 and 19 mg of deposit were recorded respectively, showing equivalent performance to the 1% DPA formulation.

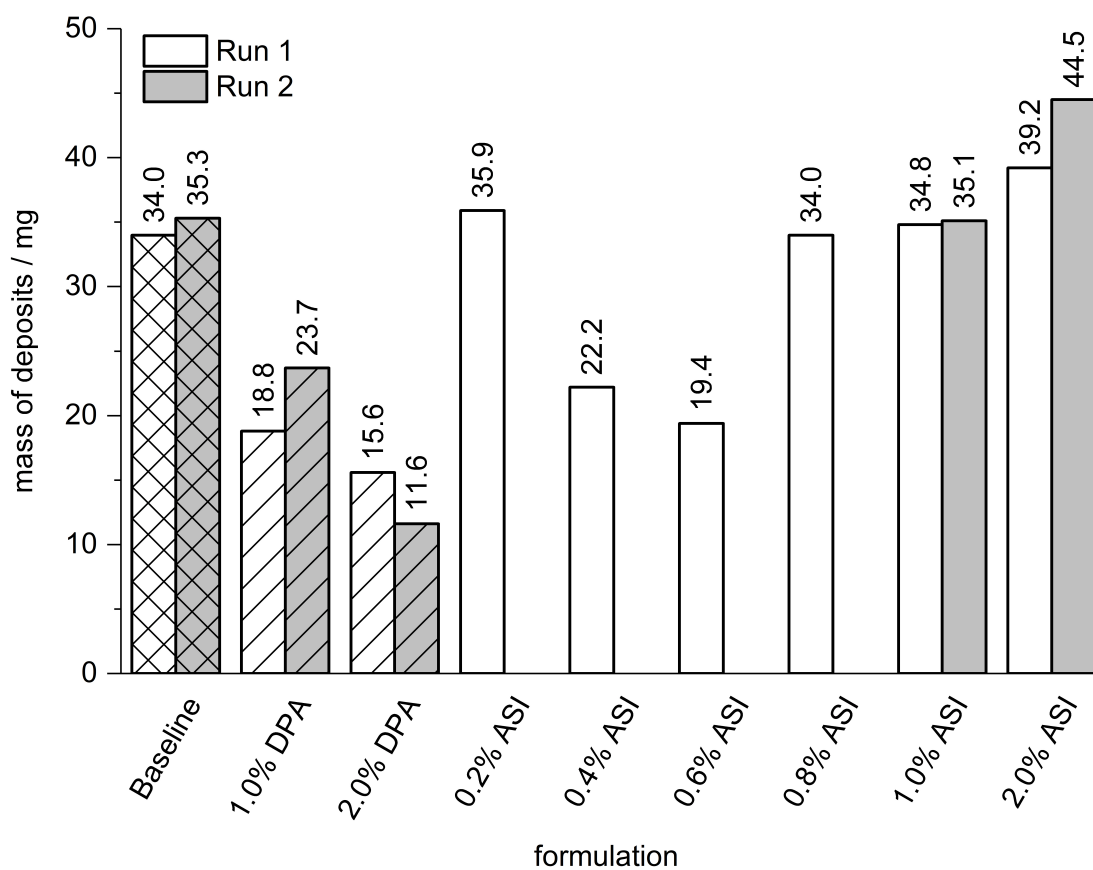


Figure 5.20 – The mass of deposits formed during the TEOST test. Where possible, two runs were performed to indicate test repeatability.

5.3 Discussion

The results reported in this chapter reveal the unexpected antioxidant effect of amine-containing ASIs. Structures with a tertiary-amine-containing head group showed remarkable reductions in squalane autoxidation. The major autoxidative degradation products, **1**, **1'** and **4** provide an insight into the mechanism of antioxidant activity.

The mechanisms behind this may be similar to that of hindered amine light stabilisers (HALSs) (Figure 5.21). HALS contain sterically hindered aliphatic amines and are used to stabilise polymers to photodegradation. The mode of action is reported to proceed through oxidation at the nitrogen to yield a nitroxyl radical that initiates a highly complex chain reaction that consumes peroxides, preventing oxidation.¹⁷²

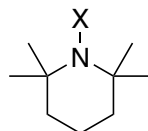


Figure 5.21 – The structure of a piperidine-based HALS where X is typically a hydrogen or an alkyl chain.

The chain reaction that destroys peroxides and imparts antioxidant activity is known as the Denisov Cycle.¹⁷³ The full mechanism is complex and still not entirely understood. A simplified version is shown in Figure 5.22, reproduced from Hodgson *et al.*¹⁷³ The important, and accepted, aspect of the cycle is the oxidation of the aminic nitrogen to a nitroxyl radical which then couples with an alkyl radical to form an alkoxyamine.¹⁷⁴ The alkoxyamine can react with peroxide radicals to produce non-radical products and regenerate the nitroxyl radical. The nature of this reaction is a subject of much debate with multiple mechanisms possible.¹⁷⁵ As such, this will not be covered in great detail here.

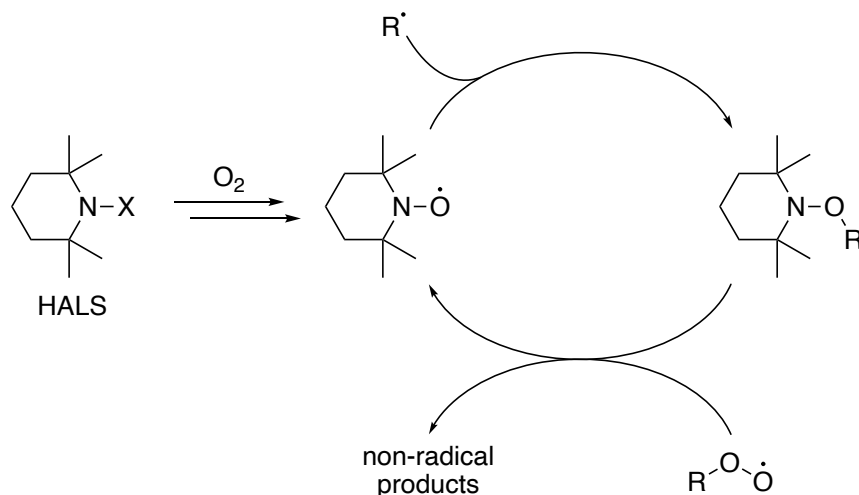


Figure 5.22 – A simplified mechanism of the Denisov cycle applied to HALS, reproduced from Hodgson *et al.*¹⁷³ X is typically a hydrogen or an alkyl chain.

5.3.1 Formation of products 1 and 4

One of the key aspects of the design of a HALS is the piperidine ring. This prevents decay of the nitroxyl radical via an intramolecular Cope elimination reaction. Cope elimination—not to be confused with the Cope rearrangement—is an intramolecular elimination reaction that *N*-oxides undergo upon the application of heat (Figure 5.23).¹⁷⁶

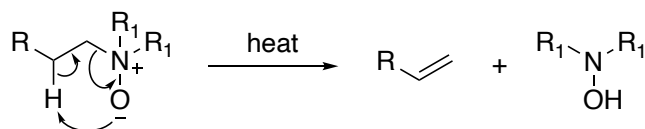
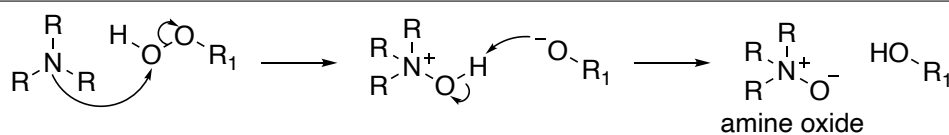


Figure 5.23 – The Cope elimination of an *N*-oxide to yield an alkene and a hydroxylamine.

In commercially applied HALSs, the ring constraints of the piperidine ring prevent the Cope elimination reaction from occurring. However, the amines of the amino ASIs in this study were linear with no ring structure meaning Cope elimination was possible. The *N*-oxide could form by reaction with alkyl peroxides within the system (Scheme 5.1).¹⁷⁷ The temperature of the reaction (170 °C) is sufficient to promote the elimination step.¹⁷⁶

Scheme 5.1 The oxidation of a tertiary amine to an amine oxide (*N*-oxide) where R and R₁ are alkyl chains.¹⁷⁷



Application of Cope elimination to *N*-oxides of DMA-ASI and DEA-ASI forms the same alkene, Product **1**, shown in Figure 5.24. When the mechanism is applied to the hydrogenated DMA-ASI analogue, H₂-DMA-ASI, the hydrogenated version of product **1** is formed, observed in this work as product **4**. The hydroxylamine product of Cope elimination was not observed in the liquid lubricant samples when tested by GC-FID, this is likely due to its evaporation from the oxidation reactor.

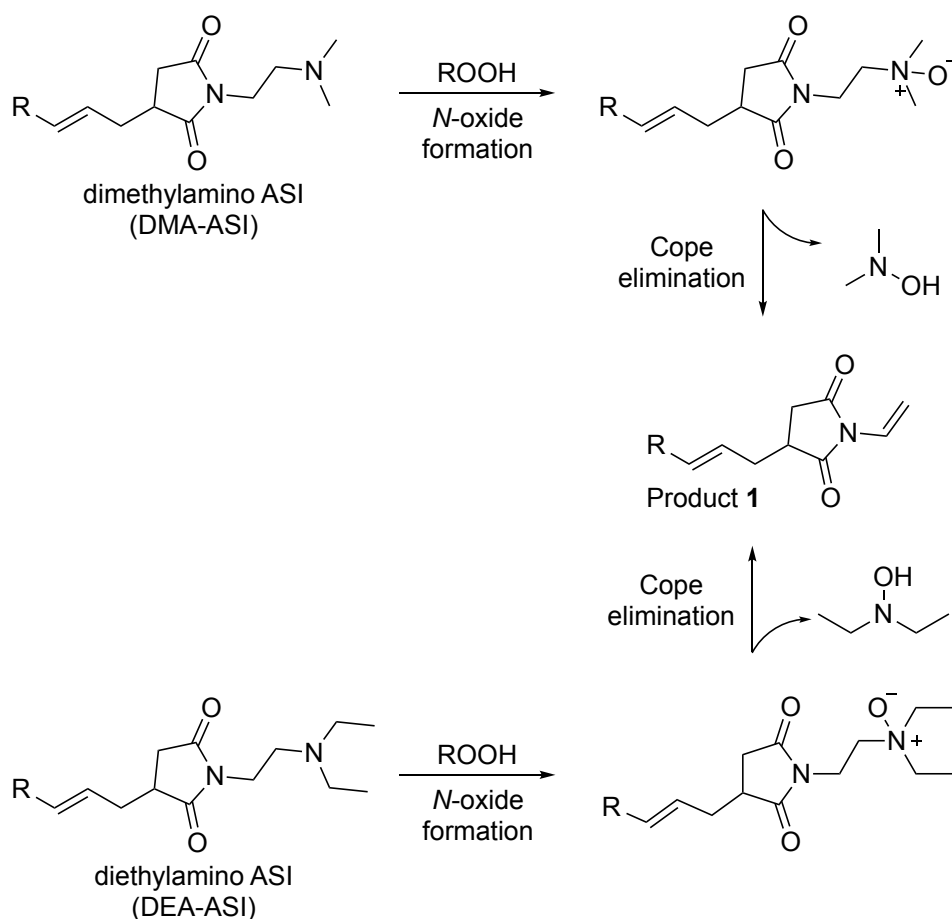


Figure 5.24 – *N*-oxide formation and Cope elimination applied to DMA- and DEA-ASI to form product **1**.

DMA-ASI decayed more rapidly than DEA-ASI to yield a greater quantity of product **1**. This can be attributed to steric effects, where the nitrogen of DMA-ASI is less sterically hindered and therefore more prone to oxidation through to the *N*-oxide. This could account for the rapid loss of antioxidant for MMA-ASI, where the amine is even less hindered and hence even more prone to oxidation and Cope elimination. This is supported by other studies that show secondary amine-containing HALS are consumed much faster than tertiary amines due to need for an activation process for tertiary HALS where an alkyl group is lost, forming a secondary

amine.¹⁷⁸ Secondary amine HALS can react immediately and are consumed rapidly whereas tertiary HALS represent a stable “reservoir” of antioxidant, increasing lifetime of antioxidant performance.

The formation of the Cope elimination product is strong evidence for oxidation at the aminic nitrogen which supports the antioxidant of amino ASIs resulting from nitroxyl radical formation and the Denisov cycle, discussed later.

5.3.2 Formation of products **2** and **3**

Products **2** and **3** were not observed during the autoxidation of *N*-alkyl ASIs (Chapter 4) and so must result from oxidation mechanisms involving the aminic nitrogen. The two products are equivalent except for whether or not the tail contained an alkene. Where the tail contained an alkene—DMA-ASI degrading to product **2**—the product was present in lower concentrations than when H₂-DMA-ASI was oxidised to yield product **3**. In terms of autoxidation, the defining characteristic of alkenes are the labile allylic hydrogens that can be easily abstracted. It is likely that an intermediate in the formation of **2** and **3** can alternatively react by hydrogen abstraction instead of forming **2** and **3**. As a result, the product is seen in higher concentrations for hydrogenated amino-ASIs where allylic hydrogens are not available to limit the formation of **3**.

The mechanism proposed in this work for the formation of **2** and **3** is shown in Figure 5.25. It is proposed that the nitroxyl radical (**A**) formed by amine oxidation can back-bite to abstract a hydrogen from the carbon α to the succinimide nitrogen. The resultant carbon-centred radical (**B**) can be oxidised thorough to an alkoxy radical (**C**). This can decay by α cleavage (as explained in Chapter 4) to yield the succinimide radical **D**. Upon hydrogen abstraction this forms **2/3**. This mechanism can be prevented by the radical **B** abstracting a hydrogen atom. This could plausibly be an allylic hydrogen in a second equivalent of DMA-ASI which would account for the observation of lower concentrations of **2** forming from DMA-ASI compared to **3** forming from H₂-DMA-ASI.

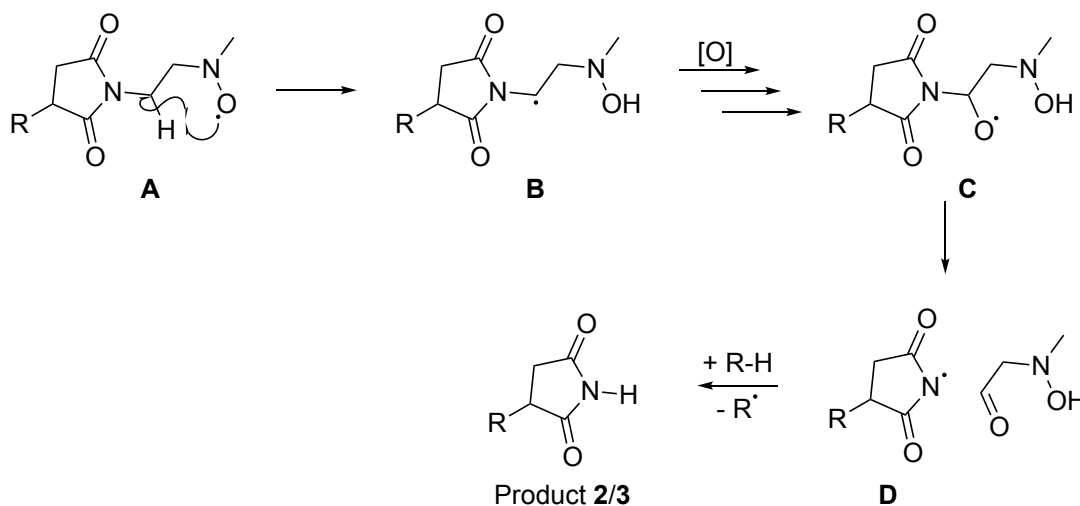


Figure 5.25 – The proposed mechanism for the formation of products **2** and **3** starting from the nitroxyl radical resulting from amine oxidation.

5.3.3 Antioxidant mechanisms of amino ASIs

The degradation products identified in this work indicate that oxidation is occurring at the aminic nitrogen of amino ASIs during their autoxidation in a model lubricant. HALS type antioxidants are effective due to an oxidised aminic nitrogen, therefore it is possible that *N* oxidation of amino ASIs activates their antioxidant behaviour. We propose that amino ASIs oxidise to form a nitroxyl radical that can enter the catalytic Denisov cycle, destroying peroxides and limiting autoxidation.

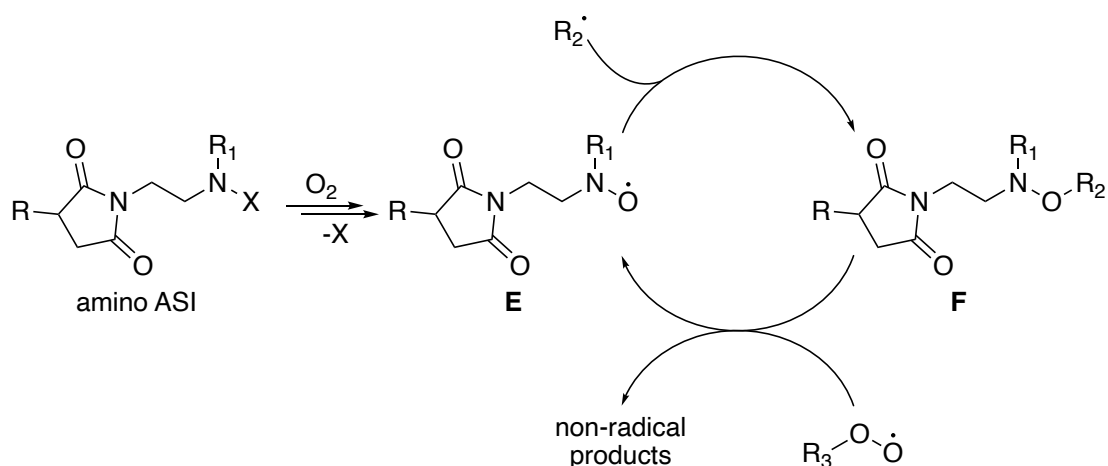


Figure 5.26 – The simplified Denisov cycle applied to amino ASIs where R is an alkyl tail, R₁ is H, methyl or ethyl, X is H, methyl or ethyl. R₂ and R₃ are lubricant-derived alkyl groups.

Step one, the activation of the ASI to form nitroxyl radical **E** has been subject to debate in the

literature. Following computational work and a review of the possible mechanisms Gryn'ova *et al.* concluded that for secondary HALS (where X = H, Figure 5.26) it is initiated by a radical (dioxygen or lubricant-derived) abstracting the hydrogen.¹⁷⁵ After this initiation step, the nitrogen radical is oxidised to a peroxide that homolyses to yield **E**.

For tertiary HALS, analogous to DMA- and DEA-ASI in this work, the reaction is more complex. Shown in Figure 5.27, in an activation step a hydrogen α to the aminic nitrogen is abstracted to yield carbon centred radical **G**. Through oxygen addition, radical **H** is formed which then, under conditions studied by Gryn'ova *et al.*, dimerises forming **I** which then homolyses to form radical **J**.¹⁷⁵ β scission of radical **J** forms aminyl radical **K**. At this point, the reaction proceeds via the same pathway as the activation of secondary HALS and **K** oxidises through to the catalytically-important radical **E**.

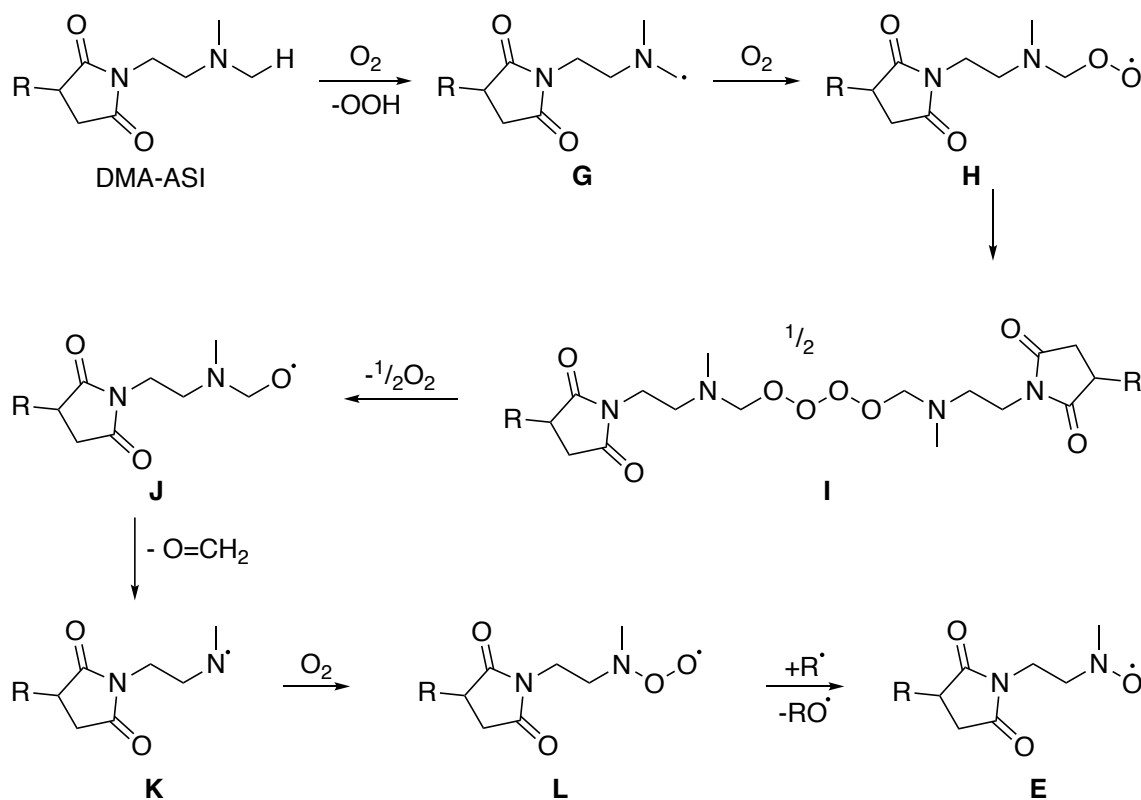
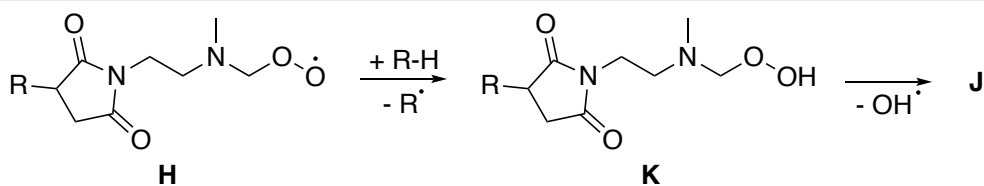


Figure 5.27 – The activation of DMA-ASI using mechanisms proposed by Gryn'ova *et al.* for the activation of tertiary HALS.¹⁷⁵

In the computational work performed by Gryn'ova *et al.*, the formation of dimer **I** was favourable at 25 °C in the gas and aqueous phases.¹⁷⁵ An alternative pathway shown in Scheme 5.2 involves radical abstraction by **H** to form **K**. By homolysis of the peroxide bond, **J** is formed.¹⁷⁵

Scheme 5.2 An alternative mechanism for the formation of radical **J** from **H**.

Due to the energetic barrier to hydrogen abstraction, at 25 °C Gryn'ova *et al.* found the mechanism in Scheme 5.2 was unfavourable. However, at 260 °C, the reaction was favourable. In this work it may be favoured as the dilute concentration of ASI in squalane would hinder dimer formation. Temperatures of 170 °C and the high availability of relatively labile hydrogens (squalane or allylic hydrogens of the ASI) would promote the hydrogen abstraction pathway. Therefore, in this work, this pathway cannot be discounted.

In this work, tertiary amines afforded far greater protection against autoxidation than secondary amines. This aligns with previous findings and is attributed to the activation mechanism of secondary amines being faster and so it is used up more rapidly.¹⁷⁹ Tertiary amines are slower to activate and represent a “stable reservoir” of antioxidant that afford longer-term protection from autoxidation. The secondary amine of DPA does not follow this trend but is still a highly effective antioxidant. DPA works—analogue to phenolic antioxidants—by donation of the aminyl hydrogen to reactive radical species, yielding a highly resonance-stabilised aminyl radical.

Through the activation mechanisms described, aliphatic amine-containing ASIs—and by analogy PIBSI dispersants—can form nitroxyl radicals that catalytically destroy peroxides via the Denisov cycle, protecting the lubricant from autoxidation. However, if nitrogen oxidation resulted in amine cleavage by the mechanisms proposed in this work, the dispersant would be rendered inactive, harming dispersant performance.

5.3.4 ASI autoxidation in fully formulated lubricants

With the apparent antioxidant behaviour shown by diethylamino alkenyl succinimide (DEA-ASI), its synthesis was scaled up and the product was subjected to selected industry-standard oxidation tests as part of a fully formulated lubricant. Two tests were conducted which measured three performance outcomes, the ability of DEA-ASI to mitigate viscosity increase, reduce oxidation as measured by carbonyl concentration by

attenuated total reflection - Fourier transform - infrared (ATR-FT-IR), and the propensity for DEA-ASI containing formulations to form deposits on a metal surface. Data from the Coordinating European Council (CEC) L-109-14 test showed a slight viscosity improvement at high (2% w/w) DEA-ASI concentrations shown by a reduction in end-of-test viscosity relative to the baseline formulation without AO present (Figure 5.18, page 150). DEA-ASI performance was significantly worse compared to formulations containing diphenylamine (DPA) antioxidant (AO).

However, when oxidation was measured by increase in the concentration of carbonyl-containing compounds, clear improvements could be observed. When DEA-ASI was present, the concentration of carbonyl-containing compounds increased at the same rate as the baseline formulation but at a significantly lower level. The effect was greater at higher DEA-ASI concentrations. This suggests DEA-ASI delayed the start of oxidation but once it was fully consumed, oxidation proceeded by the same mechanisms and at the same rate as the baseline formulation without any AO present. This suggests that DEA-ASI, in a fully formulated lubricant, did successfully inhibit oxidation for the first 72 hours of the test. It is likely that DEA-ASI was consumed in this time and therefore afterwards the formulation showed similar behaviour to the AO-free baseline formulation.

Carbonyl-containing oxidation products form from alkyl peroxide decay products.⁹⁹ The peroxide homolyses to form an alkoxy radical that undergoes α cleavage to form a carbonyl-containing degradation product. The mode of action of hindered amine light stabiliser (HALS) type antioxidants, and by analogy DEA-ASI, is to react away peroxides to non-carbonyl containing products. Therefore, DEA-ASI appears to be an effective antioxidant when measuring the production of carbonyl compounds by infrared (IR).

The thermo-oxidation engine oil simulation test (TEOST) data showed more interesting behaviour when more varied concentrations of DEA-ASI were used. Shown in Figure 5.20, the mass of deposit formed was non-linear with respect to DEA-ASI concentration. If DEA-ASI were solely acting as an antioxidant, you would expect that as its concentration increased, the degree of sample oxidation would decrease and this would be shown by a decreased mass of deposit formed during the test.

This is true for DPA, where increasing the concentration from zero to one to two percent (w/w) decreased the mass of deposit formed from 34.6 to 21.3 to 13.6 mg. For DEA-ASI,

0.2% had no impact on deposit formation, but increasing to 0.6% DEA-ASI yielded equivalent results to 1% of DPA. When you factor in the molarity—as DPA is approximately half the molecular mass of DEA-ASI—the effectiveness of DEA-ASI on a mol for mol basis doubles. When the concentration of DEA-ASI was increased to 0.8% (w/w) and above, TEOST deposit values were equivalent to the performance of the baseline lubricant without AO present.

This apparent non-linear antioxidant effect is unexpected and unusual and, due to the limited data available, difficult to develop reliable conclusions as to its origin. One potential explanation is the surfactant behaviour of DEA-ASI. DEA-ASI is an amphiphile, with a polar head group and an apolar tail and therefore it can interact with surfaces. The aminic head group may interact with the steel surfaces within the TEOST test equipment. In the test, 8.5 g of oil is used and, at a 2% (w/w) concentration, 170 mg are present in the system. A portion of the DEA-ASI could contribute to the deposits registered during the test. And so, while oxidation may be low deposits could still be high. As per the standard test procedure, no further analysis was conducted on the samples post-test and so the degree of oxidation was not determined by other means such as ATR-FT-IR.

The use of two important industrial oxidation tests has shown interesting behaviour of DEA-ASI which suggests it and similar tertiary-amine-containing additives could prove beneficial in real automotive engine lubricants.

5.3.4.1 Implications for commercial dispersant behaviour

The development of DEA-ASI was not intended to produce a stand-alone antioxidant additive, but to act as a mimic for polyisobutenyl succinimide (PIBSI) dispersants that are already commonly used in engine oil lubricants. This chapter expands on the work of Chapter 4 which concluded that PIBSI autoxidation would likely be dominated by the alkene functionality of the polyisobutene (PIB) tail. In this chapter, by adding amine functionality into the ASI model, ASI reactivity was significantly changed. The structure of the amine changes the reactivity of the ASI from being rapidly consumed while acting as a slight antioxidant for monomethylamino alkenyl succinimide (MMA-ASI), to negligible consumption of the ASI with a strong antioxidant effect for DEA-ASI.

Both amine functionalities are relevant to commercial PIBSI dispersants, as are further structures that were not included in this study, such as piperazines. When dispersants are

drawn, they are usually depicted solely containing a linear ethylene amine head group, usually tetraethylenepentamine (TEPA) (Figure 5.28).

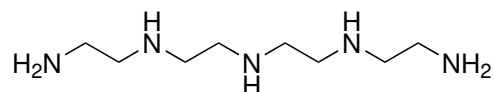


Figure 5.28 – Tetraethylenepentamine (TEPA)

Ethyleneamines are produced from the condensation of 1,2-dichloroethane with ammonia. The reaction proceeds via multiple uncontrolled routes which produce more than just linear ethylene amines. In an industrial setting, fractionation of the various products is minimal. Therefore, in an industrial setting, a sample of TEPA is an incredibly varied material containing a plethora of primary, secondary and tertiary amines with a variety of linear, branched and cyclic structures (Figure 5.29). For example, Spell determined that a sample of TEPA contained up to 10% piperazine rings.⁵¹

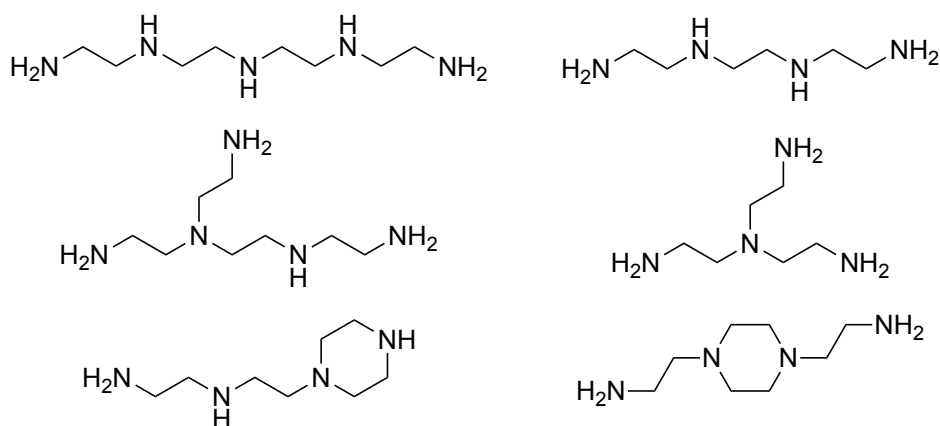


Figure 5.29 – A selection of amines that could be found in commercial samples of TEPA, including two piperazines identified by Spell (bottom).⁵¹

Piperazines could be particularly important for PIBSI dispersant autoxidation/antioxidancy performance. The most effective HALS type structures are based on a piperidine structure as the six membered ring prevents intramolecular Cope eliminations. The same would be true of the six membered rings structure in piperazines and therefore dispersant molecules containing these amines could show improved antioxidant performance.

Another factor that would impact PIBSI dispersant antioxidantancy is the acidity of the lubricant. It has been shown that surfactant amines react with Brønsted acids in lubricants to form ion pairs that bind amine-containing surfactants to surfaces.¹⁸⁰ In polymers, HALS are not used in chlorine-containing polymers due to HCl—which is slowly eliminated from

the polymer—protonating the HALS nitrogen, rendering it ineffective as an antioxidant. Therefore as lubricant acidity—measured by the total acid number (TAN)—increases due to autoxidative carboxylic acid formation, PIBSI amines would become protonated, preventing their action as HALS-type antioxidants.

5.3.4.2 Implications for commercial dispersant development

This work has two main implications for the development and use of amine-containing dispersants in lubricants. Firstly, the effect of amine type on antioxidant behaviour should be investigated to determine if different commercially relevant amine structures have a significant impact on lubricant lifetime. This would help to understand the impact of amine batch numbers and different suppliers on dispersant and lubricant performance. Secondly, the use of different amine structures to intentionally introduce robust antioxidant properties into dispersants, such as hindered piperazines, would be both academically interesting and industrially relevant.

5.4 Conclusion

The introduction of secondary and tertiary aliphatic amines into the head-group of alkenyl succinimide (ASI) dispersant mimics has been investigated. Amines dramatically reduced or stopped model lubricant autoxidation in a bench-top reactor over 90 minutes at 170 °C. This behaviour is attributed to chemistry similar to that of hindered amine light stabiliser (HALS) type polymer stabilisers whereby nitroxyl radicals resulting from direct amine autoxidation catalytically destroy peroxides through the Denisov cycle, preventing autoxidation. This was evidenced by observation of the Cope elimination product that results from direct nitrogen autoxidation. The ASI that showed the best antioxidant behaviour, diethylamino alkenyl succinimide (DEA-ASI), was taken forward to industrial oxidation tests as part of a fully formulated automotive lubricant. Results suggested that DEA-ASI did behave as an antioxidant in this setting, even out-performing a traditional diphenylamine (DPA) antioxidant when employed at low (0.6%) treat rates in the TEOST deposit formation test. The results contained in this chapter suggest the possibility of developing dual function dispersant-antioxidant additives and may help to explain the impact of different dispersants on lubricant performance.

Chapter 6

Conclusions and future work

6.1 Radicals in polyisobutenyl succinic anhydride (PIBSA) synthesis

In Chapter 3, the synthesis of PIBSA was explored. Conventionally, PIBSA is formed by reacting polyisobutene (PIB) with maleic anhydride (MAH) via the Alder-ene reaction. A serendipitous surfactant synthesis, where the product distribution changed solely as a result of changing the reaction scale, did not support the PIBSA 3 (Figure 6.1) formation mechanism proposed by Balzano *et al.*³²

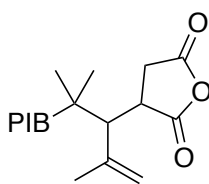


Figure 6.1 – PIBSA 3.

The reaction was scaled down and nuclear magnetic resonance (NMR) spectroscopy was used to characterise and quantify the products. Using air-sensitive handling techniques, it was shown that the addition of a radical scavenging antioxidant stopped the production of PIBSA 3. This suggested a radical mechanism. Further experiments showed that the mechanism could be initiated both by air and by alkyl peroxide contaminants in the starting material. Furthermore, the intentional addition of a radical initiator gave PIBSA 3 yields of 40%. The proposed radical chain reaction starts by the site-selective abstraction of a hydrogen from the secondary allylic carbon of α PIB. This radical adds to MAH which forms a succinic anhydride radical. This radical performs a site-selective hydrogen abstraction from a second equivalent of α PIB, perpetuating the chain mechanism.

While this mechanism was highly selective, PIBSA yields of 100% were never achieved. Investigated using GC-FID, this was shown to result from the evaporation of low molecular weight PIB oligomers. This work is important because it highlights the prevalence of these low molecular weight structures in dispersants. While constituting a low proportion by mass, their low molecular weight means they make up a large proportion of the dispersant on a molar basis. These small molecules cannot be called dispersants as their short PIB tails would not provide adequate solubility or dispersancy in a lubricant, negatively impacting performance.

The work in Chapter 3 highlights both the complexity of the mechanisms behind dispersant synthesis and the variability of the products. Due to these complexities, the autoxidation of polyisobutenyl succinimide (PIBSI) dispersants was studied using chemical mimics in Chapters 4 and 5.

6.2 The autoxidation of *N*-alkyl alkenyl succinimides (ASIs)

In Chapter 4, high-purity chemical mimics for PIBSI dispersants were developed so that product studies could be used to determine autoxidation mechanisms. The main mimic studied, *N*-butyl ASI (Figure 6.2), was oxidised both in the bulk phase and as a model lubricant dissolved in squalane.

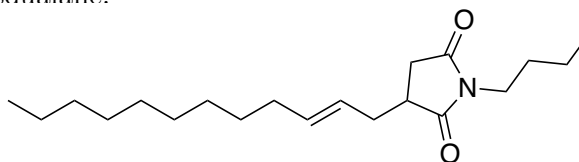


Figure 6.2 – *N*-butyl ASI.

When oxidised at 170 °C—a temperature representative of the operating temperature of the piston ring pack in an internal combustion engine—*N*-butyl ASI degraded at or around the alkene. This was shown by the bulk phase autoxidation where 15 autoxidation products were identified using GC-EI-MS. These products solely resulted from autoxidation at the alkene.

The products were categorised into three main groups. The biggest group were the dehydrodimers that formed from the recombination of carbon-centred radicals. These higher molecular weight structures contributed to a 300-fold viscosity increase after oxidation. The second group of products were oxygenated ASI products, where autoxidation formed alcohols, ketones, and diols on the ASI tail. The third group were the degradation products resulting from cleavage of the ASI structure. Site-selective cleavage split the hydrophilic head group from the solubilising tail which, when applied to PIBSI dispersants, would render the dispersant inactive. When oxidised in a model lubricant, the ASI degraded 2.3 times faster than squalane which means ASI hydrogens are 3.5 times more reactive than hydrogens on squalane tertiary carbons at 170 °C. The implications of this work are that dispersants would degrade rapidly during use in an engine. The degradation increases lubricant viscosity and renders the dispersant inactive, both effects that have negative lubricant performance implications.

6.3 The autoxidation of amine-containing alkenyl succinimides (ASIs)

The ASI model used in Chapter 4 was expanded in Chapter 5 to include aminic hydrophiles. Autoxidation of these amino ASIs in a model lubricant at 170 °C showed they behaved as antioxidants. The antioxidant effect was stronger for tertiary amines than for secondary amines. Tertiary amino ASIs decayed slowly forming two major products which showed autoxidation had occurred at the amine and not at the alkene. Nitrogen autoxidation suggested antioxidant activity was provided by nitroxyl radicals through the Denisov cycle. The cycle destroys peroxy radicals, breaking the autoxidation chain reaction. The most effective antioxidant ASI studied was diethylamino alkenyl succinimide (DEA-ASI) (Figure 6.3).

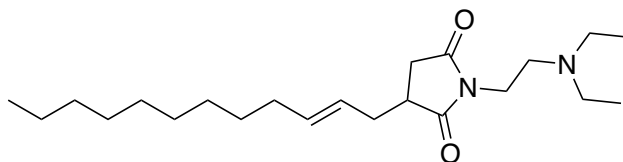


Figure 6.3 – Dimethylamino ASI (DEA-ASI).

DEA-ASI was used as an antioxidant additive in two industry-standard oxidation tests. These tests showed that DEA-ASI behaved as an antioxidant in a fully formulated lubricant.

6.4 Key learnings

The key learnings from this thesis are as follows:

- Radicals impact dispersant synthesis and should be controlled by antioxidants to give a more uniform product.
- The alkene of a dispersant is a weak point for oxidation during use, leading to degradation products that would severely limit lubricant performance.
- With the right amine structure dispersants can act as antioxidants, a behaviour that was observed in fully formulated engine oil lubricants.

6.5 Future work

Future work on dispersant synthesis should aim to narrow the range of structures present in a sample of PIBSI. This can be done by optimising the distribution of structures with the PIB. GC-FID of low molecular weight PIBs in Chapter 3 showed the range of molecular weights present within a sample of PIB. This broad range follows through the synthesis to give a large range of dispersant structures in a sample. Each of these individual structures would have individual performance characteristics based on its hydrophilic-lipophilic balance. As an example, tri-isobutene was identified in the PIB used in this study despite the nominal average molecular weight of 950 g mol^{-1} . When a dispersant is formed from tri-isobutene and tetraethylenepentamine (TEPA) (Figure 6.4) its hydrophile is larger than the hydrophobe. This is far detached from the average 950 g mol^{-1} starting material and would give a vastly different performance.

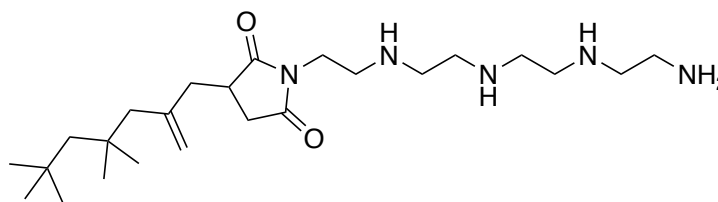


Figure 6.4 – PIBSI with a tri-isobutene tail.

Work to narrow the molecular weight distribution of PIBSI dispersants would be valuable for optimising dispersant performance and for understanding the mode of action of different molecular weight dispersants. Chapter 3 showed the formation of PIBSAs was impacted by the presence of radicals. However, the performance impact of the unconventional PIBSA 3 structure is not yet known and may be of industrial interest. Also, lab PIBSA was compared to an industrial sample which showed the industrial sample to have multiple unknown PIBSA structures. These structures should be characterised in order to further understand the range of structures present in a real dispersant. Work on dispersant synthesis should also include determining the formation mechanism and the performance implications of bis-PIBSAs which were briefly discussed in Chapter 3.

Future work should include further study of the ASI mimic. Particularly, the impact of a wider range of amine structures on antioxidant behaviour. The linear tertiary amine of DEA-ASI afforded good antioxidant behaviour despite not having the optimised hindered

piperazine structure of a hindered amine light stabiliser (HALS). The use of piperazines equivalent to the amine structures found in HALS type antioxidants in engine oil lubricants should be investigated. This would be interesting both from an AO perspective and from a dispersancy perspective as piperazines are known to bind less strongly to soot surfaces.⁵⁰ However, how this affects real-world dispersant performance is unknown.

Both of these areas, PIBSI synthesis and amine structure, could combine to yield higher performing dispersants and lubricants. Narrowing the molecular weight distribution and the range of structures within a given PIBSI would allow formulators to be more precise when choosing dispersants meaning dispersants could be used in a more targeted way. By further investigating the effect of amine structure on antioxidantancy, higher performing ASIs could be developed as stand-alone antioxidant additives. PIBSI dispersants with built-in antioxidantancy behaviour could also be developed. Developing better dispersants will allow the use of lower dispersant treat rates, helping the development of ultra-low viscosity lubricants, lowering frictional losses and reducing greenhouse gas emissions.

6.6 The future of engine oil lubricants

There is an obvious barrier to the future development of lubricants for internal combustion engines: the electric motor. As the demand for cleaner transportation using electric vehicles (EVs) steadily increases, the demand for engine oil lubricants will surely stagnate. While the global Covid-19 pandemic put the brakes on the internal combustion engine market, the drive for EVs has resisted this pressure with sales remaining at 2019 levels, when EVs made up 2.6% of global car sales.¹⁸¹ From a dispersant chemist's perspective, the problem with EVs is that they do not need dispersants. Dispersants are used to solubilise soot from combustion; if there is no combustion and no soot, there is little need for dispersants. Instead the focus of lubricating the motors of EVs is on three main areas; copper corrosion and plastic compatibility, extreme low viscosity, and electrical compatibility.^{182,183}

While bad news for the dispersant chemist, the rise of the EV is progress in the right direction in the fight to reduce emissions and minimise climate change. However, the other 97.4% of cars sold in 2019 all used internal combustion engines.¹⁸¹ While there have been immense efforts put into increasing fleet efficiency and longevity, it is difficult not to be disheartened by the trend of rising CO₂ emissions across the global car fleet. According to a 2019 report

by the International Energy Agency (IEA)¹⁸⁴ global emissions from private vehicles have been increasing since 2010. In the United Kingdom (UK), average new car emissions have increased steadily since 2017. Despite efficiency improvements in small cars reducing global oil consumption by two million barrels a day, and a modest one hundred thousand barrel a day saving from EVs, the situation is worsening.¹⁸¹

The culprit? Sports utility vehicles.

The global market for sports utility vehicles (SUVs) has doubled since 2010 and now almost half the cars sold in the United States of America (USA) are gas-guzzling SUVs.¹⁸¹ The rise in demand for large vehicles that use 25% more energy than smaller counterparts means SUVs are responsible for the second highest increase in global emissions since 2010—a larger increase than that of heavy industry, trucks or aviation, only bested by increased global power generation.¹⁸⁴ This 3.3 million barrel a day increase in oil consumption vastly outweighs the admirable gains made by the smaller internal combustion engine and EV car market.¹⁸¹

The marginal lubricant efficiency improvements demanded by the newest industry specifications fade into insignificance against a backdrop of the vehicular arms race of SUV culture. Without sweeping social and societal changes our future is one where cars do not fit in parking spaces and the targets to limit global temperature increase have been woefully missed. It will be interesting to see in 100 years time whether the status symbols of today—big cars, big houses, big money—are still desired above clean air, clean water and verdant natural landscapes.

Chapter 7

Appendix

7.1 Supplementary information for Chapter 3

7.1.1 Structural assignment of PIBSA 3

Table 7.1 – Olefinic, allylic, and succinic ^1H -NMR shifts for PIBSA 3.

Proton	^1H	Coupled protons (COSY)	Coupled carbon (HMQC)
1	4.97 (1 H, s)	2, 7	4
2	4.82 (1 H, s)	1, 7	4
3	3.02 (1 H, m)	4, 5, 6	6
4	2.68 (1 H, d, $J=3.7$ Hz)	3	5
5	2.51 (1 H, m)	3	7
6	2.44 (1 H, m)	3	7
7	1.76 (3 H, s)	1, 2	8

Table 7.2 – Olefinic, allylic, and succinic ^{13}C -NMR shifts for PIBSA 3.

Carbon	^{13}C shift	^{13}C environment (DEPT-135)
1	173.5	CR_4
2	171.7	CR_4
3	140.0	CR_4
4	116.4	CR_2H_2
5	58.2	CH/H_3
6	42.0	CH/H_3
7	40.8	CH_2
8	21.9	CH/H_3

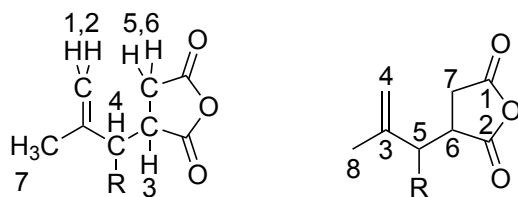


Figure 7.1 – Proton (left) and carbon (right) numbering for PIBSA 3.

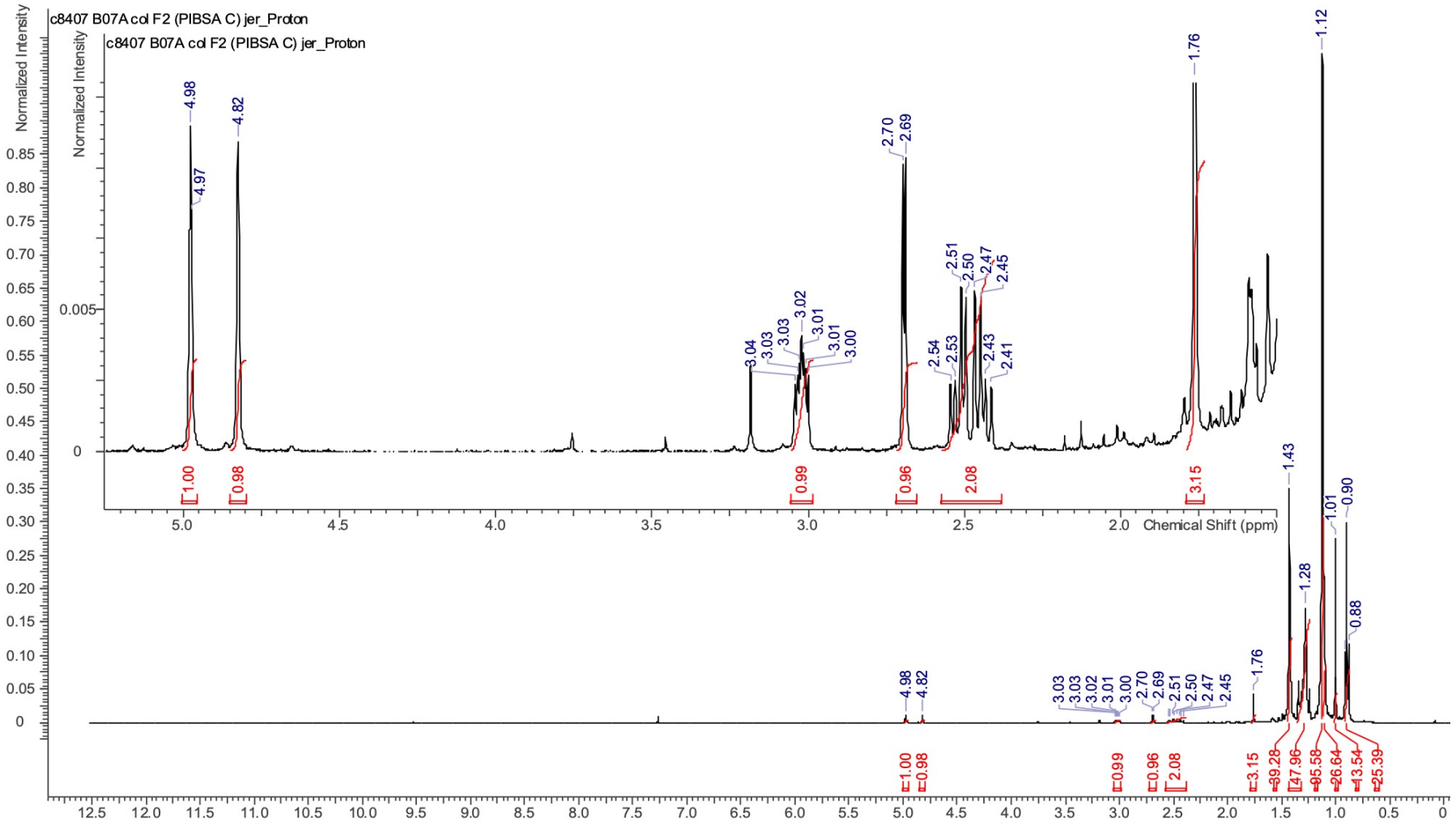


Figure 7.2 – ^1H -NMR spectrum of PIBSA 3.

7.1.2 The effect of MAH purity on PIBSA synthesis

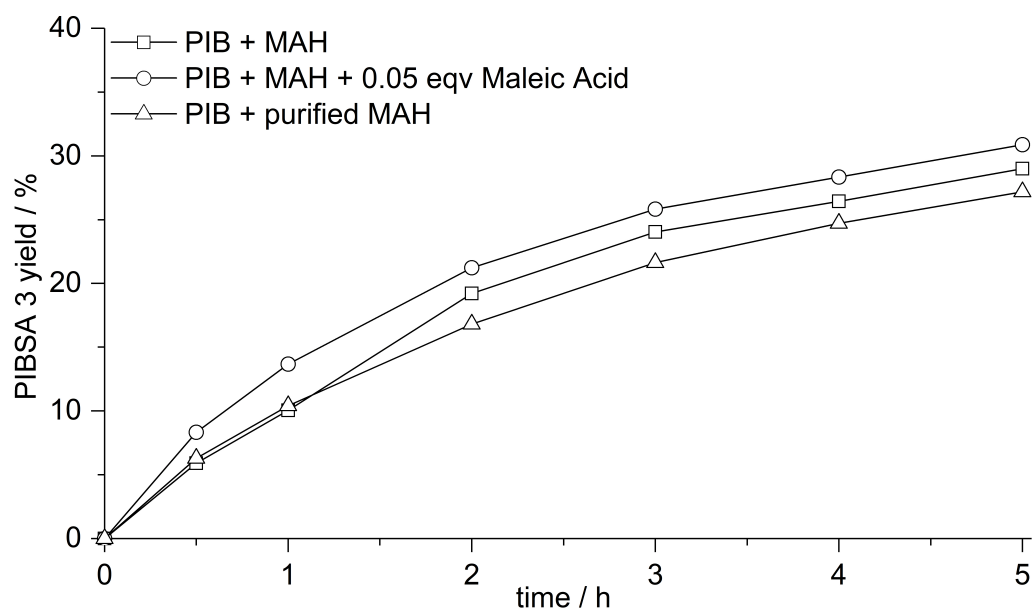


Figure 7.3 – The effect of MAH purification and maleic acid addition on the yield of PIBSA 3 in a 20 g scale reaction.

7.1.3 Characterisation of low molecular weight polyisobutenes

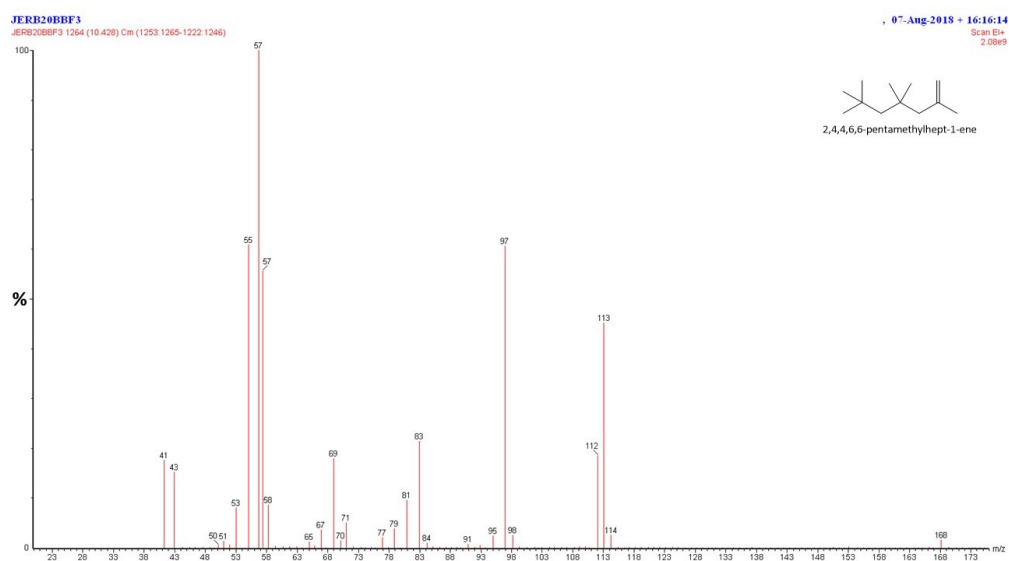


Figure 7.4 – The EI mass spectra of the α isomer of tri-isobutene, characterised by cross reference to the NIST database.

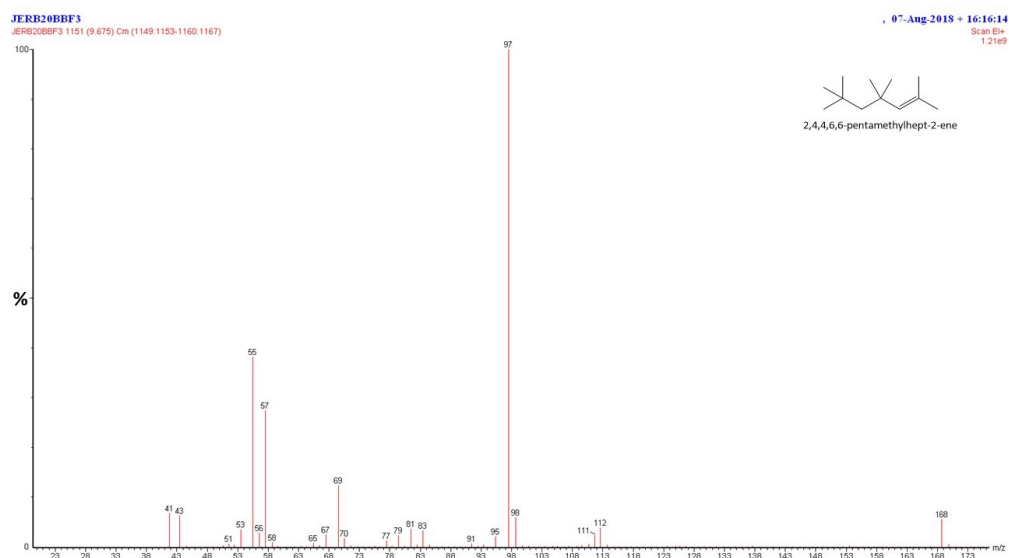


Figure 7.5 – The EI mass spectra of the β isomer of tri-isobutene, characterised by cross reference to the NIST database.

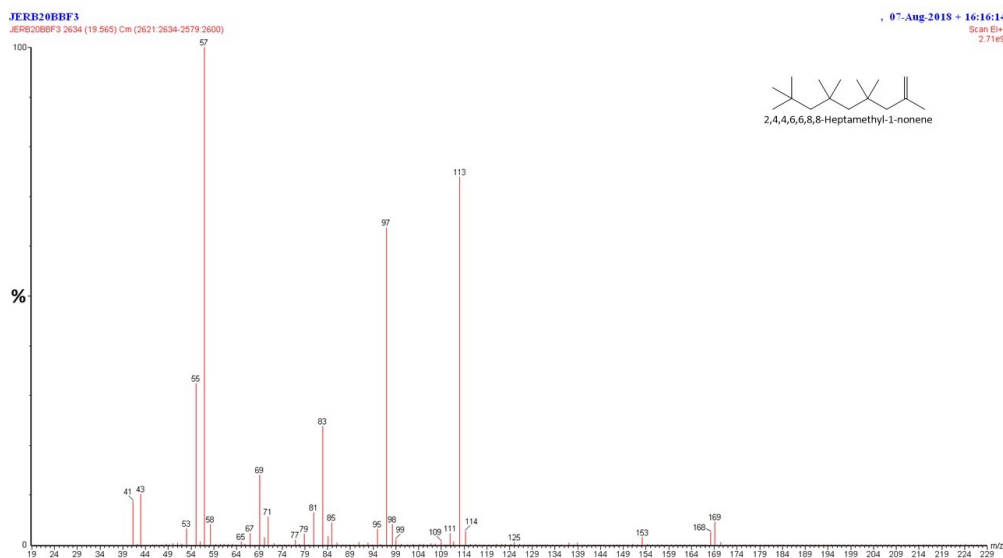


Figure 7.6 – The EI mass spectra of the α isomer of tetra-isobutene, characterised by cross reference to the NIST database.

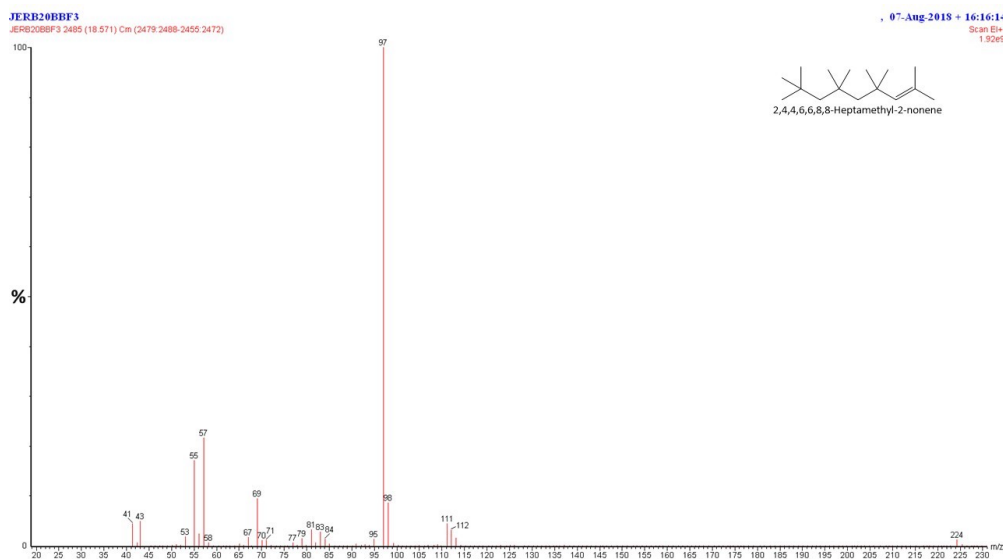


Figure 7.7 – The EI mass spectra of the β isomer of tetra-isobutene, characterised by cross reference to the NIST database.

7.2 Supplementary information for Chapter 4

7.2.1 Alkyl ASI characterisation

All ASIs are believed to be previously unreported novel compounds.

7.2.1.1 *N*-propyl ASI

ESI-MS: C₁₉H₃₃NO₂

[M-H]⁺ calculated mass 308.2584, measured mass 308.2589, mass accuracy -1.5 ppm

[M-Na]⁺ calculated mass 330.2404, measured mass 330.2405, mass accuracy -0.6 ppm

¹H-NMR spectroscopy (CDCl₃): 5.55 ppm (1 H, dt, J=15.0, 6.9 Hz), 5.26 (1 H, dt, J=15.0, 6.9 Hz), 3.46 (2 H, t, J=7.3 Hz), 2.86 (1 H, tt, J=8.4, 4.2 Hz), 2.74 (1 H, dd, J=16, 12 Hz), 2.50 (1 H, m), 2.46 (1 H, dd, J=16, 4 Hz), 2.34 (1 H, m), 1.98 (2 H, q, J=7.2 Hz), 1.59 (2 H, m), 1.27 (14 H, m), 0.90 (3 H, t), 0.88 (3 H, t)

EI-MS: 41 (8) 42 (3) 43 (10) 44 (1) 53 (3) 54 (4) 55 (13) 56 (3) 57 (3) 58 (2) 65 (1) 66 (2) 67 (8) 68 (3) 69 (5) 70 (1) 71 (1) 77 (2) 78 (1) 79 (6) 80 (5) 81 (15) 82 (3) 83 (4) 84 (5) 85 (2) 86 (1) 91 (1) 93 (1) 94 (2) 95 (5) 96 (2) 97 (2) 98 (4) 99 (6) 100 (1) 107 (1) 109 (2) 110 (1) 111 (2) 112 (7) 113 (2) 123 (1) 124 (1) 137 (1) 138 (1) **141 (100)** 142 (13) 143 (1) 152 (1) 153 (1) 154 (17) 155 (2) 166 (1) 167 (1) 168 (1) 180 (4) 181 (1) 182 (1) 193 (1) 194 (6) 195 (2) 196 (1) 208 (3) 209 (1) 210 (1) 222 (1) 236 (1) 252 (1) 307 (7) 308 (2)

GC-FID purity 99.0%

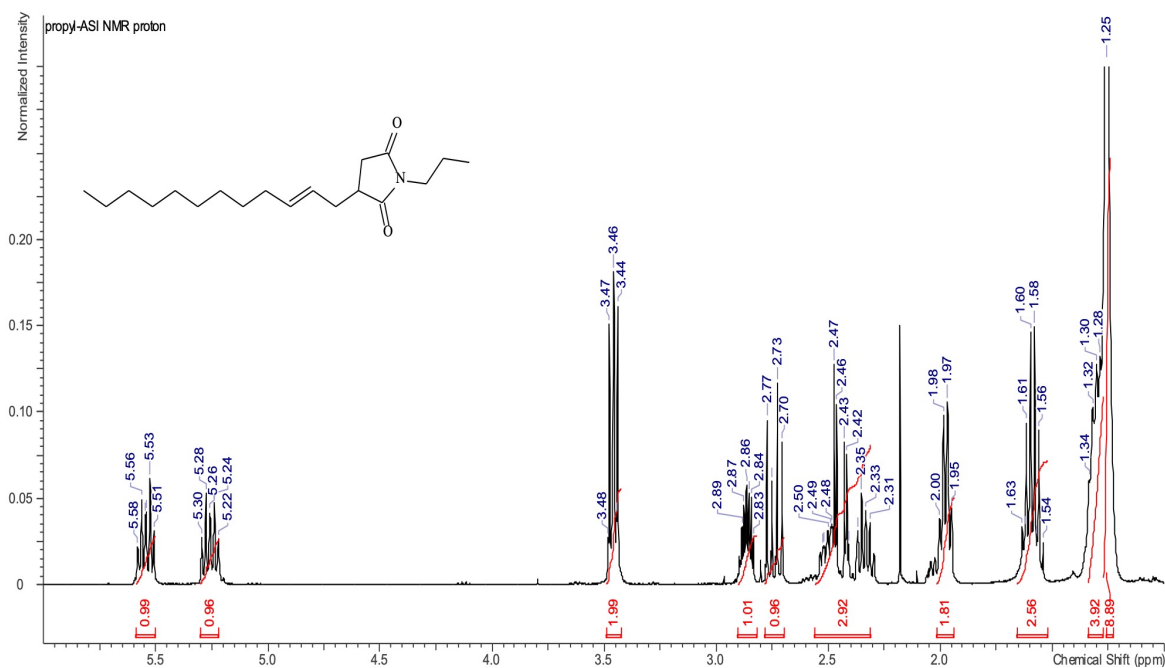
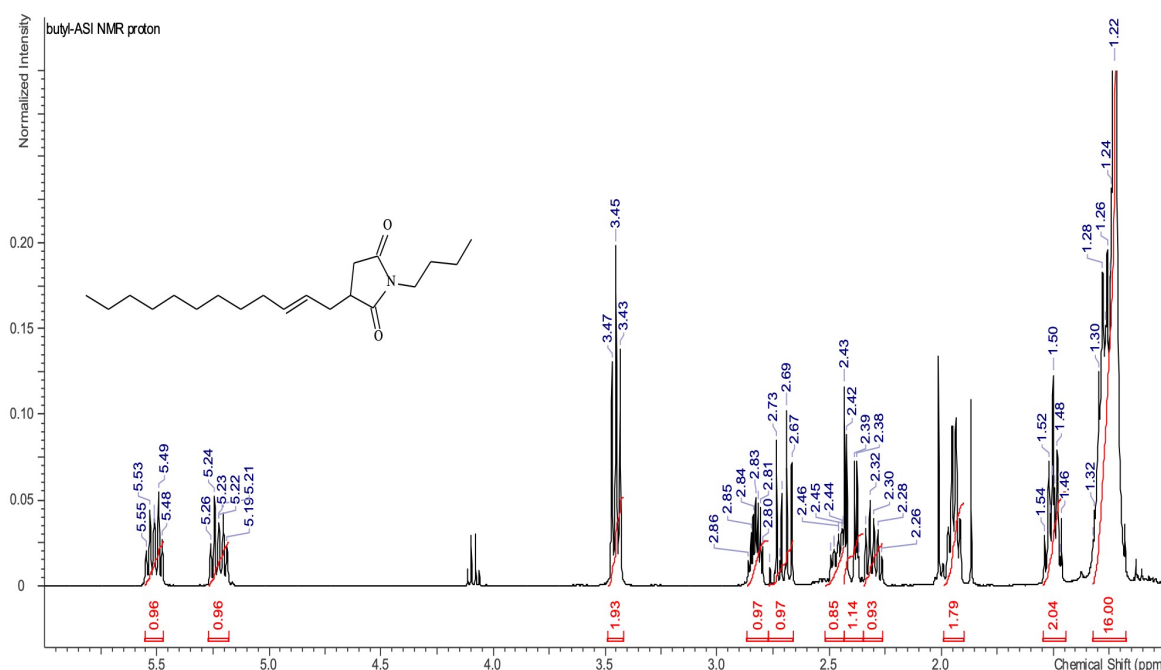


Figure 7.8 – ¹H-NMR spectrum of *N*-propyl ASI.

7.2.1.2 *N*-butyl ASI**ESI-MS:** C₂₀H₃₅NO₂[M-H]⁺ calculated mass 322.2741, measured mass 322.2750, mass accuracy -3.0 ppm[M-Na]⁺ calculated mass 344.2560, measured mass 344.2570, mass accuracy -3.0 ppm**¹H-NMR spectroscopy** (CDCl₃): 5.54 ppm (1 H, dt, J=15.1, 7.1 Hz), 5.25 ppm (1 H, dt, J=15.1, 7.1 Hz), 3.48 (2 H, t, J=7.3 Hz), 2.85 (1 H, tt, J=8.4, 4.2 Hz), 2.72 (1 H, dd, J=16, 12 Hz), 2.43 (1 H, dd, J=16, 4 Hz), 1.96 (2 H, q, J=7.3 Hz), 1.52 (2 H, m), 1.29 (18 H, m), 0.91 (3 H, t), 0.87 (3 H, t)**EI-MS:** 41 (3) 42 (1) 43 (4) 53 (1) 54 (1) 55 (6) 56 (1) 57 (2) 67 (3) 68 (1) 69 (2) 70 (1) 71 (1) 77 (1) 79 (3) 80 (1) 81 (6) 82 (1) 83 (2) 84 (2) 85 (1) 93 (1) 95 (2) 96 (1) 97 (1) 98 (2) 99 (4) 100 (3) 109 (1) 110 (1) 111 (1) 112 (4) 113 (3) 126 (2) 127 (2) 138 (2) 154 (3) **155 (100)** 156 (7) 157 (1) 167 (1) 168 (8) 169 (1) 182 (1) 194 (2) 208 (3) 209 (1) 222 (1) 223 (1) 236 (1) 250 (1) 266 (1) 321 (4) 322 (1)**GC-FID purity** 98.0%Figure 7.9 – ¹H-NMR spectrum of *N*-butyl ASI.7.2.1.3 *N*-pentyl ASI**ESI-MS:** C₂₁H₃₇NO₂[M-H]⁺ calculated mass 336.2897, measured mass 336.2897, mass accuracy 0.1 ppm[M-Na]⁺ calculated mass 358.2717, measured mass 358.2715, mass accuracy -0.5 ppm**¹H-NMR spectroscopy** (CDCl₃): 5.54 ppm (1 H, dt, J=15.1, 7.1 Hz), 5.25 (1 H, dt, J=15.1, 7.1 Hz), 3.47 (2 H, t, J=7.3 Hz), 2.86 (1 H, m), 2.73 (1 H, dd, J=16, 12 Hz), 2.49 (1 H, m), 2.44 (1 H, dd, J=16, 4 Hz), 2.34 (1 H, m), 1.98 (2 H, q, J=7.3 Hz), 1.55 (2 H, m), 1.28 (18 H, m), 0.88 (6 H, m)**EI-MS:** 41 (5) 42 (2) 43 (8) 44 (1) 53 (1) 54 (2) 55 (9) 56 (2) 57 (3) 65 (1) 66 (1) 67 (6) 68 (2) 69 (5) 70 (2) 71 (2) 77 (1) 79 (5) 80 (2) 81 (11) 82 (2) 83 (3) 84 (4) 85 (2) 86 (1) 91 (1) 93 (1) 94 (1) 95 (4) 96 (2) 97 (2) 98 (3) 99 (7) 100 (11) 101 (1) 107 (1) 109 (2) 110 (1) 111 (2) 112 (5) 113 (9) 114 (3) 123 (1) 124 (1) 125 (1) 126 (9) 127 (8) 128 (1) 138 (1) 139 (1) 140 (2) 141 (2) 151 (1) 152 (4) 153 (1) 154 (3) 166 (1) 167 (1) 168 (5) **169 (100)** 170 (11) 171 (1) 180 (1) 181 (1) 182 (14) 183 (2) 196 (1) 208 (3) 209 (1) 210 (1) 222 (5) 223 (2) 224 (1) 236 (3) 237 (1) 250 (1) 264 (1) 278 (1) 280 (1) 335 (6) 336 (2)**GC-FID purity** 97.7%

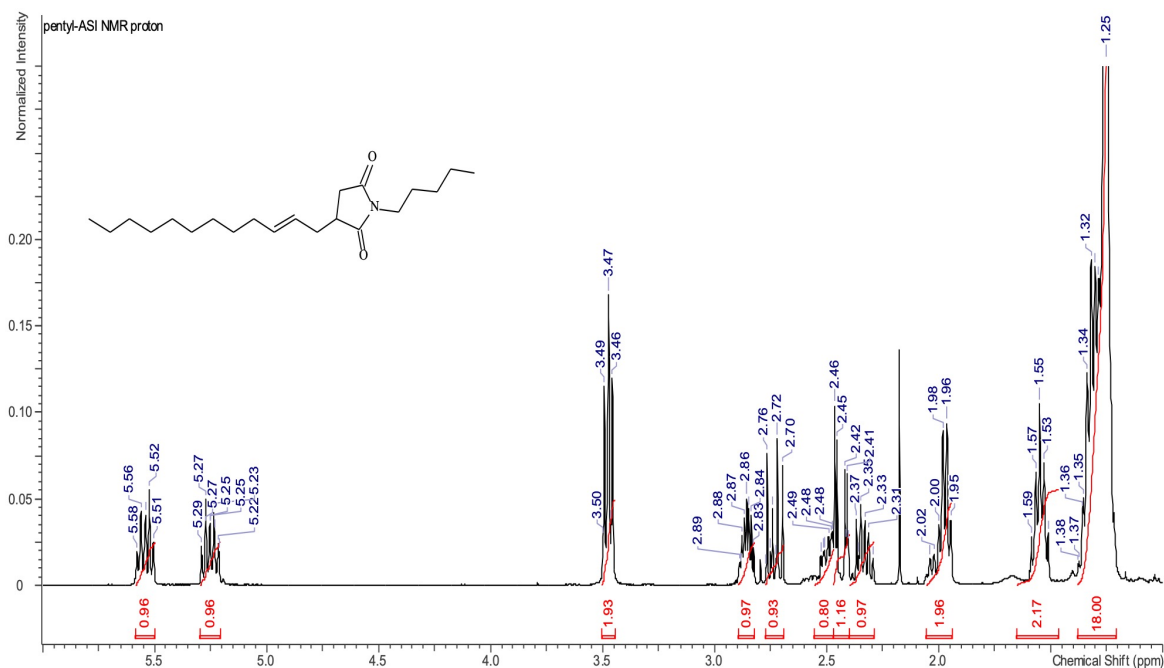


Figure 7.10 – $^1\text{H-NMR}$ spectrum of *N*-pentyl ASI.

7.2.1.4 *N*-hexyl ASI

ESI-MS: $\text{C}_{22}\text{H}_{39}\text{NO}_2$

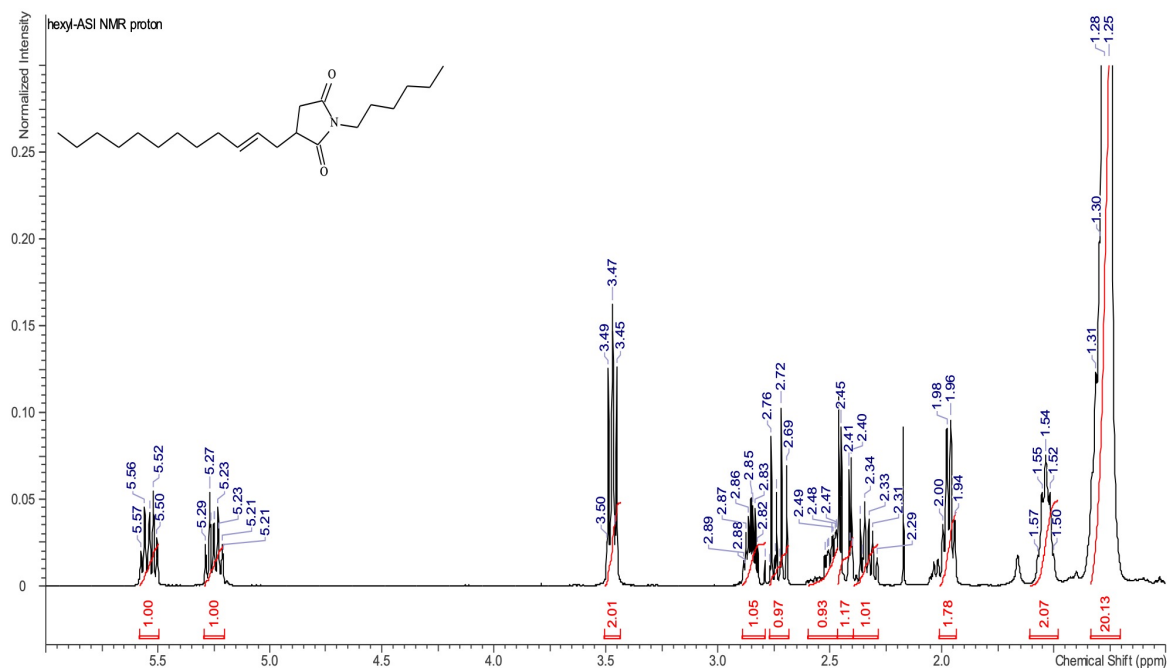
$[\text{M-H}]^+$ calculated mass 350.3054, measured mass 350.3061, mass accuracy -2.2 ppm

$[\text{M-Na}]^+$ calculated mass 372.2873, measured mass 372.2878, mass accuracy -1.3 ppm

$^1\text{H-NMR}$ spectroscopy (CDCl_3): 5.54 ppm (1 H, dt, $J=15$, 7 Hz), 5.25 (1 H, dt, $J=15$, 7 Hz), 3.47 (2 H, t, $J=7.3$ Hz), 2.85 (1 H, m), 2.73 (1 H, dd, $J=16$, 12 Hz), 2.49 (1 H, m), 2.43 (1 H, dd, $J=16$, 4 Hz), 2.33 (1 H, m), 1.97 (2 H, q, $J=7.3$ Hz), 1.54 (2 H, m), 1.27 (20 H, m), 0.88 (6 H, m)

EI-MS: 41 (10) 42 (4) 43 (17) 44 (2) 53 (3) 54 (6) 55 (25) 56 (6) 57 (7) 58 (1) 65 (2) 66 (2) 67 (14) 68 (5) 69 (11) 70 (3) 71 (4) 72 (1) 77 (2) 78 (1) 79 (10) 80 (5) 81 (25) 82 (6) 83 (9) 84 (11) 85 (4) 86 (1) 91 (2) 92 (1) 93 (3) 94 (2) 95 (10) 96 (4) 97 (5) 98 (7) 99 (15) 100 (52) 101 (3) 102 (1) 105 (1) 107 (1) 108 (1) 109 (5) 110 (3) 111 (4) 112 (10) 113 (24) 114 (4) 115 (1) 121 (1) 122 (1) 123 (2) 124 (2) 125 (2) 126 (18) 127 (10) 128 (2) 135 (1) 136 (1) 137 (1) 138 (2) 139 (1) 140 (5) 141 (7) 142 (1) 151 (1) 152 (1) 153 (2) 154 (8) 155 (3) 165 (1) 166 (4) 167 (1) 168 (5) 169 (1) 178 (1) 179 (1) 180 (1) 181 (1) 182 (15) **183 (100)** 184 (18) 185 (2) 194 (1) 195 (2) 196 (29) 197 (4) 208 (1) 209 (1) 210 (2) 221 (1) 222 (5) 223 (1) 224 (1) 236 (10) 237 (3) 238 (2) 250 (5) 251 (2) 252 (1) 264 (2) 265 (1) 266 (1) 278 (2) 279 (1) 292 (1) 294 (1) 306 (1) 308 (1) 320 (1) 334 (1) 348 (2) 349 (14) 350 (5)

GC-FID purity 98.4%

Figure 7.11 – ¹H-NMR spectrum of *N*-hexyl ASI.

7.2.1.5 *N*-heptyl ASI

ESI-MS: C₂₃H₄₁NO₂

[M-H]⁺ calculated mass 364.3210, measured mass 364.3216, mass accuracy -1.8 ppm

[M-Na]⁺ calculated mass 386.3030, measured mass 386.3032, mass accuracy -0.6 ppm

¹H-NMR spectroscopy (CDCl₃): 5.54 ppm (1 H, dt, J=15, 7 Hz), 5.25 (1 H, dt, J=15, 7 Hz), 3.47 (2 H, t, J=7.3 Hz), 2.86 (1 H, m), 2.73 (1 H, dd, J=16, 12 Hz), 2.50 (1 H, m), 2.43 (1 H, dd, J=16, 4 Hz), 2.34 (1 H, m), 1.99 (2 H, q, J=7.3 Hz), 1.54 (2 H, m), 1.28 (22 H, m), 0.88 (6 H, m)

EI-MS: 41 (6) 42 (2) 43 (8) 44 (1) 53 (2) 54 (3) 55 (16) 56 (4) 57 (6) 58 (1) 65 (1) 66 (1) 67 (9) 68 (3) 69 (8) 70 (2) 71 (2) 72 (1) 77 (1) 78 (1) 79 (6) 80 (3) 81 (18) 82 (4) 83 (7) 84 (7) 85 (2) 86 (1) 91 (1) 93 (2) 94 (2) 95 (8) 96 (4) 97 (5) 98 (8) 99 (12) 100 (53) 101 (3) 102 (1) 107 (1) 108 (1) 109 (3) 110 (2) 111 (3) 112 (9) 113 (24) 114 (3) 115 (1) 121 (1) 123 (1) 124 (1) 125 (1) 126 (11) 127 (6) 128 (1) 136 (1) 137 (1) 138 (2) 139 (1) 140 (4) 141 (3) 142 (1) 151 (1) 152 (1) 153 (1) 154 (6) 155 (7) 156 (1) 165 (1) 166 (1) 167 (1) 168 (5) 169 (1) 179 (1) 180 (3) 181 (1) 182 (3) 192 (1) 194 (1) 196 (5) **197 (100)** 198 (10) 199 (1) 208 (1) 209 (1) 210 (18) 211 (2) 222 (1) 224 (1) 236 (3) 237 (1) 238 (1) 250 (6) 251 (2) 252 (1) 264 (3) 265 (1) 266 (1) 278 (1) 279 (1) 292 (1) 306 (1) 308 (1) 320 (1) 334 (1) 362 (1) 363 (9) 364 (3) 365 (1)

GC-FID purity 99.1%

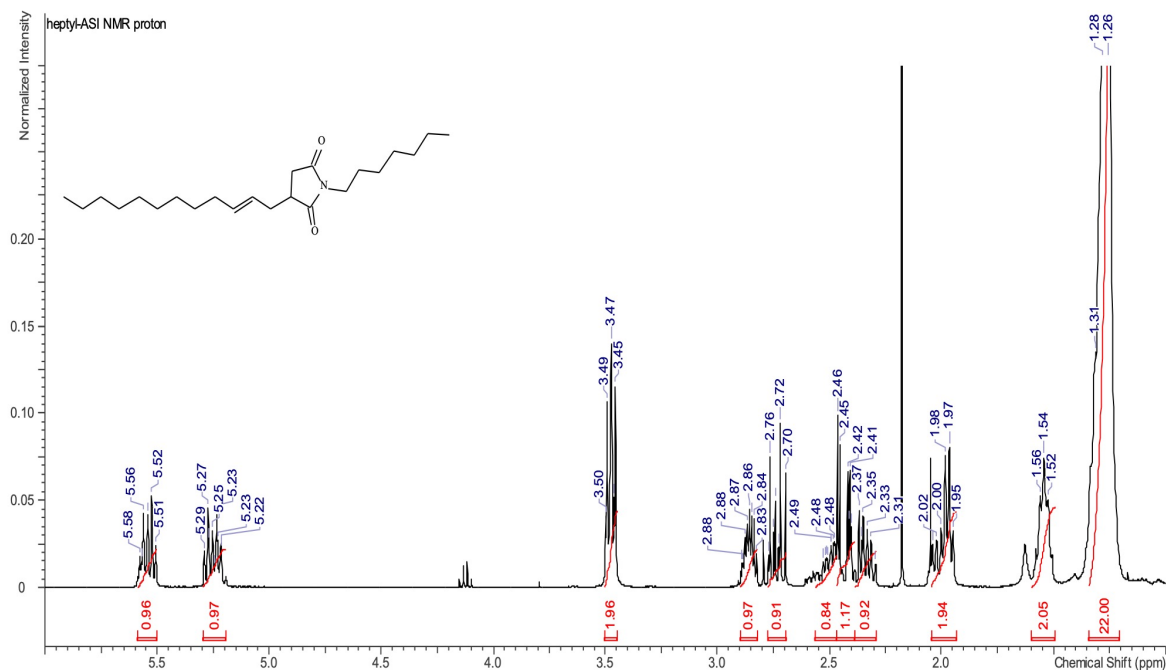


Figure 7.12 – $^1\text{H-NMR}$ spectrum of *N*-heptyl ASI.

7.2.1.6 H_2 -*N*-butyl ASI

ESI-MS: $\text{C}_{20}\text{H}_{37}\text{NO}_2$

$[\text{M-H}]^+$ calculated mass 324.2897, measured mass 324.2900, mass accuracy -1.0 ppm

$[\text{M-Na}]^+$ calculated mass 346.2717, measured mass 346.2717, mass accuracy -0.1 ppm

$^1\text{H-NMR}$ spectroscopy (CDCl_3): 3.49 ppm (2 H, t, $J=7.6$ Hz), 2.81 (1 H, dd, $J=16, 12$ Hz), 2.77 (1 H, m), 2.37 (1 H, dd, $J=16, 4$ Hz), 3.83 (4 H, m), 1.28 (24 H, m), 0.92 (3 H, t), 0.88 (3 H, t)

EI-MS: 41 (5) 42 (2) 43 (7) 44 (1) 53 (1) 54 (1) 55 (8) 56 (3) 57 (4) 67 (1) 68 (1) 69 (4) 70 (1) 71 (1) 72 (1) 81 (1) 82 (1) 83 (4) 84 (2) 85 (1) 95 (1) 96 (1) 97 (2) 98 (3) 99 (5) 100 (3) 109 (1) 111 (1) 112 (6) 113 (6) 114 (1) 125 (1) 126 (6) 127 (2) 138 (2) 140 (1) 154 (4) **155 (100)** 156 (9) 157 (1) 167 (1) 168 (26) 169 (3) 182 (1) 196 (1) 210 (1) 224 (1) 268 (6) 269 (1) 281 (1) 322 (1) 323 (5) 324 (2)

GC-FID purity 97.7%

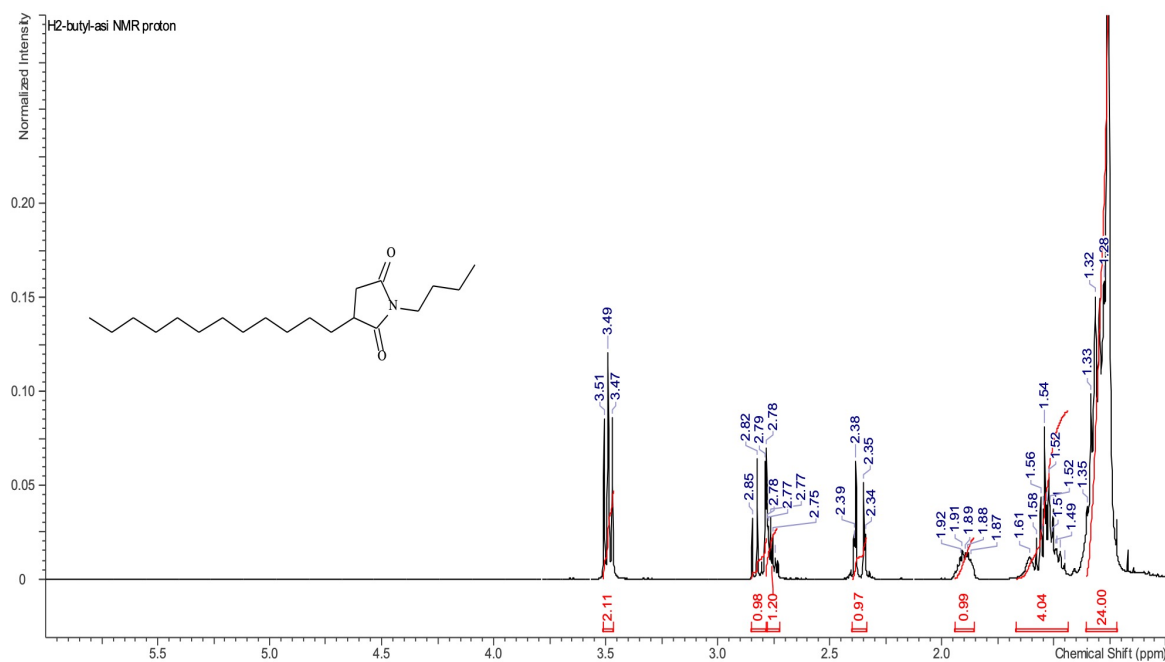


Figure 7.13 – ^1H -NMR spectrum of H_2 -*N*-butyl ASI.

7.2.2 Autoxidation product identification

Table 7.3 – Summary of EI fragmentation patterns obtained using accurate mass GC-EI-MS for compounds **1-4**, **6**, **7** and **13**. and their comparison to NIST library data.

Peak	Name	EI Fragmentation Pattern (this work)	EI Fragmentation Pattern (NIST)
1	octane	38 (1) 39 (23) 40 (4) 41 (84)	30 (1) 38 (1) 39 (12) 40 (2) 41
		42 (22) 43 (56) 44 (5) 51 (1)	(44) 42 (15) 43 (100) 44 (3)
		52 (1) 53 (4) 54 (2) 55 (24)	51 (1) 53 (2) 54 (1) 55 (11) 56
		56 (38) 57 (71) 58 (4) 65 (1)	(18) 57 (33) 58 (1) 69 (2) 70
		67 (1) 70 (31) 71 (64) 72 (4)	(12) 71 (20) 72 (1) 84 (7) 85
		84 (32) 85 (100) 86 (12) 114	(26) 86 (2) 114 (6) 115 (1)
		(34) 115 (3)	
2	nonane	39 (11) 40 (2) 41 (44) 42 (13)	30 (1) 39 (7) 40 (1) 41 (31) 42
		43 (72) 44 (3) 51 (1) 53 (3) 54	(12) 43 (100) 44 (3) 53 (1) 54
		(1) 55 (17) 56 (23) 57 (100)	(1) 55 (11) 56 (17) 57 (76) 58
		58 (5) 67 (1) 68 (1) 70 (20) 71	(4) 69 (3) 70 (12) 71 (22) 72
		(33) 72 (2) 83 (1) 84 (17) 85	(1) 84 (7) 85 (26) 86 (2) 98 (3)
		(59) 86 (5) 98 (11) 99 (22) 128	99 (6) 128 (4) 129 (1)
		(25) 129 (2)	

Table 7.3 – Summary of EI fragmentation patterns obtained using accurate mass GC-EI-MS for compounds **1-4**, **6**, **7** and **13**. and their comparison to NIST library data.

Peak	Name	EI Fragmentation Pattern (this work)	EI Fragmentation Pattern (NIST)
3	decanal	38 (1) 39 (28) 40 (3) 41 (100)	30 (1) 31 (2) 38 (1) 39 (19) 40
		42 (32) 43 (73) 44 (52) 45 (16)	(3) 41 (81) 42 (30) 43 (100)
		46 (1) 51 (2) 52 (1) 53 (10) 54	44 (54) 45 (17) 46 (1) 51 (1)
		(23) 55 (87) 56 (56) 57 (84)	52 (1) 53 (5) 54 (15) 55 (62)
		58 (11) 59 (1) 65 (1) 66 (8) 67	56 (43) 57 (62) 58 (5) 59 (1)
		(61) 68 (70) 70 (79) 71 (53)	60 (3) 65 (1) 66 (4) 67 (26) 68
		72 (17) 77 (1) 79 (6) 80 (3) 81	(34) 69 (30) 70 (47) 71 (34) 72
		(62) 82 (94) 83 (66) 84 (37) 85	(7) 73 (3) 77 (1) 79 (1) 80 (1)
		(10) 86 (4) 91 (1) 93 (1) 94 (2)	81 (22) 82 (33) 83 (28) 84 (16)
		95 (55) 96 (52) 97 (16) 98 (1)	85 (4) 86 (1) 87 (1) 94 (1) 95
		99 (6) 109 (28) 110 (46) 111	(17) 96 (15) 97 (5) 98 (1) 99
		(5) 112 (71) 113 (11) 123 (2)	(2) 100 (1) 109 (7) 110 (12)
		127 (1) 128 (17) 129 (1) 138	111 (1) 112 (22) 113 (3) 123
		(10) 139 (1) 141 (1) 156 (1)	(1) 128 (4) 129 (1) 138 (2)
4	<i>N</i> -butyl succinimide	39 (5) 40 (1) 41 (17) 42 (7) 43	41 (23) 42 (10) 43 (8) 44 (5) 45
		(1) 44 (11) 52 (1) 53 (2) 54 (4)	(18) 54 (3) 55 (46) 56 (38) 57
		55 (48) 56 (35) 57 (6) 58 (3)	(8) 58 (2) 70 (3) 71 (3) 72 (12)
		70 (1) 71 (1) 72 (23) 82 (18)	82 (11) 84 (25) 85 (12) 99 (2)
		84 (57) 85 (19) 86 (1) 98 (4)	100 (100) 101 (13) 112 (13)
		99 (4) 100 (93) 101 (26) 102	113 (51) 114 (5) 126 (10) 127
		(2) 112 (21) 113 (100) 116	(1) 140 (4) 155 (28) 156 (5)
		(1) 126 (24) 138 (2) 140 (5)	
		155 (58) 156 (6)	
		6	2-undecenal
42 (15) 43 (41) 44 (1) 51 (3)	40 (4) 41 (94) 42 (22) 43 (82)		
52 (2) 53 (15) 54 (16) 55 (66)	50 (1) 51 (2) 52 (1) 53 (10) 54		
56 (22) 57 (67) 65 (2) 66 (2)	(18) 55 (80) 56 (29) 57 (89)		
67 (30) 68 (25) 70 (100) 71	58 (4) 60 (1) 63 (1) 65 (2) 66		
(19) 72 (1) 77 (2) 79 (20) 80	(3) 67 (23) 68 (18) 69 (47) 70		
(10) 81 (28) 82 (50) 83 (63)	(100) 71 (13) 72 (2) 73 (1) 75		
84 (31) 85 (10) 86 (12) 87 (1)	(1) 77 (2) 78 (1) 79 (10) 80 (6)		
91 (1) 93 (13) 94 (8) 95 (18)	81 (19) 82 (30) 83 (57) 84 (26)		
96 (14) 97 (31) 98 (28) 99 (3)	85 (4) 86 (7) 87 (1) 91 (2) 92		
107 (11) 108 (9) 109 (7) 111	(1) 93 (6) 94 (4) 95 (11) 96 (7)		
(22) 112 (8) 121 (36) 122 (8)	97 (18) 98 (16) 99 (1) 100 (6)		
123 (1) 124 (19) 125 (5) 126	107 (4) 108 (3) 109 (3) 110 (1)		
(1) 135 (7) 136 (3) 137 (7) 139	111 (12) 112 (9) 113 (2) 121		
(1) 141 (2) 150 (6) 151 (1) 153	(10) 122 (2) 123 (1) 124 (9)		
(1) 168 (1)	125 (3) 126 (1) 135 (2) 137 (2)		
	138 (1) 139 (1) 150 (3) 151 (1)		
	168 (1)		

Table 7.3 – Summary of EI fragmentation patterns obtained using accurate mass GC-EI-MS for compounds **1-4**, **6**, **7** and **13**. and their comparison to NIST library data.

Peak	Name	EI Fragmentation Pattern (this work)	EI Fragmentation Pattern (NIST)
7	2-dodecenal	38 (1) 39 (28) 40 (4) 41 (79) 42 (15) 43 (52) 51 (2) 52 (1) 53 (14) 54 (14) 55 (56) 56 (26) 57 (52) 58 (3) 65 (2) 66 (4) 67 (36) 68 (23) 70 (100) 71 (21) 72 (1) 77 (2) 78 (1) 79 (24) 80 (13) 81 (37) 82 (49) 83 (71) 84 (39) 85 (6) 86 (2) 91 (2) 93 (18) 94 (15) 95 (25) 96 (48) 97 (43) 98 (35) 99 (2) 107 (12) 108 (10) 109 (12) 110 (11) 111 (29) 112 (18) 113 (1) 114 (5) 121 (34) 122 (10) 123 (5) 124 (1) 125 (6) 126 (9) 127 (4) 128 (7) 135 (24) 136 (7) 137 (1) 138 (19) 139 (6) 140 (2) 141 (12) 142 (1) 149 (2) 151 (5) 154 (3) 155 (8) 156 (1) 164 (7) 165 (2) 166 (1) 182 (2)	30 (2) 31 (7) 37 (1) 38 (1) 39 (26) 40 (5) 41 (89) 42 (21) 43 (94) 44 (3) 45 (3) 50 (1) 51 (2) 52 (1) 53 (11) 54 (16) 55 (74) 56 (28) 57 (76) 58 (4) 59 (3) 65 (2) 66 (3) 67 (25) 68 (20) 69 (43) 70 (100) 71 (22) 72 (2) 73 (1) 74 (2) 77 (2) 78 (1) 79 (10) 80 (7) 81 (22) 82 (28) 83 (62) 84 (29) 85 (5) 86 (2) 91 (1) 93 (6) 94 (5) 95 (13) 96 (20) 97 (25) 98 (19) 99 (2) 100 (4) 107 (4) 108 (3) 109 (5) 110 (4) 111 (12) 112 (6) 113 (1) 114 (4) 121 (9) 122 (2) 123 (1) 124 (1) 125 (3) 126 (4) 127 (1) 135 (4) 136 (1) 137 (1) 138 (5) 139 (2) 153 (1) 164 (2) 182 (1)
13	n-decanoic acid	31 (1) 38 (1) 39 (16) 40 (4) 41 (45) 42 (10) 43 (39) 45 (12) 53 (6) 54 (5) 55 (41) 56 (8) 57 (51) 58 (2) 59 (1) 60 (93) 61 (11) 67 (7) 68 (9) 70 (9) 71 (48) 73 (100) 74 (9) 81 (6) 82 (3) 83 (23) 84 (10) 85 (11) 87 (20) 94 (2) 95 (3) 96 (7) 97 (12) 98 (5) 99 (1) 101 (8) 102 (1) 109 (1) 110 (8) 111 (4) 112 (32) 115 (19) 116 (1) 123 (2) 124 (3) 125 (23) 129 (78) 130 (7) 136 (2) 137 (1) 138 (4) 139 (3) 141 (24) 142 (3) 143 (16) 144 (2) 152 (1) 167 (7) 168 (1) 172 (13) 173 (1)	30 (1) 31 (2) 39 (13) 40 (2) 41 (48) 42 (11) 43 (44) 44 (2) 45 (7) 51 (1) 53 (4) 54 (3) 55 (36) 56 (9) 57 (42) 58 (2) 59 (4) 60 (100) 61 (14) 62 (1) 65 (1) 67 (3) 68 (3) 69 (19) 70 (8) 71 (34) 72 (2) 73 (89) 74 (8) 75 (1) 79 (1) 81 (2) 82 (2) 83 (11) 84 (7) 85 (1) 86 (1) 87 (14) 88 (1) 93 (1) 95 (1) 97 (4) 98 (4) 99 (1) 101 (5) 102 (1) 110 (5) 111 (2) 112 (8) 113 (4) 115 (10) 116 (1) 125 (1) 129 (33) 130 (3) 136 (1) 143 (5) 144 (1) 155 (1) 172 (7) 173 (1)

Table 7.4 – Accurate mass data for compounds **1-4**, **6**, **7** and **13**.

Peak	m/z (measured)	m/z (calculated)	Mass accuracy / ppm	Chemical Formula
1	114.1409	114.1409	0.0	C ₈ H ₁₈
2	128.1569	128.1565	3.1	C ₉ H ₂₀
3	156.1493	156.1514	-13.1	C ₁₀ H ₂₀ O
4	155.0953	155.0946	4.5	C ₈ H ₁₃ NO ₂
6	168.1544	168.1514	17.8	C ₁₁ H ₂₀ O
7	182.1655	182.1671	-8.8	C ₁₂ H ₂₂ O
13	172.1457	172.1463	-3.5	C ₁₀ H ₂₀ O ₂

7.2.3 Analysis of condensed-volatiles from the autoxidation of model lubricants with and without *N*-butyl ASI

When model lubricants were oxidised, the reactor exhaust gases were passed through a 0°C cold trap to condense products that had evaporated from the reactor. The volatile products include water and short chain hydrocarbons. As a result, separate aqueous and organic layers form.

The volatiles collected during the autoxidation of *N*-butyl ASI in squalane were compared to those collected from the autoxidation of pure squalane. The volatiles were analysed by GC-EI-MS. The samples were prepared using the same methods reported for model lubricant analysis. Aqueous samples were dissolved in acetone instead of ethyl acetate to ensure proper dissolution.

Samples from the organic layer of the volatiles contained very similar products for both the pure squalane and the ASI dissolved in squalane model lubricants. Neither squalane or *N*-butyl ASI were observed showing they were not significantly volatile at the reaction temperature of 170 °C.

A clear difference was shown by the aqueous layer of volatiles. The chromatogram of aqueous volatiles obtained from pure squalane is shown in Figure 7.14. Two extra peaks were shown when *N*-butyl ASI was present in the model lubricant (Figure 7.15). EI-MS identified the two peaks as *N*-butyl succinimide (Figure 7.16, product **4**) and methyl *N*-butyl succinimide (Figure 7.16, product **5**).

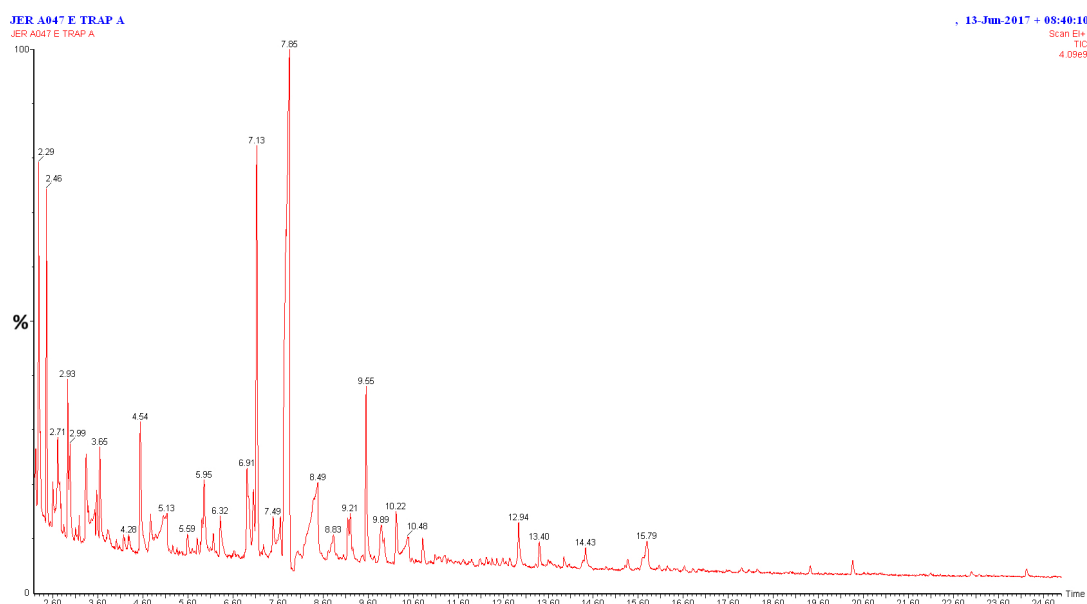


Figure 7.14 – The GC-MS TIC chromatogram from analysis of the aqueous phase of the volatiles condensed from exhaust gases during the autoxidation of squalane at 170 °C for 90 minutes. The products **4** and **5** cannot be observed.

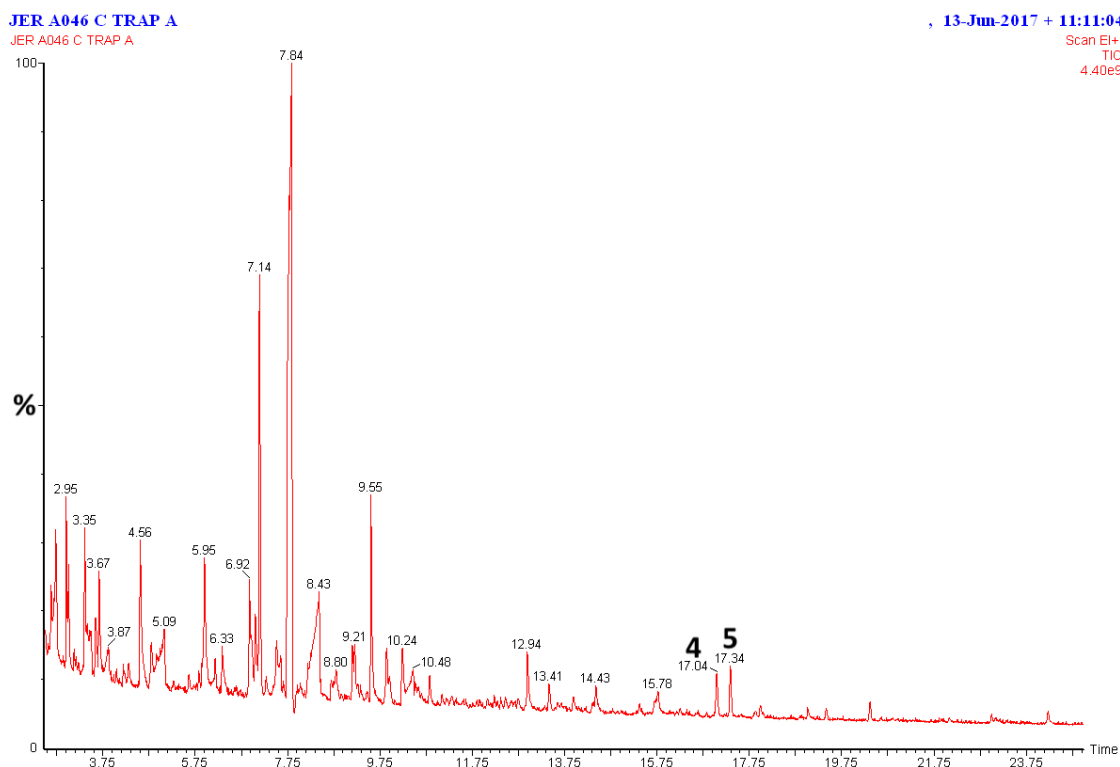


Figure 7.15 – The GC-MS TIC chromatogram from analysis of the aqueous phase of the volatiles condensed from exhaust gases during the autoxidation of a 5% (w/w) solution of *N*-butyl ASI in squalane at 170 °C for 90 minutes. The presence of products **4** and **5** were confirmed by their characteristic EI mass spectra.

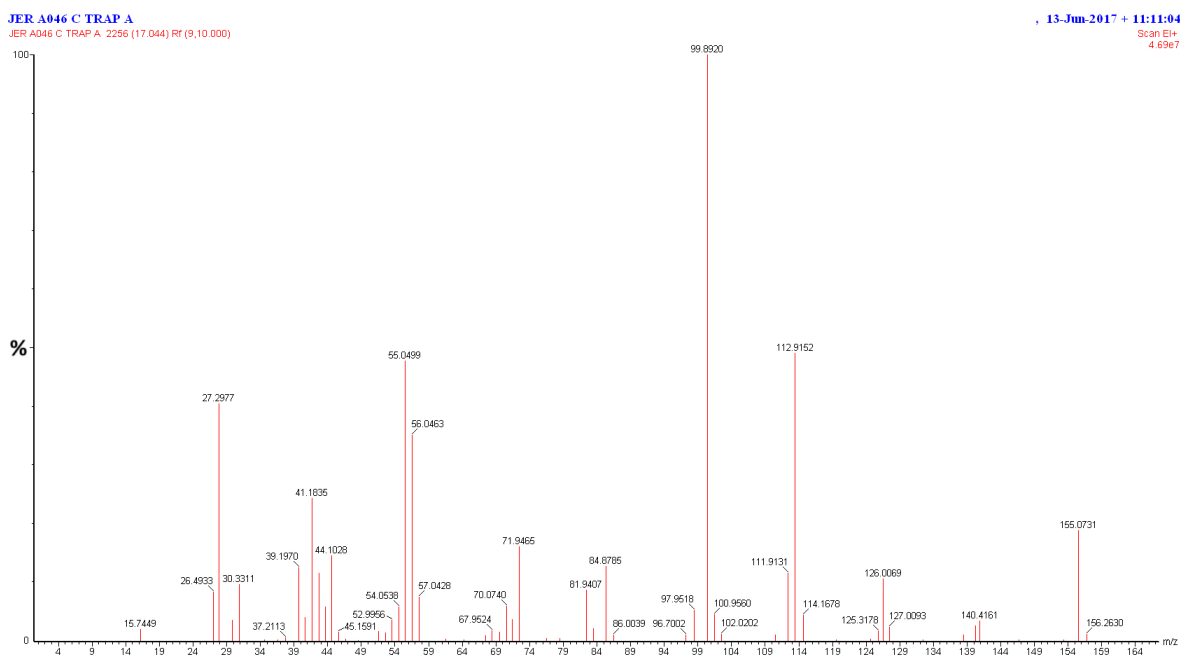


Figure 7.16 – The EI-MS spectrum of product **4** identified in the aqueous phase of the condensed exhaust gases from the autoxidation of a 5% (w/w) solution of *N*-butyl ASI in squalane at 170 °C for 90 minutes. Characterised by NIST database comparison. See Section 4.2.2.1 Page 97 and Section 7.2.2 Page 184 for further information.

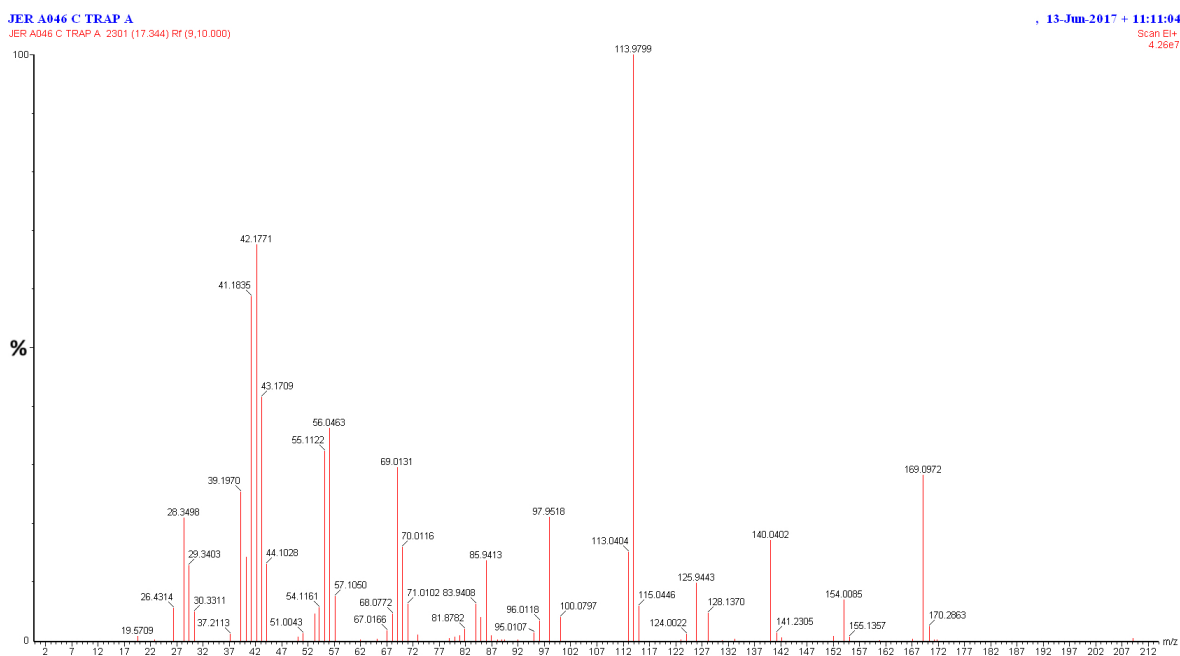


Figure 7.17 – The EI-MS spectrum of product **5** identified in the aqueous phase of the condensed exhaust gases from the autoxidation of a 5% (w/w) solution of *N*-butyl ASI in squalane at 170 °C for 90 minutes. See Section 4.2.2.1 Page 97 for further information.

7.3 Supplementary information for Chapter 5

7.3.1 Amino ASI characterisation

All ASIs are believed to be previously unreported novel compounds.

7.3.1.1 Diethylamino ASI

ESI-MS: C₂₂H₄₀N₂O₂

[M-H]⁺ calculated mass 365.3163, measured mass 365.3168, mass accuracy -1.5 ppm

[M-Na]⁺ calculated mass 387.2982, measured mass 387.2985, mass accuracy 0.8 ppm

¹H-NMR spectroscopy (CDCl₃): 5.53 ppm (1 H, t, J=15, 7 Hz), 5.28 (1 H, t, J=15, 7 Hz), 3.57 (2 H, t, J=6 Hz), 2.85 (1 H, m), 2.73 (1 H, m), 2.59 (2 H, m), 2.52 (4 H, m), 2.43 (1 H, m), 2.31 (1 H, m), 1.98 (2 H, m), 1.27 (14 H, bs), 0.99 (6 H, m), 0.88 (3 H, m)

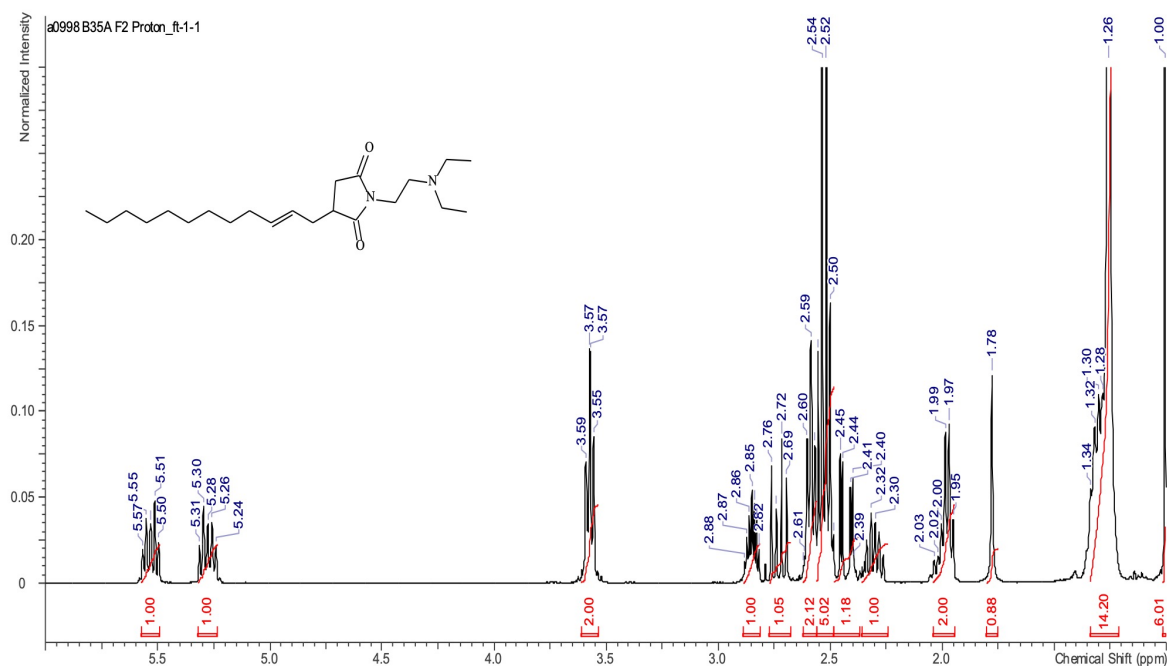


Figure 7.18 – ¹H-NMR spectrum of diethylamino alkenyl succinimide (DEA-ASI).

7.3.1.2 Dimethylamino ASI

ESI-MS: C₂₀H₃₆N₂O₂

[M-H]⁺ calculated mass 337.2850, measured mass 337.2846, mass accuracy 0.9 ppm

[M-Na]⁺ calculated mass 359.2669, measured mass 359.2663, mass accuracy 1.7 ppm

¹H-NMR spectroscopy (CDCl₃): 5.53 ppm (1 H, dt, J=15, 7 Hz), 5.28 (1 H, dt, J=15, 7 Hz), 3.61 (2 H, t, J=6 Hz), 2.88 (1 H, m), 2.75 (1 H, dd), 2.59 (2 H, m), 2.47 (2 H, m), 2.43 (1 H, m), 2.34 (1 H, m), 2.25 (6 H s), 1.98 (2 H, m), 1.27 (14 H, bs), 0.88 (3 H, m)

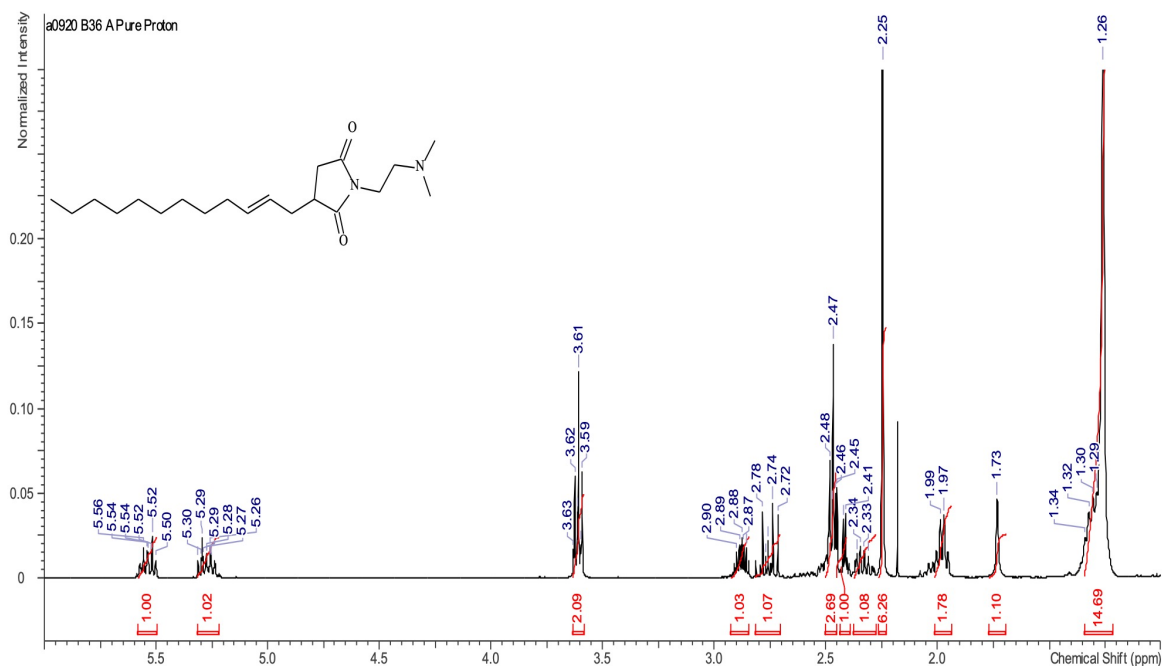


Figure 7.19 – $^1\text{H-NMR}$ spectrum of dimethylamino alkenyl succinimide (DMA-ASI).

7.3.1.3 Monomethylamino ASI

ESI-MS: $\text{C}_{19}\text{H}_{34}\text{N}_2\text{O}_2$

$[\text{M-H}]^+$ calculated mass 323.2693, measured mass 323.2090, mass accuracy 1.1 ppm

$[\text{M-Na}]^+$ calculated mass 345.2512, measured mass 345.2506, mass accuracy 1.8 ppm

$^1\text{H-NMR}$ spectroscopy (CDCl_3): 5.54 ppm (1 H, dt, $J=15, 7$ Hz), 5.28 (1 H, dt, $J=15, 7$ Hz), 3.63 (2 H, t, $J=6$ Hz), 2.89 (1 H, m), 2.77 (3 H, m), 2.46 (1 H, m), 2.42 (3 H, s), 2.33 (1 H, m), 1.98 (2 H, m), 1.27 (14 H, bs), 0.99 (6 H, m), 0.88 (3 H, m)

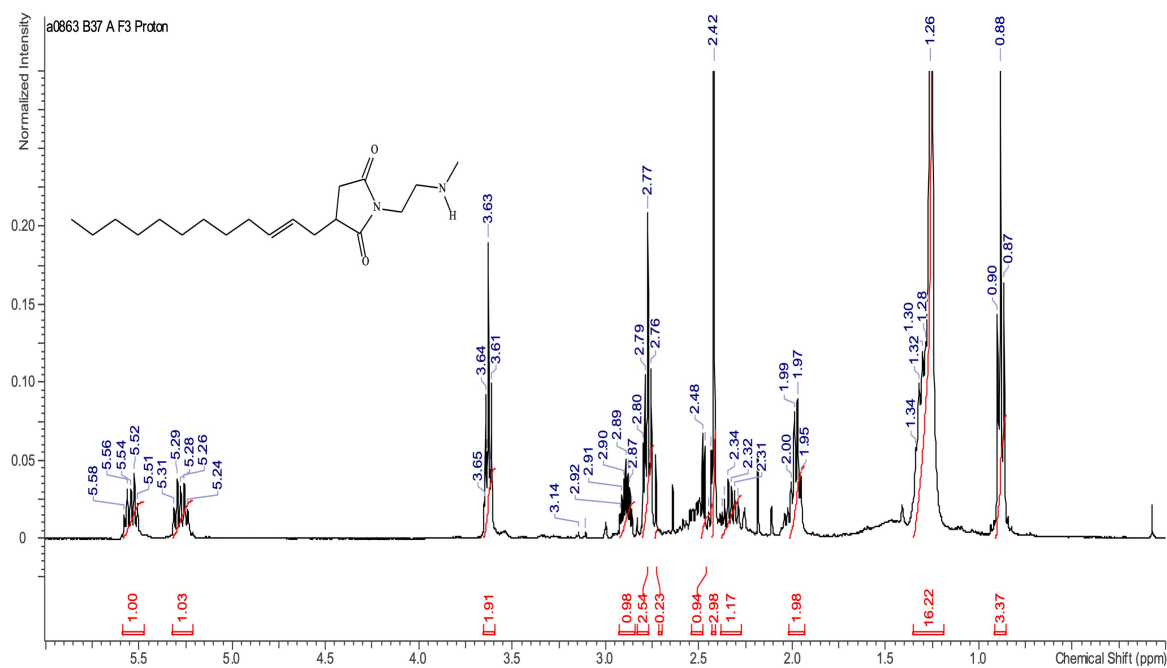


Figure 7.20 – $^1\text{H-NMR}$ spectrum of monomethylamino alkenyl succinimide (MMA-ASI).

7.3.1.4 H_2 -Dimethylamino ASI

ESI-MS: $\text{C}_{20}\text{H}_{38}\text{N}_2\text{O}_2$

$[\text{M-H}]^+$ calculated mass 339.3006, measured mass 339.3008, mass accuracy -0.6 ppm

$[\text{M-Na}]^+$ calculated mass 361.2825, measured mass 361.2823, mass accuracy -0.6 ppm

$^1\text{H-NMR}$ spectroscopy (CDCl_3): 3.61 (2 H, t, $J=6$ Hz), 2.83 (1 H, m), 2.80 (1 H, m), 2.49 (2 H, m), 2.38 (1 H, m), 2.25 (6 H, s), 1.89 (1 H, m), 1.51 (1 H, m), 1.27 (20 H, bs), 0.88 (3 H, m)

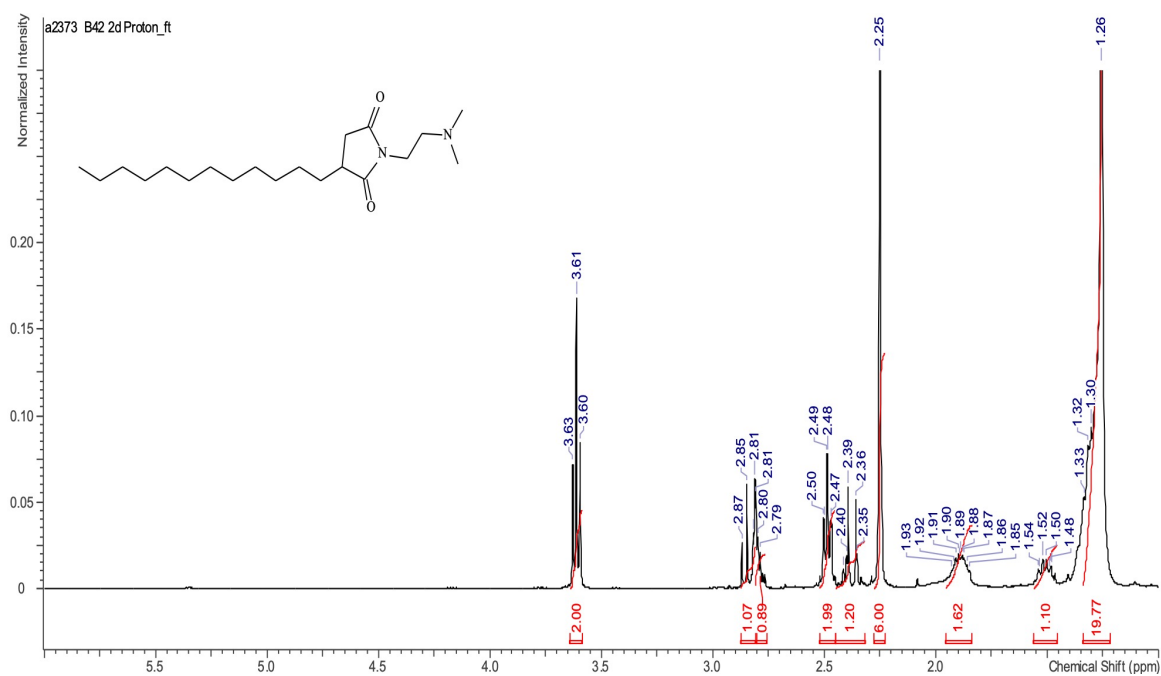


Figure 7.21 – ¹H-NMR spectrum of H₂-DMA-ASI.

Abbreviations

AO	antioxidant
API	American Petroleum Institute
ASI	alkenyl succinimide
ASTM	ASTM International, formerly known as American Society for Testing and Materials
ATR-FT-IR	attenuated total reflection - Fourier transform - infrared
BDE	bond dissociation enthalpy
BHT	butylated hydroxytoluene
CA	citric acid
CAH	citraconic anhydride
CEC	Coordinating European Council
COSY	correlation spectroscopy
DEA-ASI	diethylamino alkenyl succinimide
DEPT	distortionless enhancement by polarization transfer
DMA-ASI	dimethylamino alkenyl succinimide
DPA	diphenylamine
ECN	effective carbon number
EI	electron ionisation
ESI-MS	electron spray ionisation - mass spectrometry
EV	electric vehicle

FID	flame ionisation detector
FM	friction modifier
FPT	freeze pump thaw
GC-EI-MS	gas chromatography - electron ionisation - mass spectrometry
GC-FID	gas chromatography - flame ionisation detector
GC	gas chromatography
HALS	hindered amine light stabiliser
HMQC	heteronuclear multiple quantum coherence
HPLC	high performance liquid chromatography
IAH	itaconic anhydride
IEA	International Energy Agency
IR	infrared
IUPAC	International Union of Pure and Applied Chemistry
KV	kinematic viscosity
KV₁₀₀	kinematic viscosity measured at 100 °C
KV₄₀	kinematic viscosity measured at 40 °C
M_N	number averaged molecular weight
MA	maleic acid
MAH	maleic anhydride
MMA-ASI	monomethylamino alkenyl succinimide
MoDTC	molybdenum dithiocarbamate
MS	mass spectrometry

NIST	National Institute of Standards and Technology
NMR	nuclear magnetic resonance
PAO	polyalphaolefin
PIB	polyisobutene
PIBSA	polyisobutenyl succinic anhydride
PIBSI	polyisobutenyl succinimide
PPD	pour point depressant
RDBE	ring double bond equivalents
RMS	root mean square
SAH	succinic anhydride
SUV	sports utility vehicle
TAN	total acid number
TBN	total base number
TEOST	thermo-oxidation engine oil simulation test
TEPA	tetraethylenepentamine
TIC	total ion count
TMS	trimethylsilyl
ToF	time of flight
UK	United Kingdom
USA	United States of America
VII	viscosity index improver
ZDDP	zinc dialkyldithiophosphate

Bibliography

1. Fall, A.; Weber, B.; Pakpour, M.; Lenoir, N.; Shahidzadeh, N.; Fiscina, J.; Wagner, C.; Bonn, D. *Physical Review Letters* **2014**, *112*, 175502.
2. Davison, C. *Wear* **1957**, *1*, 155–159.
3. Jost, P., *Lubrication (tribology) education and research; a report on the present position and industry's needs*; HM Stationery Office, Department of Education and Science, Great Britain: 1966.
4. Holmberg, K.; Erdemir, A. *Friction* **2017**, *5*, 263–284.
5. Mobil 1™ Annual Protection <https://www.mobil.com/en/lubricants/for-personal-vehicles/our-products/products/mobil-1-annual-protection-5w-20> accessed on 02/09/2020.
6. Atkinson, D.; Brown, A. J.; Jilbert, D.; Lamb, G. In *Chemistry and Technology of Lubricants*; Springer Netherlands: Dordrecht, 2009, pp 293–324.
7. Prince, R. In *Chemistry and Technology of Lubricants*; Springer Netherlands: Dordrecht, 2009, pp 3–33.
8. Sinninghe Damsté, J. S.; Irene, W.; Rijpstra, C.; de Leeuw, J. W.; Schenck, P. *Organic Geochemistry* **1988**, *13*, 593–606.
9. Fahim, M. A.; Alsahhaf, T. A.; Elkilani, A. In *Fundamentals of Petroleum Refining*; Elsevier: 2010, pp 11–31.
10. Brown, M.; Fotheringham, J.; Hoyes, T.; Mortier, R.; Orszulik, S.; Randles, S.; Stroud, P. In *Chemistry and Technology of Lubricants*; Springer Netherlands: Dordrecht, 2009, pp 35–74.
11. Henderson, H.; Mack, P. D.; Steckle, W.; Swinney, B. In *SAE Technical Papers*, 1998.

BIBLIOGRAPHY

12. Stambaugh, R.; Kinker, B. In *Chemistry and Technology of Lubricants*; Springer Netherlands: Dordrecht, 2009, pp 153–187.
13. Rizvi, S. Q. A., *Lubricant Additives*, 2nd ed.; Rudnick, L. R., Ed.; CRC Press: Boca Raton, 2009; Chapter 5, pp 143–172.
14. Zheng, M.; Reader, G. T.; Hawley, J. G. *Energy Conversion and Management* **2004**, *45*, 883–900.
15. Forbes, E.; Groszek, A.; Neustadter, E. *Journal of Colloid and Interface Science* **1970**, *33*, 629.
16. Ghiassi, H.; Lignell, D.; Lighty, J. S. *Energy & Fuels* **2017**, *31*, 2236–2245.
17. Growney, D. J.; Mykhaylyk, O. O.; Middlemiss, L.; Fielding, L. A.; Derry, M. J.; Aragrag, N.; Lamb, G. D.; Armes, S. P. *Langmuir* **2015**, *31*, 10358–10369.
18. Bagi, S.; Sharma, V.; Aswath, P. B. *Carbon* **2018**, *136*, 395–408.
19. Vyavhare, K.; Bagi, S.; Patel, M.; Aswath, P. B. *Energy & Fuels* **2019**, *33*, 4515–4530.
20. Wood, R.; Ramkumar, P.; Wang, L.; Wang, T.; Nelson, K.; Yamaguchi, E.; Harrison, J.; Powrie, H.; Otin, N. *Tribology and Interface Engineering Series* **2005**, *48*, 109–121.
21. Colyer, C. C.; Gergel, W. C. *SAE Transactions* **1985**, *94*, 915–922.
22. Seddon, E.; Friend, C.; Roski, J. In *Chemistry and Technology of Lubricants*; Springer Netherlands: Dordrecht, 2009, pp 213–236.
23. Erhan, S. Z.; Sheng, Q.; Adhvaryu, A. *Journal of Applied Polymer Science* **2002**, *86*, 1684–1691.
24. Delgado, J; Castillo, E; Nieto, A **2015**.
25. Lacarriere, A.; Seguelong, T.; Harle, V.; Fabre, C. In *SAE Technical Papers*, 2015.
26. Horowitz, S.; Currie, J. K. *Journal of Dispersion Science and Technology* **1990**, *11*, 637–659.
27. Li, L.; Zhang, J.; Sun, H.; Xu, J.; Sun, D. *Colloids and Surfaces A: Physicochemical and Engineering Aspects* **2012**, *415*, 180–186.
28. Zhiwen, Y.; Chunxu, L.; Zuliang, L. *Speciality Petrochemicals* **2003**, *1*.
29. Anna, C.; Xuguang, W. *Mining And Metallurgy* **1994**, *3*.
30. Yang, L.; Xiao, J.; Shen, Y.; Liu, X.; Li, W.; Wang, W.; Yang, Y. *Environmental Science and Pollution Research* **2017**, *24*, 24214–24222.

31. Nguyen, T. M.; Jung, J.; Lee, C. W.; Cho, J. *Fuel* **2018**, *214*, 174–186.
32. Balzano, F.; Pucci, A.; Rausa, R.; Uccello-Barretta, G. *Polymer International* **2012**, *61*, 1256–1262.
33. Bezot, P.; Hesse-Bezot, C.; Diraison, C.; Faure, D. In *SAE Technical Papers*, 1998.
34. Ganguly, S.; Mohan, V.; Bhasu, V.; Mathews, E.; Adisheshaiah, K.; Kumar, A. *Colloids and Surfaces* **1992**, *65*, 243–256.
35. Ghaicha, L.; Leblanc, R. M.; Chattopadhyay, A. K. *Langmuir* **1993**, *9*, 288–293.
36. Shen, Y.; Duhamel, J. *Langmuir* **2008**, *24*, 10665–10673.
37. Pirouz, S.; Wang, Y.; Chong, J. M.; Duhamel, J. *The Journal of Physical Chemistry B* **2015**, *119*, 12202–12211.
38. Van der Merwe, M. M.; Landman, M.; van Rooyen, P. H.; Jordaan, J. H. L.; Otto, D. P. *Journal of Surfactants and Detergents* **2017**, *20*, 193–205.
39. Harrison, J. J.; Mijares, C. M.; Cheng, M. T.; Hudson, J. *Macromolecules* **2002**, *35*, 2494–2500.
40. Dyke, P. H.; Sutton, M.; Wood, D.; Marshall, J. *Chemosphere* **2007**, *67*, 1275–1286.
41. Liu, Q.; Wu, Y.-X.; Zhang, Y.; Yan, P.-F.; Xu, R.-W. *Polymer* **2010**, *51*, 5960–5969.
42. Vasilenko, I. V.; Frolov, A. N.; Kostjuk, S. V. *Macromolecules* **2010**, *43*, 5503–5507.
43. Vasilenko, I. V.; Shiman, D. I.; Kostjuk, S. V. *Journal of Polymer Science Part A: Polymer Chemistry* **2012**, *50*, 750–758.
44. Kumar, R.; Zheng, B.; Huang, K.-W.; Emert, J.; Faust, R. *Macromolecules* **2014**, *47*, 1959–1965.
45. Kostjuk, S. V. *RSC Advances* **2015**, *5*, 13125–13144.
46. Rajasekhar, T.; Emert, J.; Wolf, L. M.; Faust, R. *Macromolecules* **2018**, *51*, 3041–3049.
47. Harrison, J. J.; Young, D. C.; Mayne, C. L. *The Journal of Organic Chemistry* **1997**, *62*, 693–699.
48. Dyke, P.; Sutton, M.; Thiele, T.; Collins, M. *Organohalogen Compounds* **2006**, *68*, 1418–1421.
49. Dubois-Clochard, M.-C.; Durand, J.-P.; Delfort, B.; Gateau, P.; Barré, L.; Blanchard, I.; Chevalier, Y.; Gallo, R. *Langmuir* **2001**, *17*, 5901–5910.

BIBLIOGRAPHY

50. Chevalier, Y.; Dubois-Clochard, M. C.; Durand, J. P.; Delfort, B.; Gateau, P.; Barré, L.; Frot, D.; Briolant, Y.; Blanchard, I.; Gallo, R. In *Trends in Colloid and Interface Science XV*; Springer Berlin Heidelberg: Berlin, Heidelberg, 2001; Vol. 118, pp 110–114.
51. Spell, H. L. *Analytical Chemistry* **1969**, *41*, 902–905.
52. Bartha, L.; Hancsok, J.; Bobest, E. *Lubrication Science* **1992**, *4*, 83–92.
53. Cox, A. R.; Vincent, B.; Harley, S.; Taylor, S. E. *Colloids and Surfaces A: Physicochemical and Engineering Aspects* **1999**, *146*, 153–162.
54. Hancsók, J.; Bartha, L.; Baladincz, J.; Kocsis, Z. *Lubrication Science* **1999**, *11*, 297–310.
55. Chongxiang, X; Wei, X; Qiao, G *Petroleum processing and petrochemicals* **1999**, *03*.
56. Malins, E. L.; Waterson, C.; Becer, C. R. *RSC Advances* **2016**, *6*, 71773–71780.
57. Tang, Z.; Feng, Z.; Jin, P.; Fu, X.; Chen, H. *Industrial Lubrication and Tribology* **2017**, *69*, 683–689.
58. Naga, H. H. E.; Mohamed, M. M.; El Meneir, M. F. *Lubrication Science* **1994**, *6*, 351–361.
59. Spadaro, F; Rossi, A.; Lainé, E.; Woodward, P.; Spencer, N. D. *Tribology Letters* **2017**, *65*, 11.
60. Spadaro, F; Rossi, A; Lainé, E; Woodward, P; Spencer, N. *Applied Surface Science* **2017**, *396*, 1251–1263.
61. Gupta, M. K.; Bijwe, J. *Tribology International* **2018**, *127*, 264–275.
62. Nassar, A. M.; Ahmed, N. S.; Abd El-Aziz, K. I.; Abdel Azim, A. A. A.; El-Kafrawy, A. F. *International Journal of Polymeric Materials and Polymeric Biomaterials* **2006**, *55*, 703–713.
63. Kim, Y.; Kim, J.; Hyeon, D. H.; Han, J. S.; Chun, B.-H.; Jeong, B. H.; Kim, S. H. *Fuel* **2015**, *158*, 91–97.
64. Qin, Z.; Liu, Z.; Wang, L.; Zhang, X.; Fu, Y.; Xu, G.; Liu, G. *Energy & Fuels* **2020**, *34*, 5634–5640.
65. Mohamed, M. M.; Naga, H. H.A. E.; Meneiry, M. F. E. *Journal of Chemical Technology & Biotechnology* **1993**, *56*, 347–354.

66. Chávez-Miyauchi, T. E.; Zamudio-Rivera, L. S.; Barba-López, V. *Energy & Fuels* **2013**, *27*, 1994–2001.
67. Mena-Cervantes, V. Y.; Hernández-Altamirano, R.; Buenrostro-González, E.; Beltrán, H. I.; Zamudio-Rivera, L. S. *Fuel* **2013**, *110*, 293–301.
68. Ganc, J. R.; Nagarajan, R. In *SAE Technical Papers*, 1991.
69. Moritani, H.; Nozawa, Y. *The proceedings of the JSME annual meeting* **2000**, *4*, 347–348.
70. Taylor, R. I.; Evans, P. G. *Proceedings of the Institution of Mechanical Engineers, Part J: Journal of Engineering Tribology* **2004**, *218*, 185–200.
71. Pucci, A.; Rausa, R.; Ciardelli, F. *Macromolecular Chemistry and Physics* **2008**, *209*, 900–906.
72. Pirouz, S.; Wang, Y.; Chong, J. M.; Duhamel, J. *The Journal of Physical Chemistry B* **2014**, *118*, 3899–3911.
73. Spikes, H. *Tribology Letters* **2004**, *17*, 469–489.
74. Vipper, A.; Krein, S.; Bauman, V.; Tarasov, V. *Petroleum Chemistry U.S.S.R.* **1972**, *12*, 104–108.
75. Lashkhi, V.; Maryakhin, N.; Vipper, A.; Bauman, V. *Petroleum Chemistry U.S.S.R.* **1974**, *14*, 255–260.
76. Harrison, P. G.; Brown, P.; McManus, J. *Wear* **1992**, *156*, 345–349.
77. Kapur, G. S.; Chopra, A.; Ramakumar, S. S.; Sarpal, A. S. *Lubrication Science* **1998**, *10*, 309–321.
78. Bartha, L.; Deák, G.; Kovács, M.; Kocsis, Z.; Vuk, T. *Lubrication Science* **1997**, *9*, 173–180.
79. Masuko, M.; Ohkido, T.; Suzuki, A.; Ueno, T.; Okuda, S.; Sagawa, T. *Tribology Transactions* **2008**, *50*, 310–318.
80. Masuko, M.; Ohkido, T.; Suzuki, A.; Ueno, T.; Okuda, S.; Sagawa, T. In *Tribology and Interface Engineering Series*; Elsevier Masson SAS: 2005; Vol. 48, pp 769–777.
81. Aoki, S.; Masuko, M.; Suzuki, A. In *SAE Technical Papers*, 2007.
82. Zhang, J. Influence of Succinimide Dispersants on Film Formation, Friction and Antiwear Properties of Zinc Dialkyl Dithiophosphate., Ph.D. Thesis, 2010.

BIBLIOGRAPHY

83. Tabibi, M. Dispersant Effects on Zinc Dialkyldithiophosphate (ZDDP) Tribofilm Structure and Composition., Ph.D. Thesis, 2015.
84. Morina, A.; Neville, A.; Priest, M.; Green, J. *Tribology International* **2006**, *39*, 1545–1557.
85. Peeters, S.; Restuccia, P.; Loehlé, S.; Thiebaut, B.; Righi, M. C. *The Journal of Physical Chemistry A* **2019**, *123*, 7007–7015.
86. Guerret-Piécourt, C.; Grossiord, C.; Le Mogne, T.; Martin, J. M.; Palermo, T. *Surface and Interface Analysis* **2000**, *30*, 646–650.
87. Guerret-Piécourt, C.; Grossiord, C.; Le Mogne, T.; Martin, J.-M.; Palermo, T. *Lubrication Science* **2001**, *13*, 201–218.
88. Wei, D.; Song, H.; Wang, R. *Lubrication Science* **1991**, *4*, 51–72.
89. Ma, P. In *Lubricant Additives*; CRC Press: Third edition. — Boca Raton : CRC Press, Taylor & Francis Group, 2017., 2017, pp 67–85.
90. Papke, B. L.; Bartley, L. S.; Migdal, C. A. *Langmuir* **1991**, *7*, 2614–2619.
91. Papke, B. L.; Robinson, L. M. *Langmuir* **1994**, *10*, 1741–1748.
92. Papke, B. L.; Rubin, I. D. In *SAE Technical Papers*, 1992.
93. Kapur, G. S.; Chopra, A.; Sarpal, a. S.; Ramakumar, S. S. V.; Jain, S. K. *Tribology Transactions* **1999**, *42*, 807–812.
94. Yasutomi, S.; Maeda, Y.; Maeda, T. *Industrial & Engineering Chemistry Product Research and Development* **1981**, *20*, 530–536.
95. Stark, M.; Gamble, R.; Hammond, C.; Gillespie, H.; Smith, J. L.; Nagatomi, E.; Priest, M.; Taylor, C.; Taylor, R.; Waddington, D. *Tribology Letters* **2005**, *19*, 163–168.
96. Larsen, R. G.; Thorpe, R. E.; Armfield, F. A. *Industrial & Engineering Chemistry* **1942**, *34*, 183–193.
97. George, P.; Rideal, E. K.; Robertson, A. *Proceedings of the Royal Society of London. Series A. Mathematical and Physical Sciences* **1946**, *185*, 288–309.
98. George, P.; Robertson, A. *Proceedings of the Royal Society of London. Series A. Mathematical and Physical Sciences* **1946**, *185*, 309–336.
99. Stark, M. S.; Wilkinson, J. J.; Smith, J. R. L.; Alfadhl, A.; Pochopien, B. A. *Industrial & Engineering Chemistry Research* **2011**, *50*, 817–823.

100. Hammond, C. J.; Lindsay Smith, J. R.; Nagatomi, E.; Stark, M. S.; Waddington, D. J. *New Journal of Chemistry* **2006**, *30*, 741–750.
101. Jensen, R. K.; Korcek, S.; Mahoney, L. R.; Zinbo, M. *Journal of the American Chemical Society* **1979**, *101*, 7574–7584.
102. Jensen, R. K.; Korcek, S.; Zinbo, M. *Journal of the American Chemical Society* **1992**, *114*, 7742–7748.
103. Igarashi, J.; Jensen, R. K.; Luszyk, J.; Korcek, S.; Ingold, K. U. *Journal of the American Chemical Society* **1992**, *114*, 7727–7736.
104. Jensen, R. K.; Korcek, S.; Mahoney, L. R.; Zinbo, M. *Journal of the American Chemical Society* **1981**, *103*, 1742–1749.
105. Jensen, R. K.; Korcek, S.; Zinbo, M. *International Journal of Chemical Kinetics* **1994**, *26*, 673–680.
106. Jensen, R. K.; Korcek, S.; Zinbo, M.; Johnson, M. D. *International Journal of Chemical Kinetics* **1990**, *22*, 1095–1107.
107. Hamilton, E. J.; Korcek, S.; Mahoney, L. R.; Zinbo, M. *International Journal of Chemical Kinetics* **1980**, *12*, 577–603.
108. Blaine, S.; Savage, P. E. *Industrial & Engineering Chemistry Research* **1991**, *30*, 2185–2191.
109. Blaine, S.; Savage, P. E. *Industrial & Engineering Chemistry Research* **1991**, *30*, 792–798.
110. Blaine, S.; Savage, P. E. *Industrial & Engineering Chemistry Research* **1992**, *31*, 69–75.
111. Aguilar, G.; Mazzamaro, G.; Rasberger, M. In *Chemistry and Technology of Lubricants*; Springer Netherlands: Dordrecht, 2009, pp 107–152.
112. Jensen, R. K.; Korcek, S.; Zinbo, M.; Gerlock, J. L. *The Journal of Organic Chemistry* **1995**, *60*, 5396–5400.
113. Erdman, T. R. *SAE Transactions* **1981**, *90*, 37–48.
114. Lacarriere, A.; Seguelong, T.; Spivey, D.; DAS, A. In *SAE Technical Papers*, 2017.
115. Shurvell, H. F.; Clague, A. D. H.; Southby, M. C. *Applied Spectroscopy* **1997**, *51*, 827–835.
116. Blanksby, S. J.; Ellison, G. B. *Accounts of Chemical Research* **2003**, *36*, 255–263.

BIBLIOGRAPHY

117. Ruffell, J. E.; Farmer, T. J.; Macquarrie, D. J.; Stark, M. S. *Industrial & Engineering Chemistry Research* **2019**, *58*, 19649–19660.
118. *Oxidation Test For Engine Oils Operating In The Presence Of Biodiesel Fuel*; Coordinating European Council L–109–14: 2019.
119. *Standard Test Method for Determination of Moderately High Temperature Piston Deposits by Thermo-Oxidation Engine Oil Simulation Test—TEOST MHT*; ASTM International D7097-19: 2019.
120. Scanlon, J. T.; Willis, D. E. *Journal of Chromatographic Science* **1985**, *23*, 333–340.
121. Sternberg, J.; Gallaway, W.; Jones, D. In *Gas chromatography*, Brenner, N., Callen, J. E., Weiss, M. D., Eds.; Academic Press: New York, 1962, pp 261–217.
122. Capella, P.; Zorzut, C. M. *Analytical Chemistry* **1968**, *40*, 1458–1463.
123. Halket, J. M.; Zaikin, V. G. *European Journal of Mass Spectrometry* **2003**, *9*, 1–21.
124. Issariyakul, T.; Dalai, A. K. *Renewable and Sustainable Energy Reviews* **2014**, *31*, 446–471.
125. McCloskey, J. A.; McClelland, M. J. *Journal of the American Chemical Society* **1965**, *87*, 5090–5093.
126. Zaikin, V. G.; Halket, J. M. *European Journal of Mass Spectrometry* **2004**, *10*, 555–568.
127. Tessier, M; Maréchal, E. *European Polymer Journal* **1984**, *20*, 269–280.
128. Pucci, A.; Barsocchi, C.; Rausa, R.; D’Elia, L.; Ciardelli, F. *Polymer* **2005**, *46*, 1497–1505.
129. Shi, D.; Yang, J.; Yao, Z.; Wang, Y.; Huang, H.; Jing, W.; Yin, J.; Costa, G. *Polymer* **2001**, *42*, 5549–5557.
130. Nakason, C.; Kaesaman, A.; Supasanthitikul, P. *Polymer Testing* **2004**, *23*, 35–41.
131. Qiu, W.; Endo, T.; Hirotsu, T. *European Polymer Journal* **2005**, *41*, 1979–1984.
132. Richardson, W. H.; Yelvington, M. B.; Andrist, A. H.; Ertley, E. W.; Smith, R. S.; Johnson, T. D. *The Journal of Organic Chemistry* **1973**, *38*, 4219–4225.
133. Lamarque, G.; Cretenet, M.; Viton, C.; Domard, A. *Biomacromolecules* **2005**, *6*, 1380–1388.
134. Dasler, W.; Bauer, C. D. *Industrial & Engineering Chemistry Analytical Edition* **1946**, *18*, 52–54.

135. Coates, J. In *Encyclopedia of Analytical Chemistry*; John Wiley & Sons, Ltd: Chichester, UK, 2006, pp 1–23.
136. Pazur, R.; Troquet, M.; Gardette, J.-l. *Journal of Polymer Science Part A: Polymer Chemistry* **1997**, *35*, 1689–1701.
137. Shriner, R.; Ford, S.; Roll, L. *Organic Syntheses* **1931**, *11*, 28.
138. Li, Y.; Xie, X.-M.; Guo, B.-H. *Polymer* **2001**, *42*, 3419–3425.
139. Bettini, S. H. P.; de Mello, L. C.; Muñoz, P. A. R.; Ruvolo-Filho, A. *Journal of Applied Polymer Science* **2013**, *127*, 1001–1009.
140. Dong, Q.; Liu, Y. *Journal of Applied Polymer Science* **2003**, *90*, 853–860.
141. Zhao, Y.; Ma, Y.; Yao, W.; Huang, B. *Polymer Engineering & Science* **2011**, *51*, 2483–2489.
142. Luo, W.; Liu, X.; Fu, Y. *Polymer Engineering & Science* **2012**, *52*, 814–819.
143. Rao, H.; Zhang, Z. *Polymers for Advanced Technologies* **2008**, *19*, 770–774.
144. Chen, X.; Wu, H.; Yu, J.; Guo, S.; Luo, Z. *Polymer Engineering & Science* **2008**, *48*, 2289–2296.
145. Ma, P.; Jiang, L.; Ye, T.; Dong, W.; Chen, M. *Polymers* **2014**, *6*, 1528–1543.
146. Zhao, Y.; Han, L.; Li, D.; Xu, W. *Colloid and Polymer Science* **2017**, *295*, 463–469.
147. Snider, B. B.; Ron, E. *Journal of the American Chemical Society* **1985**, *107*, 8160–8164.
148. McMillen, D. F.; Golden, D. M. *Annual Review of Physical Chemistry* **1982**, *33*, 493–532.
149. Mahoney, L. R.; Ferris, F. C.; DaRooge, M. A. *Journal of the American Chemical Society* **1969**, *91*, 3883–3889.
150. Moad, G. *Progress in Polymer Science* **1999**, *24*, 81–142.
151. Kellou, M. S.; Jenner, G. *European Polymer Journal* **1976**, *12*, 883–887.
152. Russell, K. E. *Journal of Polymer Science Part A: Polymer Chemistry* **1995**, *33*, 555–561.
153. Giese, B. *Angewandte Chemie International Edition in English* **1983**, *22*, 753–764.
154. Caronna, T.; Citterio, A.; Ghirardini, M.; Minisci, F. *Tetrahedron* **1977**, *33*, 793–796.
155. Baban, J. A.; Roberts, B. P. *Journal of the Chemical Society, Perkin Transactions 2* **1981**, *33*, 161.

BIBLIOGRAPHY

156. Kumar, A. *Tribology and lubrication technology* **2019**, *75*, 20.
157. Duffield, A. M.; Budzikiewicz, H.; Djerassi, C. *Journal of the American Chemical Society* **1965**, *87*, 2913–2919.
158. Christiansen, K.; Mahadevan, V.; Viswanathan, C. V.; Holman, R. T. *Lipids* **1969**, *4*, 421–427.
159. Badertscher, M.; Bischofberger, K.; Munk, M. E.; Pretsch, E. *Journal of Chemical Information and Computer Sciences* **2001**, *41*, 889–893.
160. Bowles, A. J.; Brittain, E. F. H.; George, W. O. *Organic Mass Spectrometry* **1969**, *2*, 809–818.
161. Jalan, A.; Alecu, I. M.; Meana-Pañeda, R.; Aguilera-Iparraguirre, J.; Yang, K. R.; Merchant, S. S.; Truhlar, D. G.; Green, W. H. *Journal of the American Chemical Society* **2013**, *135*, 11100–11114.
162. Mielczarek, D. C.; Matrat, M. M.; Amara, A. B.; Bouyou, Y.; Wund, P.; Starck, L. *Energy & Fuels* **2017**, *31*, 12893–12913.
163. Chatelain, K.; Nicolle, A.; Ben Amara, A.; Catoire, L.; Starck, L. *Energy & Fuels* **2016**, *30*, 1294–1303.
164. Chatelain, K.; Nicolle, A.; Ben Amara, A.; Starck, L.; Catoire, L. *Energy & Fuels* **2018**, *32*, 9415–9426.
165. Pfaendtner, J.; Broadbelt, L. J. *Industrial & Engineering Chemistry Research* **2008**, *47*, 2886–2896.
166. Pfaendtner, J.; Broadbelt, L. J. *Industrial & Engineering Chemistry Research* **2008**, *47*, 2897–2904.
167. Frankel, E. *Progress in Lipid Research* **1984**, *23*, 197–221.
168. Frankel, E. *Progress in Lipid Research* **1983**, *22*, 1–33.
169. Knox, J. *Combustion and Flame* **1965**, *9*, 297–310.
170. Stark, M. S.; Waddington, D. J. *International Journal of Chemical Kinetics* **1995**, *27*, 123–151.
171. Ray, D. J. M.; Redfearn, A.; Waddington, D. J. *Journal of the Chemical Society, Perkin Transactions 2* **1973**, *94*, 540–543.
172. Denisov, E. T. *Kinetics and Catalysis* **2015**, *56*, 56–70.

173. Hodgson, J. L.; Coote, M. L. *Macromolecules* **2010**, *43*, 4573–4583.
174. Denisov, E. *Polymer Degradation and Stability* **1991**, *34*, 325–332.
175. Gryn'ova, G.; Ingold, K. U.; Coote, M. L. *Journal of the American Chemical Society* **2012**, *134*, 12979–12988.
176. Cope, A. C.; Foster, T. T.; Towle, P. H. *Journal of the American Chemical Society* **1949**, *71*, 3929–3934.
177. March, J., *March's advanced organic chemistry*, 4th ed.; Wiley: New Jersey, 1992.
178. Paine, M. R.; Barker, P. J.; Blanksby, S. J. *Analytica Chimica Acta* **2014**, *808*, 190–198.
179. Liauw, C. M.; Quadir, A.; Allen, N. S.; Edge, M.; Wagner, A. *Journal of Vinyl and Additive Technology* **2004**, *10*, 79–87.
180. Soltanahmadi, S.; Esfahani, E. A.; Nedelcu, I.; Morina, A.; van Eijk, M. C. P.; Neville, A. *Tribology Letters* **2019**, *67*, 80.
181. Global EV Outlook 2020, International Energy Agency, Paris, <https://www.iea.org/reports/global-ev-outlook-2020> accessed on 14/09/2020.
182. Farfan-Cabrera, L. I. *Tribology International* **2019**, *138*, 473–486.
183. Beyer, M.; Brown, G.; Gahagan, M.; Higuchi, T.; Hunt, G.; Huston, M.; Jayne, D.; McFadden, C.; Newcomb, T.; Patterson, S.; Prengaman, C.; Shamszad, M. *Tribology Online* **2019**, *14*, 428–437.
184. World Energy Outlook 2019, International Energy Agency, Paris, <https://www.iea.org/reports/world-energy-outlook-2019> accessed on 14/09/2020.

